Targeting Mitochondrial Metabolism as a Promising Therapeutic Strategy in Cancer

Megan Louise Stoker

St Peter's College





A thesis submitted for the degree Doctor of Philosophy

The University of Oxford

Nuffield Department of Women's and Reproductive Health

Trinity Term 2024

Word Count 50 000

Acknowledgements

Although the work in this thesis is my own, I could not have completed it without the people around me. I will forever be grateful for my family for their love and support, without which I would not have been able to study here at Oxford, which has always been a dream of mine.

First and foremost, I would like to thank my supervisor, Professor Karl Morten, for without him this project, and all I have learned along the way, would not have been possible. He greatly supported my academic development, both as a placement and a DPhil student, through the tough times of COVID restrictions and rowing pursuits. I would also like to give thanks to the rest of the Morten group: to Dr Tiffany Lodge and Janet Carver for their help and training in the laboratory and to Sarah, Edie, Inga, Holly, and Maisy for making the laboratory a highly enjoyable place to work. I would also like to thank the Poulton group for their support in the mitochondrial space, and to the rest of NDWRH for being such a friendly, welcoming, and social place to work.

I would like to thank those in the Department of Oncology who provided support with reagents and knowledge in the cancer space. In particular, thanks go to Professor Geoffrey Higgins, my secondary supervisor, as well as Dr James Hulit, who's array of collaborative work on NBS037 is truly impressive, and who's animal work made a whole chapter of my thesis possible. I would also like to thank Dr Jon Lees for his informatics data, which provided a key starting point for my work in the laboratory.

Rowing was a huge part of my Oxford experience. I would like to acknowledge the amazing women at OUBC, and all those at SPCBC, for being such great teammates and providing a challenging yet fun outlet from my research. I feel honoured to have spent so much time alongside such driven and inspirational women. In particular I would like to thank Zoi, Sophie,

Emily, Charlotte, Harriet, Esther, Sara, and Sophie for the constant morale support during my DPhil and rowing (and rowing retirement), through many a coffee and bubble tea. This DPhil has been by far the greatest challenge for me and I could not have achieved this without help of all my friends who also supported me along the way, whether from home, Bath or Oxford.

Finally, I would like to thank Harvey, who's love and support helped me through the latter half of my DPhil journey and made the end of university, and the huge world of life after university, a whole lot less daunting.

Declaration of authorship

I confirm that the entirety of the work presented in this thesis is my own unless otherwise stated, and does not constitute part of any other thesis. The work described here was carried out while I was a graduate student of the Nuffield Department of Women's and Reproductive Health working at the John Radcliffe Hospital Women's Centre, under the supervision of Professor Karl Morten and Professor Geoffrey Higgins.

Megan Stoker

10th May 2024

Abstract

Since the discovery of the Warburg effect in the 1920s, our understanding of cancer metabolism has evolved. Increasing evidence shows cancer cells are metabolically plastic systems, utilising both glycolysis and mitochondrial respiration (OXPHOS) to generate energy. OXPHOS is upregulated in some cancers and is a key feature of transition to metastatic disease, suggesting mitochondria are a vulnerability in subtypes of tumour and metastatic cells. Therefore, OXPHOS inhibitors may be a highly effective therapeutic strategy in these high OXPHOS cancers. We have developed one such OXPHOS inhibitor, NBS037, which exploits differences in mitochondrial biology between cancer and normal tissue. The specific mitochondrial targeting group allows targeted drug delivery, improving the therapeutic index and limiting the impact on normal tissue.

In this study, NBS037 treatment caused a significant decrease in cell viability and mitochondrial respiration in susceptible cancer cell lines, without increasing production of reactive oxygen species. Successful target engagement of mitochondrial ribosomes was observed, suggesting the mechanism of action lies in inhibition of mitochondrial protein translation, as expected. When tested in non-small cell lung cancer (NSCLC) xenograft models, NBS037 showed promising results in delaying tumour growth and synergised well with current standard of care treatments to potentiate their efficacy. *In vivo*, NBS037 had significant effects on mitochondrial mass, and subsequently the mitochondrial proteins, in tumour tissue but limited effects in normal tissue. These findings were coupled with evidence of increased cell death and alleviation of hypoxia in tumour, but more work is needed to fully validate the NBS037 mechanism of action *in vivo*.

Overall, this study shows preclinical data that the novel drug, NBS037, has promising anticancer activity and could be an effective treatment for some cancers as a single agent, or when used in combination with other chemotherapy agents.

Abbreviations

1,3BPG	1,3- bisphosphoglycerate
2DG	2-deoxy-D-glucose
2-HG	2-hydroxyglutarate
2PG	2-phosphoglycerate
3PG	3-phosphoglycerate
8-OHdG	8-hydroxy-2-deoxyguanosine
AA	Antimycin A
ADMET	Absorption, distribution, metabolism, and excretion–toxicity
ADP	Adenosine diphosphate
AKT	Protein kinase B
AML	Acute myeloid leukaemia
AMPK	AMP-activated protein kinase
ANOVA	Analysis of variance
ATCC	American tissue culture collection
ATP	Adenosine triphosphate
ATQ	Atovaquone
AZM	Azithromycin
BCA	Bicinchoninic acid
BSA	Bovine serum albumin
CAIX	Carbonic anhydrase IX
CAT	Carnitine-acylcarnitine translocase
CCCP	Carbonyl cyanide 3-chlorophenylhydrazone
CD31	Cluster of differentiation 31
c-Myc	Cellular myelocytomatosis oncogene
CO_2	Carbon dioxide
CoA	Coenzyme A
$CoCl_2$	Cobalt chloride
Complex I	NADPH:ubiquinone oxidoreductase
Complex II	Succinate dehydrogenase
Complex III	Ubiquinol–cytochrome c reductase
Complex IV	Cytochrome c oxidase
Complex V	ATP synthase
CoQ	Coenzyme Q
CPT	Carnitine palmitoyltransferase
CSC	Cancer stem cell
DAPI	4′,6-diamidino-2-phenylindole
DHAP	Dihydroxyacetone phosphate
DHE	Dihydroethidium
DLBCL	Diffuse large B-cell lymphoma
DMEM/F-12	Dulbecco's Modified Eagle Medium/Nutrient Mixture F-12
DMSO	Dimethyl sulfoxide
DNA	Deoxyribonucleic acid
ECAR	Extracellular acidification rate

ECM	Extracellular matrix
EDTA	Ethylenediaminetetraacetic acid
EGFR	Epidermal growth factor receptor
ERK	Extracellular signal-regulated kinases
ETC	Electron transport chain
F16BP	Fructose-1,6-bisphosphate
F6P	Fructose-6-phosphate
FAO	Fatty acid oxidation
FA	Fatty acid
FBS	Foetal bovine serum
FDA	Food and Drug Administration
G6P	Glucose-6-phosphate
GAP	Glyceraldehyde-3-phosphate
GLUT	Glucose transporter
GPx	Glutathione peroxidase
H_2O	Water
H_2O_2	Hydrogen peroxide
HIF-1	Hypoxia inducible factor 1
HK	Hexokinase
HRP	Horseradish peroxidase
IDH	Isocitrate dehydrogenase
IMM	Inner mitochondrial membrane
IMS	Intermembrane space
IV	Intravenous
LDA	Linear discriminant analysis
LDH	Lactate dehydrogenase
MAPK	Mitogen-activated protein kinase
MCT	Monocarboxylate transporter
MEM	Minimal essential media
mPTP	Mitochondrial permeability transition pore
mRNA	Messenger ribonucleic acid
MS	Mass spectrometry
MTD	Maximum tolerated dose
mtDNA	Mitochondrial deoxyribonucleic acid
MTOR	Mammalian target of rapamycin
MTT	3-[4,5-dimethylthiazol-2-yl]-2,5-diphenyltetrazolium bromide
NAD^+	Nicotinamide adenine dinucleotide
$NADP^+$	Nicotinamide adenine dinucleotide phosphate
NADH	Reduced nicotinamide adenine dinucleotide
NADPH	Reduced nicotinamide adenine dinucleotide phosphate
nDNA	Nuclear deoxyribonucleic acid
NMR	Nuclear magnetic resonance
NSCLC	Non-small cell lung cancer
$O2^{\cdot -}$	Superoxide
OCR	Oxygen consumption rate
OCT	Optimal cutting temperature

OMM	Outer mitochondrial membrane
OXPHOS	Oxidative phosphorylation
PBS	Phosphate-buffered saline
PCA	Principal component analysis
PDAC	Pancreatic ductal adenoma cells
PDVF	Polyvinylidene difluoride
PEP	Phosphoenolpyruvate
PET	Positron emission tomography
PFA	Paraformaldehyde
PFK-1	Phosphofructokinase 1
Pi	Inorganic phosphate
PI	Propidium iodide
PI3K	Phosphoinositide-3-kinase
PK	Pyruvate kinase
PNS	Peripheral nervous system
PPP	Pentose phosphate pathway
PTEN	Phosphatase and tensin homolog
PTP	Protein tyrosine phosphatases
R5P	Ribose-5-phosphate
REDOX	Reduction-oxidation
ROS	Reactive oxygen species
RPMI	Roswell Park Memorial Institute
rRNA	Ribosomal ribonucleic acid
RT	Room temperature
SDHA	Succinate dehydrogenase subunit A
SEM	Standard error of the mean
SOD	Superoxide dismutase
TAM	Tumour associated macrophage
TBST	Tris buffered saline with Tween-20
TCA	Tricarboxylic acid cycle
TIM	Translocase of the inner membrane
TMRM	Tetramethylrhodamine methyl ester
TOM	Translocase of the outer membrane
Tom20	Translocase of the outer membrane 20
TPP^+	Triphenylphosphonium cation
tRNA	Transfer ribonucleic acid
VEGF	Vascular endothelial growth factor
WB	Western blot
$\Delta\psi m$	Mitochondrial membrane potential

Table of Contents

1. Introduction: Mitochondria, Metabolism and Cancer 1

1.1 The mitochondrion 1

1.1.1 Mitochondrial structure 1

1.1.2 Mitochondrial function 3

1.1.2.1 Metabolism 3

1.1.2.2 Cell signalling 4

1.1.2.3 Apoptosis 5

1.2 Cell metabolism 6

1.2.1 Glycolysis 7

1.2.2 TCA cycle 9

1.2.3 OXPHOS 11

1.2.4 Fatty acid oxidation 14

1.3 Changes in cell metabolism are a hallmark of cancer 16

1.3.1 Warburg effect 16

1.3.2 Pentose phosphate pathway 19

1.3.3 OXPHOS 20

1.3.4 Reverse Warburg 21

1.3.5 Tumour microenvironment 23

1.4 Importance of mitochondrial metabolism in cancer 24

1.4.1 Synthesis of ATP and macromolecules 25

1.4.2 Survival in harsh tumour microenvironment 26

1.4.3 ROS signalling 27

1.4.4 Oncometabolites 28

1.4.5 Metastasis 29

1.4.6 Therapy resistance 30

1.5 Targeting OXPHOS as a therapeutic strategy 31
1.5.1 Repurposing old drugs 32
1.5.2 Novel OXPHOS inhibitors 34
1.6 Limitations in current drug therapies 36
1.6.1 Toxicity 36
1.6.2 Efficacy 37
1.6.3 Resistance and relapse 38
1.7 NBS037 45
1.7.1 Structure of NBS037 45
1.7.2 Proposed mechanism of action 47
1.7.3 NBS037 work to date 48
1.8 Aims and hypothesis 50
1.8.1 Overall hypothesis 50
1.8.2 Overall aim 50
1.8.3 Specific objectives 50

2 Materials and Methods 51
2.1 Cell culture 51
2.1.1 Cell growth and maintenance 51
2.1.2 Cryopreservation 53
2.1.3 Mycoplasma testing 53
2.1.4 Low glucose conditions 54
2.2 Drug treatments 54
2.3 Propidium iodide assay for cell viability 55
2.4 Oxygen consumption assay 55
2.4.1 Oxygen consumption at baseline 56
2.4.2 Oxygen consumption assay with acute NBS037 treatment 57

2.4.3 Oxygen consumption assay with chronic NBS037 treatment 57
2.5 Extracellular acidification assay 58
2.6 Dihydroethidium assay for reactive oxygen species production 59
2.6.1 DHE assay for acute drug treatment 59
2.6.2 DHE assay for chronic drug treatment 60
2.7 Tetramethylrhodamine methyl ester assay for mitochondrial membrane potential 60
2.8 JC-1 staining for mitochondrial membrane potential 61
2.9 ATP assay 62
2.10 Protein extraction from cultured cells 63
2.11 Protein extraction from frozen tissue 64
2.12 Protein quantification 64
2.13 Polyacrylamide gel electrophoresis and transfer to a polyvinylidene difluoride membrane 65
2.14 Immunoblotting and detection 65
2.15 Xenograft mouse studies (Hulit) 67
2.16 Cryosectioning 68
2.17 Immunofluorescence 69
2.18 Click-iT™ Plus TUNEL Assay 71
2.19 Single-cell Raman spectroscopy 72
2.20 Raman data pre-processing and analysis 73
2.21 Statistical analysis 74

3 The Effect of NBS037 *in Vitro* 76
3.1 Introduction 76
3.2 Aims 77
3.3 Selection of cell culture lines 78
3.4 NBS037 potently decreases cell viability in cancer lines 82

3.5 Glucose manipulation affects the sensitivity to NBS037 84

3.6 NBS037 has little effect in MRC-5 but reduces cell viability in ARPE-19 89

3.7 AZM lacking the mitochondrial targeting group does not decrease cell viability 92

3.8 Cellular bioenergetics may impact sensitivity to NBS037 95

3.9 Mitochondrial membrane potential does not explain differences in NBS037 sensitivity 99

3.10 NBS037 elicits a decrease in mitochondrial encoded protein expression in all lines but A549 101

3.11 SDHA expression is decreased in non-cancer lines upon NBS037 treatment 103

3.12 The ratio of mitochondrial encoded protein to nuclear encoded protein is largely decreased with NBS037 treatment 105

3.13 Tom20 expression tends to increase in A549 and decrease in H460 and ARPE-19 cells 107

3.14 Changes in respiratory proteins are not only caused by changes in mitochondrial mass 109

3.15 NBS037 inhibits respiration in NSCLC lines with 72-hour treatment 112

3.16 NBS037 decreases mitochondrial membrane potential in cancer lines 114

3.17 High doses of NBS037 increase ROS generation in H460 cells 116

3.18 NBS037 elicits an increase in SOD2 protein expression in A549 but a decrease in H460 and ARPE-19 lines 117

3.19 Aconitase expression tends to decrease with NBS037 treatment in H460 and MRC-5, but no significant effects are observed 120

3.20 Changes in antioxidant proteins are independent of changing Tom20 levels 122

3.21 Acute NBS037 treatment increases OCR at high doses 124

3.22 Acute NBS037 treatment has little effect on ROS generation 128

3.23 When used in combination with glycolysis inhibitor 2DG, NBS037 decreases cell viability further than when used as a single agent 131

3.24 High doses of 2DG deplete ATP 134

3.25 When used in combination with plasma concentrations of 2DG, NBS037 decreases cell viability in cancer and non-cancer lines 135

3.26 Discussion 140

3.26.1 Choice of cancer cell lines 140

3.26.2 Sensitivity to NBS037 140

3.26.2.1 Sensitivity to NBS037 in cancer cell lines 140

3.26.2.2 Sensitivity to NBS037 in non-cancer cell lines 143

3.26.3 NBS037 mechanism of action 145

3.26.3.1 AZM linked to a mitochondrially targeting sequence has enhanced efficacy compared to unconjugated AZM 145

3.26.3.2 Membrane dependent specificity 146

3.26.3.3 Mitochondrial proteins 146

3.26.3.4 OXPHOS capacity 149

3.26.3.5 Redox mechanisms 151

3.26.4 Adverse uncoupling effects 153

3.26.5 NBS037 in combination treatment 154

3.27 Future directions 155

3.28 Chapter summary 158

4 The Effects of NBS037 *in Vivo* 159

4.1 Introduction 159

4.2 Aims 162

4.3 Tumours successfully grew in nine mice out of twelve 162

4.4 Notable differences in bodyweight were observed between treatment groups 164

4.5 NBS037 has no effect on mitochondrial proteins in brain, heart and kidney tissue 166

4.6 NBS037 reduces mitochondrial protein and mitochondrial mass in liver 170

4.7 NBS037 reduces mitochondrial protein and mitochondrial mass in tumour 172
4.8 NBS037 exerts no significant effects on antioxidant protein with the exception of liver 175
4.9 Normal tissues show no clear evidence of change in cell death with NBS037 treatment 178
4.10 Cell death is increased in tumour, with differences observed between periphery and core of the tumour 182
4.11 Normal tissues maintain markers for cell proliferation with NBS037 treatment 185
4.12 Cell proliferation is upregulated in tumour compared to normal tissue, but is unaffected by NBS037 treatment 189
4.13 CD31 staining indicates vasculature is localised around the periphery of the tumour 191
4.14 Minimal 8-OHdG staining is observed in normal tissue 194
4.15 Tumours have upregulated ROS compared to normal tissue, but little change is observed with NBS037 treatment 198
4.16 NBS037 treatment decreases CAIX expression 200
4.17 Discussion 204
4.17.1 NBS037 tolerability 204
4.17.2 Mechanism of action 205
4.17.2.1 NBS037 selectivity 205
4.17.2.2 Mitochondrial proteins 205
4.17.2.3 Apoptosis and hypoxia 206
4.17.2.4 Redox mechanisms 209
4.18 Future directions 211
4.19 Chapter summary 215

5 Developing Raman Spectroscopy for Determination of Cell Metabolism 216

5.1 Introduction 216

5.2 Aims 218

5.3 Microscopic imaging indicates cellular health under different drug treatments 219

5.4 Spectral acquisition 222

5.5 Glucose manipulation creates distinct phenotypes in A549 and H460 cells 223

5.6 Use of metabolism inhibitors create distinct phenotypes in A549 and H460 229

5.7 Treatment with NBS037 creates distinct phenotypes similar to that of antimycin A in A549 cells 233

5.8 Treatment with NBS037 creates distinct phenotypes similar to that of antimycin A in H460 cells 239

5.9 Discussion 245

5.9.1 Generation of metabolic phenotypes 245

5.9.2 Separation of treated groups based off Raman spectra 246

5.9.3 Key biomolecules separating groups with differences in cell metabolism 248

5.9.4 Detection of NBS037 inside cells 249

5.9.5 Effects of NBS037 treatment on Raman spectra 252

5.9.6 Raman spectroscopy for analysis of cytochromes 254

5.10 Future directions 256

5.11 Chapter summary 259

6 Summary and future directions 260

6.1 Summary 260

6.2 Future directions 268

6.2.1 NBS037 mechanism of action 268

6.2.2 Improvement of *in vitro* models to test 268

6.2.3 Improvements in tissue analysis 269

6.2.4 Future animal studies 270

6.2.5 Further development of Raman spectroscopy in cell metabolism 271

6.3 Summary statement 271

Bibliography 273

Appendix 305

Appendix A. Full complex I gene ranking of cell lines conducted by Dr Jonanthan Lees (Oxford Brookes University) 305

Appendix B. Top contributing wavelengths separating treatment groups by LDA, comparing A549 and H460 cells under different glucose concentrations 315

Appendix C. Top contributing wavelengths separating treatment groups by LDA, comparing A549 cells under NBS037 and AA treatment 316

Appendix D. Top contributing wavelengths separating treatment groups by LDA, comparing H460 and A549 cells under NBS037 and AA treatment 318

Appendix E. Achievements throughout the duration of my DPhil 320

List of Figures

Figure 1.1 Mitochondrial structure 3

Figure 1.2. Glycolysis pathway 9

Figure 1.3 The TCA cycle 11

Figure 1.4. Structure of ETC 13

Figure 1.5. The β-oxidation of FAs in mitochondria 15

Figure 1.6. The reverse Warburg effect and metabolic symbiosis 23

Figure 1.7. The structure of NBS037 46

Figure 1.8. Proposed mechanism of action of NBS037 49

Figure 2.1. Treatment schedule in the SP237857 study 68

Figure 2.2. Workflow for Raman Spectroscopy and spectra analysis 74

Figure 3.1. Summary of data collected by Dr Jon Lees in ranking human cancer cell lines according to dependency on OXPHOS (complex I) 80

Figure 3.2. Growth curves of cancer cell lines with NBS037 treatment 84

Figure 3.3. Cell viability of cancer cell lines with NBS037 treatment in various glucose conditions 87

Figure 3.4. Cell viability of cancer cell lines with NBS037 treatment in various glucose conditions 88

Figure 3.5. Growth curves of non-cancer cell lines with NBS037 treatment 90

Figure 3.6. Cell viability of non-cancer cell lines with NBS037 treatment in various glucose conditions 91

Figure 3.7. Growth curves of cell lines with azithromycin treatment 93

Figure 3.8. Cell viability in cell lines with azithromycin treatment in various glucose conditions 94

Figure 3.9. The bioenergetics of chosen cell lines 96

Figure 3.10. Relative OXPHOS protein expression in NSCLC lines 98

Figure 3.11. Mitochondrial membrane potential in cell lines 100

Figure 3.12. MTCO1 protein expression in cell lines treated with NBS037 102

Figure 3.13. SDHA protein expression in cell lines treated with NBS037 104

Figure 3.14. Ratio of mitochondrially encoded protein expression to nuclear encoded protein expression with NBS037 treatment 106

Figure 3.15. Tom20 protein expression in cell lines treated with NBS037 108

Figure 3.16. ETC protein levels normalised to mitochondrial mass in cell lines treated with NBS037 111

Figure 3.17. Oxygen consumption in cells treated with NBS037 113

Figure 3.18. Mitochondrial membrane potential in cancer cell lines treated with NBS037 115

Figure 3.19. ROS generation in cell lines treated with NBS037 117

Figure 3.20. SOD2 protein expression in cell lines treated with NBS037 119

Figure 3.21. Aconitase protein expression in cell lines treated with NBS037 121

Figure 3.22. Antioxidant protein expression normalised to mitochondrial mass in cell lines treated with NBS037 123

Figure 3.23. Oxygen consumption in cells treated with NBS037 in 11 mM glucose 126

Figure 3.24. Oxygen consumption in cells treated with NBS037 in 1 mM glucose 127

Figure 3.25. ROS levels in cell lines with acute NBS037 treatment 130

Figure 3.26. Growth curves of cancer cell lines with a combination of NBS037 and 2DG treatment 133

Figure 3.27. ATP levels of cell lines with 2DG treatment. 134

Figure 3.28. Growth curves of cancer cell lines with a combination of NBS037 and 2DG treatment in 11 mM glucose 138

Figure 3.29. Growth curves of cancer cell lines with a combination of NBS037 and 2DG treatment in 1 mM glucose 139

Figure 4.1. The effect of NBS037 on H460 tumour growth in CD-1 mice 161

Figure 4.2. Tumour growth in CD-1 nude mice treated with PBS or NBS037 163

Figure 4.3 Body weight of CD-1 nude mice over the experimental period 165

Figure 4.4. Mitochondrial protein expression in brain lysates from PBS and NBS037 treated mice 167

Figure 4.5. Mitochondrial protein expression in heart lysates from PBS and NBS037 treated mice 168

Figure 4.6. Mitochondrial protein expression in kidney lysates from PBS and NBS037 treated mice 169

Figure 4.7. Mitochondrial protein expression in liver lysates from PBS and NBS037 treated mice 171

Figure 4.8. Mitochondrial protein expression in tumour lysates from PBS and NBS037 treated mice 173

Figure 4.9. Tumours do not display heterogeneity in mitochondrial protein expression between animals 174

Figure 4.10. SOD2 expression in tissue lysates from PBS and NBS037 treated mice 177

Figure 4.11. TUNEL staining for apoptosis in heart tissue 179

Figure 4.12. TUNEL staining for apoptosis in kidney tissue 180

Figure 4.13. TUNEL staining for apoptosis in liver tissue 181

Figure 4.14. TUNEL staining for apoptosis in tumour tissue 184

Figure 4.15. Ki67 staining for cell proliferation in heart tissue 186

Figure 4.16. Ki67 staining for cell proliferation in kidney tissue 187

Figure 4.17. Ki67 staining for cell proliferation in liver tissue 188

Figure 4.18. Ki67 staining for cell proliferation in tumour tissue 190

Figure 4.19. CD31 staining for endothelial markers in tumour tissue 193

Figure 4.20. 8-OHdG staining for ROS in heart tissue 195

Figure 4.21. 8-OHdG staining for ROS in kidney tissue 196

Figure 4.22. 8-OHdG staining for ROS in liver tissue 197

Figure 4.23. 8-OHdG staining for ROS in tumour tissue 199

Figure 4.24. CAIX expression in tumour tissue lysates from PBS and NBS037 treated mice 201

Figure 4.25. CAIX staining for hypoxia in tumour tissue 203

Figure 4.26. The effect of NBS037 and standard of care combination treatment on survival in H460 mouse xenograft models (Hulit). 214

Figure 5.1. Photon scattering patterns in Raman spectroscopy 218

Figure 5.2. Imaging of two NSCLC cell lines under various metabolism inhibitors 221

Figure 5.3. Key regions in Raman spectra 222

Figure 5.4. The effect of glucose in cell culture media on oxygen consumption in A549 and H460 NSCLC cells 223

Figure 5.5. The effect of glucose manipulation on Raman spectra in A549 and H460 NSCLC cells 226

Figure 5.6. The effect of glucose manipulation on biomolecules in A549 and H460 cells 228

Figure 5.7. The effect of metabolism targeting drugs on Raman spectra in A549 cells 231

Figure 5.8. The effect of metabolism targeting drugs on Raman spectra in H460 cells 232

Figure 5.9. Average spectral profile of NBS037 (Hutchinson) 233

Figure 5.10. The effect of OXPHOS inhibition on Raman spectra in A549 cells 234

Figure 5.11. The effect of OXPHOS inhibition on biomolecules in A549 cells 238

Figure 5.12. The effect of OXPHOS inhibition on Raman spectra in H460 cells 241

Figure 5.13. The effect of OXPHOS inhibition on biomolecules in H460 cells 244

Figure 5.14. Raman spectral profile of NBS037 and NBS037 treated NSCLC cells 251

Figure 6.1. The mechanism of action of NBS037 as suggested by this project 267

List of Tables

Table 1.1. Current OXPHOS inhibitors in development for cancer treatment 39

Table 2.1. Immortalised cell lines used in this project 52

Table 2.2. Drug treatments utilised in this study 54

Table 2.3. Primary antibodies used in this study 66

Table 2.4. Cutting temperatures on the cryostat for each tissue 69

Table 2.5. Primary antibodies used in immunofluorescence staining 71

Table 3.1. OXPHOS ranking of commonly used human cancer cell lines (data provided by Dr Jon Lees) 81

Table 3.2. IC50 (μM) of NBS037 in cancer cell lines tested at 72 hours 83

Table 3.3. IC50 (μM) of NBS037 in non-cancer cell lines tested at 72 hours 90

1

Introduction:
Mitochondria, Metabolism, and Cancer

1.1 The mitochondrion

Mitochondria, small intracellular organelles, are well known to every biologist as the "powerhouse" of the cell due to their vital function in synthesising adenosine triphosphate (ATP) through aerobic respiration. Much evidence suggests that mitochondria are derived from aerobic prokaryotes, which were once engulfed by eukaryotic cells[1]. The endosymbiotic relationship with the host eukaryote that ensued, caused the evolution from prokaryote into the mitochondrion[2], with mitochondria now ubiquitous in nearly every eukaryotic cell.

1.1.1 Mitochondrial structure

Mitochondria are bound by a double membrane, with a plethora of proteins populating both the outer mitochondrial membrane (OMM) and inner mitochondrial membrane (IMM). Such proteins act to transport cargo molecules as well as carry out its primary function in ATP generation through oxidative phosphorylation (OXPHOS). The electron transport chain (ETC)

is a series of five respiratory protein complexes on the IMM, which utilise the movement of electrons between proteins, and subsequent translocation of protons into the intermembrane space (IMS), to generate an electrochemical gradient (Figure 1.1)[3]. The electrochemical gradient is then used to drive ATP synthesis (see 1.2.3). To maximise the capacity to synthesise ATP, the IMM is folded to increase its surface area, and forms invaginations called cristae.

Alongside respiratory machinery, mitochondria possess their own genome consisting of 37 genes. Mitochondrial deoxyribonucleic acid (mtDNA) is located in the mitochondrial matrix and exists as a 16.6 kbp closed, circular, double-stranded DNA genome which encodes 13 messenger ribonucleic acids (mRNAs), two ribosomal RNAs (rRNA), and 22 transfer RNAs (tRNAs)[4]. Mitochondrial encoded mRNAs are translated by in house protein synthesis machinery to produce subunits of complex I, III, IV and V of the ETC. Protein synthesis machinery in mitochondria consist of 55S ribosomes, comprised of a 39S large subunit and 28S small subunit, which differs from the bacterial 70S and eukaryotic 80S ribosomes[5]. However, most of the proteins required for mitochondrial function are nuclear encoded and synthesised as preproteins in the cell cytosol, after which they are imported through translocases of the outer membrane (TOM) and translocases of the inner membrane (TIM) for use in the mitochondria. The entirety of complex II and the remaining subunits of complex I, III, IV and V are all encoded by nuclear DNA (nDNA). Although more similar in structure to bacterial DNA, mtDNA is also susceptible to the effects of mutations, aging, oxidative damage and damage through exogenous agents, similar to that of nDNA[6]. Very few mtDNA repair mechanisms exist in mitochondria, with base excision repair, double strand break repair, direct reversal, and mismatch repair the only known mechanisms[6]. When combined with a lack of introns and histones, mtDNA is particularly susceptible to DNA damage[7].

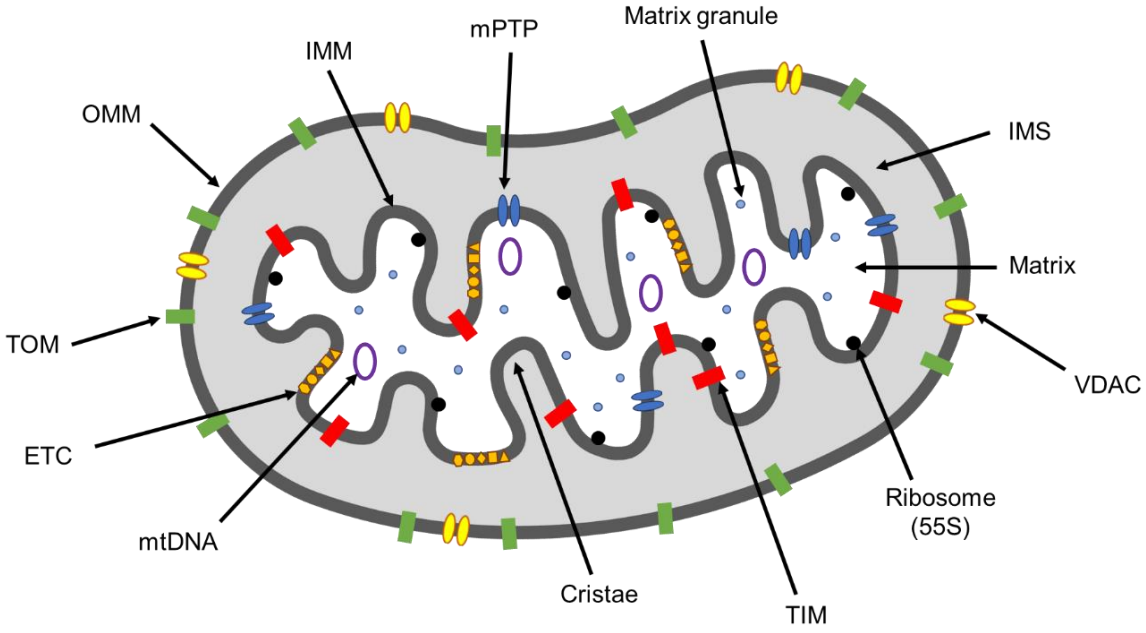

Figure 1.1. Mitochondrial structure. *Mitochondria are bound by a double membrane, with both membranes populated with a variety of proteins. Various components are contained within the mitochondrial matrix. Abbreviations are defined in the main text.*

1.1.2 Mitochondrial function

1.1.2.1 Metabolism

Mitochondria are crucial organelles for cell survival. The most notable function of mitochondria is the metabolism of a variety of substrates in order to generate large quantities of cellular ATP, predominantly from glucose and pyruvate metabolism. Aside from ATP production, mitochondrial metabolism has another role in the synthesis of biomolecule building blocks. The tricarboxylic acid (TCA) cycle produces key metabolites which are utilised for building macromolecules for cell growth (see 1.2.2). For example, citrate is an important carbon source for fatty acid (FA), cholesterol, and ketone body synthesis, with cholesterol also being a vital building block in hormones[8].

1.1.2.2 Cell Signalling

Mitochondria have a key role in cell signalling through a variety of pathways. In mitochondrial metabolism, reactive oxygen species (ROS) are a by-product of normal cell metabolism, and are essential for a variety of biological processes including maintenance of stem cells[9], differentiation, proliferation, and cell signalling[10]. ROS include the oxygen singlet, the superoxide anion ($O_2 \cdot^-$), hydrogen peroxide (H_2O_2) and the hydroxyl radical ($OH \cdot^-$). In some cases, ROS are formed when one electron is transferred to molecular oxygen, and the resulting free radical is converted to H_2O_2 by superoxide dismutase (SOD) enzymes[11]. Other enzymatic systems may generate H_2O_2 directly, from which $OH \cdot^-$ may be then be produced[12].

ROS are potent oxidising agents and contribute to the cellular reduction-oxidation (REDOX) state, the sum of all oxidising and reducing components within a cell, which are tightly balanced. ROS can oxidise important macromolecules such as proteins and lipids, as well as disrupt cellular signalling, so when produced excessively through upregulated metabolism, pharmacological agents, or environmental stressors, ROS can be damaging to cells. In this state, cells are in oxidative stress. Antioxidants populate the cell cytoplasm and mitochondrial matrix to detoxify excess ROS. SOD, catalase and glutathione peroxidase (GPx) are endogenous antioxidant enzymes, with highly protective effects against ROS and are therefore have key roles in health and disease[13]. With ROS tightly regulated, levels can be utilised for cell signalling. ROS are able to oxidise cysteine and methionine residues in REDOX sensitive proteins to change protein activity and conformation, leading to a change in signal transduction in a variety of proteins such as kinases, proteases, phosphatases, and transcription factors[14]. ROS can also directly alter the function and morphology of mitochondria, with low levels causing filamentation and higher levels causing mitochondrial fragmentation[15].

Metabolites from the TCA cycle can also act as second messenger molecules[16] which can affect gene expression and subsequent cellular activities. For example, acetyl-CoA can provide acetyl groups for acetylation of histones, thereby regulating chromatin dynamics[17]. Similarly, α-ketoglutarate (α-KG) is a required substrate for many histone modifying enzymes, and therefore α-KG availability impacts gene expression and cell fate[17]. Alongside α-KG, the TCA cycle metabolites succinate and fumarate have also been shown to be implicated in cellular gene expression and cell fate[17].

Mitochondria also conduct cell signalling through molecules which are not produced during metabolism. For example, mtDNA itself can act as a messenger molecule when released into the cell cytosol. MtDNA can activate the innate immune system through acting as a damage-associated molecular pattern, causing potent immunostimulatory effects[18,19]. Mitochondria also play a role in calcium signalling, through buffering of calcium to mitigate its propagation signals, controlling the magnitude of the response[20]. Calcium signalling has a vital role in cellular function from transduction of neuronal signals, to cell proliferation and gene transcription[21], therefore regulation through mitochondria is essential for many cellular processes.

1.1.2.3 Apoptosis

Mitochondria can initiate cell death through the intrinsic apoptotic pathway, where mitochondria release cytochrome *c*, as well as other IMS proteins, for caspase activation and constitution into the apoptosome[22]. Mitochondria may also regulate cell death through opening of the mitochondrial permeability transition pore (mPTP), a pore localised in the IMM which can open to allow diffusion of molecules across the membrane[23]. Sustained opening can cause severe disruption of OXPHOS and necrotic cell death as a result[24]. Activation of the mPTP can also cause osmotic dysregulation and subsequent swelling of mitochondria which can rupture the OMM and release cytochrome *c*, initiating apoptotic cell death[23].

1.2 Cell Metabolism

Metabolism refers to all of the biochemical reactions which take place for an organism to survive, and is subdivided into catabolism, the breakdown of complex molecules, and anabolism, the building of complex molecules[25]. The two types are coupled to one another, with metabolic reactions often forming interconnected pathways between one another. Cells utilise a variety of different metabolic pathways, dependent on the cell type, substrates available, and the environment around them such as oxygen availability and environmental stressors[25]. Such metabolic pathways act to convert food into chemical energy (ATP) which cells can use for cellular processes, synthesis of important macromolecules for growth, and removal of waste products.

Many key metabolic pathways are localised in the mitochondria. OXPHOS can be regarded as the most vital pathway due to its high yield of ATP to meet cellular ATP demands. Mitochondria also house the TCA cycle, which generates cofactors necessary for the ETC and metabolites utilised in anabolism of a variety of macromolecules. Mitochondrial β-oxidation of fatty acids (FAs) generates energy and provide cofactors for the TCA cycle during interprandial periods when other nutrients are limited. Mitochondria are also the site of glutamine catabolism, in which carbon atoms are incorporated into TCA cycle intermediates, amino acids, nucleotides, and lipids[26]. Mitochondria are also central in amino acid synthesis[27] and metabolism[28].

Whilst mitochondria are vital for a range of metabolic pathways, the cell cytosol encompasses all of the remaining pathways, some of which aid mitochondrial function. For example, glycolysis provides pyruvate necessary for the TCA, and the pentose phosphate pathway (PPP) functions to generate and ribose-5-phosphate (R5P) for nucleotide biosynthesis and contributes to the reduced nicotinamide adenine dinucleotide phosphate (NADPH) : nicotinamide adenine dinucleotide phosphate ($NADP^+$) ratio. Whilst the PPP does not directly

involve mitochondria, it is an important pathway for REDOX homeostasis, particularly by maintaining the NADPH : $NADP^+$ ratio during times of mitochondrial oxidative stress[29]. Additionally, the cytosol is the site of important metabolic pathways for carbohydrate, amino acid, nucleotide, and vitamin metabolism, alongside mitochondria.

1.2.1 Glycolysis

Glycolysis involves the metabolism of glucose into pyruvate, independent of oxygen levels in the surrounding environment. The biochemical reactions for glycolysis take place in the cell cytosol and are a central metabolic pathway conserved in all cells. Whilst the multistep process requires initial ATP investment, the reaction regenerates two molecules of ATP, two molecules of the cofactor NADH and two molecues of pyruvate per glucose molecule (Figure 1.2)[30].

Glucose is transported across the plasma membrane into the cell via glucose transporters (GLUTs) by means of facilitated diffusion[31]. Glucose is phosphorylated by hexokinase (HK), utilising a phosphate molecule from ATP as it is hydrolysed to adenosine diphosphate (ADP). This results in generation of glucose-6-phosphate (G6P) which cannot cross back through the cell membrane. Phosphoglucose isomerase then isomerises the G6P into fructose-6-phosphate (F6P). F6P is phosphorylated into fructose-1,6-bisphosphate (F1,6BP) by phosphofructokinase-1 (PFK-1), again utilising a phosphate molecule from ATP. Aldolase splits the F1,6BP into glyceraldehyde-3-phosphate (GAP) and dihydroxyacetone phosphate (DHAP). DHAP is rapidly converted into GAP by triose phosphate isomerase.

In the ATP earning stages of glycolysis, GAP is dehydrogenated into 1,3-bisphosphoglycerate (1,3BPG) by GAP dehydrogenase, a reaction which generates NADH. Phosphoglycerate kinase transfers a phosphate from 1,3BPG to ADP to create 3-phosphoglycerate (3PG) and ATP. 3PG is metabolised to 2-phosphoglycerate (2PG) by phosphoglycerate mutase. The final

reactions convert 2PG into phosphoenolpyruvate (PEP) by enolase, and further phosphorylation by pyruvate kinase (PK) into pyruvate. Glycolytic flux is regulated by HK, PFK-1, and PK, which all catalyse irreversible reactions and commits the fate of molecules throughout the pathway[32].

Glycolysis plays an important role in functional mitochondrial metabolism as the pyruvate and NADH generated are transported into the mitochondria for use in the TCA cycle. Under low oxygen conditions, or in cells which do not have mitochondria such as erythrocytes, glycolysis is a means to still create ATP. Here, the resulting pyruvate is converted into lactate via lactate dehydrogenase (LDH) during fermentation (differing from fermentation in microbial cells)[30]. Fermentation yields one molecule of lactate and one molecule of nicotinamide adenine dinucleotide (NAD^+) per pyruvate molecule (Figure 1.2), to be recycled into further glycolysis reactions.

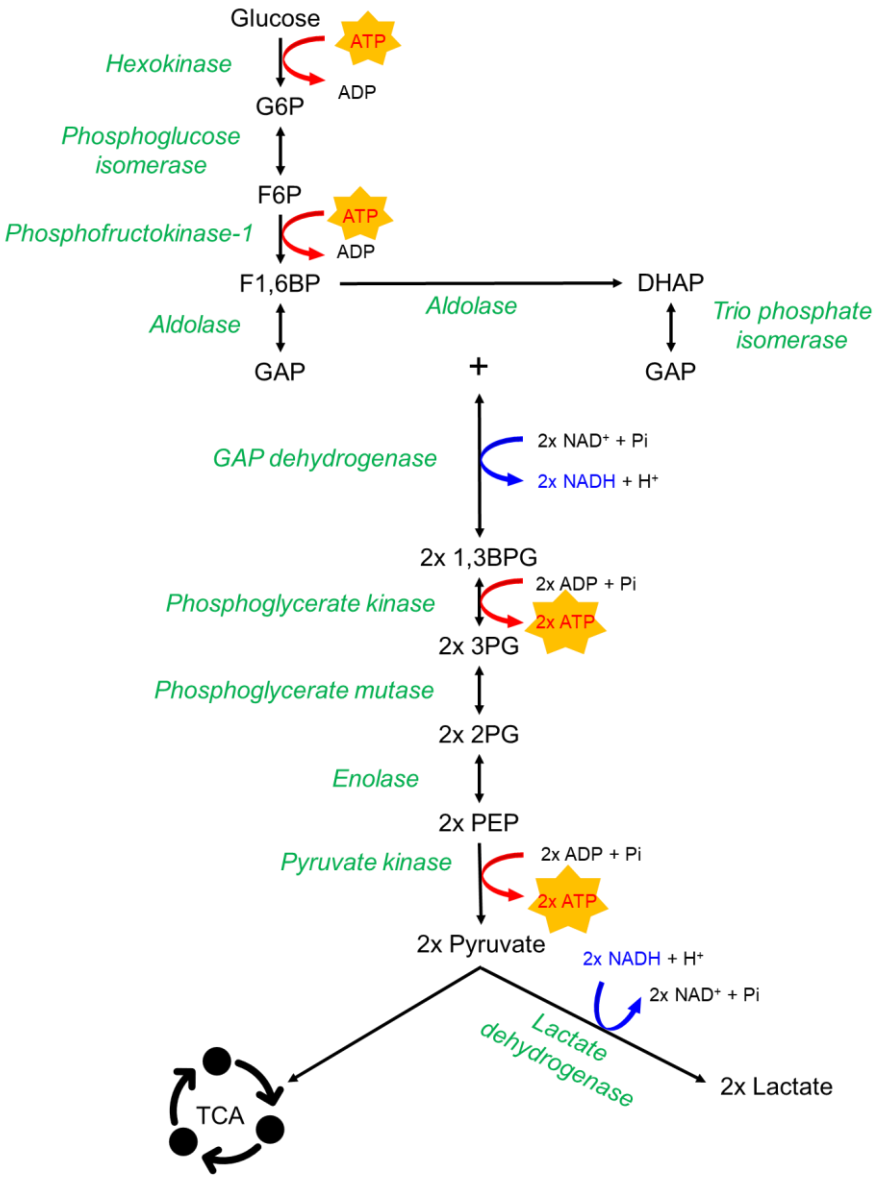

Figure 1.2. Glycolysis pathway. *Glucose metabolism into pyruvate is a multistep process involving multiple enzyme catalysed reactions. The resulting pyruvate is utilised in the TCA cycle or fermented into lactate depending on oxygen in the environment. Abbreviations are defined in the main text.*

1.2.2 TCA Cycle

The TCA cycle, commonly known as the Krebs cycle, is a series of enzyme catalysed reactions in the mitochondrial matrix. These reactions serve to produce the cofactors necessary for a functional ETC and ATP production through OXPHOS, as well as provide intermediate metabolites used as precursors for biosynthesis. The pyruvate generated from

glycolysis enters the mitochondria through voltage dependent anion channels (VDACs) on the OMM and through the IMM by the mitochondrial pyruvate carrier (MPC)[33].

In the matrix, pyruvate dehydrogenase converts pyruvate into acetyl-CoA, utilising the cofactors NAD^+ and CoA. NADH and carbon dioxide (CO_2) are released from the reaction. From here, acetyl-CoA enters the TCA cycle. Acetyl-CoA, along with water (H_2O), is combined with oxaloacetate to form citrate (citric acid) by citrate synthase. This 'first step' in the TCA cycle, is the rate determining step. The rate of TCA cycle will be limited by concentration of substrates and activity of citrate synthase, which is negatively regulated by ATP levels[34]. Citrate is isomerised into isocitrate by aconitase, and the resulting isocitrate is oxidatively decarboxylated by isocitrate dehydrogenase (IDH) into α-KG, yielding NADH and CO_2. Glutamine metabolism supports the TCA cycle in producing α-KG which feeds into the TCA reactions[35]. Glutamine enters the cell and is converted first into glutamate by glutaminase, which is then converted into α-KG by glutamate dehydrogenase. Alternatively, glutamine can undergo transamination by cellular transaminases to form α-KG during amino acid synthesis.

α-KG is converted into succinyl-CoA, again producing NADH and CO_2. Succinyl-CoA is converted to succinate by succinate-CoA synthase, yielding GTP from GDP and Pi during the reaction. Succinate dehydrogenase oxidises succinate into fumarate, passing electrons to flavin adenine dinucleotide (FAD) to form $FADH_2$. Fumarate is converted to malate by fumarase and subsequently malate is converted to oxaloacetate by malate dehydrogenase.

The TCA cycle will continue cycling through the various enzyme reactions until substrates diminish, with various intermediates also transported elsewhere for use in other metabolic pathways. NADH and $FADH_2$ are generated throughout the TCA cycle and are utilised in the ETC on the IMM, to act as electron donors for complex I and II respectively. In order to ensure continual turning of the TCA cycle, replenishment of TCA intermediates and acetyl-CoA may be provided by supplementary anaplerotic reations[36].

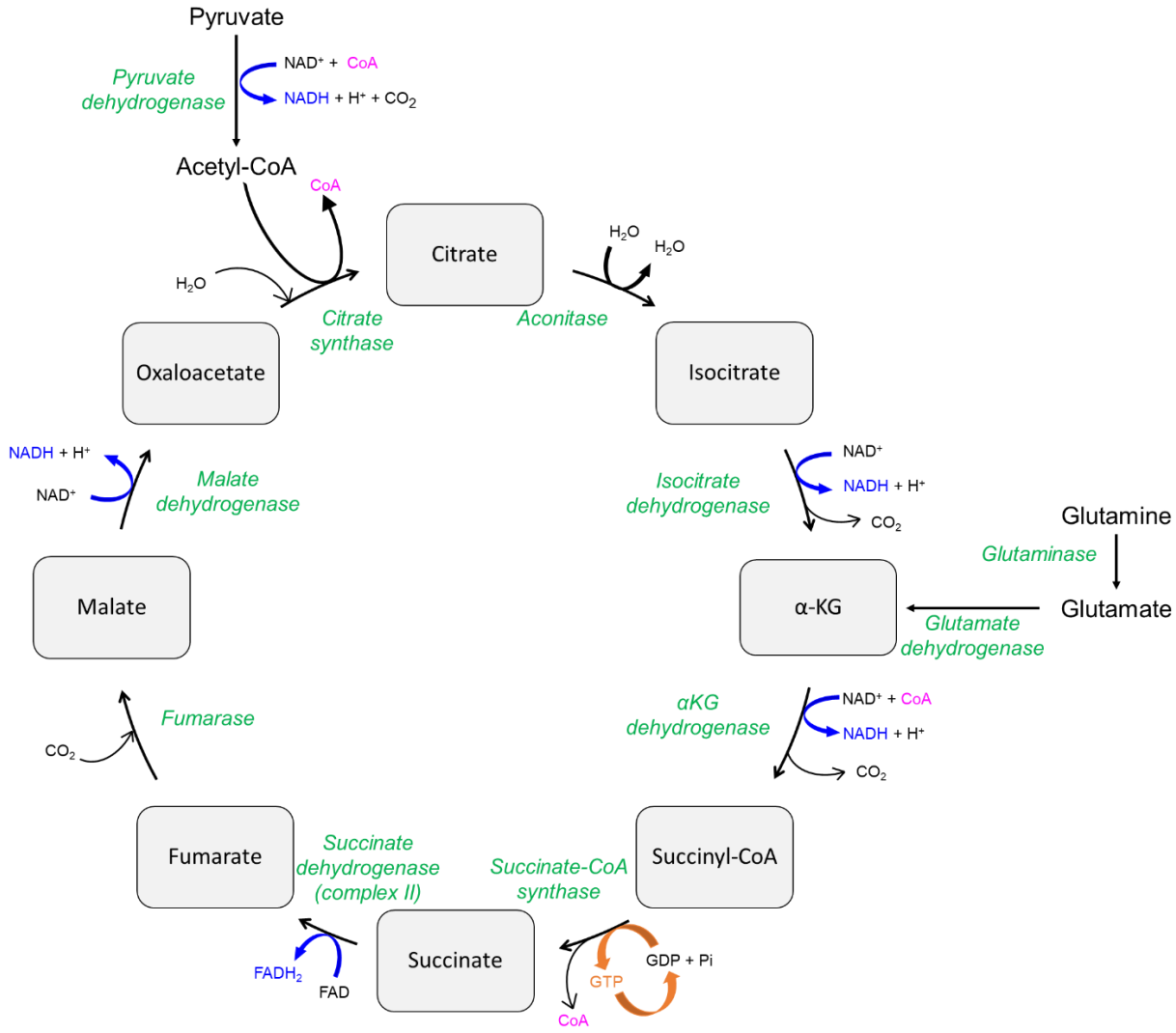

Figure 1.3. The TCA cycle*. The TCA cycle is a series of enzyme catalysed reactions which generate multiple metabolites and cofactors. Abbreviations are defined in the main text.*

1.2.3 OXPHOS

OXPHOS refers to the process by which ADP is phosphorylated oxidatively using the energy derived from the passage of high energy electrons along the ETC from reduced cofactors to oxygen. The ETC is a chain of four protein complexes which sit on the IMM: NADPH:ubiquinone oxidoreductase (complex I), succinate dehydrogenase (complex II), ubiquinol– cytochrome c reductase (complex III), and cytochrome *c* oxidase (complex IV), with a fifth respiratory complex, ATP synthase (complex V), the site of OXPHOS (Figure 1.4).

The ETC receives electrons from cofactors produced in the TCA cycle, where complex I, the largest and most complex of the respiratory complexes, oxidises NADH into NAD^+. This results in the transfer of a free pair of electrons to coenzyme Q (CoQ) (also known as ubiquinone)[37]. As the first enzyme reaction in the ETC, the REDOX reaction at complex I is often thought to be the rate limiting step of the ETC[37]. Simultaneously, complex II oxidises succinate to fumarate in the TCA, which reduces FAD. Complex II then oxidises $FADH_2$ into FAD and the pair of free electrons from the reaction are passed to CoQ to form reduced CoQ ($CoQH_2$). Complex II is not a proton pump so it does not transfer any protons to the IMS and contribute to the proton gradient formation[38].

$CoQH_2$ is oxidised by complex III, and the resulting free electrons are donated via cytochromes *b* and c_1 to cytochrome *c*, a small protein bound to the outer face of the IMM[38]. Cytochrome *c* can only transfer one electron at a time, resulting in the need for two electron donating cycles (Q cycles) in complex III[39], rather than a single electron transfer step as in complex I and II. Cytochrome *c* transfers its electron to complex IV. Complex IV deposits electrons onto molecular oxygen, the terminal acceptor of electrons, and when combined with free protons, water is created as a byproduct.

The electron transfer during these REDOX reactions provides energy for the transport of free protons from the matrix into the IMS[40]. As protons are pumped into the IMS by complex I, III and IV, a positive charge accumulates on the exterior of the IMM and an electrochemical gradient builds up. The electrochemical gradient, known as the proton-motive force, is a combination of both a pH gradient and electric potential gradient across the IMM[41]. An influx of protons back into the mitochondrial matrix via ATP synthase down the potential gradient provides the energy to drive the rotation of two rotary motors in ATP synthase. This provides the energy to synthesise ATP from ADP and P_i[41]. In mammals, the amount of ATP synthesised with respect to protons is 8 : 3 protons to ATP, therefore it is calculated that each mole of NADH results in the generation of 2.5 moles ATP, and a mole of $FADH_2$ generates 1.5 moles

ATP, resulting in approximately 31 ATP produced per glucose molecule oxidised[42]. This highlights the importance of mitochondrial metabolism as the key contributor of ATP to cells when compared to the lower yield of ATP synthesised in glycolysis.

As well as generating NAD^+, FAD, water, and ATP, OXPHOS is also the site of ROS synthesis. Under physiological conditions, 0.2-2% of electrons in the ETC leak out and interact with oxygen to form ROS[43]. ROS are generated predominantly through complex I[37] and complex III[39], with negligible amounts from complex II and complex IV[43].

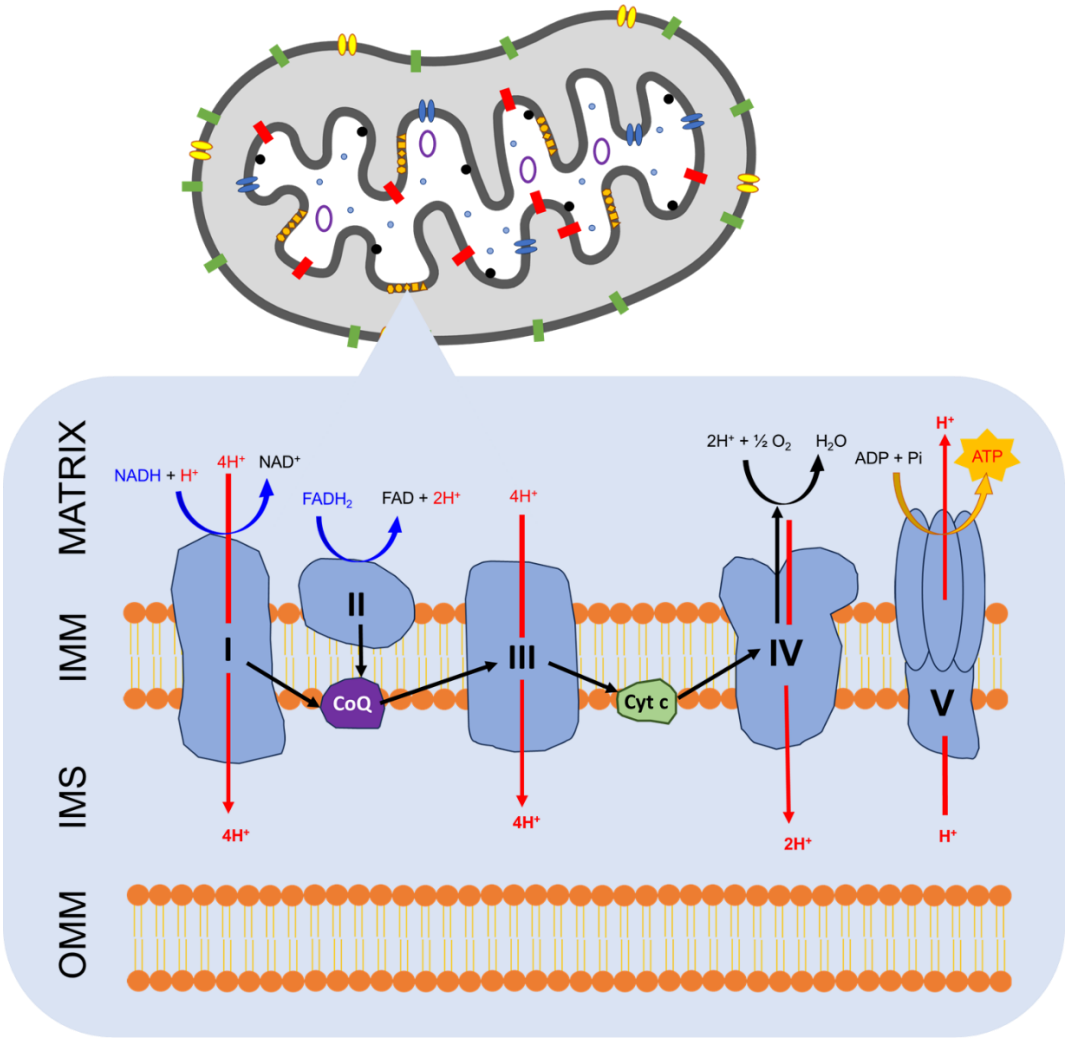

Figure 1.4. Structure of ETC. *Complexes I to IV sequentially transfer electrons, driving protons into the IMS, and forming an electrochemical gradient. Complex V then utilises the electrochemical gradient to drive ATP synthesis from ADP and Pi. Abbreviations are defined in the main text. Black arrows indicate movement of electrons and red arrows movement of protons.*

1.2.4 Fatty acid oxidation

Mitochondria are key organelles in the metabolism of plasma free FAs into acetyl-CoA via fatty acid oxidation (FAO), another aerobic process. FAO can be utilised as the preferred source of oxidising power to generate ATP in resting cardiac tissue as well as moderately exercising skeletal muscle, highlighting the heterogeneity of substrate use based on cell type[44]. FAO can also be utilised in fasting periods when glucose is in low availability, preserving glucose for use in the brain which cannot utilise FAs[44].

FAs are first converted to long chain acyl-CoA by acyl-CoA synthetase, requiring energy from ATP. Acyl-CoA cannot pass through the IMM, so carnitine is utilised as a shuttle. Carnitine palmitoyltransferase-1 (CPT-1) catalyses the conversion of acyl-CoA into acyl-carnitine in the IMS, though adding available carnitine. Acyl-carnitine is transported through the IMM by carnitine-acylcarnitine translocase (CAT) where it is metabolised back to acyl-CoA by CPT-2 on the IMM[44]. Carnitine is transported back into the IMS to be recycled in further reactions.

Inside the mitochondria, acyl-CoA dehydrogenase adds a double bond between carbon 2 (C2) and carbon 3 (C3) in FAD-dependent dehydrogenation. The resulting trans-2-enoyl-CoA is then hydrated by enoyl-CoA hydratase, which converts the double bond into a C3 hydroxyl group to form 3-hydroxyacyl-CoA[45]. 3-hydroxyacyl-CoA dehydrogenase converts the hydroxyl group into a ketone group in an NAD^+ mediated reaction to yield 3-ketoacyl-CoA. Finaly, thiolytic cleavage of the bond between C2 and C3 gives acyl-CoA with a shorter carbon chain length, and acetyl-CoA[46].

The shorter chain acyl-CoA can continue cycling through the FAO pathway, yielding shorter acyl-CoA molecules, until only two acetyl-CoA molecules are produced, or in the case of odd carbon chain length molecules, acetyl-CoA and propionic acid. In order to accommodate for the shorter length acyl-CoA substrates, FAO machinery contains various chain length specific

enzymes[45]. Acetyl-CoA then enters the TCA cycle, as well as the NADH and $FADH_2$ also produced.

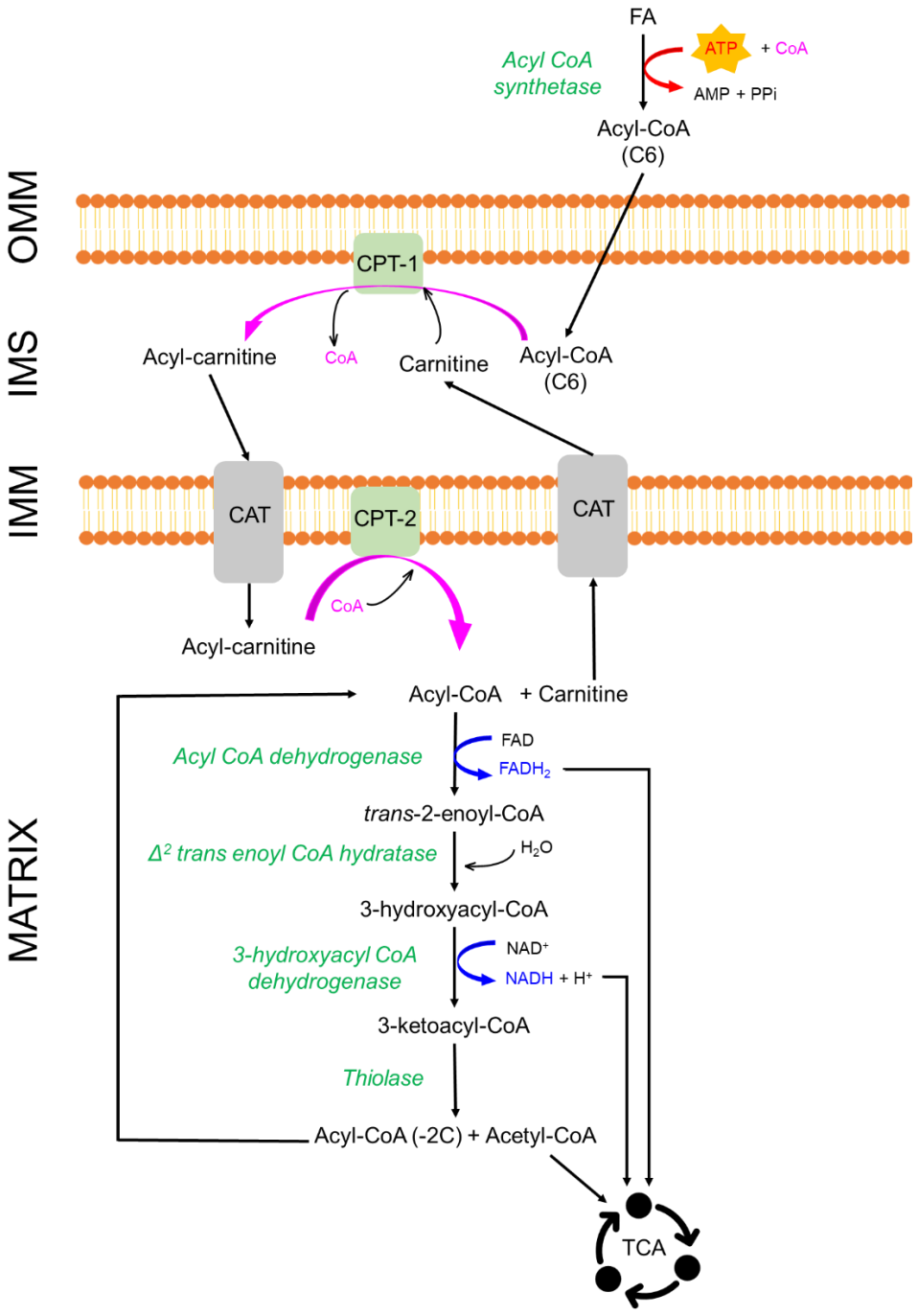

Figure 1.5. β-oxidation of FAs in mitochondria. *FAs are converted into acyl-CoA and shuttled into the mitochondrial matrix via a carnitine transporter. A series of enzyme catalysed reactions split the acyl-CoA into shorter chain acyl-CoA molecules which can be further oxidised. The acetyl-CoA produced in the process enters the TCA cycle. The cofactors $FADH_2$ and NADH are also produced for use in TCA cycle. Abbreviations are defined in the main text.*

1.3 Changes in cell metabolism are a hallmark of cancer

Cancer, one of the leading causes of death globally, is a multifaceted disease involving changes in a variety of cellular functions and behaviours in order to sustain a tumourigenic phenotype. Transition to a neoplastic state is defined by the acquisition of key hallmark behaviours according to Hanahan and Weinberg[47], which allow cancer cells to proliferate, survive, and disseminate. Whilst six key hallmarks were first suggested, recent evidence shows four additional attributes are necessary for cancer cell function, with the deregulation of cellular energetics proposed as an emerging hallmark of cancer[47,48]. Metabolic reprogramming aims to change the flux of metabolites into key pathways for tumourigenesis. Cancer cells increase their capacity to acquire nutrients and can change the metabolic pathways nutrients are assigned to, in order to produce metabolites which aid in biosynthetic pathways and gene regulation[49]. These mechanisms allow adaption to the environment and act as a driver for cancer cell growth and survival. Rewiring of cellular metabolism allows cells to sustain the energetic and biosynthetic demands of uncontrolled and chronic proliferation, as well as allow survival in the hostile and nutrient poor tumour microenvironment (TME)[50].

1.3.1 Warburg effect

Changes in cancer cell metabolism were first noted in the 1920s by Otto Warburg, who observed elevated lactate production and excretion in cancer cells from tumour slices compared to normal tissue. Furthermore, these malignant cells predominantly fermented glucose to lactate even in the presence of oxygen[51,52]. This phenomenon, named the ‘Warburg effect’, was considered a metabolic switch from OXPHOS to aerobic glycolysis, and suggested mitochondrial injury or dysfunction. The marked elevation in glucose uptake has later been used in diagnosis, providing the rationale behind Positron Emission Tomography (PET) scans

for cancer staging and is correlated to poor tumour prognosis[49]. Such findings led to the first ideas of targeting metabolism for cancer treatment, through starving cells of glucose[52].

The Warburg effect is driven by a range of cellular modifications in the early stages of cancer in response to cells shifting to a proliferative state. This allows cells to regenerate the cytosolic NAD^+ required for other cytosolic reactions[53]. Changes in glycolytic enzymes and glucose transporters are implicated in the Warburg effect. The master regulator of glycolytic enzymes is the transcription factor hypoxia inducible factor-1 (HIF-1). In normal cells, HIF-1 is only activated under hypoxia. The HIF-1α subunit is stabilised and translocated to the nucleus and upregulates expression of glycolytic enzymes and the glucose transporters GLUT1 and GLUT3[54]. Mammalian target of rapamycin (mTOR) is a serine/threonine kinase with a key role in regulating cell survival, growth, metabolism, and autophagy, however, in 70% of cancers, mTOR is aberrantly overactivated[55,56]. This occurs due to mutations in the mTOR gene leading to its overactivation, mutations in mTORC1 or mTORC2 resulting in overactive signalling, or mutations in upstream genes which include loss-of-function in tumour suppression genes or gain-of-function in oncogenes[57]. mTOR stimulates the upregulation of HIF-1 under normoxia, via phosphorylation of the transcription factors 4E-binding protein-1 and ribosomal protein S6 kinase-1, in order to increase HIF-1 synthesis and stimulate a shift to glycolysis even during normoxia[58]. In cancer, the cellular myelocytomatosis oncogene (c-Myc) is also deregulated, with elevated activity and expression. Such amplification results from duplications of the oncogene, single nucleotide polymorphisms enhancing c-Myc transcription, and enhanced MYC protein stabilisation[59.] In normal cells, c-Myc would be inhibited by HIF-1 but in cancer cells c-Myc associates with HIF-1 to further enhance the expression of glycolytic enzymes such as GAP dehydrogenase or HK2, the latter of which expression levels can be increased by up to 10 times that of normal cells to facilitate increased aerobic glycolysis[60,61]. HIF-1α also exerts effects on mitochondrial metabolism, inhibiting essential transcription factors for mitochondrial biogenesis for decreased mitochondrial mass and directly affecting the TCA

cycle[62]. HIF-1α can upregulate LDHA which enhances the conversion of pyruvate into lactic acid, diminishing flux into the TCA cycle to reduce OXPHOS[62].

As opposed to gain of function mutations in oncogenes, loss of function in tumour suppression genes can also play a role in cancer development and growth. p53 is a tumour suppressor gene which acts to suppress glycolysis through reduction in glucose transporters and PFK-1, as well as increasing expression of phosphatase and tensin homolog (PTEN) which inhibits the phosphoinositide 3-kinase (PI3K)/ protein kinase B (Akt)/ mTOR pathway[60]. Mutated p53 is the most common gene mutation in cancer[63], with loss of function of p53 driving increased glycolysis and reduced OXPHOS. Most data at present indicates wild type p53 supports OXPHOS in most cell types through enhancing oxidation of pyruvate into acetyl-CoA for the TCA cycle, enhancing anaplerotic reactions, enhancing mitochondrial biogenesis, and enhancing activity of the ETC via transcriptional regulation[64]. Loss of p53 therefore negatively impacts OXPHOS.

Although the Warburg effect has been extensively studied, the precise function of the glycolytic switch and subsequent benefits to cancer cells is yet to be fully understood. With glycolysis a less efficient method of ATP production, only yielding two ATP molecules per molecule of glucose, it is seemly counter intuitive that cells with high ATP demands would preferentially switch to glycolysis. However, the rate of glucose metabolism through aerobic glycolysis is far higher than mitochondrial metabolism, so ATP can be regenerated faster[65]. In larger tumours with hypoxic cores, the poor availability of oxygen would cause OXPHOS dependent cells to starve, giving glycolytic cells a selective advantage in oxygen depleted conditions.

The Warburg effect was also thought to aid the biosynthetic needs of the cell, in which increasing glucose metabolism increases the availability of carbon atoms for anabolic pathways and increases production of NADH[65,66.] However, with most of the pyruvate further converted into lactate, which utilises carbon atoms and the newly synthesised NADH, the role

of the Warburg effect for biosynthesis is limited[65]. To overcome this, the PPP is also deregulated in cancer and allows generation of reducing potential in the form of NADPH and nucleic acids (see 1.3.2)[67]. The fermentation process, converts NADH to NAD^+, regenerating the cofactor for use in continued and rapid glucose metabolism. The lactate produced also provides advantages for cancer cells through providing an alternative fuel for high OXPHOS cancer cells (see 1.3.4) and lowering the pH of the microenvironment which can enhance immune evasion and tumour invasiveness[68,69]. Acidosis also contributes to chemoresistance through neutralising drugs, improved removal of drugs through transporters and vesicles, and promoting chemotherapy resistance pathways[70].

1.3.2 Pentose phosphate pathway

The PPP, which acts parallel to glycolysis, is also dysregulated in cancer and has a key role in supporting cancer cell growth and survival[67]. The PPP consists of two branches of reactions, one being the oxidative branch which converts G6P into R5P for use in other reactions, and reducing potential in the form of NADPH. The non-oxidative branch is a bidirectional pathway between F6P + glycerol-3-phosphate and R5P, with all of the other metabolites functioning effectively as intermediates[71]. Key PPP enzymes such as G6P dehydrogenase, transaldolase, and transketolase are all upregulated in cancers through various oncogenic signalling pathways such as HIF-1α, p53, and PI3K/Akt/mTOR[71]. The NADPH generated in the PPP acts to maintain REDOX balance and is a crucial cofactor for other metabolic pathways, allowing sustained growth and proliferation particularly when under oxidative stress[29]. For cancer cells this is particularly important for maintaining controlled ROS levels, since they have naturally higher levels of ROS compared to normal cells[72]. R5P is an important precursor for many biomolecules, including nucleotides, in which R5P is utilised in both *de novo* purine synthesis and salvage synthesis pathways[73]. In conjunction with heightened glycolysis, enhancement of the PPP pathway allows cancer cells to meet their biosynthetic needs, and remains an important metabolic pathway for tumourigenesis.

1.3.3 OXPHOS

In recent years, evidence suggests that rather than 'respiratory injury', the Warburg effect is an early and rapid adaptation of cancer cells through oncogenic gain-of-function, and loss-of-function of suppressor genes, which allows cells to meet the biosynthetic and bioenergetic demands of a growing tumour[74]. Substantial data shows that OXPHOS and normal Krebs cycle persist in most malignant tumours, so the Warburg effect exists alongside functional mitochondrial respiration[75–78].

With an elevation in glycolysis leading to rapid generation of ATP, it is unsurprising that a downregulation of OXPHOS is observed in some cancers[17,49], often due to mtDNA mutations or reduced mtDNA content[79]. In poorly perfused, hypoxic regions of the tumour where there is limited oxygen to act as a terminal electron acceptor in the ETC, OXPHOS capacity will also be limited[80]. However, studies show OXPHOS is upregulated in some cancer types including melanoma, breast, B-cell lymphomas and prostate[81–83], with increased mtDNA content, increased oxygen consumption rate (OCR), increased expression of OXPHOS genes, and higher expression of OXPHOS proteins in malignant cells[79,81]. OXPHOS upregulation is also heterogenous within a cancer type, with OXPHOS high and OXPHOS low subtypes of cancers, and different spatial localisations of such subtypes within a tumour[84]. Cancer stem cells (CSCs) and metastatic cells also display a distinct metabolic phenotype which is predominantly OXPHOS driven[84].

Similar to the Warburg effect, upregulation of OXPHOS can be driven by genetic mutations. For example SMARCA4 is a commonly mutated subunit in the genomic SWI/SNF complex in lung cancers, and leads to enhanced OXPHOS and increased sensitivity to OXPHOS inhibition[85]. Similarly, non-small cell lung cancers (NSCLCs) with activation of oncogenic Kras or deletion of tumour suppressor LKB1 are also sensitive to OXPHOS inhibition[79,86]. It has

been shown deletions in retinoblastoma-1 gene upregulates OXPHOS in breast cancer[87] and mutations in IDH upregulates OXPHOS in acute myeloid leukaemia (AML)[88].

Other key aspects of mitochondrial metabolism are also vital in some cancer types, with FAO and glutamine metabolism proving to be key metabolic pathways in cancer through providing building blocks for biosynthesis, and energy in glucose depleted environments[89,90].

1.3.4 Reverse Warburg effect

Whilst cancer cells retain the capacity to utilise both glycolysis and OXPHOS for survival and tumourigenesis, some cells will predominantly utilise one or the other, giving cells a more glycolytic or OXPHOS phenotype[91]. An updated view on cancer cell metabolism highlights a phenomenon of metabolic crosstalk which occurs between cancer cells and cells in the TME, predominantly stromal cells and cancer associated fibroblasts (CAFs).

The Reverse Warburg effect suggests that cancer cells have the ability to induce oxidative stress in CAFs due to over production of ROS and subsequent DNA damage[92]. The resulting oxidative stress in CAFs helps drive further adaptions in their neighbouring cancer cells, causing these cancer cells to upregulate anti-apoptotic proteins and anti-oxidants, increasing their protection from cell death. CAFs upregulate HIF-1α during oxidative stress, driving the upregulation of aerobic glycolysis which produces energy rich fuels such as pyruvate, ketone bodies, and lactate[93]. Higher levels of HIF-1α also drives the upregulation of the monocarboxylate transporter (MCT), MCT-4, which is responsible for the export of lactate[94]. Lactate, as well as other energy rich fuels, is exported and consumed by the neighbouring cancer cells, which express the lactate importer MCT-1. Any lactate not consumed by neighbouring cells, remain in the extracellular matrix (ECM), causing acidification of the TME. Once consumed by cancer cells, lactate is converted to pyruvate in the cell cytoplasm by LDH,

and used in the mitochondria for the TCA cycle and OXPHOS[80]. These cancer cells can predominantly utilise lactate as an oxidative fuel rather than glucose, causing upregulation of OXPHOS in these cells[95] and subsequently spares glucose for glycolysis dependent cancer cells. Upregulated OXPHOS in these cancer cells causes further overproduction of ROS which results in further oxidative stress and HIF-1α expression in neighbouring CAFs. This leads to a cycle of exchanges between cancer and stromal cells. Activated CAFs also display heightened autophagy, leading to increased FA utilisation and release of alanine which can be utilised by cancer cells; therefore, the Reverse Warburg effect is not limited in providing only lactate for cancer cell utilisation, but also other metabolic intermediates[96].

A similar phenomenon is found within the tumour itself. Metabolic symbiosis exists between glycolytic cancer cells, the cells localised in areas of hypoxia, and OXPHOS driven cancer cells, cells localised close to the tumour vasculature and supply of oxygen[97] (Figure 1.6). In this manner, cancer cells can continue to survive and proliferate by supporting one another, as opposed to competing with one another for resources, which are already limited within the TME.

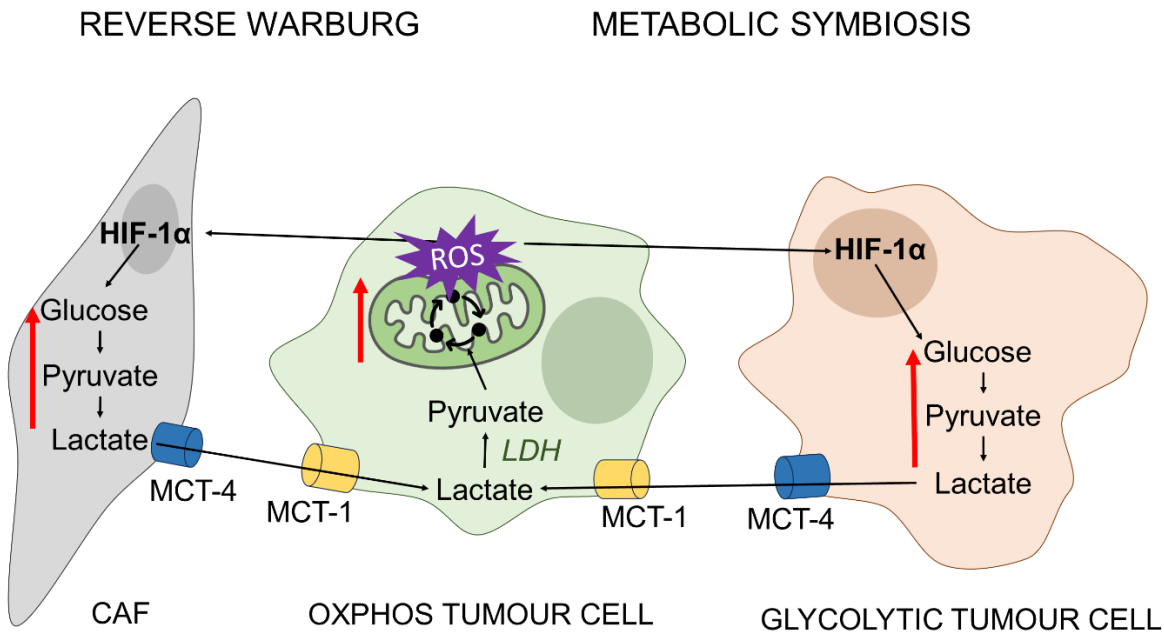

Figure 1.6. The Reverse Warburg effect and metabolic symbiosis. *Metabolic crosstalk exists between CAFs in the TME and cancer cells, known as the reverse Warburg effect. Overproduction of ROS in cancer cells leads to oxidative stress in neighbouring CAFs, leading to a glycolytic phenotype. Upregulated glycolysis, causes increased lactate production which is shuttled into the high OXPHOS cancer cells for use in the TCA cycle and OXPHOS. A similar phenomenon is observed within a tumour, with metabolic symbiosis between hypoxic cancer cells and oxygenated cancer cells. Red arrows denote upregulation. Abbreviations are defined in the main text.*

1.3.5 Tumour microenvironment

The TME, a complex environment containing immune cells, stromal cells, blood vessels and ECM, is an active promoter of cancer progression[98]. The supply of nutrients and oxygen in the TME is determined by the tumour vasculature, which does not exhibit uniform distribution across the tumour. Differences in nutrients and oxygen tension in the TME heavily shapes the metabolic adaptions in cancer cells, as cells adapt to utilise different substrates and metabolic pathways for sustained growth and proliferation[96,99]. In areas of limited vascular perfusion, acidosis and hypoxia drive further metabolic changes, and create an immunosuppressive environment, allowing cancer cells to evade immune destruction[96]. With dysregulated and accelerated metabolism, accumulation of metabolites in the TME also inhibit immune cell

functions. For example, high levels of adenosine accumulating in hypoxic and highly glycolytic regions of tumour can bind to A2 receptors in various immune cell types, inhibiting their anti-tumour functions[100]. As observed with the reverse Warburg effect, the TME does not only inhibit immune cells but can form a dynamic and reciprocal relationship with tumour cells in order to facilitate many of the key hallmarks of cancer. Non-cancer cells also contribute to metastasis through cytokine secretion and facilitation of ECM remodelling to promote a metastasis promoting environment[101].

Changes in cellular metabolism plays an important role in facilitation of metabolic plasticity, allowing utilisation of a range of nutrients dictated by the TME and adaption to overcome metabolism targeted chemotherapies. Dysregulated metabolism also permits intercellular signalling, and modelling of the extracellular tumour environment, to create an environment which facilitates growth, survival, and dissemination of cancer cells. Therefore, the metabolic cross-talk between different cell types in the TME is an important consideration in dysregulated cancer cell metabolism.

1.4 Importance of mitochondrial metabolism in cancer

After the Warburg effect was first noted in 1920s, it was assumed that cells upregulated glycolysis to compensate for mitochondrial injury and impaired OXPHOS in order to avoid ATP depletion. Emerging evidence shows that OXPHOS is vital for tumour cell survival through a variety of processes. In cancer, changes in mitochondrial metabolism are regulated by multiple oncogenes and tumour suppressor genes. These genes alter the metabolic pathways utilised, as well as the expression of fuel transporters and enzyme activity, with many cancers exhibiting mutations in key TCA cycle enzymes themselves[102].

1.4.1 Synthesis of ATP and macromolecules

Despite glycolysis being a faster means of ATP generation, OXPHOS still remains the most efficient means of ATP production, with over 30 molecules of ATP produced per molecule of glucose[66]. Cancer cells have a huge demand for ATP as growth signalling, driver gene activation, mTOR activation, DNA and RNA synthesis machineries and protein translation machineries all require ATP[66]. These demands must be sufficiently met and therefore mitochondrial metabolism still acts as a key contributor to ATP synthesis.

Furthermore, as previously mentioned, functional mitochondria and TCA cycle are essential for biosynthesis of macromolecules which are required for cancer cell proliferation and homeostasis[103]. For example, the generation of malate is a key process for NADH production[8] and citrate can be cleaved by ATP citrate lyase back into acetyl-CoA, which is used as a key building block in lipid and cholesterol synthesis[104]. Both aspartate and glutamine which are metabolised in the mitochondrial matrix, can be utilised for purine and pyrimidine biosynthesis to increase DNA synthesis and stimulate cancer growth[105]. Mutations in c-Myc and Kras drive glutamine metabolism into aspartate generating pathways to sustain high proliferation rates[105]. Other non-essential amino acids are also produced in the mitochondrial metabolism. Alanine is synthesised from pyruvate by glutamate–pyruvate transaminases, and glucose metabolism can be reprogrammed for serine and glycine synthesis[105].

Higher rates of glycolysis aid in increasing the flux of pyruvate into mitochondria for utilisation for biosynthesis, however the flux into biosynthetic pathways and ATP synthesis pathways must be balanced, as both require intermediates from the TCA cycle[106]. Removing TCA intermediates for biosynthetic pathways will naturally reduce the intermediates available for the ETC and ATP synthesis. To maintain high rates of ATP synthesis, anaplerotic reactions, for example those implicating glutamine and FA metabolism, are also upregulated for replenishment of TCA cycle intermediates[107].

1.4.2 Survival in the harsh tumour microenvironment

The uncontrolled cell proliferation in tumours, coupled with poor perfusion, leads to depletion of nutrients and build-up of metabolism by-products. This results in an increasingly harsh TME, characterised by hypoxia, acidosis, and nutrient competition. As discussed previously, these conditions can shape the metabolism of cancer cells and facilitate hallmarks of cancer, however, increasing evidence suggests functional mitochondrial metabolism is required for survival in these harsh conditions. For this reason, OXPHOS can occur even in hypoxic tissues with little oxygen, due to ROS dependent HIF regulation of metabolism and mitochondrial morphology. COX4, a subunit of complex IV which is usually regulated by oxygen levels, can be directly regulated by HIF[108], with complex I and II also modulated in order to prevent excessive ROS generation in hypoxia[109]. Furthermore, a CRISPR screen from Michl et al., (2022) showed 51 genes were required for cancer cells to survive at low pH, with many of these genes involved in mitochondrial metabolism and OXPHOS, such as NDUFS1, NDUFS2, NDUFA11, COX8A[110]. This is in agreement with other findings, showing mRNA levels of OXPHOS genes are upregulated at low pH, whilst glycolysis is inhibited, and the function of glycolytic genes become dispensible[111].

The deregulation of cellular energetics in cancer results in high metabolic plasticity, with these cells highly adaptable to the extracellular environment. In normal cells, OXPHOS is ultimately driven by catabolism of glucose into pyruvate to fuel ETC; however, with highly glycolytic CAFs and hypoxic cancer cells consuming large quantities of glucose, glucose in the TME becomes very sparse, particularly as many cells are too far from vasculature for glucose replenishment. In low glucose conditions, mitochondrial metabolism maintains cancer cell proliferation and survival due to utilisation of different fuels which are available in the TME such as lactate (see 1.3.4), glutamine, and FAs. It has been shown that cancer cells are ‘addicted’ to glutamine, with the amino acid utilised as a major energy source and a key building block for other macromolecules as it feeds into the TCA cycle[105,106,112].

1.4.3 ROS signalling

ROS, predominantly produced during OXPHOS or through exogenous carcinogens, have been heavily implicated in cancer initiation, survival, and progression. The importance of ROS in cancer is highlighted by the evidence that almost all cancers have upregulated ROS[72,113,114]. Oxidation and subsequent damage of DNA through ROS can result in genetic mutations, and when such mutations arise in key oncogenes or tumour suppressor genes, tumour initiation and progression can occur[115,116].

ROS act as a secondary signalling molecule in normal cells, as well as in transformed cells where ROS mediate mitogenic signalling[117]. For example, H_2O_2 activates epidermal growth factor receptor (EGFR), part of the receptor tyrosine kinase family, and inactivates protein tyrosine phosphatases (PTPs) which dampen EGFR signalling[118]. H_2O_2 also regulates downstream signalling molecules of EGFR pathway such as PTEN. PTEN acts as an inhibitor of the PI3K/Akt/mTOR survival pathway; however, ROS can oxidise and inactivate PTEN to give hyperactive survival signalling[119]. EGFR signalling and it's downstream Ras/Raf/ mitogen-activated protein kinase (MAPK) and PI3K/Akt/mTOR pathways terminate at nuclear targets which confer sustained cell growth, proliferation, migration, and differentiation in cancer. This results in EFGR over expression in many types of cancer, particularly lung, breast, and glioblastoma[114,120].

ROS signalling is also prominent in facilitation of metastasis (see 1.4.5) and angiogenesis. Angiogenesis, the process of new blood vessel formation from a pre-existing vessel, is a hallmark of cancer[47]. An efficient blood supply is needed in order for a tumour to grow more than a few millimetres, therefore tumours will stimulate angiogenesis through induction of proangiogenic factors such as vascular endothelial growth factor (VEGF) and matrix metalloproteinases[121]. Exogenous ROS leads to increased expression of VEGF in various cell

types and therefore increased stimulation of angiogenesis[121]. ROS induced activation of HIF-1α, which together with increased extracellular lactate, increases the transcription of proangiogenic genes in order to increase proliferation and survival of endothelial cells for vascular formation[122].

Whilst ROS signalling is highly important in cancer, excessive ROS production can lead to unrepairable DNA damage and apoptosis through ASK1/JNK and ASK1/p38 signalling pathways[123]. In hypoxic regions, HIF acts to remodel the ETC to dampen the overproduction of ROS[109] but ROS levels must also be balanced by antioxidants. ROS signalling can act on the transcription factors NF-κB and NRF2 which regulate the expression of antioxidants[124]. Catalase, glutathione, SODs, GPx, and S-transferases are all regulated by NFκB, and as a result, it is not uncommon for cancer cells to have higher levels of antioxidants than normal cells to combat their increased levels of ROS.

1.4.4 Oncometabolites

With deregulation of cellular energetics being a feature of all cancers, deregulation of cellular metabolites can be expected. In cancer, changes in metabolic pathways and mutations in TCA cycle enzymes result in abnormal production and accumulation of specific metabolites which can impact the TME and confer tumourigenesis. These are known as oncometabolites and can be produced by all cells in the TME, including malignant cells, CAFs, and tumour associated macrophages (TAMs)[125]. Many of these oncogenes are derived from the TCA cycle, including succinate, fumarate, 2-hydroxyglutarate (2-HG), and itaconate[126] which highlights the importance of OXPHOS albeit dysfunctional. Succinate is thought to exert its effects through increasing the accumulation of HIF-1α via an increase in HIF-1α transcription and inhibition of HIF-1α hydroxylation[125]. Succinate induced activation of extracellular signal-regulated kinases (ERK) and PI3K pathways, as well as transcription factor STAT3,

upregulates angiogenesis to enable survival of a growing tumour[125]. Due to its similarity in structure to succinate, fumarate is also able to confer tumourigenesis through stabilisation of HIF-1α[126]. Fumarate also acts to downregulate immune cells and inhibit secretion of proinflammatory cytokines for immunosuppression and evasion[125].

Oncometabolites also have the ability to cause epigenetic alterations. 2-HG, produced through oncogenic mutations in IDH enzymes 1 and 2, is found to alter the methylation pattern of DNA and histones, promoting tumourigenesis at the epigenetic level[127]. Succinate can also exert effects in this manner, with succinate able to inhibit DNA and histone demethylases to cause cancer promoting epigenetic changes[105,128]. Itaconate on the other hand, exerts different effects, whereby the metabolite is found to facilitate FAO, providing a fuel source for enhanced OXPHOS in the glucose deprived TME[129].

1.4.5. Metastasis

Many studies have shown that metabolic reprogramming and OXPHOS facilitates epithelial-mesenchymal transition (EMT) and metastasis[130], as well as metastasis subsequently shaping cell metabolism. Mitochondrial metabolism facilitates metastasis in many ways. There is evidence to show mitochondrial ROS can modulate cytoskeletal arrangements and promote invasion, adhesion, and EMT, whether through signalling mechanisms or transcriptional modifications to favour metastasis[17,131]. Furthermore, oncogenic mutations in succinate dehydrogenase and fumarate hydratase lead to accumulation of succinate and fumarate respectively. Both may act as retrograde signalling molecules and activate nuclear transcription factors to promote EMT[132]. In metastatic breast cancer, upregulation of OXPHOS and subsequent activation of SMAD activated transforming growth factor-β (TGFβ) signalling and MAPK pathways facilitated EMT[133]. Once disseminated, studies have shown circulating

tumour cells have enhanced mitochondrial biogenesis and respiration, indicating a reliance on OXPHOS for survival[134,135].

Whilst OXPHOS holds an important role in metastasis, this is not the same for all cancers. Gaude and Frezza (2016) conducted a genetic analysis of metabolic genes across 20 cancer types, and found suppression of mitochondrial genes was a key metabolic signature in metastatic melanoma and renal cancers, with downregulation of OXPHOS correlating to poorer clinical outcomes[136]. Similarly, analysis of over 180 RNA-seq cancer cell datasets shows a general trend of EMT correlating positively with glycolysis and negatively with OXPHOS and FA metabolism, but not in all cases[137]. This highlights the importance in considering cancer metabolic heterogeneity as different cancer types and subsets can behave differently from one another.

1.4.6. Therapy resistance

Resistance to therapy is the primary barrier to curing cancer, with populations of resistant cells remaining after treatment. These residual cells repopulate the original tumour, leading to poor survival rates and poor quality of life in patients. Drug resistance arises from the conditions in the TME, genetic mutations, and cellular drug removal via transporters; however, recent evidence indicates OXPHOS is necessary for acquired drug resistance and survival responses in a range of cancers when under treatment[88].

With the Warburg effect the first insight into cancer metabolism, many treatment efforts were focused on the inhibition of aerobic glycolysis, such as the use of BRAF and MAPK inhibitors which have downstream effects on the HIF-1 pathway. Cells undergoing treatment have been shown to switch metabolism from elevated glycolysis to elevated OXPHOS, allowing continued ATP synthesis and biosynthetic capabilities for cell growth[81,138].

OXPHOS is also highly important in resistance to immunotherapy. Immune checkpoint therapy has been highly successful in cancer treatment, through enhancing T-cell responses and subsequently inducing a response to treatment[88] . However, some patients do not respond to immune checkpoint inhibitors, and in the case of melanoma and melanoma brain metastases, non-responsive tumours had higher OXPHOS activity[139–141]. In cancers, resistance to immunotherapy is due to a combination of hypoxia and excessive ROS production. Both alter the metabolism and function of T-cells, which leads to an exhausted phenotype and the inability to exert cytotoxic effects on cancer cells[139]. High OXPHOS cancer cells consume the available oxygen in the TME, inducing hypoxia and limiting the efficacy of immunotherapies.

CSCs are a population of self-renewing progenitor cells which can differentiate and give rise to new populations of cancer cells. To maintain dormant and stemness properties, CSCs have a distinct metabolic phenotype which is predominantly OXPHOS[142]. Due to their dormant and slow-proliferating nature, CSCs are often therapy resistant as most cancer treatments target highly proliferating cells[143]. After treatment cessation, these circulating CSCs still remain, and with mitogenic signalling they are able to proliferate and form chemotherapy resistant tumours. CSCs are also metabolically plastic, and display rewiring of metabolism when metabolic inhibitors are utilised[142].

1.5 Targeting OXPHOS as a therapeutic strategy

Over the past decades, many drugs which have a significant impact on human health and disease have targeted metabolism, including statins, metformin, and SGLT2 inhibitors; however, effective cancer treatment remains an unmet clinical need. Although targeting the immune system is proving an effective treatment, the formidable ability of cancer cells to develop resistance mechanisms necessitates new therapeutic approaches. With mitochondrial metabolism an essential component of cancer progression, a range of drugs targeting mitochondrial function are in development[144]. These efforts include inhibition of

oncometabolite production[145,146], knockdown of proteins involved in mitochondrial dynamics[147,148], and disruption of REDOX homeostasis[149]. However, as OXPHOS is vital in a variety of processes supporting tumourigenesis, many drugs which target proteins of the ETC are in development. To inhibit OXPHOS, the TCA cycle is also a promising therapeutic target, as a non-functioning TCA cycle cannot provide cofactors needed for a functional ETC and OXPHOS. Efforts to target the TCA cycle include inhibition of glutaminolysis and inhibition of specific enzymes, particularly those which produce oncometabolites[107,150]. For this project, drugs directly targeting OXPHOS and respiratory protein complexes will be discussed.

1.5.1 Repurposing old drugs

Targeting mitochondrial metabolism is not a novel concept in therapeutics. Many other diseases implicate mitochondria and utilise ETC inhibitors for treatment. As these drugs are already approved by the Food and Drug Administration (FDA) and available on the market, some have been repurposed for cancer treatment, including antipsychotics, antimalarials, antivirals, and antidiabetics[151]. The most notable is metformin, a biguanide used as an antidiabetic. For diabetes treatment, the metformin induced inhibition of complex I results in the activation of the AMP-activated protein kinase (AMPK) pathway. AMPK inhibits transcription of key genes for gluconeogenesis and stimulates glucose uptake in muscle, resulting in decreased blood glucose levels[152]. In 2005, an observational case-control analysis of over 11000 patients with type 2 diabetes showed a 23% reduction in incidence rate of cancer in metformin users[153]. Later studies showed metformin had an anti-proliferative effect in a range of cancer cells, both *in vitro* and *in vivo*[154], due to its activation of AMPK. AMPK acts as a tumour suppressor through modulating energy levels, activating p53 apoptotic cell death programs, and reducing insulin levels[155]. Multiple Phase I, II, and III clinical trials have been conducted as a result, testing metformin in non-diabetic cancer patients (see Table 1.1). Anticancer outcomes with few side effects have been reported[156,157], showing encouraging

data that metformin can be used to both prevent disease and decrease mortality in cancer. However, late-phase efficacy studies testing metformin as a cancer therapeutic have been disappointing, and subsequently led to a diminished interest in testing metformin in cancer, and a halt in progressing this therapeutic strategy[158].

Atovaquone (ATQ), an antimalarial, also exerts its effects through inhibition of OXPHOS. ATQ binds directly to the transmembrane cytochrome *bc*1 complex of complex III in the ETC, diminishing OXPHOS, increasing ROS, and shifting cells to a more glycolytic phenotype[159]. In parasites, the reduction in OXPHOS causes ATP deficiencies and alterations of metabolites in the pyrimidine biosynthetic pathway[160], resulting in parasitic death. ATQ has recently gained interest for its use in cancer and is currently being tested as a radiosensitiser. ATQ inhibition of OXPHOS results in a reduction in oxygen consumption and alleviation of tumour hypoxia[161]. Tumour hypoxia facilitates tumour cell survival and confers resistance to both chemo- and radiotherapy treatment attempts, therefore diminished hypoxia acts to sensitise cells to insults[161,162]. When tested in a Phase I clinical trial of 30 patients (NCT02628080), ATQ was able to increase tumour oxygenation and inhibit hypoxia gene expression with no adverse side effects, indicative that anti-tumour effects may be possible at the mRNA level[163].

Antibiotics have recently gained increasing interest in the cancer space, with many different types of antibiotics being tested for cancer treatment. The most well studied is use of doxorubicin, which interrupts DNA synthesis and repair mechanisms, and has promising anti-tumour effects in a variety of cancers such as liver, lung, gastric, lymphoma, and breast[164]. However, some antibiotics have off target effects on mitochondria, which could be harnessed for cancer therapy[164]. Macrolide and tetracycline antibiotics inhibit the 50S and 30S subunits of the bacterial ribosomes respectively, which prevents translation of mitochondrially encoded proteins[165,166]. With mtDNA predominantly coding for proteins in the OXPHOS subunits, OXPHOS is heavily inhibited across complex I, III, IV, and V. The subsequent mitochondrial

dysfunction leads to bacterial cell death[166]. With the protein translation machinery in mitochondria resembling that of bacteria, antibiotics may also act on mitochondrial ribosomes, inhibiting OXPHOS with no effect on the eukaryotic ribosomes in the cytosol. OXPHOS inhibition and mitochondrial dysfunction would cause cancer cell death through a variety of mechanisms. Such mechanisms may include ATP depletion, increased oxidative stress and induction of apoptotic pathways, cell cycle arrest, and activation of both mitophagy and autophagy[167]. Antibiotics are currently in clinical trials for cancer treatment, testing OXPHOS inhibition at the mitochondrial protein translation level as a therapeutic strategy. For example, tigecycline has been tested in a Phase I clinical study in patients with AML (NCT01332786, n=27) where maximum tolerated dose could be deduced; however, sustained target inhibition was not observed and no clinical response recorded[168].

Other FDA approved drug classes have also been tested as potential cancer treatments including statins, anticestodes, and antipsychotics, but each with their limitations so are yet to be administered routinely for treatment of cancers (see Table 1.1).

1.5.2 Novel OXPHOS inhibitors

With new OXPHOS drug targets being explored, groups have not only attempted to repurpose old drugs, but also synthesise new ones, with enhanced specificity and efficacy. IACS-010759 is a small molecule OXPHOS inhibitor, which binds to the quinone binding channel of the complex I ND1 subunit[169]. Promising anticancer effects were observed with IACS-010759 *in vitro*, shown by decreases in oxygen consumption and decreased cell viability in glycolysis deficient cancer cells and AML cells[169]. Consequently, IACS-010759 was tested in dose-escalation Phase I trials to assess safety and tolerability in advanced solid tumours and lymphoma (NCT03291938, n=23), and to test efficacy in AML (NCT02882321, n=17)[170]. IACS-010759 treatment resulted in only a modest and transient reduction in OXPHOS and

anti-tumour effects[170] and therefore both trials were halted. IACS-01059 was also tested as a potential synergistic therapy alongside AZD3965, a MCT-1 inhibitor, resulting in a simultaneous inhibition of glycolysis and OXPHOS in diffuse large B-cell lymphoma (DLBCL). Monotherapy treatments were able to induce a cytostatic response whilst combination therapy was able to induce DLBCL cell death[171]. Noble et al., (2022), showed combination treatment of IACS-010759 and AZD3965 markedly improved the tumour response with 10/10 tumour regressions at the end of the treatment period, whilst single-agent treatment saw no regressions[171].

With metformin demonstrating promising results in cancer treatment, a novel biguanide, IM156, was developed and tested in Phase I clinical trials in patients with advanced solid tumours (NCT03272256, n=22)[172]. Again, only modest clinical activity was observed so further work for IM156 is needed in OXPHOS dependent tumours. IM156 may also be a good candidate for combination treatment with clinically used agents, which when given alone cause compensatory increases in mitochondrial metabolism. These compensatory increases in OXPHOS would then be inhibited by IM156.

One approach for disease treatment now relies upon targeted delivery of therapeutic agents to mitochondria via a mitochondriotropic carrier, which may include lipophilic cations driven by potential gradient, or mitochondria-targeting peptides[173]. Mitochondrial targeted antioxidants were first synthesised at the start of the century, with the natural antioxidant α-tocopherol linked to a lipophilic cation (MitoVitE)[174]. MitoQ, SkQ1, Mito-chromanol, and MitoTEMPO, all mitochondrial targeted antioxidants, have since been developed for use as potential cancer therapies[175,176]. Similarly, OXPHOS inhibitors have also been included as cargo for mitochondrial targeted drug delivery. In an attempt to enhance the efficacy of metformin, various analogues have been created, which feature a positively charged triphenylphosphonium (TPP^+) group to specifically target mitochondria[177]. Cheng et al. (2016)

showed the analogue Mito-Met_{10} was 1000-fold more effective than metformin alone in inhibiting the proliferation of pancreatic ductal adenoma cells (PDACs) *in vitro*, with limited effects in non-malignant cells. When tested *in vivo*, Mito-Met_{10} inhibited PDAC tumour growth and was more potent than metformin alone in sensitising the PDACs to radiotherapy. These findings were accompanied by complex I inhibition, reduced oxygen consumption, and increased ROS production in treated PDACs[178].

1.6 Limitations in current drug therapies

Current strategies in targeting mitochondrial metabolism in cancer have some encouraging preliminary results; however, many have limited clinical potential, highlighted by diminished efficacy during *in vivo* studies or unsatisfactory Phase I trials.

1.6.1 Toxicity

With mitochondria and their metabolism important in the vast majority of somatic cells, it is unsurprising that side effects occur with use of OXPHOS inhibitors. With heart, muscle, kidney, adrenal gland, liver, and brain tissues harbouring the greatest expression of OXPHOS genes, these organs are particularly susceptible to OXPHOS inhibition and related toxicities[179]. Cardiotoxicity has been reported with doxorubicin and cisplatin use[180], neuropathy with IACS-010759[170], and hepatotoxicity associated with many mitochondrial agents[181]. IM156 was better tolerated than some mitochondrial agents, only causing mild symptoms of nausea in 73% of patients and other gastrointestinal issues affecting half of the patient cohort[172]. The most frequent side effect in mitochondrial targeted agents, and the cause for many trials to halt, is the onset of lactic acidosis. Cells shift their metabolism to upregulate glycolysis upon the inhibition of OXPHOS and subsequent energy deficiency, which causes increased production

of lactic acid. High levels of lactate production over a prolonged period increases the potential to develop lactic acidosis, a life threatening condition characterised by elevated arterial lactate and lowered arterial pH[182]. Elevated lactic acid contributed to the discontinuation of both Phase I trials of IACS-010759, as 50% of AML trial patients with elevated lactic acid developed lactic acidosis. Phase I studies of the complex I inhibitor ASP_{4132} (NCT02383368, n=39) showed a third of patients experienced increased serum lactate, two further developed lactic acidosis, and more dose limiting toxicities were observed[183]. Whilst metformin has no such effects, phenformin from the same biguanide family but with higher potency and bioavailability[184], was withdrawn from clinical use in 1977 due to causing hundreds of cases of acidosis with 50% fatality rate[182,185].

1.6.2 Efficacy

Metformin acts as proof that OXPHOS inhibitors can be well tolerated in patients; however, metformin is non-specific and has low efficacy in cancer, with some cancer patients non-responders to metformin treatment[186]. Many of its encouraging anti-tumour results *in vitro* relied upon supra physiological doses which cannot be maintained in patients[187]. Similarly, a Phase I trial of VLX600 in advanced solid tumours was terminated in 2018 due to lack of efficacy, despite the drug being well tolerated (NCT02222363, n=19)[179]. Furthermore, OXPHOS inhibitors harbouring toxicities have highly limited doses and dosing schedules so administration tends to be intermittent and interrupted to mitigate any toxicity[188]. This leads to a lack of efficacy and poorer outcome measures. As an added complexity, tumours display metabolic heterogeneity, with differences in metabolism between tumours of the same type and cells within the same tumour. This heterogeneity leads to OXPHOS high and OXPHOS low subsets of cells and would highly impact the response to OXPHOS inhibitors[189].

1.6.3 Resistance and relapse

Tumour recurrence and treatment resistance are key barriers to successful cancer treatment, with tumours often growing again after a period of disease remission[190]. Whilst OXPHOS is vital in chemoresistance mechanisms (see 1.4.6), cancer cells can also become resistant to OXPHOS inhibition. Tumours show metabolic plasticity, a process driven by mitochondrial signalling[191,192] which leads to easy adaption and the use of alternative biosynthetic or bioenergetic pathways if a particular metabolic pathway is targeted in treatment. With drug induced OXPHOS deficiencies, compensatory upregulation of glycolysis allows tumour cell survival, shown by the increased serum lactate and risk of lactic acidosis observed with some OXPHOS inhibitors[193–195]. Furthermore, several studies utilising novel small molecule OXPHOS inhibitors showed these drugs had limited efficacy when glucose, and glycolytic capacity, was available[196]. Whilst OXPHOS inhibitors can prevent tumour relapse through targeting of OXPHOS driven CSCs which lay dormant[190], the lack of efficacy attributed with some OXPHOS inhibitors could cause tumour relapse. This may occur when some, but not all, of the primary tumour and CSCs are eradicated[197], leaving cells available to proliferate into a new tumour.

Table 1.1. Current OXPHOS inhibitors in development for cancer treatment.

Drug	Drug Class	Target Complex	Stage	Trial Number	Limitations as Anticancer Agent	References
ADDA5	Small molecule inhibitor	IV	Preclinical		Further optimisation of doses required.	[198]
AG311	Small molecule inhibitor	I	Preclinical		Steep dose response curve.	[199]
Angiostatin	Statin	V	Phase I, II	NCT00086723 NCT00049790	Requires combination treatment as it only targets angiogenesis.	[200]
Apoptoldin	Macrolide antibiotic	V	Preclinical		More work on mechanism of action required.	[201]
Arsenic trioxide	Chemotherapy	IV	Phase II	NCT00045565	A larger cancer panel to test is required.	[202]
ASP_{4132}	Small molecule AMPK activator	I	Phase I (discontinued)	NCT02383368	Increased serum lactate and lactic acidosis.	[195]
Atorvastatin	Statin	I, III	Phase II	NCT02029573	Used as therapy sensitiser so not effective enough as single agent.	[203]

Atovaqone	Antimalarial	III	Phase I	NCT02628080	Lack of efficacy alone so used as radiosensitiser.	[163]
BAY 87-2243	Small molecule inhibitor	I	Phase I (discontinued)	NCT01297530	Lack of efficacy alone so used as radiosensitiser, treatment schedule needs further work.	[204–207]
Bedaquiline	Antibiotic	V	Preclinical		Lack of efficacy in some cancer types.	[208]
Canagliflozen	Antidiabetic	I	Phase II	NCT04073680	Used as combination treatment so lack of efficacy alone.	[209,210]
Carboxyamidotriazole		I	Preclinical		Lack of efficacy alone, needs to be used in combination.	[211,212]
Chlorpromazine	Antipsychotic	V	Phase II	NCT04224441	Cholestasis.	[213]
Deguelin	Rotenoid	I	Preclinical		Multiple adverse side effects.	[214,215]
Fenofibrate		I	Preclinical		Studies *in vivo* required before clinical trials.	[216,217]
Gboxin		V	Preclinical		Limited studies to date.	[218,219]
IACS -010759	Small molecule inhibitor	I	Phase I (discontinued)	NCT03291938 NCT02882321	Neuropathy, elevated lactic acid.	[170,220,221]

IM156	Small molecule inhibitor	I	Phase I (discontinued)	NCT03272256	Nausea, fatigue, gastrointestinal issues.	[222]
Kalkitoxin	Biologically active lipopeptide	I	Preclinical		Limited studies to date.	[223]
Lonidamide		II	Phase I, II, III		Adverse effects led to dose modifications and patients removed from the study.	[224–226]
ME-344	Isoflavonoid	I	Phase I	NCT02806817	Some cancers are intrinsically resistant.	[227,228]
Metformin	Biguanide antidiabetic	I	Phase I, II, III	NCT04114136 NCT04275713 NCT02394652	Lack of efficacy, slow accrual, hepatotoxicity.	[213,229–234]
Mito-ATQ	Small molecule inhibitor from ATQ	I, III	Preclinical		Optimisation of linker length required.	[235–237]
Mito-HNK	Small molecule inhibitor from honokiol	I	Preclinical		Well tolerated, but lack of efficacy in mice.	[238]

Mito-LND	Small molecule inhibitor from lonidamine	I, II	Preclinical		Low toxicity, but only tested in a few studies.	[238]
Mito-MGN	Small molecule inhibitor from magnolol	I	Preclinical		No detailed toxicology studies completed as of yet.	[238]
Mito-Met	Small molecule inhibitor from metformin	I	Preclinical		Studies *in vivo* required before clinical trials.	[239,240]
Mito-Tamoxifen	Small molecule inhibitor from tamoxifen	I, III, IV, V	Phase I	EuraCT 2017-004441-25	Anaemia was a statistically significant adverse effect, with two deaths from thrombocytopenia and stroke.	[241,242]
Mito-TPP-Tig-NP	Small molecule inhibitor from tigecycline	I, III, IV, V	Preclinical		Limited studies to date.	[243,244]
MS-L6	Small molecule inhibitor	I	Preclinical		Limited studies to date. Molecule exerts potent upregulation of glycolysis and	[245]

					lactate production in cancer cells which may cause adverse effects in patients.	
Mubritinib		I	Phase I (discontinued)	NCT00034281	Cardiotoxic.	[246]
Neoantimycin F		III	Preclinical		Studies *in vivo* required before clinical trials.	[247]
Niclosamide	Anticestode	I, II, III, IV, V (ETC uncoupler)	Phase I, II	NCT02687009 NCT05188170 NCT02519582	Poor oral bioavailability, low plasma concentrations achieved.	[248–250]
Nitric Oxide		IV	Phase II	NCT01210378 NCT01171170	Difficulty in uniform delivery, can stimulate mitogenic pathways.	[251,252]
Oligomycin	Macrolide antibiotic	V	Preclinical		Clinical trials required.	[253,254]
OPB-51602	Small molecule inhibitor	I	Phase I	NCT01184807 NCT01344876 (discontinued)	Nausea, peripheral sensory neuropathy, gastrointestinal issues, increased lactic acid, lack of efficacy long term.	[193,255,256]

Papaverine	Vasodilator	I	Phase I	NCT03824327	Used as a radiosensitiser only, effects on cell signalling need to be further elucidated.	[257]
Phenformin	Biguanide antidiabetic	I	Phase I	NCT03026517	Lactic acidosis.	[184,185]
Rosiglitazone	Antidiabetic	I	Phase II	NCT04114136	Hepatotoxicity.	[213]
Simvastatin	Statin	III, V	Phase II	NCT02104193	Muscle toxicity.	[213]
Tamoxifen (MitoTAM)	Hormone therapy	I, III, IV, V	Phase II	NCT03280563 NCT00003857	Retinopathy with other minor side effects.	[213]
Tigecycline	Antibiotic	I, III, IV, V	Phase I	NCT01332786	Lack of efficacy.	[167,168]
VLX600	Small molecule inhibitor	I, II, IV	Phase I (discontinued)	NCT02222363	Lack of efficacy.	[84]
Alpha Tocopherol Succinate (α-TOS)	Mitocan	II	Preclinical		Clinical trials required.	[258]

1.7 NBS037

Whilst many OXPHOS inhibitors are in development, the most recent being MS-L6 published in 2024[245], currently there is a clear unmet need for an effective mitochondrial metabolism disruptor in the cancer therapeutics space. Previous attempts at disrupting OXPHOS have struggled to balance the potency found with targeted drug therapies, with the lack of toxicity noted with less efficacious strategies. We have developed a novel OXPHOS inhibitor, NBS037, which we hope will meet this unmet need. The synthesis of the drug has been outlined by Cochrane et al. (2021)[259].

1.7.1 Structure of NBS037

The structure and function of NBS037 is not dissimilar to other OXPHOS inhibitors currently in preclinical trials, with an FDA approved drug linked to a TPP^+ cation. The drug is composed of three distinct groups (Figure 1.7). The TPP^+ cation acts as a mitochondrial targeting group, with the cargo, azithromycin (AZM), linked to the cation via an 11-carbon linker region. In drug development, multiple possible NBS compounds with a variety of linker length regions and cargo drugs were tested.

AZM has been tested in Phase II clinical trials assessing safety, pharmacokinetics, and efficacy in cancer (for example NCT00644176, n=6), where it was well tolerated with only mild adverse effects (nausea and diarrhoea). AZM also displayed low anticancer efficacy shown by one study which found only 25% of patients responded to treatment[260]. AZM was therefore chosen for its safety characteristics and favourable ADMET (absorption, distribution, metabolism, and excretion–toxicity) profile, with the hopes that mitochondrial targeting would improve its efficacy as a cancer therapeutic, as observed with other TPP^+ drugs tested in cancer[236,239,240,261].

It has been observed in various studies that the TPP^+ cation and linker region can affect mitochondrial bioenergetics, with additional mitochondrial uncoupling effects[262]. In the cation, modifications to the phenyl rings, charge density, and lipophilicity can all have effects on the behaviour of the molecule. For example, decreasing the Huckel charge will increase uncoupling capacity[262]. Different lengths of the linker region also affect the efficacy and toxicity of the drug, with longer linkers resulting in a more lipophilic compound and better mitochondrial targeting, but increased mitochondrial uncoupling[262]. Such structural groups have been modified and tested in order to mitigate the uncoupling effects but without affecting the accumulation into mitochondria (data not shown). We were able to develop a structure with an encouraging ADMET profile, and promising efficacy in initial *in vitro* screens (data not shown).

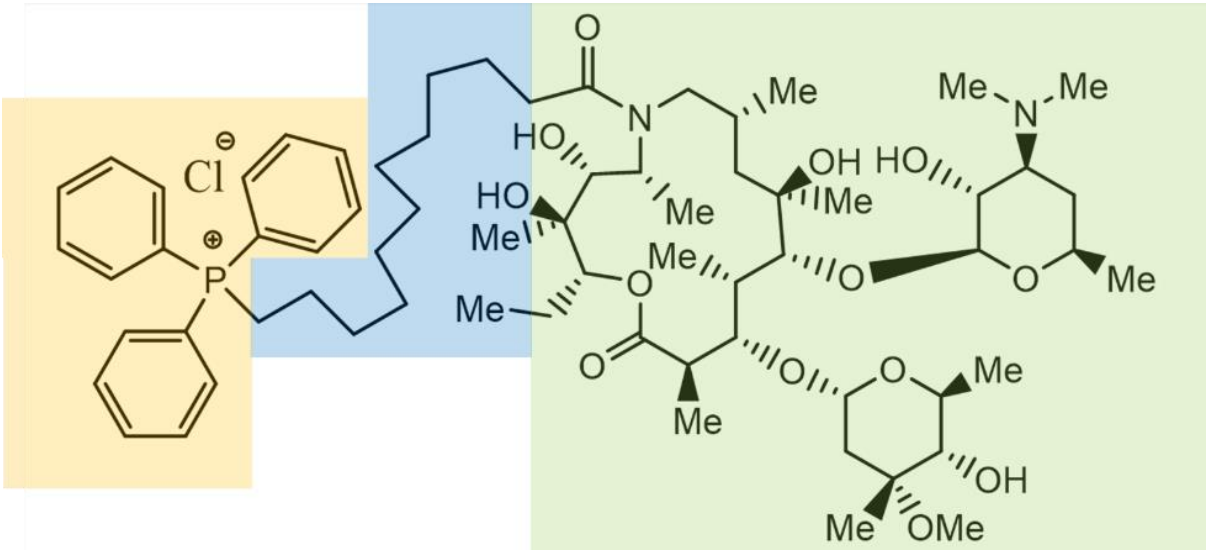

Figure 1.7. The structure of NBS037. *NBS037 is comprised of 3 key regions. Green denotes the TPP^+ region, which acts as a mitochondrial targeting sequence. The TPP^+ cation is linked to AZM (orange) via an 11-carbon linker region (blue). Abbreviations are defined in the main text.*

1.7.2 Proposed mechanism of action

The mechanism by which NBS037 would exert anti-tumour effects is through selective inhibition of OXPHOS in cancer cells (Figure 1.8). Selectivity for cancer cells is achieved through the TPP^+ cation. The TPP^+ cation accumulates in the cytoplasm of cells due to the negative plasma membrane potential. Malignant cells and non-malignant cells have a similar plasma membrane potential so drug selectivity is achieved through differences in the mitochondrial membrane potential ($\Delta\Psi m$). The membrane potential across mitochondrial membranes is greater (more negative) than across plasma membranes, therefore, the TPP^+ cation is highly attracted to mitochondria once inside the cell. The lipophilic nature of the cation allows the drug to pass through the mitochondrial membranes, and allow drug accumulation inside the mitochondria.

In healthy cells, $\Delta\Psi m$ ranges from -140 to -180 mV for optimal ATP production, although this differs slightly dependent on tissue type[263]. In cancer cells, the mitochondrial membrane becomes more depolarized and can reach two-fold higher than normal cells due to aberrant metabolism, high energetic output, and high rates of proliferation[238,264]. Therefore, the TPP^+ cation will have a stronger attraction to mitochondria in cancer cells, and accumulate at a higher concentration in mitochondria of malignant cells.

Once inside the mitochondrial matrix, AZM exerts its effects. Due to the prokaryotic origin of mitochondria, similar protein synthesis machinery is shared between bacteria and mitochondria, rendering the mitochondria sensitive to macrolide antibiotics such as AZM. In bacteria, AZM binds to the 23S rRNA of the bacterial 50S ribosomal subunit, inhibiting the assembly of the subunit as well as occluding the nascent peptide exit tunnel[265]. In mitochondria, AZM binds to the 39S subunit of ribosomes. This inhibits protein translation of mitochondrial encoded proteins. Nuclear proteins should remain unaffected as eukaryotic ribosomes are insensitive to antibiotics[266].

Many of the mitochondrial encoded proteins build the subunits of the ETC, and therefore all complexes of the ETC, with the exception of complex II, would harbour defects upon ribosomal inhibition with AZM. This would cause dysfunctional OXPHOS and affect multiple vital processes involved in cancer cell survival (see section 1.4). Through this mechanism, NBS037 has the capacity to kill cancer cells which rely on OXPHOS. NBS037 may also sensitise cells to radio- or chemotherapies through alleviation of tumour hypoxia and inability to utilise OXPHOS to facilitate therapy resistance.

1.7.3 NBS037 work to date

Various analogues of mitochondrial targeted AZM have previously been developed and tested by Cochrane et al., (2021)[259], with NBS037 further developed based off these findings. However, NBS037 is the first drug to be tested which inhibits the large subunit of the mitochondrial ribosome, with no published work to date, making NBS037 a unique and an exciting new compound to test in the cancer space. Most OXPHOS inhibitors to date focus on inhibiting a specific complex of the ETC, and whilst many do have anticancer effects *in vitro*, most show low efficacy in clinical trials. Instead these agents can cause off target side effects (Table 1.1), causing doubts whether OXPHOS inhibition is a viable method of cancer treatment. Therefore, the exploration of a novel type of OXPHOS inhibitor is highly significant work which could either lead to a promising new anticancer drug, or the knowledge that a different target is needed. The mitochondrial targeted analogues of AZM showed promise in initial developmental stages, with decreases in cancer cell number, OCR, and cytochrome *c* oxidase subunit I (COX1) protein expression in MDA-MB-231 cells[259]. NBS037 has the potential to do the same. The mechanism of action of NBS037 *in vitro* and *in vivo*, however, will need to be fully elucidated before NBS037 can be tested in a clinical setting.

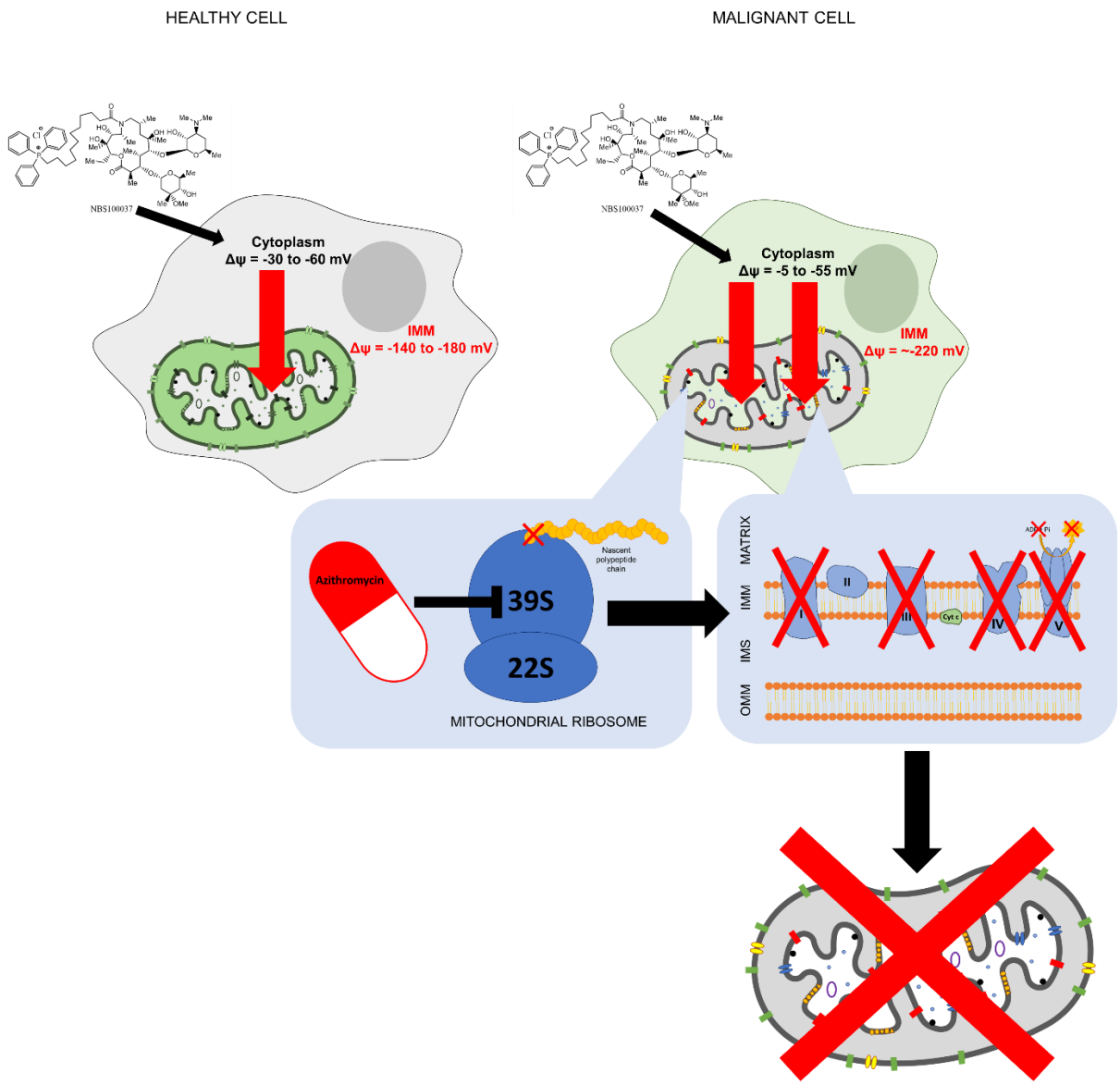

Figure 1.8. Proposed mechanism of action of NBS037. *The TPP^+ cation allows NBS037 to accumulate inside the cellular cytosol due to the negative plasma membrane potential. The ΔΨm is more negative than the plasma membrane, leading to the accumulation of NBS037 inside mitochondria. Cancer cell mitochondria have a higher ΔΨm than normal cell mitochondria, resulting in higher accumulation of NBS037 in cancer mitochondria. The conjugated AZM inhibits the 39S subunit of the mitochondrial ribosome, preventing translation of mitochondrial proteins, and subsequently preventing the formation of complex I, III, IV, and V of the ETC. This causes inhibition of OXPHOS and mitochondrial dysfunction. Abbreviations are defined in the main text.*

1.8 Aims and hypotheses

1.8.1 Overall hypothesis

A drug targeting OXPHOS would be toxic to tumour, metastatic, and therapy resistant cells, and provide a promising new treatment strategy in cancer, whether as a single agent or in combination with current standard of care treatments.

1.8.2 Overall aim

The overall aim of this thesis is to investigate the mechanisms of action of a novel mitochondrial metabolism disruptor, NBS037, to evaluate if targeting metabolism in this manner is an effective therapeutic strategy in cancer.

1.8.3 Specific objectives

a. To identify the mechanisms of action of NBS037 *in vitro*.
b. To identify the mechanisms of action of NBS037 *in vivo*, from mouse xenograft models.
c. To explore the potential of Raman microspectroscopy for determining the OXPHOS /glycolysis status of tumours, with a view to predict susceptibility to NBS037.

2

Materials and Methods

2.1 Cell culture

2.1.1 Cell growth and maintenance

Immortalised human cell lines (summarised in 2.1) were a gift from Professor Geoffrey Higgins, University of Oxford. A549, H460, and H520 non-small cell lung cancer (NSCLC) cell lines, Cal51, and FaDu cancer cell lines were maintained in Roswell Park Memorial Institute (RPMI) 1640 medium (Cat. 21875034, ThermoFisher). MRC-5 and ARPE-19 cell lines were maintained in Minimal Essential Media (MEM) (Cat. 11095080, ThermoFisher) and Dulbecco's Modified Eagle Medium/Nutrient Mixture F-12 (DMEM/F-12) (Cat. 11330032, ThermoFisher) respectively. All growth media was supplemented with 10% heat-inactivated foetal bovine serum (FBS) (Cat. F7524, Sigma-Aldrich) and 1% penicillin-streptomycin (Cat. P4458, Sigma-Aldrich). All cell lines were maintained in a humidified 5% CO_2 atmosphere at 37°C. For experiments requiring maintenance in phenol red free media, phenol red free RPMI 1640 media (Cat. 32404014, Sigma-Alrich) was supplemented with 10% FBS and 1% penicillin-streptomycin.

Medium was replaced every 2 days and cell lines were passaged at approximately 80% confluency to avoid over-confluency. Medium was removed and the cell monolayer washed with phosphate-buffered saline (PBS) (Cat. D8537, Sigma-Aldrich). Cells were detached using enzymatic dissociation with trypsin/ethylenediaminetetraacetic acid (EDTA) (0.5 g trypsin, 0.2 g EDTA) (Cat. T3924, Sigma-Aldrich) at 37°C and 5% CO_2. Trypsin/EDTA was deactivated by addition of fresh medium and the resulting cell suspension was centrifuged (1300 rpm, 3 minutes). Cells were counted using an automated cell counter (TC20, BioRad) and seeded in fresh tissue culture flaks in a ratio of 1:4 - 1:10 depending on the growth rate of cell line. To maintain cell characteristics, cells were maintained for a maximum of 20 passages before being discarded and replaced with cryopreserved stock.

Table 2.1. Immortalised cell lines used in this project.

Cell Line	Organism	Tissue	Disease	Morphology	Culture Media
A549	Human	Lung	Adenocarcinoma (NSCLC)	Epithelial	RPMI
NCI-H460	Human	Lung	Large cell cancer (NSCLC)	Epithelial	RPMI
NCI-H520	Human	Lung	Squamous cell carcinoma (NSCLC)	Epithelial	RPMI
Cal51	Human	Breast	Carcinoma	Epithelial	RPMI
FaDu	Human	Pharynx	Squamous cell carcinoma	Epithelial	RPMI
MRC-5	Human	Lung	Normal	Fibroblast	MEM
ARPE-19	Human	Eye	Normal	Epithelial	DMEM/F-12

2.1.2 Cryopreservation

Cells for cryopreservation were resuspended in freezing media comprised of 10% FBS and 90% dimethyl sulfoxide (DMSO) (Cat. D2650, Sigma-Aldrich), and 0.5 mL aliquoted into cryovial tubes. Cryovials were cooled slowly in cooling containers (Cat. 5100-0001, ThermoFisher) at -80°C. For long term storage, cells were transferred to liquid nitrogen tanks and maintained at -196°C. For retrieval of cells from storage, cryovials were thawed in a water bath at 37°C and resuspended dropwise into pre-warmed cell culture medium. The cell suspension was centrifuged (1300 rpm, 3 minutes), the DMSO containing supernatant discarded, and cell pellet resuspended in the appropriate complete culture medium for growth.

2.1.3 Mycoplasma testing

All cell lines were routinely tested for mycoplasma contamination using the MycoAlert® Mycoplasma Detection Kit (Cat. LT07-418, Lonza) according to manufacturer's instructions. Briefly, 2 mL of cell culture medium was removed from each cell culture flask and centrifuged (1500 rpm, 5 minutes). 100 µL of supernatant was added to a luminometer cuvette. MycoAlert® reagent and substrate was reconstituted in assay buffer and left to equilibrate for 15 minutes at room temperature (RT). 100 µL of MycoAlert® reagent was added to each cuvette. After 5 minutes, the luminescence was measured by luminometer (TD-20/20, Turner Designs) (reading A). 100 µL of MycoAlert® substrate was added, and after 10 minutes luminescence was measured again (reading B). The ratio of reading B:reading A was calculated. A ratio below 0.9 was interpreted as a negative result for mycoplasma. A ratio of 0.9 – 1.2 was considered borderline contamination and required a retest after 24 hours. A ratio over 1.2 was indicative of mycoplasma contamination. All cell lines were free from mycoplasma contamination throughout the project.

2.1.4 Low glucose conditions

For experiments requiring low glucose conditions, cells were maintained in glucose free RPMI 1640 medium (Cat. 11879020, ThermoFisher) supplemented with 10% FBS, 1% penicillin-streptomycin and 1 M glucose (Cat. G8270, Sigma-Alrich) to give a final concentration of 5 mM or 1 mM glucose. For experiments requiring low glucose and no phenol red, glucose and phenol red free SILAC RPMI 1640 Flex media (Cat. A2494201) was supplemented with 10% FBS. 1% penicillin-streptomycin and 1 M glucose for a final concentration of 5 mM or 1 mM glucose. SILAC RPMI also required supplementation with 1% L-glutamine (Cat. G7513, Sigma-Alrich), 0.04 g/L L-lysine (Cat. L5501, Sigma-Alrich) and 0.2 g/L L-arginine (Cat. A5006, Sigma-Alrich).

2.2 Drug treatments

All drugs (Table 2.2) were reconstituted in DMSO, aliquoted for single use, and stored at -20ºC. Working stock solutions of each drug were made immediately prior to use in pre-warmed media, such that final DMSO concentration was <1%.

Table 2.2. Drug treatments utilised in this study.

Drug	Manufacturer	Stock (mM)
NBS037	Novintum	20
Azithromycin (AZM)	Cat. 75199, Sigma-Alrich	33.38
Carbonyl cyanide 3-chlorophenylhydrazone (CCCP)	Cat. C2759, Sigma-Aldrich	1000
Antimycin A (AA)	Cat. A8674, Sigma-Alrich	1
Menadione (M)	Cat. PHR1411, Sigma-Alrich	100
2-Deoxy-D-glucose (2DG)	Cat. D8375, Sigma-Alrich	1000

2.3 Propidium iodide assay for cell viability

Propidium iodide (PI) (Cat. P4170, Sigma-Aldrich) was reconstituted in ultrapure (Milli-Q) water to a concentration of 1 mM. PI solution was protected from light and stored at 4°C until used.

With the doubling time of the cell lines between 20 - 36 hours, initial seeding density was calculated from the surface area of the wells and time to confluency[267], in order to prevent overcrowding. Cells were seeded at 1.5 x 10^4 cells per well in a clear, 96 well plate in phenol red free 11 mM, 5 mM, or 1 mM glucose RPMI, containing the appropriate drug treatment. Media was replaced daily to maintain glucose levels. 1, 3, 5, and 7 days after seeding, PI solution was added to a final concentration of 50 μM per well, and the plate incubated in the dark at 37°C for 30 minutes. Fluorescence (excitation filter 544 nm; emission filter 590 nm) was measured using a FLUOstar Omega plate reader (BMG Labtech). Plates were frozen at -20°C overnight and thawed at RT. Plates were subjected to a further two freeze thaw cycles at -80°C before fluorescence intensity was measured again. To correct for background fluorescence, cell free, blank control wells were subtracted from each reading and the cell viability then calculated.

TOTAL CELL POPULATION – DEAD CELL POPULATION

second fluorescence reading (blank corrected) – first fluorescence reading (blank corrected)

2.4 Oxygen consumption assay

Prior to experiments, cell seeding titrations were conducted for each cell line at 2 x 10^4, 3 x 10^4, 4 x 10^4, 5 x 10^4, 8 x 10^4, and 10 x 10^4 cells in order to determine the optimal signal. 4 x 10^4 was selected as the optimal cell seeding density to allow adequate signal during

OXPHOS inhibition and OXPHOS uncoupling, such that the signal would not be too low or too saturated respectively.

2.4.1 Oxygen consumption at baseline

For measurement of oxygen consumption, cells were seeded at 4 x 10^4 cells per well in a black, clear bottom 96 well plate in 11 mM and 1 mM glucose RPMI. Cells were left to attach overnight in a humidified 5% CO_2 atmosphere at 37°C. The next day, the MitoXpress Xtra assay (Cat. MX-200-4, Agilent) was performed following manufacturer's instructions. Briefly, media was replaced by 90 µL fresh RPMI or RPMI containing test compounds (10 µM CCCP, 10 µM AA, 500 µM 2DG). On a pre-warmed 37°C heating block, 10 µL of reconstituted MitoXpress regent was added to each well and sealed with 2 drops of pre-warmed HS mineral oil. Fluorescence (excitation filter 340 ± 50 nm; emission filter 665 ± 50 nm) was immediately measured kinetically on a CLARIOstar plate reader (BMG Labtech) with a TRF-Optical attachment. Dual-read time-resolved fluorescence was measured every 5 minutes for 2 hours, using delay/window times of 30 µs and 70 µs. Blank control wells containing cells and 10 µM of water in the place of Xtra probe were included and utilised to correct the raw data. Calculation of fluorescence lifetime was performed as described in the MitoXpress Xtra user guide, using MARS software (BMG Labtech):

$$Lifetime\ (\mu s)[\tau] = \frac{D2 - D1}{\ln\left(\frac{I_{W1}}{I_{W2}}\right)}$$

Where IW1/ and IW2 represent the two measurement windows and D1 and D2 represent the delay time. Lifetime, which takes into account decay of the probe, provides advantages over utilising signal intensity such as providing a more stable measurement of oxygen consumption with a greater dynamic range[268]. The gradient of the linear segment of the lifetime signal was used to calculate the OCR.

2.4.2 Oxygen consumption assay with acute NBS037 treatment

For measurement of oxygen consumption with acute NBS037 treatment, cells were seeded at 4 x 10^4 cells per well in a black, clear bottom 96 well plate in 11 mM and 1 mM glucose RPMI. Cells were left to attach for 8 hours in a humidified 5% CO_2 atmosphere at 37°C, and the MitoXpress Xtra assay was performed following manufacturer's instructions as above. 0.5 - 10 μM NBS037 was added as the test compound, and DMSO added as a vehicle control. 10 μM CCCP and 10 μM AA were added to control wells for positive and negative controls respectively. Blank control wells containing cells and 10 μM of water in the place of Xtra probe were included and utilised to correct the raw data. Fluorescence was measured kinetically every 5 minutes for 12.5 hours.

2.4.3 Oxygen consumption assay with chronic NBS037 treatment

For measurement of oxygen consumption with chronic drug treatment, cells were seeded at 1 x 10^6 cells per flask and grown in 11 mM and 1 mM RPMI containing 0.5 - 2 μM NBS037 for 72 hours in a humidified 5% CO_2 atmosphere at 37°C. Media was replaced daily to maintain glucose levels. After 72 hours, cells were trypsinised and seeded at 4 x 10^4 cells per well in a black, clear bottom 96 well plate in 11 mM and 1 mM glucose RPMI containing 0.5 - 2 μM NBS037 or DMSO. Cells were left to attach to the plate for 6 hours in a humidified 5% CO_2 atmosphere at 37°C. 10 μM CCCP and 10 μM AA were added to control wells for positive and negative controls respectively. Blank control wells containing cells and 10 μM of water in the place of Xtra probe were included and utilised to correct the raw data. The oxygen consumption assay was repeated as above but fluorescence was measured kinetically every 5 minutes for 6 hours.

2.5 Extracellular acidification assay

Prior to experiments, cell seeding titrations were conducted for each cell line at 2 x 10^4, 3 x 10^4, 4 x 10^4, 5 x 10^4, 8 x 10^4, and 10 x 10^4 cells in order to determine the optimal signal. 4 x 10^4 was selected as the optimal cell seeding density to allow adequate signal during OXPHOS inhibition and OXPHOS uncoupling such that the signal would not be too low or too high.

For measurement of extracellular acidification rate (ECAR), cells were seeded at 4 x 10^4 cells per well in a black, clear bottom 96 well plate in 11 mM and 1 mM glucose RPMI. Cells were left to attach overnight in a humidified 5% CO_2 atmosphere at 37°C. The next day, the pH-Xtra glycolysis assay (Cat. PH-200-4, Agilent) was performed following manufacturer's instructions. Briefly, plates underwent a CO_2 purge by incubation in a humidified, CO_2 free atmosphere at 37°C for at least 2 hours prior to the experiment. A respiration buffer tablet was reconstituted in 50 mL of Milli-Q water, adjusted to pH 7.4, and sterilised through a 0.22 µM filter. After CO_2 was purged, each well underwent two wash steps with 200 µL of respiration buffer. 90 µL of fresh respiration buffer or respiration buffer containing test compounds (10 µM CCCP, 10 µM AA, 500 µM 2DG) was added. On a pre-warmed 37°C heating block, 10 µL of reconstituted pH-Xtra regent was added to each well. Blank control wells containing cells and 10 µM of water in the place of pH-Xtra probe were included and utilised to correct the raw data. Fluorescence (excitation filter 340 ± 50 nm; emission filter 615 ± 18 nm) was immediately measured kinetically on a CLARIOstar plate reader (BMG Labtech) with a TRF-Optical attachment. Dual-read time-resolved fluorescence was measured every 5 minutes for 2 hours, using delay times of 100 µs and 300 µs and window times of 30 µs. Calculation of fluorescence lifetime was performed as described in the pH Xtra user guide, using MARS software (BMG Labtech):

$$Lifetime\ (\mu s)[\tau] = \frac{D2 - D1}{\ln\left(\frac{I_{W1}}{I_{W2}}\right)}$$

Where IW1/ and IW2 represent the two measurement windows and D1 and D2 represent the delay time. The gradient of the linear segment of the lifetime signal was used to calculate the ECAR.

2.6 Dihydroethidium assay for reactive oxygen species production

Dihydroethidium (DHE) (Cat. 12013, Cayman Chemical) was reconstituted in DMSO, aliquoted into single use aliquots and stored protected from light at -20°C until use. Prior to experiments, cell seeding titrations were conducted for each cell line at 2 x 10^4, 3 x 10^4, 4 x 10^4, 5 x 10^4, 8 x 10^4, and 10 x 10^4 cells in order to determine the optimal signal. 4 x 10^4 was selected as the optimal cell seeding density to allow adequate signal such that the signal would not be too low or too saturated. For chronic experiments, cells were seeded at 1.5 x 10^4 cells per well such that cell number after 72 hours would reach approximately 4 x 10^4 cells.

2.6.1 DHE assay for acute drug treatment

Cells were seeded at 4 x 10^4 cells per well in a black, clear bottom 96 well plate in 11 mM and 1 mM glucose RPMI. Cells were left to attach for 8 hours in a humidified 5% CO_2 atmosphere at 37ºC. Once attached, media was replaced RPMI containing DHE at a final concentration of 10 µM per well, and the plate incubated in the dark at 37ºC for 30 minutes. Following incubation, DHE was replaced by 11 mM glucose, phenol red free RPMI containing 0.5 - 10 µM NBS037 or DMSO as a vehicle control. 50 µM menadione and 10 µM AA were added to control wells for positive and negative controls respectively. Fluorescence (excitation filter 494

± 20 nm; emission filter 567 ± 20 nm) was measured every 5 minutes for 10 hours using a CLARIOstar (BMG Labtech) plate reader. To correct for background fluorescence, cell free, blank control wells were subtracted from each reading.

2.6.2 DHE assay for chronic drug treatment

Cells were seeded at 1.5 x 10^4 cells per well in a black, clear bottom 96 well plate in 11 mM glucose RPMI containing 0.5 - 10 μM NBS037 or DMSO as a vehicle control. 50 μM menadione and 10 μM AA were added to control wells for positive and negative controls respectively. A duplicate plate was also set up in a black, clear bottom, 96 well plate for a PI assay to determine cell number. Cells were grown for 72 hours in a humidified 5% CO_2 atmosphere at 37°C, and media replaced daily to maintain glucose levels. After 72 hours, media was replaced RPMI containing DHE at a final concentration of 10 μM per well, and the plate incubated in the dark at 37°C for 30 minutes. Following incubation, DHE was replaced by 11 mM glucose, phenol red free RPMI containing drug treatments. Fluorescence (excitation filter 494 ± 20 nm; emission filter 567 ± 20 nm) was measured using a CLARIOstar (BMG Labtech) plate reader. To correct for background fluorescence, cell free, blank control wells were subtracted from each reading. To correct for cell number due to differential rates of growth, after 72 hours a PI assay was performed as previously described (see 2.3) on the duplicate plate cultured simultaneously. DHE measurements were then normalised to viable cell number.

2.7 Tetramethylrhodamine methyl ester assay for mitochondrial membrane potential

Prior to experiments, cell seeding titrations were conducted for each cell line at 2 x 10^4, 3 x 10^4, 4 x 10^4, 5 x 10^4, 8 x 10^4, and 10 x 10^4 cells in order to determine the optimal signal.

4×10^4 was selected as the optimal cell seeding density to allow adequate signal such that the signal would not be too low or too saturated. Tetramethylrhodamine methyl ester (TMRM) (Cat. T668, Sigma-Alrich) was reconstituted in DMSO to a concentration of 50 µM and stored in singe use aliquots at -20°C, protected from light. The TMRM assay was conducted in non-quenching mode, where TMRM fluorescence correlates to the negative charge on the mitochondria (less fluorescence being depolarisation and more fluorescence indicating hyperpolarisation)[269].

Cells were seeded at 4×10^4 cells per well in a black, clear bottom 96 well plate in 11 mM and 1 mM glucose RPMI. Cells were left to attach overnight in a humidified 5% CO_2 atmosphere at 37°C. The next day, media was replaced with phenol red free 11 mM or 1 mM glucose RPMI containing 20 nM TMRM and the plate incubated in the dark at 37°C for 30 minutes. Following incubation, media was replaced by 100 µL fresh, phenol red free RPMI. Fluorescence (excitation filter 544 ± 15 nm; emission filter 590 ± 20 nm) was measured immediately using a CLARIOstar (BMG Labtech) plate reader every 5 minutes for a total of 30 minutes. To correct for background fluorescence, cell free, blank control wells were subtracted from each reading.

2.8 JC-1 staining for mitochondrial membrane potential

JC-1 cationic dye (Cat. 15003, Cayman Chemical) was reconstituted in DMSO at a stock concentration of 1 mg/mL. JC-1 solution was aliquoted for single use and stored at -20ºC. Prior to experiments, cell seeding titrations were conducted for each cell line at 2×10^4, 3×10^4, 4×10^4, 5×10^4, 8×10^4, and 10×10^4 cells in order to determine the optimal signal. 5×10^4 was selected as the optimal cell seeding density to allow adequate signal such that the signal would not be too low or too saturated.

Cells were seeded at 1 x 10^6 in T-75 cm^2 flasks in 11 mM glucose RPMI containing 0 - 2 µM NBS037, 10 µM CCCP or 10 µM AA. Cells were maintained in a humidified 5% CO_2 atmosphere at 37°C for 72 hours, and media replaced daily to maintain glucose concentration. After 72 hours, cells were washed with PBS, detached with trypsin/EDTA and centrifuged (1300 rpm, 3 minutes). After resuspension in 11 mM glucose RPMI, cells were seeded at 5 x 10^4 cells per well in a black, clear bottom 96 well plate in 11 mM glucose RPMI containing 0 - 2 µM NBS037, 10 µM CCCP or 10 µM AA. Cells were left to attach overnight in a humidified 5% CO_2 atmosphere at 37°C.

The next day, media was replaced with 2 µg/ml JC-1 dye diluted in RPMI, and plates incubated in the dark at 37ºC for 30 minutes. After incubation, JC-1 was removed and replaced with phenol red free RPMI. Fluorescence (green excitation filter 485 ± 15 nm; emission filter 535 ± 10 nm and red excitation filter 485 ± 15 nm; emission filter 595 ± 10 nm) was measured immediately on a CLARIOstar plate reader every 5 minutes for 2 hours. To correct for background fluorescence, cell free, blank control wells were subtracted from each reading. The ratio of red:green fluorescence was calculated, where a decrease in ratio indicates a lower ΔΨm, and unhealthy mitochondria.

2.9 ATP assay

For determination of ATP levels within cells, the CellTiter-Glo® 2.0 assay (Promega) was carried out according to manufacturer's instructions. Briefly, 5 x 10^4 cells were plated in white, clear bottom 96 well plates and left to attach for 6 hours in a humidified 5% CO_2 atmosphere at 37°C. A duplicate plate was also set up in a black, clear bottom, 96 well plate for a PI assay to determine cell number. Upon attachment of cells, media in both plates was replaced with 11 mM or 1 mM glucose RPMI containing 0 mM, 0.5 mM, 1 mM or 20 mM 2DG and cells incubated overnight in a humidified 5% CO_2 atmosphere at 37°C. The next day, the ATP assay

plate was equilibrised to RT for 30 minutes, after which the CellTiter-Glo Reagent was added in a 1:1 ratio with the volume of media in each well. The plate was shaken on an orbital mixer for 2 minutes to lyse the cells, and then equilibrated at RT for 10 minutes. Luminescence was measured on a CLARIOstar plate reader with an integration time of 1 second. In the duplicate plate, a PI assay was performed (see 2.3), and the resulting viable cell count was used to normalise the luminescence measurements.

2.10 Protein extraction from cultured cells

For cell line metabolism experiments, cells were seeded at 1 x 10^6 cells in T-75 cm^2 tissue culture flasks containing 11 mM or 1 mM glucose RPMI and maintained for 7 days in a humidified 5% CO_2 atmosphere at 37°C. Media was replaced daily to maintain the glucose concentration and cells passaged as needed to avoid over-confluency. For NBS037 experiments, cells were seeded at 1 x 10^6 cells in T-75 cm^2 tissue culture flasks containing 11 mM glucose RPMI containing 0 - 2 μM NBS037 or DMSO. Cells were maintained for 72 hours in a humidified 5% CO_2 atmosphere at 37°C, with daily media replacement.

After the appropriate culture conditions, cell monolayers were washed with PBS and detached by trypsin/EDTA. Trypsin/EDTA was deactivated by addition of fresh medium and the resulting cell suspensions were centrifuged (1300 rpm, 3 minutes). The supernatants were removed, and the cell pellets washed twice with PBS. The cell pellets were resuspended in ice cold Pierce™ RIPA Buffer (Cat. 89901, ThermoFisher), supplemented with 1X protease/phosphatase inhibitor cocktail (Cat. 78444, ThermoFisher). Samples were incubated at constant agitation at 4°C for 30 minutes, before centrifugation at 4°C (12000 rpm, 20 minutes). The supernatants were carefully removed, placed on ice and pellets discarded.

2.11 Protein extraction from frozen tissue

For frozen xenograft tissue samples, 10 - 20 mg of each tissue was weighed over ice and ice cold Pierce™ RIPA Buffer, supplemented with 1X protease/phosphatase inhibitor cocktail, was added. Brain, kidney, and liver samples were transferred to bead mill tubes containing 1.4 mm ceramic beads (Cat. 15-340-153, Fisher Scientific). Heart and tumour samples were transferred to bead mill tubes containing 2.8 mm ceramic beads (Cat. 15-340-154, Fisher Scientific). Tissues were homogenised using a Fisherbrand™ Bead Mill 4 Mini Homogenizer (Cat. 15-340-164, Fisher Scientific) at speed 4 for 15 seconds. Samples were incubated at constant agitation at 4°C for 2 hours, before centrifugation at 4°C (12000 rpm, 20 minutes). The supernatants were carefully removed, placed on ice and pellets discarded.

2.12 Protein quantification

The protein concentration of different lysates, whether from cultured cells or tissue samples, was determined by Pierce bicinchoninic acid (BCA) assay kit (Cat. 23225, ThermoFisher) according to manufacturer's microplate procedure. Briefly, 25 µL of each lysate was added to a clear bottom, black 96 well plate and samples mixed with working reagent. Plates were incubated in the dark at 37ºC for 30 minutes and absorbance (wavelength 562 nm) was read on a CLARIOstar plate reader. Protein concentration in each lysate was calculated utilising a standard curve generated from a dilution series of bovine serum albumin (BSA) provided in the kit. Lysates were then frozen at -20°C until use.

2.13 Polyacrylamide gel electrophoresis and transfer to a polyvinylidene difluoride membrane

Lysates were thawed and diluted in appropriate volumes of Milli-Q water. NuPAGE LDS Sample Buffer (4X) (Cat. NP0008, ThermoFisher) was added and samples denatured at 80ºC for 5 minutes. Equal amounts of protein (10 µg) and a standard protein ladder (Cat. 161-0374, Bio-Rad) were separated on a NuPAGE 4-12% Bis-Tris Gel (Cat. NP0322BOX, ThermoFisher) in 1x MOPS SDS running buffer (Cat. NP0001, ThermoFisher) at 150 V for 90 minutes. Proteins were then transferred to 0.45 µM polyvinylidene difluoride (PDVF) membrane (Cat. 88518, ThermoFisher) at 25 V for 45 minutes in cold 1x transfer buffer (Cat. NP0006, ThermoFisher). To validate a successful transfer, membranes were stained with ponceau red solution (Cat. P7170-1L, Sigma-Alrich) to visualise bands. Membranes were carefully rinsed with Milli-Q water until the ponceau red stain was removed.

2.14 Immunoblotting and detection

Membranes were washed for 5 minutes in Tris buffered saline with 0.05% Tween-20 (TBST) (Sigma-Alrich), and the washing step repeated twice more with fresh TBST. To prevent non-specific binding, membranes were incubated in blocking buffer (5% non-fat milk in TBST) for 1 hour at RT on a benchtop rocker. Blocking solution was removed and membranes were incubated overnight at 4ºC under constant agitation in the appropriate primary antibody diluted in blocking buffer, summarised in Table 2.3.

The following day, membranes were washed 3 times, for 5 minutes each in TBST, and were incubated in the appropriate secondary antibody, diluted in blocking buffer, for 1 hour at RT. For primary antibodies cultivated in mouse hosts, goat anti-mouse IgG H&L horseradish peroxidase (HRP) conjugated antibodies (Cat. ab205719, abcam) were used at 1:10000

dilution. For primary antibodies cultivated in rabbit hosts, goat anti-rabbit IgG H&L HRP conjugated antibodies (Cat. ab6721, abcam) were used at 1:10000 dilution. Antibodies were removed and membranes washed 3 times, for 5 minutes each in TBST. Immunoreactive proteins were visualized using WESTAR Supernova kit (Cat. K1-0068, GeneFlow) as per manufacturer's instructions, with a 1 minute membrane incubation in working solution. Chemiluminescent imaging was carried out using a G-box (SynGene), and analysis of blots quantified using GeneTools software (Syngene).

Table 2.3. Primary antibodies used in this study.

Target	Host	Type	Dilution	Manufacturer
Aconitase 2	Mouse	Monoclonal	1:1000	ab110321, abcam
ATP5B	Mouse	Monoclonal	1:1000	Sc-55597, Santa Cruz
β-actin	Mouse	Monoclonal	1:1000	ab68224, abcam
β-actin	Rabbit	Polyclonal	1:1000	ab8227, abcam
Carbonic Anhydrase IX	Rabbit	Polyclonal	1:1000	PA116592, ThermoFisher
MnSOD2	Rabbit	Monoclonal	1:1000	ab68155, abcam
MTCO1	Mouse	Monoclonal	1:2000	ab14705, abcam
MTCO1	Rabbit	Monoclonal	1:1000	ab203912, abcam
SDHA	Mouse	Monoclonal	1:1000	ab14715, abcam
SDHA	Rabbit	Monoclonal	1:1000	ab137040, abcam
Tom20	Rabbit	Monoclonal	1:1000	ab186735, abcam

2.15 Xenograft mouse studies (Hulit)

The following work in mice was carried out by Dr James Hulit (University of Oxford), named the SP237857 study. The project licence covering the animal work (PP5787245) was approved by the Animal Welfare and Ethical Review Body (AWERB) (University of Oxford), and granted by the UK Home Office Animals in Science Regulation Unit (ASRU) under the Animals (Scientific Procedures) Act 1986 (ASPA).

H460 NSCLC cells were grown in 11 mM glucose RPMI in a T-175 cm2 flask until 80% confluency. The cell monolayer was washed with PBS and detached with trypsin/ETDA for 5 minutes. The cell mixture was centrifuged (300 xg, 5 minutes), the pellet resuspended in 1.2 mL PBS and immediately placed on ice. 1.2 mL Matrigel (Cat no. 356237, Scientific Laboratory Supplies Limited) was added and mixed thoroughly with the cell suspension. 6 cold syringes were loaded with 200 µL of cell/Matrigel mixture and kept on ice. Immunodeficient CD-1 nude female mice were purchased from Charles River, 6-7 weeks of age. Mice were placed in an anaesthesia box in pairs, and each received a subcutaneous injection into the flank, containing 0.1 mL of H460 cell suspension (approximately 0.5 x 10^6 cells). 12 animals were inoculated in total. Mice were randomised by using RANDOM.ORG (https://www.random.org/lists/) for cage allocation and randomised once more for treatment allocation.

Diet and welfare were checked daily, before, and after tumour induction. Bodyweight was measured and recorded at least twice a week. Tumour growth (not blinded) was assessed by calliper measurement and calculated according to the formula: $length \times width^2 / 2$. When tumour size reached 55 - 65 mm^3, treatment schedule was started. If tumours failed to reach this size, mice did not receive any treatment and were culled at 21 days without any further analysis. Remaining mice were treated with 0.1 mL PBS (n=4) or 3 mg/kg NBS037 (n=5) by intravenous (IV) tail vein injection as per the treatment schedule summarised in Figure 2.1. When tumours reached a threshold size of 120-140 mm^3, mice were culled by CO_2 (Schedule

1 method). To ensure tumours in PBS and NBS037 treated mice were similar and therefore comparable, PBS treated mice were culled 2 to 3 days later than NBS037 treated mice such that the tumours had more time to reach the threshold size. Tissues (brain, heart, kidney, liver, tumour) were removed and snap frozen on dry ice. Frozen tissue samples were stored at -80ºC until use.

		PBS 0.1 mL						NBS037 3 mg/kg					
Day	Date	NC	L	R	LR	LL	RR	NC	L	R	LR	LL	RR
0	15/09/2022	Induction	Induction	Induction	Induction	Induction	Induction	Induction	Induction	Induction	Induction	Induction	Induction
1	16/09/2022												
2	17/09/2022												
3	18/09/2022												
4	19/09/2022												
5	20/09/2022	9.00	18.51	10.94	1.69	15.67	21.24	14.22	13.50	18.00	9.38	4.00	6.00
6	21/09/2022												
7	22/09/2022	23.04	17.10	18.00	18.38	16.82	27.56	17.55	21.44	16.20	15.75	9.38	16.20
8	23/09/2022	21.87	21.13	17.92	25.27	24.62	34.30	25.11	22.54	15.75	28.88	16.20	20.48
9	24/09/2022												
10	25/09/2022	21.87	21.44	17.92	30.40	20.15	40.00	32.40	24.50	18.00	36.00	26.01	30.63
11	26/09/2022	25.52	22.05	17.92	32.00	27.38	44.00	37.65	24.50	20.25	48.40	32.40	48.00
12	27/09/2022	24.34	22.66	23.10	34.46	34.40	52.95			22.05			
13	28/09/2022	26.61	23.89	26.01	36.98	44.98	62.92	60.00		28.79	59.74		59.17
14	29/09/2022	33.30	27.56	34.23	36.00	50.63	70.88	74.74	58.73	40.00	81.25		68.77
15	30/09/2022	36.04	35.30	50.40	44.38	62.21	88.75	100.14	75.63	46.75	91.04		71.79
16	01/10/2022	46.55	34.40	54.68	43.45	64.51	97.34		80.43	43.35		66.83	
17	02/10/2022	61.60	40.00	66.82	44.10	75.00	112.36	124.03		49.00	115.18	91.25	81.25
18	03/10/2022	73.96	32.17	71.42	44.98	92.70	**146.21**	**144.00**	102.75	49.00	**137.92**	126.41	96.23
19	04/10/2022	90.99	29.40	82.50	44.10	117.74			**140.40**	47.15		**149.45**	**118.80**
20	05/10/2022	108.29	32.34	99.83	44.98	127.80							
21	06/10/2022	**125.00**	**35.20**	**129.60**	**45.86**	**138.38**				**48.40**			

Figure 2.1. Treatment schedule in the SP237857 study. *CD-1 nude mice were treated with 0.1 mL PBS (n=4) or 3 mg/kg NBS037 (n=5), administered by IV tail vein injection at specified time intervals once tumours had reached 55 - 65 mm^3 in diameter. Ear clippings were used to identify individual mice: NC, L, R, LR, LL, RR. Blue boxes indicate treatments given and orange boxes denote day of culling. Values represent tumour volume (mm^3). Animals shaded grey did not grow acceptable tumours and were excluded from treatment or further analysis. Different animals were denoted by clips on the ears: NC (no clip), RR (two right), R (right), LL (two left), L (left), LR (left and right). This work was conducted by Dr James Hulit.*

2.16 Cryosectioning

Prior to cutting, the cryostat (MEV, Slee) was set to the manufacturer's suggested cutting temperatures for each tissue, summarised in Table 2.5, and allowed to equilibrate. 1 hour prior to cutting, tissue was placed inside the cryostat to allow sufficient warming to cryostat temperature. 1 drop of optimal cutting temperature (OCT) embedding matrix (Cat. 15212776, ThermoFisher) was placed on an appropriately sized tissue mount, and tissue immediately

pressed into the centre of the OCT. Once the OCT was sufficiently frozen, the mount was loaded onto the mount block and secured. The OCT was trimmed until the tissue was reached. Tissues were cut in 7 µm sections and carefully transferred onto slides. Slides were left to dry overnight at RT, protected from dust. The next day, slides were wrapped in foil and frozen at -20ºC for short term storage, or -80ºC for long term storage.

Table 2.4. Cutting temperatures on the cryostat for each tissue.

Tissue	Operating temperature (ºC)
Brain	-7 to -10
Heart	-20 to -25
Kidney	-7 to -13
Liver	-7 to -13
Tumour	-20 to -25

2.17 Immunofluorescence

Slides were thawed at RT in foil to prevent condensation. A PAP pen (Cat. ab2601, abcam) was used to draw a hydrophobic circle around each section and slides were left to dry. Slides were then fixed in 4% paraformaldehyde (PFA) diluted in PBS (Cat no. 11586711, ThermoFisher) for 10 minutes at RT. Excess PFA was tapped off, and slides were washed twice in PBS for 5 minutes each. 0.2 % Triton™ X-100 (Cat no. 11488696, ThermoFisher) diluted in PBS was added to each sample, and slides incubated for 10 minutes to permeabilise the cells. Slides were then rinsed in PBS.

For slides containing tumour sections for Carbonic Anhydrase IX (CAIX) staining, slides were fixed with ice cold methanol for 5 minutes at 4ºC. Excess methanol was tapped off, and slides were washed twice in PBS for 5 minutes each. Slides did not undergo a permealisation step as CAIX is a membrane bound protein. Tumour sections designated as positive controls were incubated with 200 μM cobalt chloride for 30 minutes at RT and then rinsed with PBS.

10% goat serum (Cat. ab7481, abcam) in PBS was added to each section and incubated for 40 minutes at RT. Excess serum was tapped off, and appropriate primary antibody diluted in PBS, summarised in Table 2.5, was added to each section. Slides were incubated in a dark, humid environment overnight at 4ºC. The next day, each section was gently washed 3 times with PBS for 5 minutes each. Goat anti-rabbit secondary antibody with an Alexa Fluor® 488 conjugate (Cat. ab150077, abcam) was diluted 1:1000 in PBS and added over each section. Slides were incubated in the dark for 1 hour at RT and then received 3 washes with PBS, for 5 minutes each. Slides were submerged in Milli-Q water for a final wash and excess water was wiped off. 3 drops of mounting media containing 4′,6-diamidino-2-phenylindole (DAPI) (Cat. ab104139, abcam) was added to the centre of each slide and a coverslip slowly placed on top, avoiding air bubbles. Slides were left to settle for 1 hour in the dark at RT before imaging.

Fluorescence microscopic analysis and image capture was completed with a Leica upright microscope controlled by Volocity 7 software (Improvision). Fluorescence filters were set to excitation filter 495 nm, emission filter 519 nm for targets and excitation filter 350 nm, emission filter 460 nm for nuclear staining (DAPI).

Table 2.5. Primary antibodies used in immunofluorescence staining.

Target	Host	Type	Dilution	Manufacturer
8-Hydroxyguanosine (8-OHdG)	Rabbit	Polyclonal	1:200	BS-1278R, ThermoFisher
Ki67	Rabbit	Polyclonal	1:200	ab15580, abcam
Cluster of differentiation 31 (CD31)	Rabbit	Monoclonal	1:100	ab222783, abcam
CAIX	Rabbit	Polyclonal	1:100	PA116592, ThermoFisher

2.18 Click-iT™ Plus TUNEL Assay

The Click-iT™ Plus TUNEL Assay kit was purchased from ThermoFisher (Cat no. C10618) and tissue staining was performed as per manufacturer's instructions but with exclusion of the deparaffinisation step. Briefly, slides were thawed at RT in foil to prevent condensation before fixation with 4% PFA for 15 minutes at 37ºC. Slides were washed twice with PBS for 5 minutes each, before permeabilization with 1X Proteinase K. Slides were incubated for 15 minutes at 37ºC and were washed again with PBS. Slides were fixed for a further 5 minutes in 4% PFA at 37ºC, before a final rinse in Milli-Q water.

The positive control was prepared through adding 1 unit of DNAse I (Cat no. 18068-015, ThermoFisher) in 1X DNase I Reaction Buffer (20 mM Tris-HCl, pH 8.4, 2 mM $MgCl_2$, 50 mM KCl) per tissue section. Slides were incubated for 30 minutes at 37ºC and tissue sections gently rinsed with Milli-Q water to remove excess DNAse I.

The TdT reaction was then performed. TdT reaction buffer was added to each section and slides were incubated for 10 minutes at 37ºC. TdT reaction buffer was replaced with TdT reaction mixture and incubated for 60 minutes at 37ºC in a humidified environment. Slides

were washed with Milli-Q water, a solution of 3% BSA (Cat no. A7638, Merck) and 0.1% Triton™ X-100 in PBS, and finally PBS for 5 minutes each.

Click-iT™ Plus TUNEL reaction cocktail was added to each slide and incubated for 30 minutes at 37ºC, protected from light. Following incubation, slides were washed in 3% BSA in PBS for 5 minutes and rinsed with PBS. 3 drops of mounting media containing DAPI was added to the centre of each slide and a coverslip slowly placed on top, avoiding air bubbles. Slides were left to settle for 1 hour in the dark at RT before imaging.

Fluorescence microscopic analysis and image capture was completed with a Leica upright microscope controlled by Volocity 7 software (Improvision). Fluorescence filters were set to excitation filter 590 nm, emission filter 615 nm for targets and excitation filter 350 nm, emission filter 460 nm for nuclear staining (DAPI).

2.19 Single-cell Raman spectroscopy

A549 and H460 NSCLC cells were seeded at 1 x 10^6 in T-75 cm^2 tissue culture flasks containing 11 mM or 1 mM glucose RPMI and maintained for 72 hours in a humidified 5% CO_2 atmosphere at 37ºC. Treatment groups were seeded in 11 mM or 1 mM glucose RPMI containing 0.5 µM or 1 µM NBS037, DMSO as a vehicle control, 10 µM AA or 500 µM 2DG. Media was replaced daily to maintain the glucose concentration. After 72 hours, cell monolayers were detached using trypsin/EDTA and cell suspensions centrifuged at 4ºC (3500 rpm, 5 minutes). For determination of ECAR and OCR prior to Raman analysis, 8 x 10^4 cells were seeded on a black, clear bottom, 96 well plate and left to attach for 6 hours in a humidified 5% CO_2 atmosphere at 37ºC. The pH Xtra assay and MitoXpress assay were carried out as previously described in sections 2.5 and 2.4.

Cells for Raman analysis were washed carefully with PBS, taking care not to lyse cells and resuspended in 4% PFA (Cat. 11586711, Thermo Scientific) diluted in PBS for 15 minutes at 4ºC. Fixed cells were centrifuged again at 4ºC (5000 rpm, 5 minutes) and washed twice with PBS. For long term storage, cells were resuspended in PBS and stored at 4ºC. Immediately prior to Raman analysis, cells were washed twice with Milli-Q water and diluted to observe single cells under 50x microscope. 2 µL of each cell suspension was spotted onto an aluminium coated glass slide (DRLI), specifically coated to give no background signal. Slides were left to dry at RT.

Single-cell Raman spectra were acquired using an HR Evolution confocal Raman microscope (Horiba) equipped with a 532 nm neodymium-yttrium aluminium garnet laser. Before the analysis of samples, the spectrometer was calibrated using silicon. The laser power used on cells was 25 mW and attenuated with neutral density filters. A 50x objective was used to focus on single cells, giving a laser spot of approximately 1 μm^2. Spectra were obtained in the range of 400–3200 cm−1 with 300 grooves/mm diffraction grating. A mapping mode was used to analyse single cells where the acquisition parameters were 5 seconds per spectrum, 10 spectra per cell and ~35 single cells per condition.

2.20 Raman data pre-processing and analysis

All spectra were pre-processed in LabSpec 6 software (Horiba Scientific) and underwent cosmic ray removal, baseline correction to minimise background, and spectral normalisation using the whole spectral range such that the area under the spectrum is 100. Spectra were averaged for each cell. Averaged spectra were analysed in an R (4.0.0) environment and groups plotted by Principle Component Analysis (PCA) or Linear Discriminant Analysis (LDA). Raman peaks at wavelengths contributing the most to group separation on LD1 and LD2 were identified and compared to existing literature to assign Raman peaks to a biological molecule.

These highest contributing Raman peaks were integrated using LabSpec 6 software, and mean peak areas plotted in GraphPad Prism for statistical analysis.

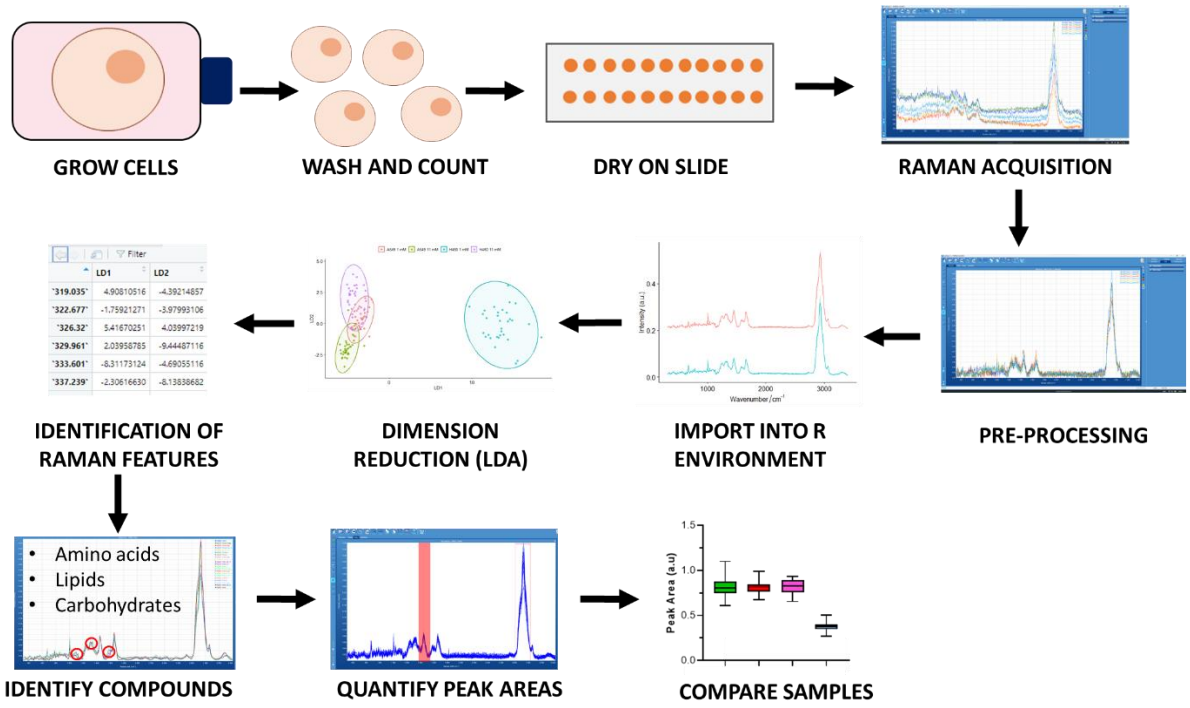

Figure 2.2. Workflow for single-cell Raman spectroscopy and spectra analysis. *A549 and H460 NSCLC cells were grown in high (11 mM) or low (1 mM) glucose for 72 hours. For treatment groups, media also contained drugs at a final concentration of 0.5 μM or 1 μM NBS037, 10 μM AA, 500 μM 2DG or DMSO as a vehicle control. Media was replaced daily to maintain glucose levels. Cells were suspended and dried on aluminium coated slides and single-cell Raman spectra were acquired using an HR Evolution confocal Raman microscope (Horiba). Spectra underwent cosmic ray removal, baseline background correction, and spectral normalisation, and averaged per cell. R (4.0.0) software was utilised to perform LDA on averaged spectra. Peaks at wavenumbers contributing to the separation on LD1 and LD2 were integrated and compared to previous literature for compound identification.*

2.21 Statistical analysis

Statistical analysis was performed using GraphPad 12 software (GraphPad Software, California, USA). For comparing two groups, an unpaired student's t-test was used. Browne-Forsythe testing was utilised to assess if standard deviations (SDs) of groups were equal. When comparing three or more groups of equal SDs, statistical analysis was performed by

one-way Analysis of Variance (ANOVA) with Dunnett's or Tukey's multiple comparisons post hoc tests to compare means to a control group, or means of other groups respectively. When comparing two independent variables, two-way ANOVA was used. If SDs were found to be significantly different, Browne-Forsythe ANOVA was used with Dunnett's T3 or Tukey's multiple comparisons post hoc test to compare means to a control group or means of other groups respectively. Data was considered significant if $p < 0.05$ (*); $p < 0.01$(**); $p < 0.001$(***); $p < 0.0001$(****). Data is represented as mean ± standard error of the mean (SEM), or in the case of Raman analysis of biological molecules, mean ± min/max. All experiments were performed in biological triplicates (N=3), unless otherwise stated.

3

The Effect of NBS037 *in Vitro*

3.1 Introduction

The ability to grow cells *in vitro*, cell culture, has revolutionised biological research since its founding in the early 20th century. Whilst primary cell lines are grown directly from animal or human tissue biopsies, many cell lines today have undergone transformation, allowing generations of cells to be cultured whilst maintaining most of their original biological characteristics[270]. Cell culture has accelerated the study and understanding of biological processes in cells and has become a key step in the drug development process due to its low cost, fast cell growth, and lack of ethical concerns compared to animal studies. It is necessary to test the pharmacokinetic and safety profile of drugs in cultured cells before animal studies or clinical trials can begin, allowing us to identify potential toxicity and mechanisms of action without causing harm to larger organisms.

Many novel cancer treatments targeting metabolism have shown promising decreases in cancer cell viability *in vitro*, including novel small molecule OXPHOS inhibitors[169], FDA approved respiratory chain inhibitors[151], and novel mitochondrial targeted drugs[178]. Many of

these exert anti-tumour effects through alleviation of hypoxia with decreased HIF-1α and downstream signalling pathways which retards cancer progression[271]. Other mechanisms include ATP depletion, loss of oncogenic signalling (ROS and oncometabolites), and an inability to adapt cell metabolism if other metabolic pathways are impaired. NBS037 is expected to behave in a similar manner as other OXPHOS inhibitors, resulting in reduced cancer cell proliferation, although the exact mechanism is yet to be elucidated.

Whilst other mitochondrially targeted antibiotics have been tested such as Mito-TPP-Tig-NP[272] and TPP-doxocycline[273], NBS037, developed from the findings from Cochrane et al. (2021) on TPP^+ conjugated AZM[273], is the first mitochondrially targeted antibiotic which targets the large subunit of the mitochondrial ribosome, making this work the first in this space. Due to the safety characteristics of AZM, it is expected that NBS037 will decrease cell viability potently in cancer cells, accompanied by a decrease in mitochondrial encoded proteins, but with limited effects in non-cancer controls.

3.2 Aims

The specific aims of this chapter are to:

a) Establish the cytotoxicity of NBS037.
b) Investigate the mechanism of action of NBS037 in these cell models through testing:
    i. Target engagement
    ii. Respiration
    iii. Uncoupling activity
    iv. ROS production

3.3 Selection of cell culture lines

The American Type Culture Collection (ATCC), the world's largest catalogue of animal and human cell lines, contains over 4000 different continuous cell lines[274]. To best investigate the effects of NBS037 in cells, suitable cell lines from this vast collection must be selected. NBS037 is expected to be more effective in tumour cells which rely more heavily on OXPHOS, therefore high OXPHOS and high glycolysis driven cells are required to compare effects of OXPHOS inhibition. To account for effects on normal tissue, some non-cancer controls are required also.

Dr Jon Lees (Oxford Brookes University) created a ranking system for OXPHOS dependency of various cell lines. The binary data matrix of essentiality for cancer dependency map was downloaded from The Cancer Dependency Map at Sanger (https://depmap.sanger.ac.uk/). This is a binary matrix classifying genes as '1' if knocking out the gene in that cell line significantly reduced growth compared to controls. He derived a score for each cell line based on how often loss of a mitochondrial gene reduced growth compared to controls, where mitochondrial genes were defined as mitochondrial-electron transport, mitoribosome, or combined. Definitions for electron transport or mito-ribosome were obtained from the CORUM protein complex database[275].

323 human cancer cell lines across 19 different tissue types were analysed, with their gene score for mitochondrial complex I of the respiratory chain determined. (Figure 3.1). In this data set endometrial, peripheral nervous system (PNS), stomach, bone, breast, and ovarian tissues had high average gene rank scores; however, most tissues proved to have cell lines which scored both very high and very low on the ranking system, highlighting the different behaviour of cell lines even within the same tissue (Appendix A).

Many human cancer cell lines commonly used for *in vitro* cancer research were included in the gene analysis (Table 3.1). Three cell lines from different tissues were chosen from the top ten ranking cell lines for testing with NBS037: Cal-51 (human breast carcinoma), FaDu (human hypopharyngeal carcinoma), and NCI-H520 (human NSCLC). With lung cancer one of the most common, and deadly types of cancer, further examples from the lung were of interest. The 11th highest scoring cell line was A549, a NSCLC line similar to NCI-H520 but with a considerably lower gene rank score. A549 was selected for testing with NBS037 to test if the theorised OXPHOS dependency from the gene rank was reflected in sensitivity to OXPHOS inhibition in practise. A549 would be expected to have lower sensitivity to NBS037 compared to NCI-H520.

With lung selected as a tissue of interest, the NSCLC line H460 was also selected for testing with NBS037. Although not analysed in initial OXPHOS gene ranking, H460 was included due to its well characterised ability to model carcinomas in xenograft models. With up to 100% tumour uptake in CD-1 mice models and fast growth time, use of H460 cells allow the opportunity for *in vivo* work in an OXPHOS sensitive cell line[276,277]. The MRC-5 lung fibroblast and ARPE-19 cell lines were selected as non-cancer controls in order to model the response to NBS037 in normal lung and epithelial tissue.

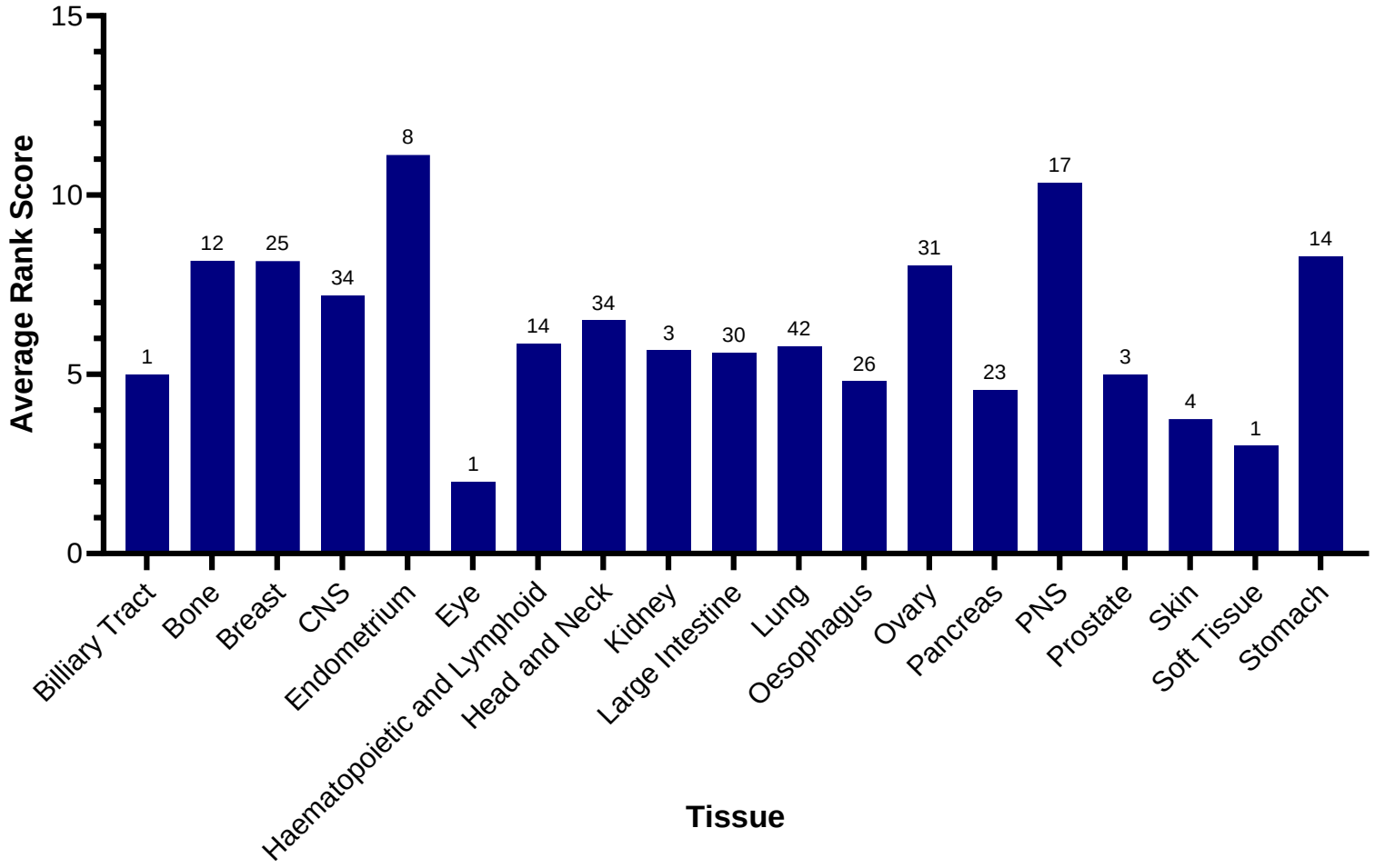

Figure 3.1. Summary of data collected by Dr Jon Lees, ranking human cancer cell lines according to dependency on OXPHOS (complex I). *Average ranking score is plotted with number of cell line types indicated above each bar. Higher ranking scores indicate higher OXPHOS reliance. CNS, central nervous system; PNS, periphery nervous system.*

Table 3.1. OXPHOS ranking of commonly used human cancer cell lines (data provided by Dr Jon Lees).

Model Name	Rank Score	Tissue	Tissue Status	Cancer Type
HGC-27	31	Stomach	Metastasis	Gastric Carcinoma
CAL-51	28	Breast	Metastasis	Breast Carcinoma
EW-7	26	Bone	Metastasis	Ewing's Sarcoma
SF295	26	Central Nervous System	Unknown	Glioblastoma
KON	25	Head and Neck	Tumour	Oral Cavity Carcinoma
FADU	21	Head and Neck	Tumour	Head and Neck Carcinoma
U251	20	Central Nervous System	Tumour	Low Grade Glioma
NCI-H520	20	Lung	Tumour	Squamous Cell Lung Carcinoma
UWB1.289	20	Ovary	Tumour	Ovarian Carcinoma
HCT-15	17	Large Intestine	Tumour	Colorectal Carcinoma
A549	13	Lung	Tumour	Lung Adenocarcinoma
A2780	12	Ovary	Tumour	Ovarian Carcinoma
DU-145	12	Prostate	Metastasis	Prostate Carcinoma
NCI-N87	10	Stomach	Metastasis	Gastric Carcinoma
AGS	10	Stomach	Tumour	Gastric Carcinoma
ESO26	9	Oesophagus	Tumour	Oesophageal Adenocarcinoma
FLO-1	9	Oesophagus	Tumour	Oesophageal Adenocarcinoma
CAPAN-1	8	Pancreas	Metastasis	Pancreatic Carcinoma
HEC-1	5	Endometrium	Tumour	Endometrial Carcinoma
OVCAR-3	5	Ovary	Metastasis	Ovarian Carcinoma
KLE	3	Endometrium	Tumour	Endometrial Carcinoma
COLO-205	3	Large Intestine	Metastasis	Colorectal Carcinoma
Caov-4	3	Ovary	Metastasis	Ovarian Carcinoma
AsPC-1	3	Pancreas	Metastasis	Pancreatic Carcinoma
KATOIII	3	Stomach	Metastasis	Gastric Carcinoma
MDA-MB-231	2	Breast	Metastasis	Breast Carcinoma
hTERT-RPE-1	2	Eye	Transformed	Non-Cancerous

SU-DHL-10	2	Haematopoietic and Lymphoid	Metastasis	B-Cell Non-Hodgkin's Lymphoma
A253	2	Head and Neck	Tumour	Head and Neck Carcinoma
RCC-FG2	2	Kidney	Tumour	Kidney Carcinoma
BxPC-3	2	Pancreas	Tumour	Pancreatic Carcinoma
SK-N-SH	2	Peripheral Nervous System	Metastasis	Neuroblastoma
CHP-212	2	Peripheral Nervous System	Tumour	Neuroblastoma
SW837	1	Large Intestine	Tumour	Colorectal Carcinoma
CAL-72	0	Bone	Tumour	Osteosarcoma
U-87-MG	0	Central Nervous System	Tumour	Glioblastoma
ESO51	0	Oesophagus	Tumour	Oesophageal Adenocarcinoma
LNCaP-Clone-FGC	0	Prostate	Metastasis	Prostate Carcinoma
SK-MEL-2	0	Skin	Metastasis	Melanoma

3.4 NBS037 potently decreases cell viability in cancer lines

To first assess if NBS037 causes any effect on cells *in vitro*, a PI screen for cell viability was carried out. PI is a fluorescent probe which can permeate dead cells due to disruption of the plasma membrane and intercalates with double stranded DNA to produce a fluorescent signal[278]. When all of the cells in a sample are killed via freeze thaw cycles, the total cell count can be measured and the viable cells in the sample can be deduced from the dead and total cell count measurements.

Whilst the cancer cell lines differ in growth rate, in all lines tested NBS037 potently decreased cell viability over the seven-day treatment period in a dose dependent manner (Figure 3.2). IC50s, the concentration of NBS037 required to reduce cell viability by 50%, were calculated in GraphPad Prism for each cell line at 72 hours of drug treatment, and summarised in Table 3.2.

Table 3.2. IC50 (μM) of NBS037 in cancer cell lines calculated at 72 hours of treatment.

Cell Line	*11 mM glucose IC50 (μM)*	*1 mM glucose IC50 (μM)*
A549	1.149	0.9786
H460	0.6037	0.2056
H520	0.8577	0.8959
Cal51	0.9200	0.6815
FaDu	0.6961	0.9162

The H460 cell line proved to be the most sensitive to NBS037 with the lowest IC50 across both glucose concentrations. A549 was the least sensitive cancer line, having the only IC50 above 1 μM in standard (11 mM) glucose conditions, despite it being a NSCLC line similar to H460 and H520. In both high and low glucose, the order in which cell lines were most to least sensitive to NBS037 did not correlate with the high to low gene rank scores in Table 3.1.

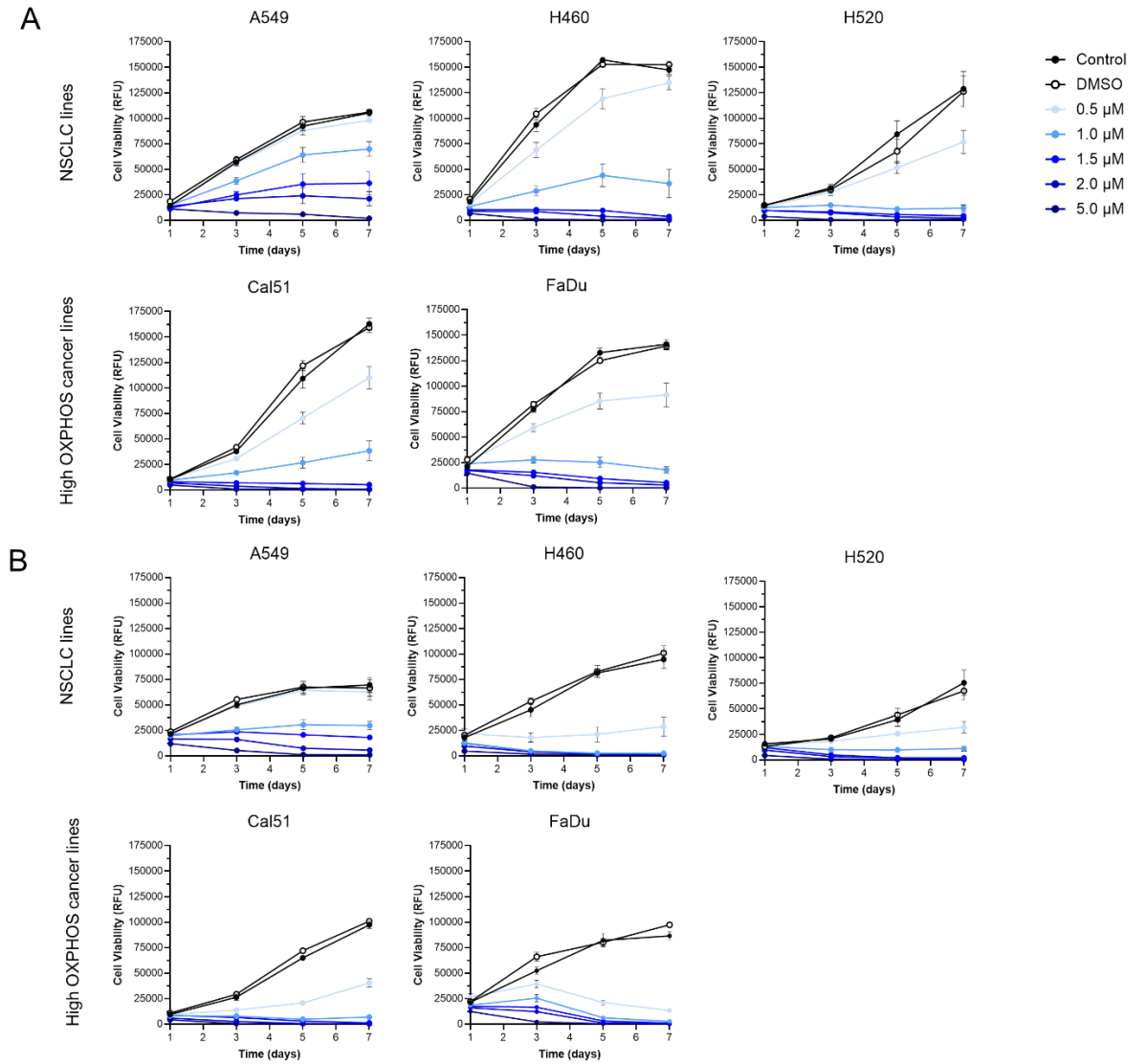

Figure 3.2. Growth curves of cancer cell lines with NBS037 treatment. *PI was used to assess cell viability with NBS037 treatment over seven days in A549, H460, and H520 NSCLC, Cal51 breast carcinoma, and FaDu hypopharyngeal carcinoma under (A) 11 mM or (B) 1 mM glucose. DMSO was used as a vehicle control. Media was replaced daily to maintain glucose levels. Data represents mean cell viability ± SEM. N=3.*

3.5 Glucose manipulation affects the sensitivity to NBS037

Standard culture conditions often contain high concentrations of glucose which promotes a preference for glycolysis, and dampens the use of OXPHOS for ATP production[279,280]. This would affect the sensitivity to OXPHOS inhibitors such as NBS037, and is not reflective of the conditions *in vivo*. In order to investigate the effect of different glucose concentrations on

NBS037 sensitivity, the PI screen was conducted in 11 mM (standard), 5 mM (physiological blood glucose) and 1 mM (low) glucose conditions.

Lowering the glucose had an impact on the potency of NBS037, indicated by a decrease in IC50 in A549, H460, and Cal51, and increased IC50 in H520 and FaDu after 72 hours of treatment (Table 3.2). In H460 cells, which were the most sensitive to NBS037, 72 hours of treatment at 1 μM NBS037 caused a 69% decrease in cell viability in 11 and 5 mM glucose, whilst lowering glucose to 1 mM caused a decrease of 89% viability under the same NBS037 dose (Figure 3.3A). Meanwhile, A549 which is the least sensitive of the cancer lines tested, still showed a greater decrease in cell viability at 1 μM NBS037 in 1 mM glucose (49%) compared to 5 mM (37%) and 11 mM (32%) when compared to controls..

After 72 hours of treatment, NBS037 elicited a significant decrease in cell viability across all cancer cell lines between 1 and 5 μM (Figure 3.3A); however, lowering the glucose allowed a lower concentration of NBS037 to be used for a significant decrease in cell viability. Within 72 hours, H460 and FaDu lines were sensitive to NBS037 at its lowest dose, 0.5 μM, in all glucose conditions (Figure 3.3A). A significant decrease in cell viability was also observed with 0.5 μM NBS037 in 5 mM glucose in A549 and H520, and in 1 mM glucose in Cal51. After seven days of treatment, A549 was still only sensitive to 0.5 μM NBS037 in 5 mM glucose, but in 11 mM glucose, 0.5 μM NBS037 no longer had any significant effects on cell viability in H460 cells (Figure 3.3B). All other cell lines remained highly sensitive to NBS037 at all drug concentrations and across all glucose conditions.

In untreated and DMSO treated cells, as well as with lower concentrations of NBS037, lowering the glucose resulted in significantly decreased cell viability compared to cells grown in 11 mM glucose (Figure 3.4), likely due to a slower growth rate. At higher concentrations of NBS037 (>1.5 μM), the number of viable cells did not significantly differ between glucose conditions as cell death was high regardless of glucose concentration.

A

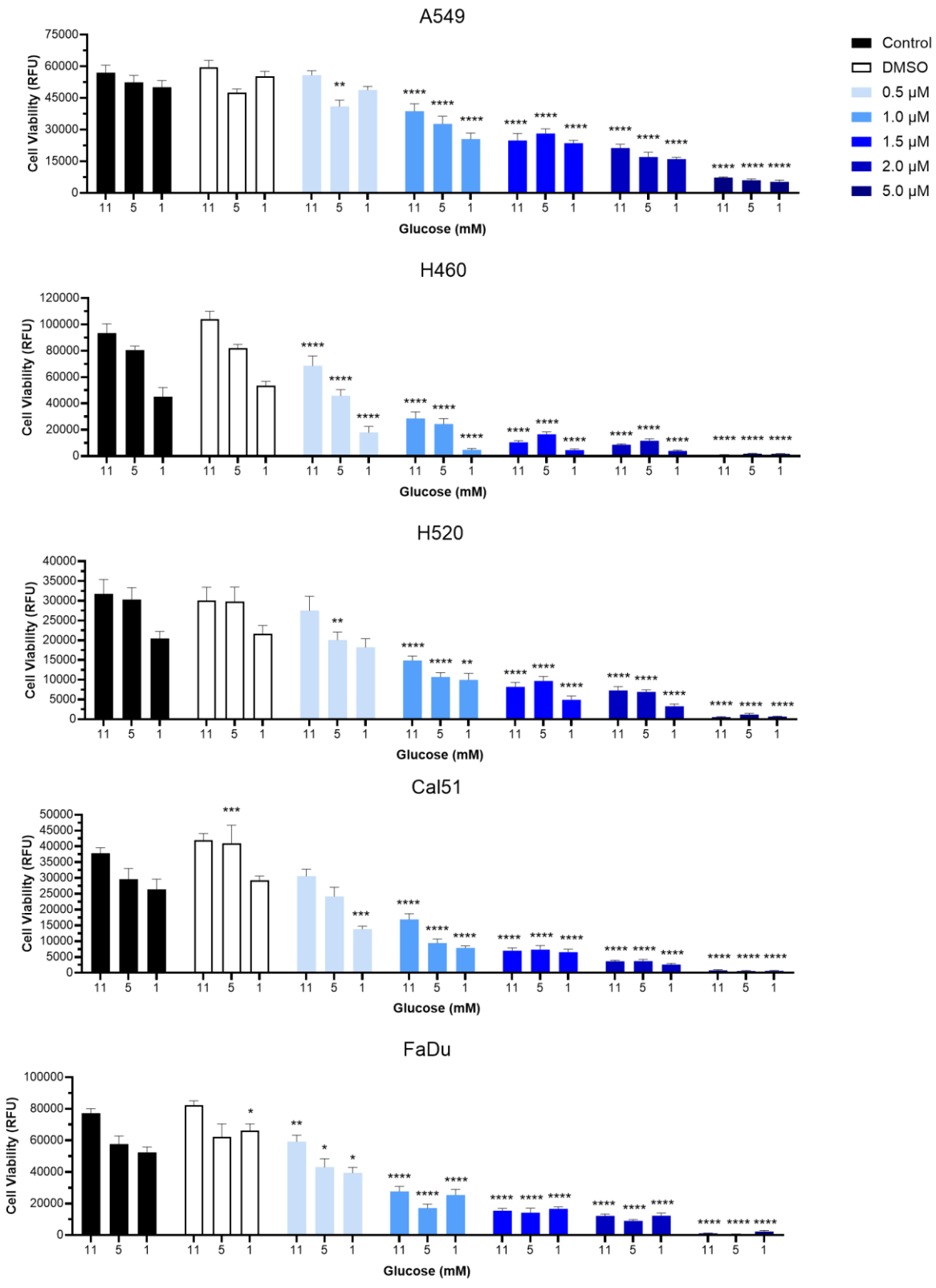
A549
H460
H520
Cal51
FaDu
Cell Viability (RFU)
Glucose (mM)
Control
DMSO
0.5 μM
1.0 μM
1.5 μM
2.0 μM
5.0 μM

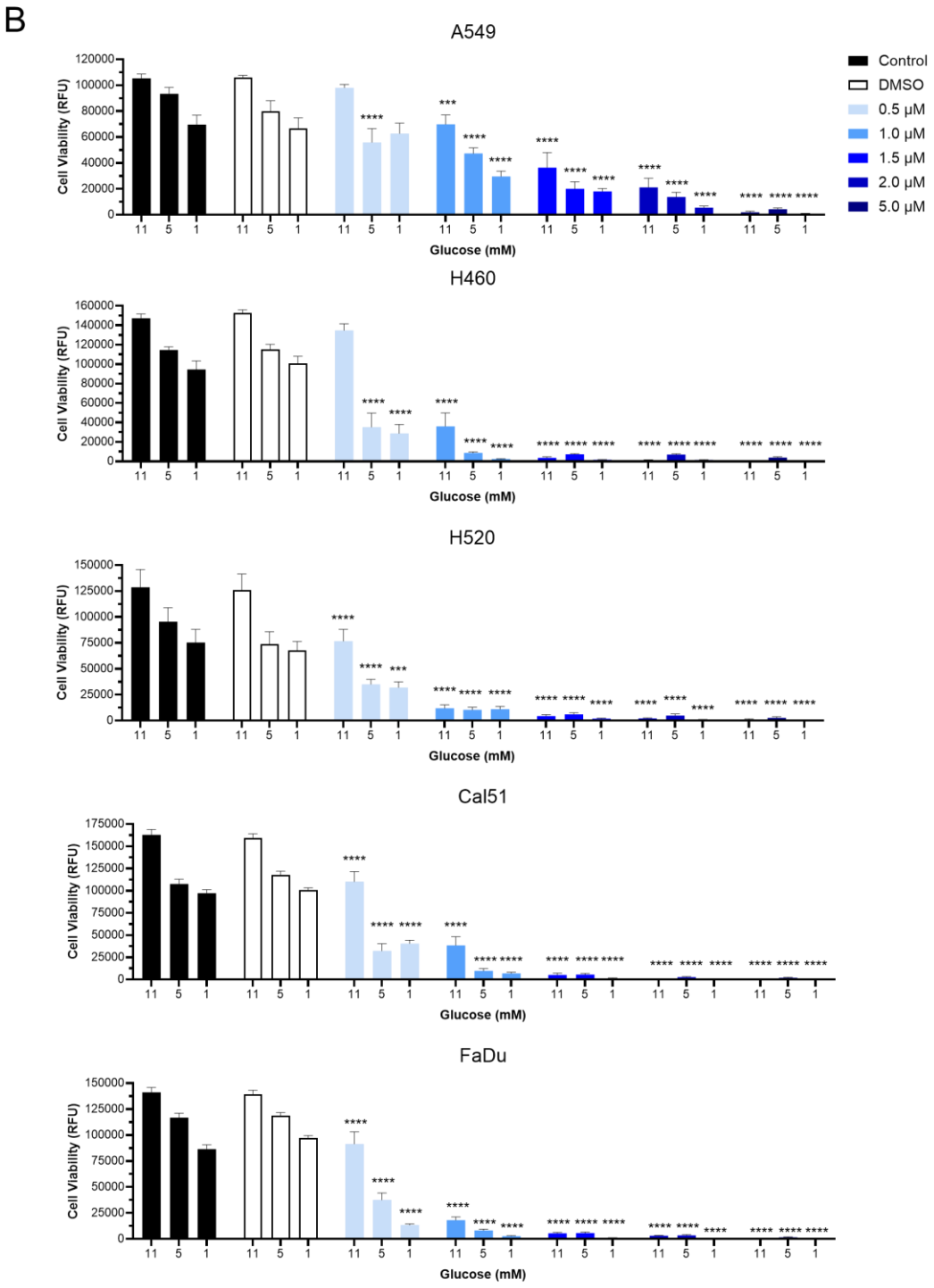

Figure 3.3. Cell viability of cancer cell lines with NBS037 treatment in various glucose conditions. *PI was used to assess cell viability with NBS037 treatment over seven days in A549, H460 and H520 NSCLC, Cal51 breast carcinoma, and FaDu hypopharyngeal carcinoma. DMSO was used as a vehicle control. Media was replaced daily to maintain glucose levels. Bars represents mean cell viability ± SEM at (A) 72 hours and (B) seven days. Statistical analysis at each time point was performed by two-way ANOVA with Dunnett's multiple comparisons post hoc tests to compare each treatment group with untreated controls in the same glucose concentration (*, p < 0.05; **, p < 0.01; ***, p < 0.001; ****, p < 0.0001). N=3.*

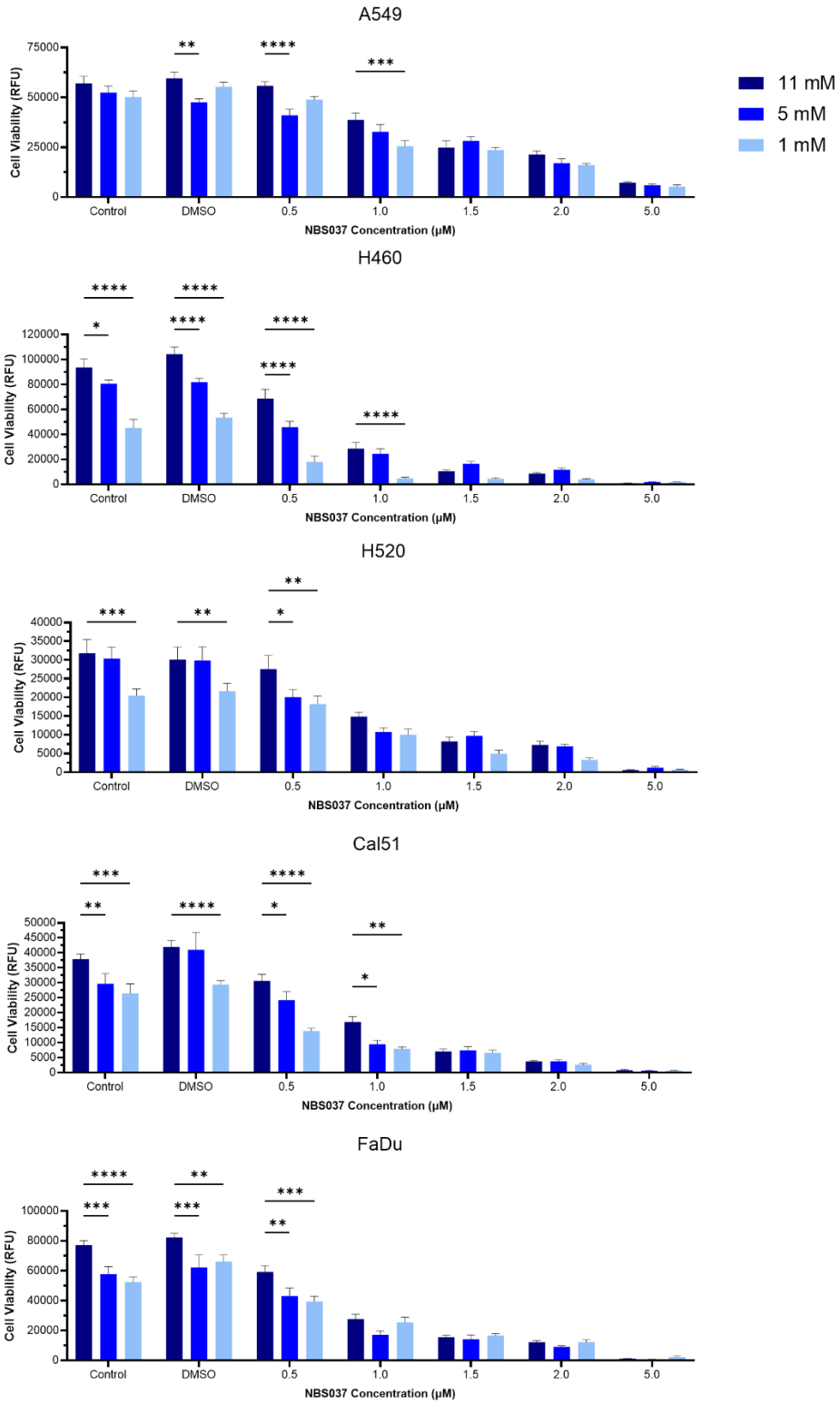

Figure 3.4. Cell viability of cancer cell lines with NBS037 treatment in various glucose conditions. *PI was used to assess cell viability with NBS037 treatment after 72 hours in A549, H460 and H520 NSCLC, Cal51 breast carcinoma, and FaDu hypopharyngeal carcinoma. DMSO was used as a vehicle control. Media was replaced daily to maintain glucose levels. Bars represents mean cell viability ± SEM. Statistical analysis was performed by two-way ANOVA with Dunnett's multiple comparisons post hoc tests to compare results from low glucose (1 mM and 5 mM) to standard culture glucose (11 mM) (*, $p < 0.05$; **, $p < 0.01$; ***, $p < 0.001$; ****, $p < 0.0001$). N=3.*

3.6 NBS037 has little effect in MRC-5, but reduces cell viability in ARPE-19

The PI assay was repeated in the non-cancer cell lines MRC-5 and ARPE-19 in order to compare the response of cancer lines to controls, and deduce if NBS037 works specifically in cancer cells as hypothesised. Cells underwent treatment for seven days in both 11 mM and 1 mM glucose to produce growth curves for each cell line (Figure 3.5). IC50 values were calculated in GraphPad Prism after 72 hours of NBS037 treatment and summarised in Table 3.3.

In MRC-5 cells, NBS037 was well tolerated. 5 μM NBS037 caused a significant decrease in cell viability regardless of glucose concentration, and 2 μM NBS037 only caused a significant decrease in viability in 1 mM glucose ($p = 0.0203$) (Figure 3.6). At all other concentrations, NBS037 caused no significant decrease in cell viability in 72 hours or seven days of treatment. The IC50 of NBS037 in MRC-5 cells was over double that of the cancer cell lines (Table 3.3), indicating poor sensitivity to the drug in this fibroblast cell line.

Interestingly, ARPE-19 was sensitive to NBS037, shown by a dose dependent decrease in cell viability (Figure 3.5). At both 72 hours and seven days of treatment, a significant decrease in cell viability was observed across all glucose concentrations with 1 - 5 μM NBS037 treatment (Figure 3.6). The IC50 of NBS037 in ARPE-19 was higher than values measured in cancer cell lines, and was further increased in 1 mM glucose (Table 3.3). For both glucose conditions, the IC50 of NBS037 in ARPE-19 remained lower than MRC-5.

.

Table 3.3. IC50 (μM) of NBS037 in non-cancer cell lines calculated at 72 hours of treatment.

Cell Line	*11 mM glucose IC50 (μM)*	*1 mM glucose IC50 (μM)*
MRC-5	2.2029	2.194
ARPE-19	1.471	1.962

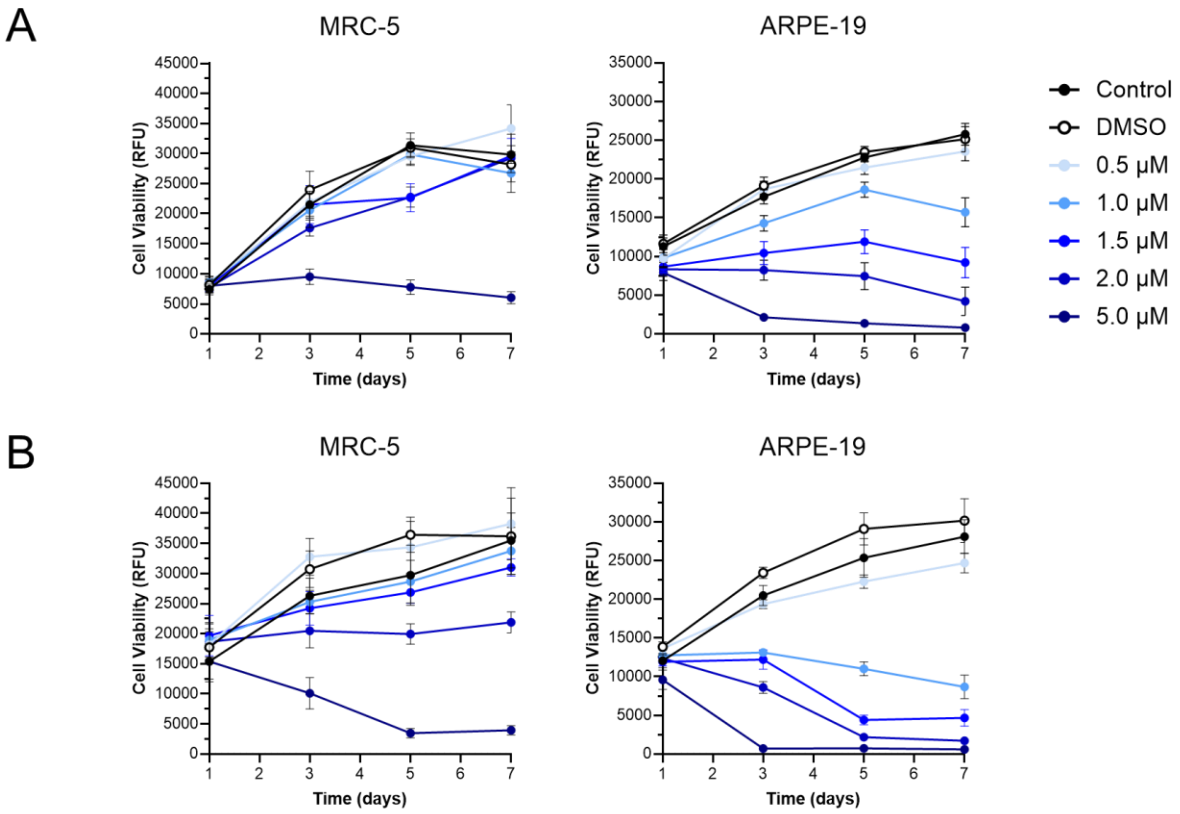

Figure 3.5. Growth curves of non-cancer cell lines with NBS037 treatment. *PI was used to assess cell viability with NBS037 treatment over seven days in MRC-5 lung fibroblast and ARPE-19 retinal epithelial cells in (A) 11 mM and (B) 1 mM glucose. DMSO was used as a vehicle control. Media was replaced daily to maintain glucose levels. Data represents mean cell viability ± SEM. N=3.*

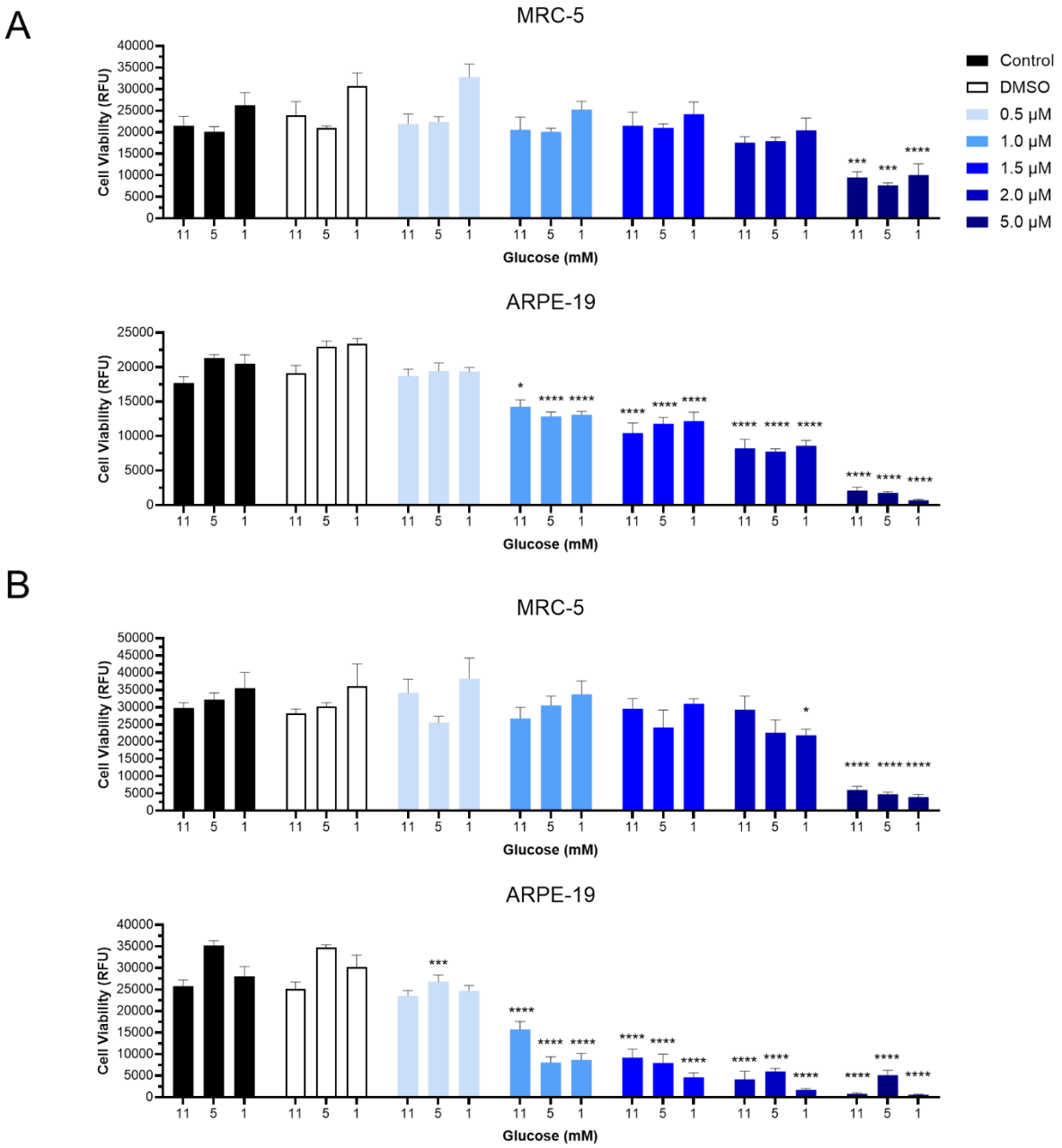

3.6. Cell viability of non-cancer cell lines with NBS037 treatment in various glucose conditions. *PI was used to assess cell viability with NBS037 treatment in MRC-5 lung fibroblast and ARPE-19 retinal epithelial cells. DMSO was used as a vehicle control. Media was replaced daily to maintain glucose levels. Bars represents mean cell viability ± SEM at (A) 72 hours and (B) seven days of treatment. Statistical analysis at each time point was performed by two-way ANOVA with Dunnett's multiple comparisons post hoc tests to compare each treatment group with untreated controls in the same glucose concentration (*, $p < 0.05$; ***, $p < 0.001$; ****, $p < 0.0001$). N=3.*

3.7 AZM lacking the mitochondrial targeting group does not decrease cell viability

As AZM is the cargo molecule of NBS037, the effects of AZM alone was tested in four cell lines to confirm if changes in cell viability were due to mitochondrial targeted NBS037 or AZM. Two NSCLC lines, A549 and H460 were selected for further testing due to their differences in sensitivity to NBS037. The cell lines MRC-5 and ARPE-19 were included in further study to investigate the response of non-cancer cell lines to NBS037, and compare such responses to cancer cells. The PI screen was repeated in 11 mM and 1 mM glucose conditions, with AZM used at the same concentrations as NBS037 (Figure 3.7).

Unlike NBS037, in all cell lines tested AZM did not cause a decrease in cell viability at any dose, regardless of glucose in the media (Figure 3.8). However, in some conditions AZM was capable of significantly increasing cell viability (Figure 3.8). In 11 mM glucose at 72 hours, AZM caused a significant increase in cell viability in A549 cells at 1.5 μM ($p = 0.0298$) and 5 μM ($p = 0.0465$) AZM, and in H460 at 0.5 μM ($p = 0.0101$) AZM (Figure 3.8A). In seven days with AZM treatment and 1 mM glucose, a tendency for cell viability to increase in ARPE-19 was observed, with 1 μM AZM causing significant effects when compared with untreated controls ($p = 0.0397$) (Figure 3.8B).

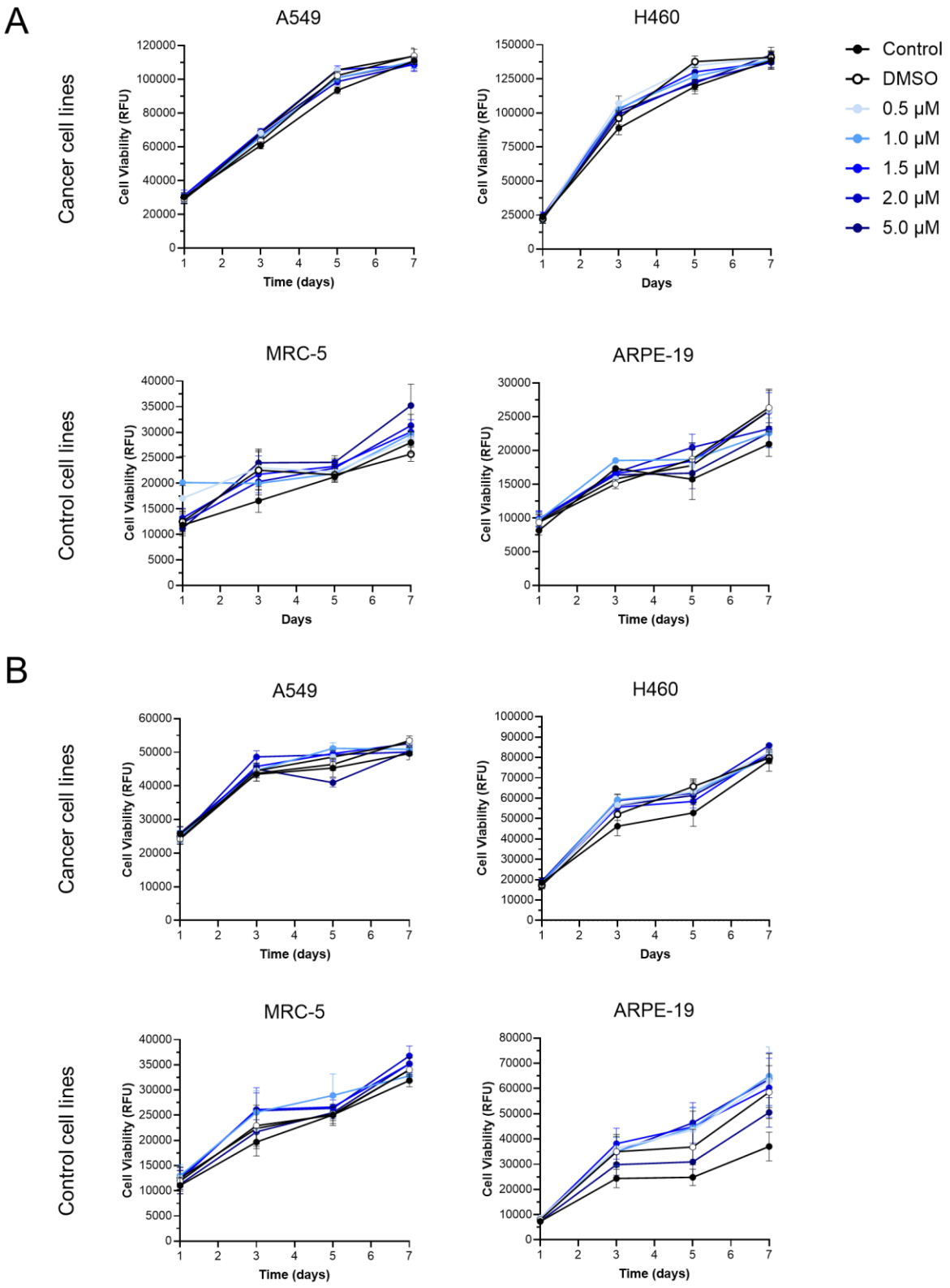

Figure 3.7. Growth curves of cell lines with AZM treatment. *PI was used to assess cell viability with NBS037 treatment over seven days in A549 and H460 NSCLC, MRC-5 lung fibroblast, and ARPE-19 retinal epithelial cells in (A) 11 mM glucose and (B) 1 mM glucose. DMSO was used as a vehicle control. Media was replaced daily to maintain glucose levels. Data represents mean cell viability ± SEM. N=3.*

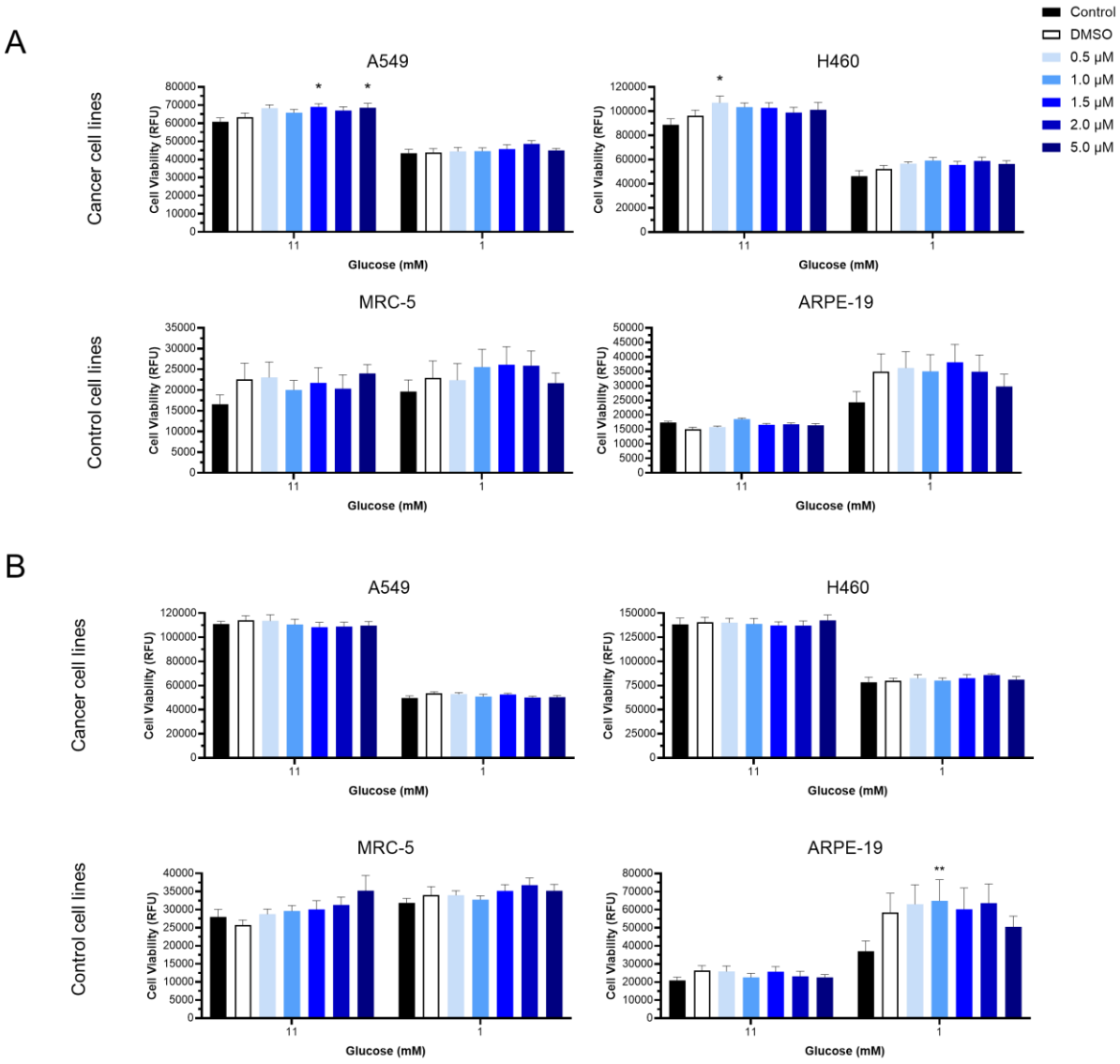

Figure 3.8. Cell viability of cell lines with AZM treatment in various glucose conditions. *PI was used to assess cell viability in A549 and H460 NSCLC, MRC-5 lung fibroblast, and ARPE-19 retinal epithelial cells. DMSO was used as a vehicle control. Media was replaced daily to maintain glucose levels. Bars represent mean cell viability ± SEM at (A) 72 hours and (B) seven days of treatment. Statistical analysis was performed by two-way ANOVA with Dunnett's multiple comparisons post hoc tests to compare each treatment group with untreated controls in the same glucose concentration (*, $p < 0.05$; **, $p < 0.01$; ***, $p < 0.001$; ****, $p < 0.0001$). N=3.*

3.8 Cellular bioenergetics may impact sensitivity to NBS037

Each type of cell will have different contributions of OXPHOS and glycolysis for ATP production. Those which have a higher reliance on OXPHOS are predicted to be more sensitive to NBS037, with more severe consequences of OXPHOS inhibition. To investigate if differential sensitivity to NBS037 is due to the bioenergetics of different cell lines, OCR and ECAR were assessed as a readout for OXPHOS and glycolysis respectively. The MitoXpress Xtra fluorescent probe provides real time measurement of oxygen consumption. The probe is quenched by extracellular oxygen through molecular collisions, and therefore fluorescence is inversely proportional to extracellular oxygen levels. The rate of oxygen consumption can be determined by fluorescence over time[281]. The pH-Xtra fluorescent signal increases with acidification and therefore fluorescent signal over time can be utilised as a readout for rate of glycolysis[282].

In 11 mM glucose, the cell lines did not vary largely in OCR and ECAR (Figure 3.9A). H460 had the highest OCR (1.853 μs/hour) but maintained a similar ECAR to A549, so H460 does maintain glycolysis as expected, since glycolysis feeds into the TCA cycle. A549 had a lower OCR (1.136 μs/hour) and slightly higher ECAR (14.11 μs/hour) than H460, indicative of a more glycolytic phenotype. MRC-5 had the lowest metabolic rate of all of the cell lines, with the lowest OCR and ECAR. ARPE-19 displayed the highest ECAR (17.01 μs/hour) with an OXPHOS contribution similar to that of A549, again, indicative of a glycolytic phenotype.

When the glucose is low, cells would be expected to shift their metabolism towards OXPHOS due to lower glucose available for glycolysis. H460 responded as expected, with a 200% increase in OCR and loss of some contribution from glycolysis in low glucose media (Figure 3.9B). Similarly, MRC-5 cells also increased OCR and decreased ECAR in low glucose conditions. Whilst A549 showed an 174% increase in OCR in low glucose conditions, the

ECAR increased by 1.5-fold. In ARPE-19 cells, the OCR did not differ much between 11 mM and 1 mM glucose, but ECAR decreased.

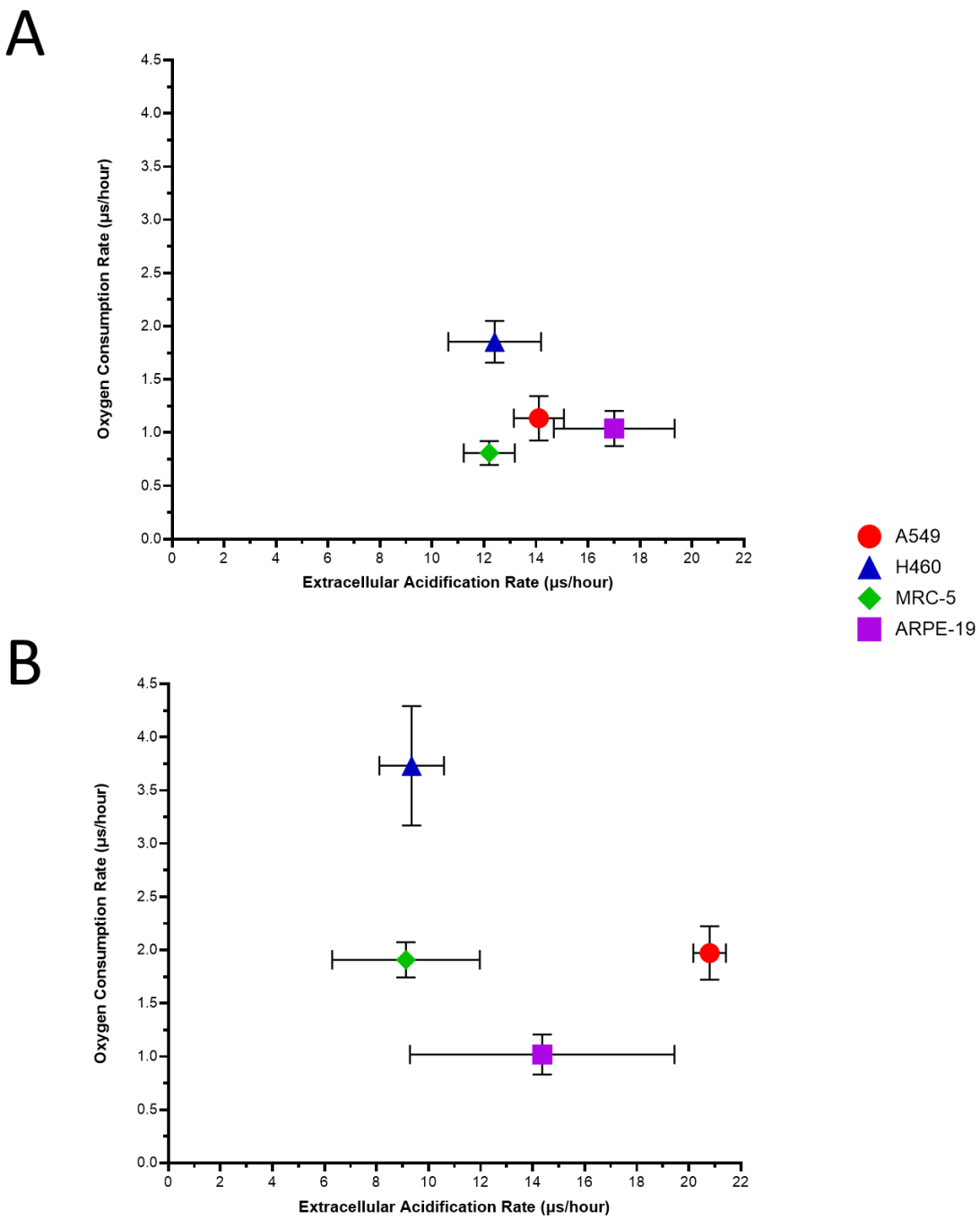

Figure 3.9. The bioenergetics of chosen cell lines. *MitoXpress Xtra probe and pH Xtra probe were used to assess OCR and ECAR respectively in A549 and H460 NSCLC, MRC-5 lung fibroblast, and ARPE-19 retinal epithelia. Data represent means ± SEM in (A) 11 mM and (B) 1 mM glucose media. N=3 for OCR and N=1 ECAR.*

Based on the previous PI assays, H460 was more sensitive to NBS037 than A549, despite both cell lines being NSCLC. To further elucidate if this is due to differences in OXPHOS dependence, WB analysis of ETC proteins was conducted. A549 and H460 cells were grown in 11 mM or 1 mM glucose for seven days, with media replaced daily to maintain glucose levels. Succinate dehydrogenase complex flavoprotein subunit A (SDHA, complex II), mitochondrial encoded cytochrome *c* oxidase 1 (MTCO1, complex IV), and ATP synthase F1 subunit beta (ATP5B, complex V) were analysed by WB (Figure 3.10A). The translocase of the outer mitochondrial membrane 20 (Tom20) protein is a key receptor expressed ubiquitously on mitochondria and a commonly used marker for mitochondrial mass[283,284]; therefore, Tom20 expression was also analysed by WB. Cells with higher OXPHOS would be expected to have higher expression of ETC proteins as well as greater mitochondrial mass.

In 11 mM glucose, MTCO1 expression did not differ significantly between A459 and H460, however, low glucose conditions caused MTCO1 expression to decrease in A549 and increase in H460 (Figure 3.10B). H460 cells had higher expression of SDHA and ATP5B than A549, although these differences failed to reach significance. In 1 mM glucose, expression of SDHA and ATP5B increased as expected in both cell lines. The cell lines had similar expression of Tom20 in 11 mM glucose, but in 1 mM glucose both cell lines had reduced Tom20 expression.

Together these data suggest A549 has lower expression of ETC machinery and subsequently lower OXPHOS rate than H460 cells which may explain the better tolerance to NBS037. Whilst A549 may be comparatively more glycolysis dependent, this is not to the detriment of mitochondrial metabolism, as A549 still maintains some OXPHOS contribution to metabolism.

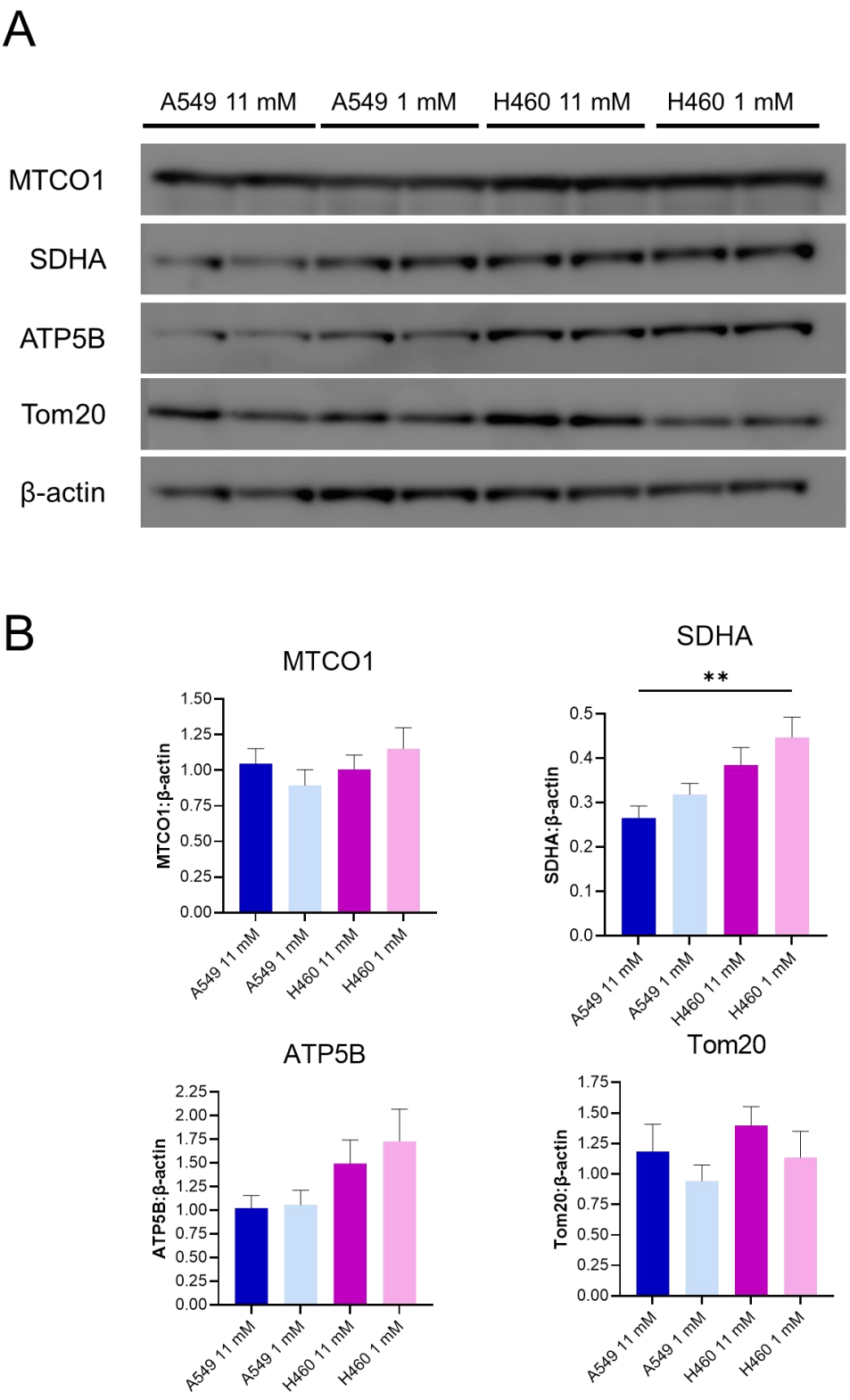

Figure 3.10. Relative OXPHOS protein expression in NSCLC lines. *WB analysis was used to investigate the mitochondrial mass and ETC protein content of A549 and H460 NSCLC lines in 11 mM and 1 mM glucose. (A) shows original blots from cell lysates run in duplicate and (B) represents mean protein expression normalised to β-actin ± SEM, quantified from blots using the G-box software. Statistical analysis was performed by one-way ANOVA with Tukey's multiple comparisons post hoc tests to compare cell lines (**, p < 0.01). N=3.*

3.9 Mitochondrial membrane potential does not explain differences in NBS037 sensitivity

A key feature of the mechanism of action of NBS037 is its specificity to cancer cell mitochondria through targeting of aberrant ΔΨm. To assess if differences in sensitivity between cell lines is due to differences in ΔΨm, TMRM dye in a non-quenching mode was used to measure ΔΨm under high and low glucose conditions. TMRM is a red-orange, fluorescent cation which accumulates inside mitochondria in proportion to the charge of the mitochondrial inner membrane, and therefore has been used to determine ΔΨm by many groups[285–287].

As noted by previous groups[285,288], the two cancer lines A549 and H460 had significantly higher ΔΨm than the non-cancer cell lines. In 11 mM glucose, the ΔΨm in A549 was 1.5 times greater ($p = 0.0028$) and in H460 was 1.6 times greater ($p = 0.0006$) than that of MRC-5, (Figure 3.11A). When cells were maintained in low glucose conditions, a significantly greater ΔΨm was observed across all cell lines, with A549 showing the smallest increase (115% of 11 mM, $p = 0.0008$) and ARPE-19 showing the largest increase (152% of 11 mM, $p = 0.0008$) (Figure 3.11C). Whilst in all cell lines ΔΨm increased in low glucose conditions, A549 and H460 maintained a significantly higher ΔΨm than MRC-5 ($p = 0.0057$ and $p = 0.0007$ respectively) (Figure 3.11B). ARPE-19 cells were sensitive to NBS037, shown by a decrease in cell viability (Figure 3.5), but had a similar ΔΨm to MRC-5, a cell line which showed little response to NBS037 treatment (Figure 3.5). Additionally, the ΔΨm was not significantly different between the two cancer cell lines, despite H460 displaying greater sensitivity to the drug (Figure 3.2). It can therefore be concluded that ΔΨm alone cannot explain the differences in sensitivity to NBS037 as its mechanism of action theorised.

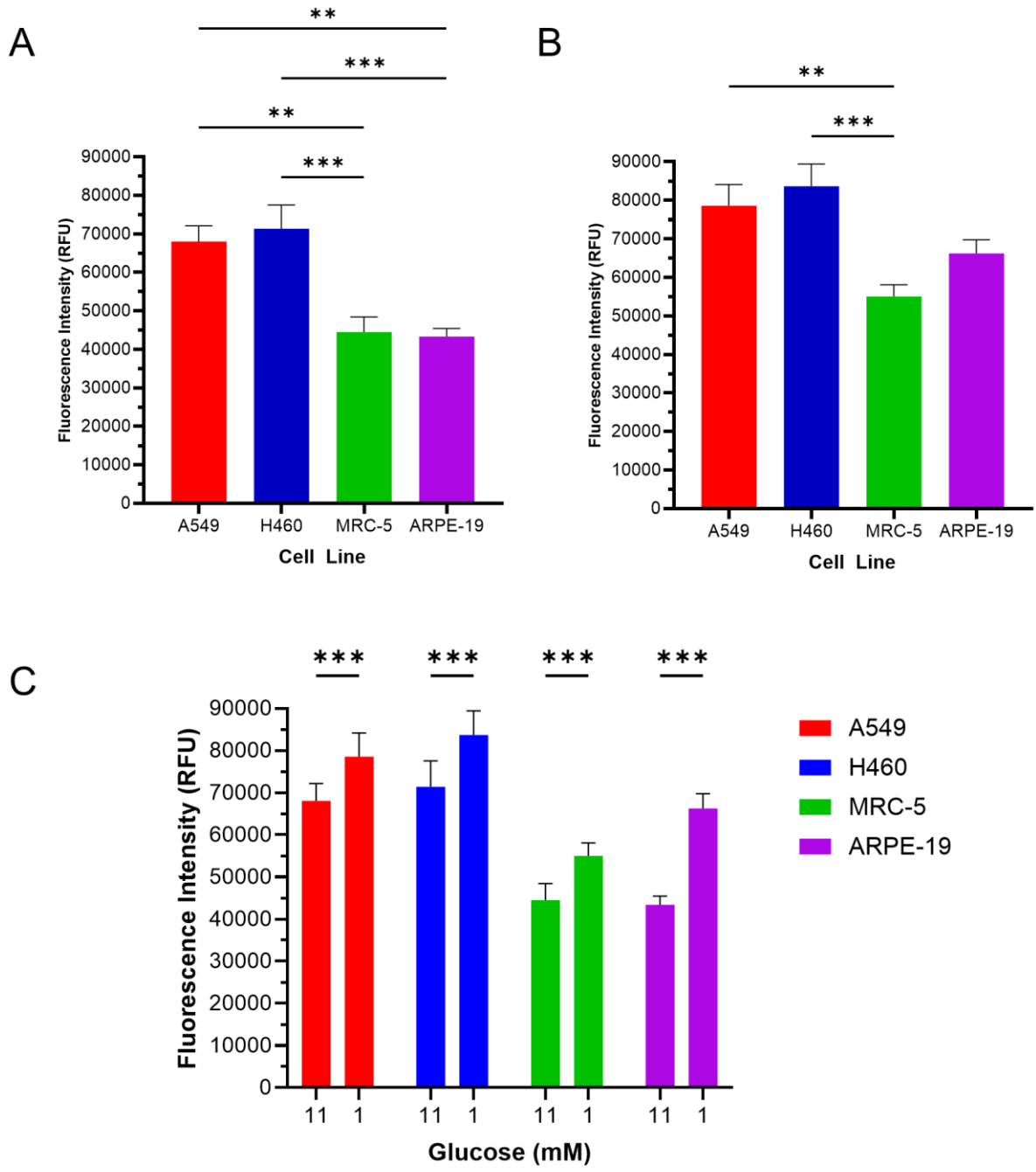

Figure 3.11. Mitochondrial membrane potential in cell lines. *TMRM dye was used to assess ΔΨm in A549 and H460 NSCLC, MRC-5 lung fibroblast, and ARPE-19 retinal epithelial cells. Data represents mean TMRM fluorescence intensity ± SEM in (A) 11 mM and (B) 1 mM glucose with (C) the effect of glucose concentration on ΔΨm in the selected cell lines. Statistical analysis was performed by one-way ANOVA with Tukey's multiple comparisons post hoc tests to compare cell lines or two-way ANOVA with Tukey's multiple comparisons post hoc tests to compare glucose concentrations (**, p < 0.01; ***, p < 0.001). N=3.*

3.10 NBS037 elicits a decrease in mitochondrial encoded protein expression in all lines but A549

Upon successful target engagement with mitochondrial ribosomes, NBS037 would cause a decrease in expression of mitochondrially encoded proteins. MTCO1, a mitochondrial encoded subunit of complex IV, was used as a readout for target engagement. MTCO1 expression was assessed and quantified by WB after 72 hours of NBS037 treatment (Figure 3.12A). The expression of MTCO1 was normalised to β-actin, the loading control (Figure 3.12B).

In H460 cells, successful target engagement was observed. A significant decrease in MTCO1 expression was observed with 1 μM ($p = 0.0064$) and 2 μM ($p = 0.0059$) NBS037, with 1 μM capable of causing MTCO1 expression to fall to 14% that of untreated controls (Figure 3.12B). Interestingly, in A549, low doses of NBS037 resulted in a tendency for MTCO1 expression to decrease, but as NBS037 dose increased, MTCO1 expression was able to recover. This could be indicative of compensatory mechanisms acting to increase mitochondrial protein levels and explain A549's better tolerance to the drug compared to H460.

Whilst successful target engagement in the high OXPHOS cancer line is encouraging, NBS037 treatment also caused a decrease in MTCO1 expression in both non-cancer controls. In MRC-5 this reached significance at 2 μM ($p = 0.0429$). In ARPE-19, 0.5 - 2 μM NBS037 elicited a significant decrease in MTCO1 expression, with the median dose of 1 μM causing an 86.8% fall in expression compared to controls ($p < 0.0001$) (Figure 3.12).

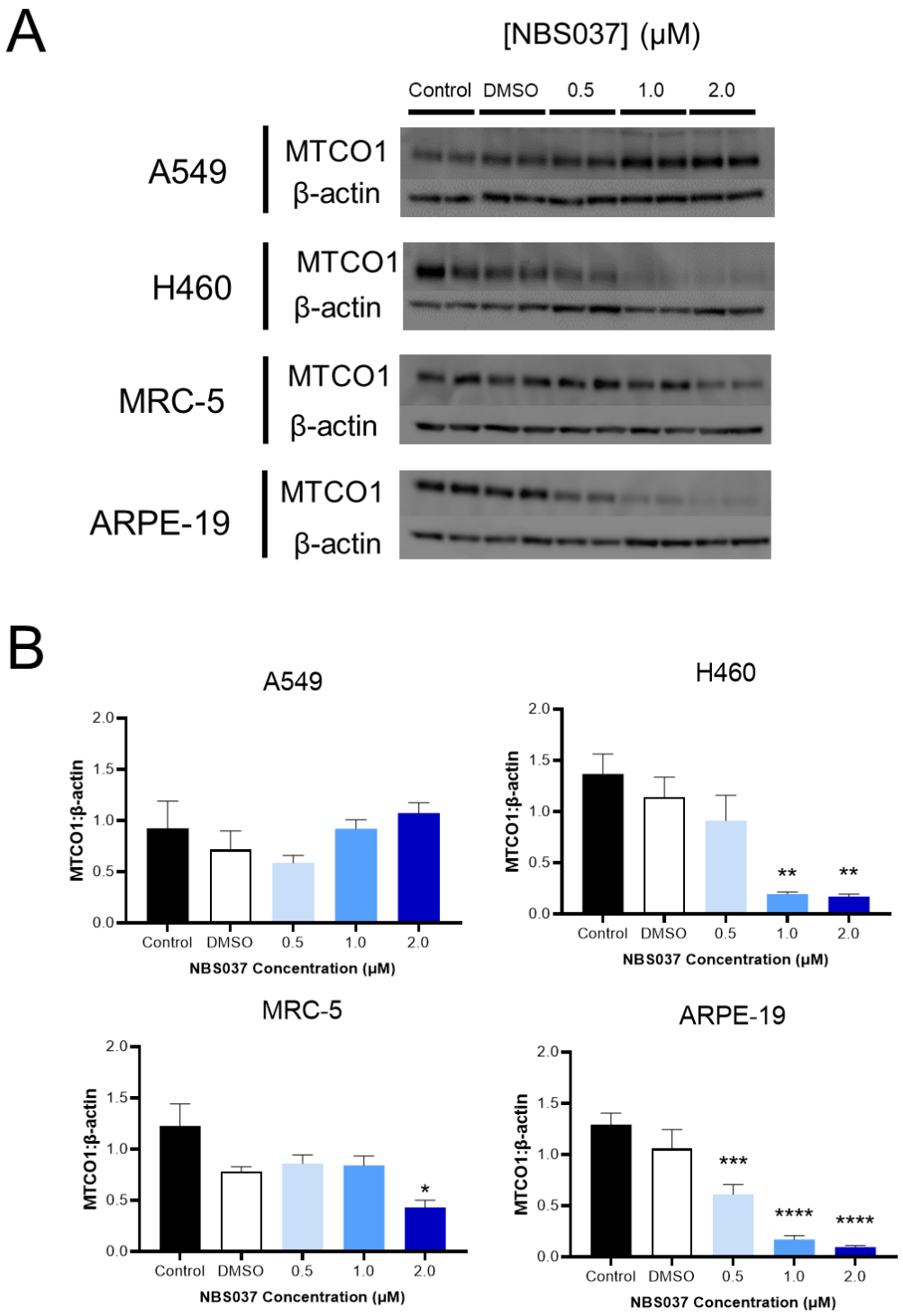

Figure 3.12. MTCO1 protein expression in cell lines treated with NBS037. *WB analysis was used to investigate the MTCO1 protein expression in A549 and H460 NSCLC lines, MRC-5 lung fibroblast, and ARPE-19 retinal epithelial cells. Cells were treated with NBS037 or DMSO as a vehicle control for 72 hours. (A) shows original blots from cell lysates run in duplicate and (B) represents mean protein expression normalised to β-actin ± SEM, quantified from blots using the G-box software. Statistical analysis was performed by Browne-Forsythe one-way ANOVA with Dunnett's T3 multiple comparisons post hoc tests to compare NBS037 treated cells to untreated controls (*, $p < 0.05$; **, $p < 0.001$, ***, $p < 0.001$; ****, $p < 0.0001$). N=3.*

3.11 SDHA expression is decreased in non-cancer cells upon NBS037 treatment

The advantage of utilising an antibiotic as the cargo for mitochondrial delivery, is its specificity to mitochondrial ribosomes, rather than ribosomes which are ubiquitous in the cytosol or endoplasmic reticulum for synthesis of nuclear encoded proteins. This should help mitigate off-target adverse effects in cells which are exposed to NBS037. After finding successful target engagement of mitochondrial ribosomes, no change in nuclear protein expression is expected. SDHA encodes the major catalytic subunit of succinate-ubiquinone oxidoreductase, complex II, of the ETC and is the only respiratory complex entirely encoded by the nucleus. SDHA expression was assessed and quantified by WB after 72 hours of NBS037 treatment (Figure 3.13A). The expression of SDHA was then normalised to β-actin, the loading control (Figure 3.13B).

Whilst no significant changes in SDHA expression were observed in cancer cell lines with NBS037 treatment, SDHA expression had a tendency to decrease in A549 and increase in H460. In MRC-5, however, 0.5 μM, 1 μM and 2 μM NBS037 caused SDHA levels to decrease significantly to approximately 50% that of untreated controls ($p = 0.0024$, $p = 0.0013$, and $p = 0.0338$ respectively). SDHA expression in ARPE-19 decreased with 1 μM NBS037 but fell significantly with 2 μM, to 56% that of untreated controls ($p = 0.0177$).

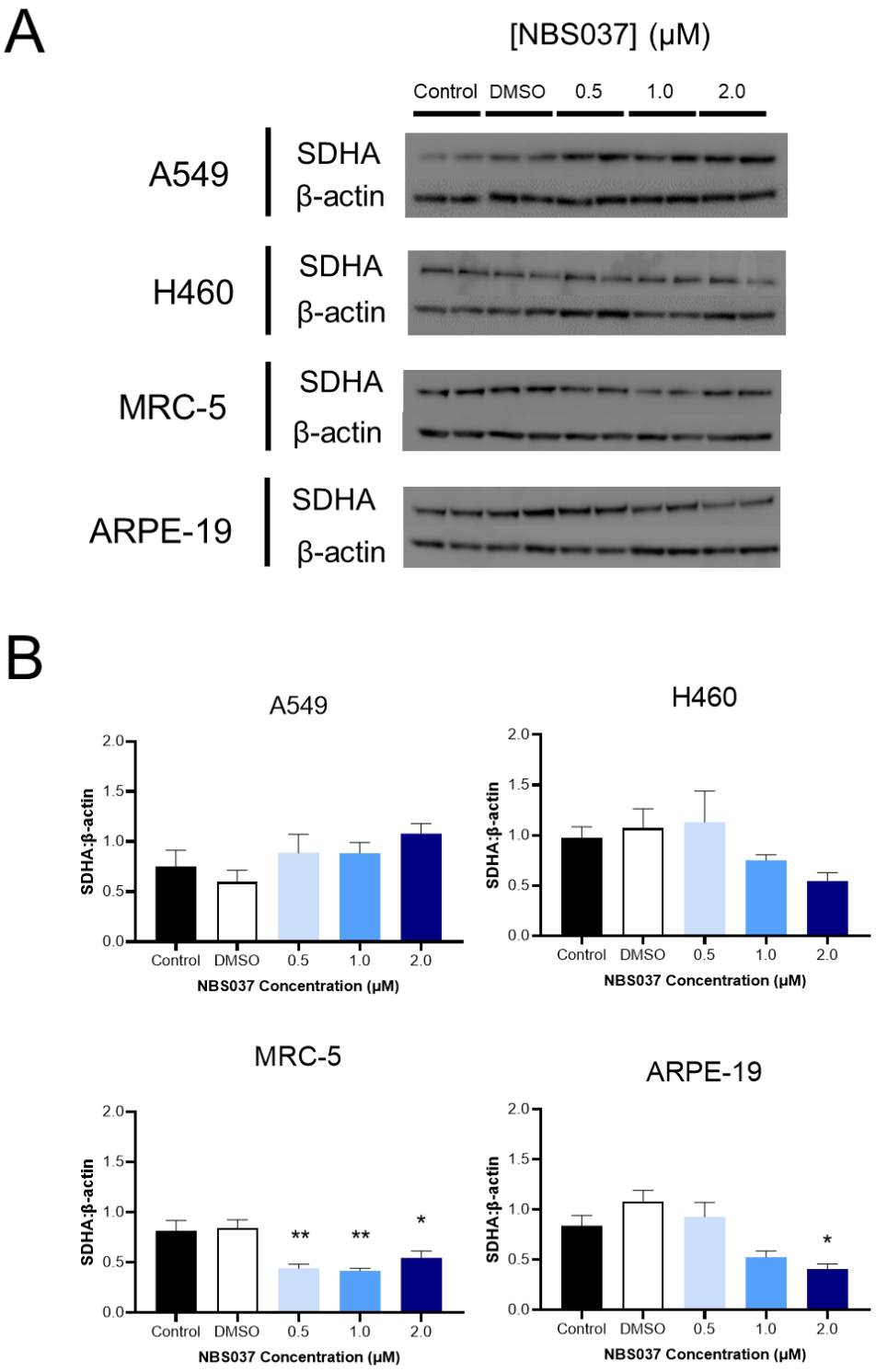

Figure 3.13. SDHA protein expression in cell lines treated with NBS037. *WB analysis was used to investigate the SDHA protein expression in A549 and H460 NSCLC lines, MRC-5 lung fibroblast, and ARPE-19 retinal epithelial cells. Cells were treated with NBS037 or DMSO as a vehicle control for 72 hours. (A) shows original blots from cell lysates run in duplicate and (B) represents mean protein expression normalised to β-actin ± SEM, quantified from blots using the G-box software. Statistical analysis was performed by one-way ANOVA with Dunnett's multiple comparisons post hoc tests to compare NBS037 treated cells to untreated controls (*, $p < 0.05$; **, $p < 0.01$). N=3.*

3.12 The ratio of mitochondrial encoded protein to nuclear encoded protein is largely decreased with NBS037 treatment

WB analysis of cell lines showed changes in MTCO1 (Figure 3.12) and SDHA (Figure 3.13) protein expression with NBS037 treatment. Expression of mitochondrially encoded MTCO1 and nuclear encoded SDHA were then directly compared to observe how NBS037 affects protein expression between the different complexes (Figure 3.14). In A549, mitochondrial protein expression was largely proportional to nuclear protein expression, with only a small decrease in ratio at 0.5 μM NBS037 (Figure 3.14A). In H460 and ARPE-19 cells, NBS037 significantly decreased mitochondrial protein expression when compared to SDHA (Figure 3.14B and D). In both of these cell lines, 1 μM reduced MTCO1:SDHA to 18% of controls ($p < 0.0001$ in H460, $p = 0.0373$ in ARPE-19), with all doses of NBS037 having significant effects in H460. Interestingly, 0.5 μM and 1 μM NBS037 caused an increase in MTCO1:SDHA in MRC-5 cells, but 2 μM caused a large decrease to 58.8% of untreated controls (Figure 3.14C).

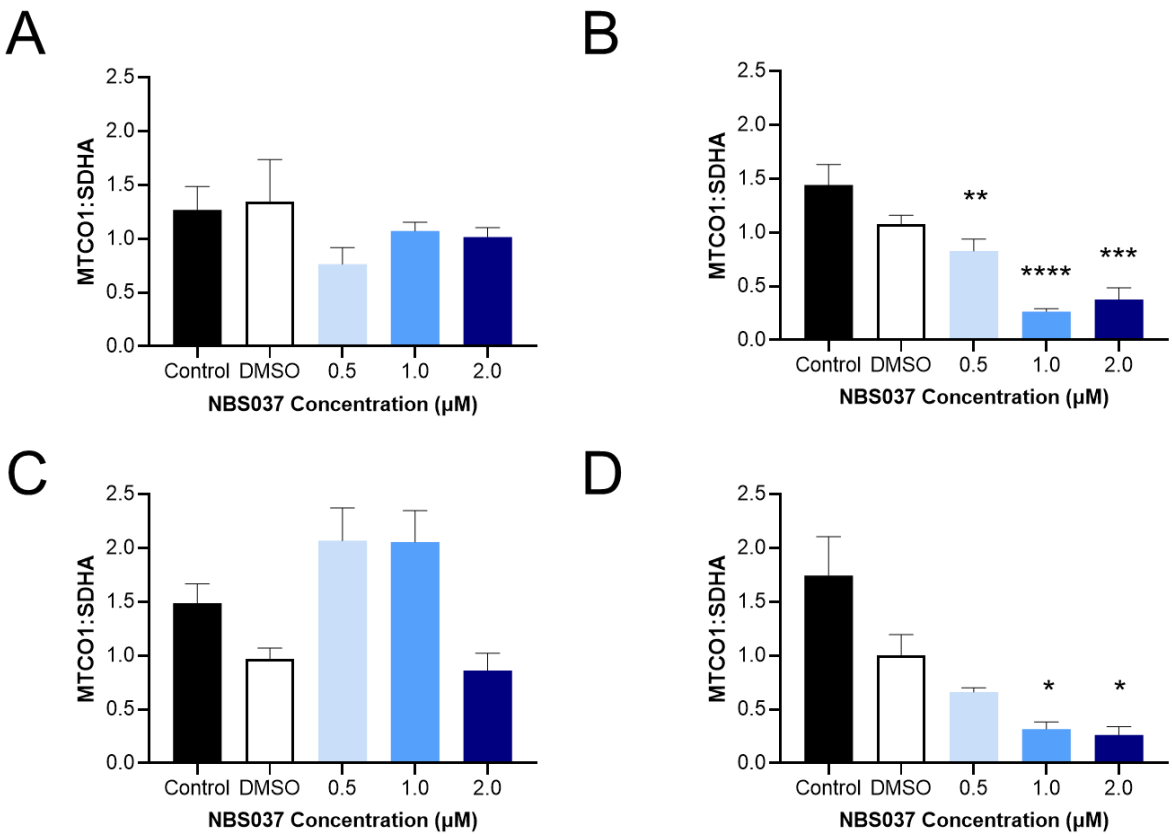

Figure 3.14. Ratio of mitochondrially encoded protein expression to nuclear encoded protein expression. *WB analysis was used to investigate the MTCO1 and SDHA protein expression in (A) A549 and (B) H460 NSCLC lines, (C) MRC-5 lung fibroblast, and (D) ARPE-19 retinal epithelial cells. Cells were treated with NBS037 or DMSO as a vehicle control for 72 hours. Blots were quantified utilising Gbox software. Data represents the ratio of MTCO1:SDHA mean protein expression ± SEM. Statistical analysis was performed by one-way ANOVA with Dunnett's multiple comparisons post hoc tests to compare NBS037 treated cells to untreated controls (*, $p < 0.05$; **, $p < 0.01$; ***, $p < 0.001$; ****, $p < 0.0001$). N=3.*

3.13 NBS037 treatment causes a tendency for Tom20 expression to increase in A549 and decrease in H460 and ARPE-19 cells

MTCO1 and SDHA, although translated in different locations, are both mitochondrially localised in the ETC. If mitochondrial mass changes, the resulting levels of mitochondrial localised proteins will also change regardless of effects NBS037 may have on mitochondrial encoded protein translation. Tom20 expression was analysed by WB after 72 hours of NBS037 treatment and blots quantified (Figure 3.15A). The expression of Tom20 was then normalised to β-actin, the loading control (Figure 3.15B).

Each cell line showed a different response to NBS037. A549 showed a small increase in Tom20, averaging approximately 30% higher than untreated controls, but failed to reach significance. With the highest dose of NBS037, Tom20 levels fell by 44% in H460 and although the decreased expression failed to reach significance, it is opposite to the response observed in A549. Expression of Tom20 remains stable in MRC-5 with NBS037 treatment but significantly decreases in ARPE-19. In ARPE-19 cells, 0.5 μM NBS037 caused the largest decrease in Tom20 expression, where expression was 52% that of untreated controls ($p = 0.0004$).

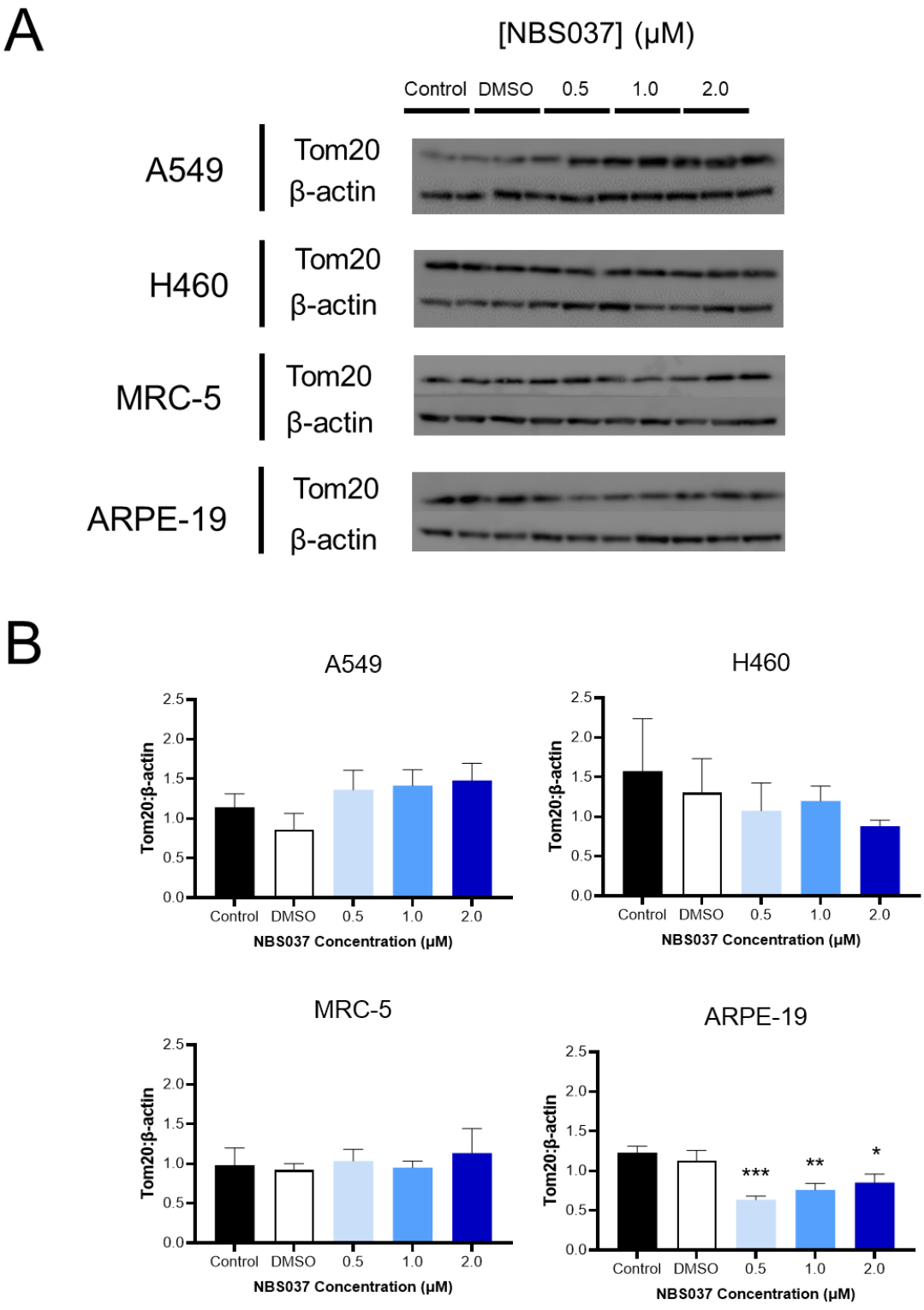

Figure 3.15. Tom20 protein expression in cell lines treated with NBS037. *WB analysis was used to investigate the Tom20 protein expression in A549 and H460 NSCLC lines, MRC-5 lung fibroblast, and ARPE-19 retinal epithelial cells. Cells were treated with NBS037 or DMSO as a vehicle control for 72 hours. (A) shows original blots from cell lysates run in duplicate and (B) represents mean protein expression normalised to β-actin ± SEM, quantified from blots using the G-box software. Statistical analysis was performed by one-way ANOVA with Dunnett's multiple comparisons post hoc tests to compare NBS037 treated cells to untreated controls (*, $p < 0.05$; **, $p < 0.01$; ***, $p < 0.001$). N=3.*

3.14 Changes in respiratory proteins are not only caused by changes in mitochondrial mass

MTCO1 and SDHA proteins are localised in the mitochondria and hence changes in physical mitochondrial mass will affect the expression of mitochondrial localised proteins measured. In order to ensure changes in expression of MTCO1 and SDHA are due to direct effects of NBS037 rather than changes in mitochondrial mass, the WBs obtained previously were normalised to the expression of Tom20 measured in Figure 3.15, rather than normalised to the loading control, β-actin. It is expected that if the mitochondrial protein expression changed proportionally with mitochondrial mass, then the ratios to Tom20 would remain constant.

When normalising MTCO1 and SDHA to Tom20, it is clear some of the changes in protein expression are in response to NBS037 and are independent of the fluctuating mitochondrial mass (Figure 3.16). The pattern of MTCO1 changes were in line with previous findings where NBS037 caused MTCO1 expression to significantly fall in H460, MRC-5, and ARPE-19 (Figure 3.12). Whilst 1 μM and 2 μM NBS037 still caused a significant decrease in MTCO1 in ARPE-19 cells ($p = 0.0002$ and $p = 0.0001$ respectively), the lowest dose of NBS037 no longer showed the same decrease, so the reduction in protein expression originally observed at this concentration was due to the fall in mitochondrial mass (Figure 3.16A).

Whilst MTCO1 expression in A549 decreased with low dose of NBS037 and then showed signs of recovery at higher doses, after Tom20 normalisation, MTCO1 expression remained below that of untreated controls, so the recovery observed was likely a result of the increased mitochondrial mass previously measured (Figure 3.15).

When normalised to Tom20, SDHA expression in A549 remained unchanged. In H460 cells, SDHA expression increased at the lowest dose of NBS037, but at 1 μM and 2 μM NBS037, expression fell back to levels of untreated controls and below (Figure 3.16B). Interestingly,

ARPE-19 cells behaved in a same manner as H460 cells, with an increase in SDHA per mitochondrion at a low dose of NBS037, but expression returning to that of untreated controls with higher NBS037 doses. In MRC-5, SDHA expression was decreased to 46% of untreated controls with 0.5 μM ($p = 0.0110$) and 1 μM ($p = 0.0144$) NBS037, and to 67% with 2 μM treatment, although this failed to reach significance.

In summary, the observed changes in MTCO1 expression in H460, MRC-5, and ARPE-19 remained independent of the changing mitochondrial mass, whilst changes induced in A549, both in MTCO1 and SDHA, were due to an upregulation of mitochondria.

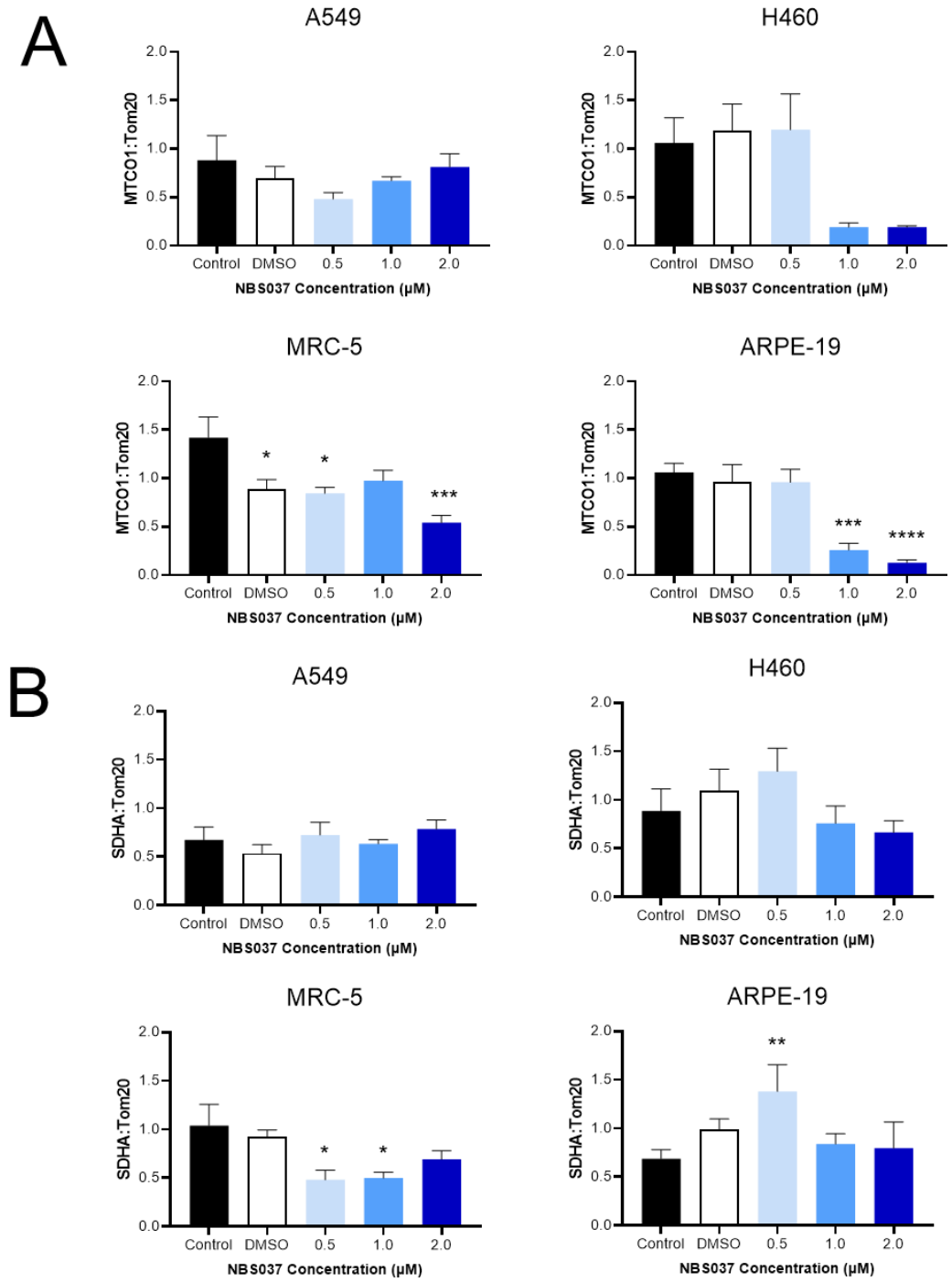

Figure 3.16. ETC protein expression normalised to mitochondrial mass in cell lines treated with NBS037. *WB analysis was used to investigate the MTCO1 and SDHA protein expression in A549 and H460 NSCLC lines, MRC-5 lung fibroblast, and ARPE-19 retinal epithelial cells and then normalised to Tom20 expression. Cells were treated with NBS037 or DMSO as a vehicle control for 72 hours. Blots were quantified utilising Gbox software. (A) represents mean protein expression of MTCO1 normalised to Tom20 ± SEM and (B) represents mean protein expression of SDHA normalised to Tom20 ± SEM. Statistical analysis was performed by one-way ANOVA with Dunnett's multiple comparisons post hoc tests to compare NBS037 treated cells to untreated controls (*, p < 0.05; **, p < 0.01; ***, p < 0.001; ****, p < 0.0001). N=3.*

3.15 NBS037 inhibits respiration in NSCLC lines with 72-hour treatment

NBS037 treatment caused changes in respiratory complexes and mitochondrial mass. Such changes would have an impact on the ability to utilise mitochondrial respiration. To investigate the effect of NBS037 on OXPHOS, the MitoXpress Xtra probe was used to measure oxygen consumption in real time after 72 hours of NBS037 treatment. The lifetime of fluorescence signal was calculated and used to visualise oxygen consumption in real time (Figure 3.17A), with OCR calculated to indicate rates of OXPHOS (Figure 3.17B).

Untreated H460 cells had the highest OCR, over double that of A549 (Figure 3.17B), in agreement with previous work earlier in this chapter. In cancer cells, NBS037 caused a dose dependent inhibition of respiration. H460 cells proved to be more sensitive to NBS037 than A549 with 1 μM ($p = 0.0007$), 1.5 μM ($p = 0.0006$), and 2 μM ($p = 0.0008$) causing a significant reduction in OCR. In H460 cells, OCR was reduced to rates similar to that observed with AA, a potent inhibitor of complex III of the ETC[289], with OCR reduced to 11.9% of controls with 2 μM NBS037 ($p = 0.0008$) (Figure 3.17B). In A549, only 2 μM NBS037 was cable of significantly reducing oxygen consumption to rates achieved with AA ($p = 0.028$). Interestingly, in H460 cells, DMSO was able to consistently increase the oxygen consumption above CCCP, the positive control, although this effect is not observed with NBS037 treatment despite DMSO being the vehicle for NBS037.

Despite changes in mitochondrial proteins, MRC-5 and ARPE-19 cells showed no significant changes in OCR with NBS037 treatment (Figure 3.17B). AA, which is used as a positive control for OXPHOS inhibition, also caused no significant effects on OCR in either non-cancer line.

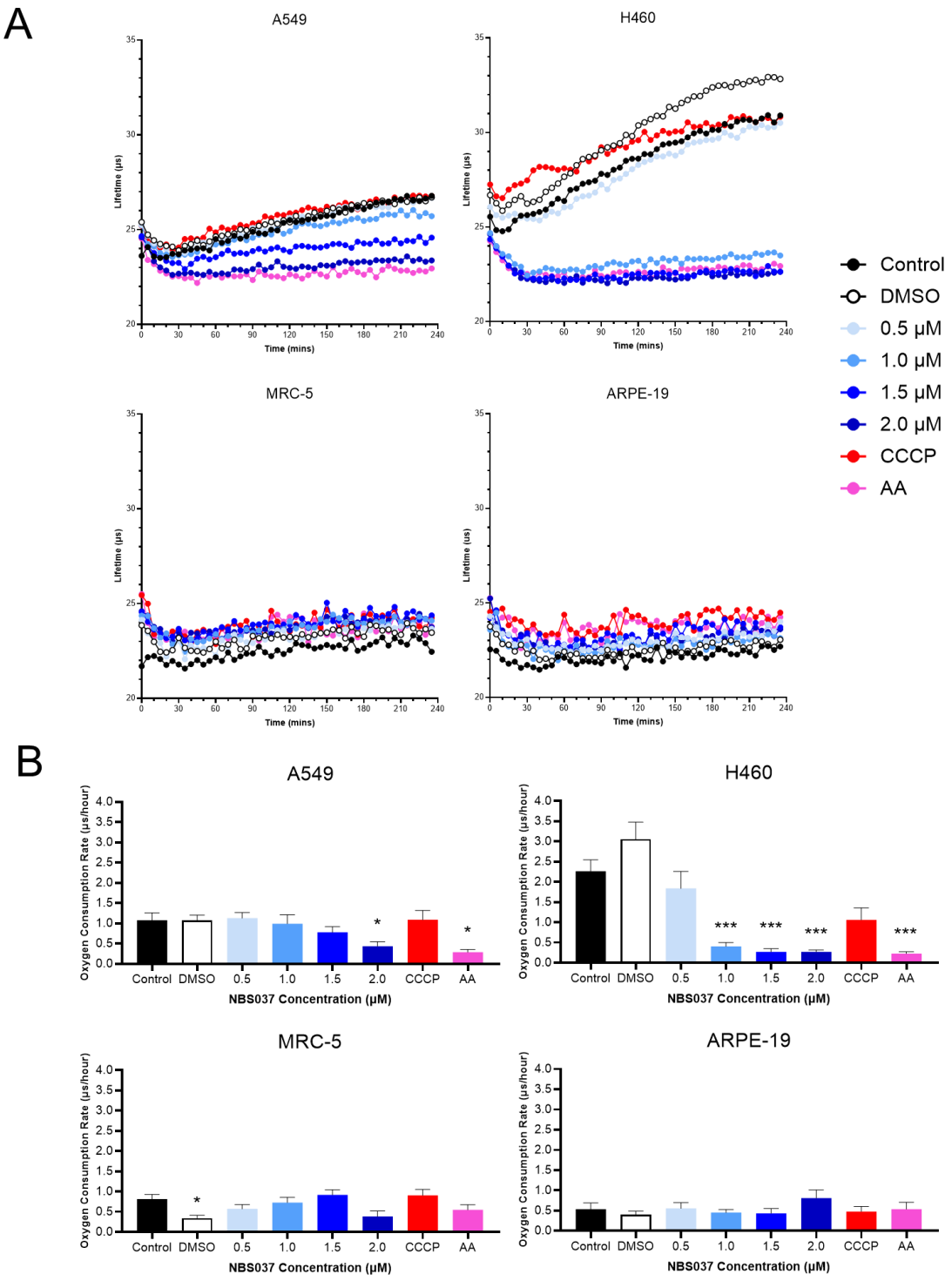

Figure 3.17. Oxygen consumption in cells treated with NBS037. *MitoXpress Xtra assay was used to assess oxygen consumption after 72 hours of drug treatments in 11 mM glucose media. DMSO was used as a vehicle control, CCCP was used as a positive control, and AA was used as a negative control. Media was replaced daily to maintain glucose levels. (A) represents typical traces of oxygen consumption in A549, H460, MRC-5, and ARPE-19. (B) shows mean OCR ± SEM. MARS software was used to calculate mean lifetime of oxygen consumption and OCR by linear regression. Statistical analysis was performed by Browne-Forsythe one-way ANOVA with Dunnett's T3 multiple comparisons post hoc tests to compare NBS037 treated cells to untreated controls (*, $p < 0.05$; ***, $p < 0.001$). N=3.*

3.16 NBS037 decreases mitochondrial membrane potential in cancer lines

ΔΨm is a key indicator of mitochondrial health and is a result of functional OXPHOS[290]. For this reason, inhibition of OXPHOS would be reflected by a decrease in ΔΨm also. To investigate if such changes occur with NBS037 treatment, JC-1 dye was utilised to measure ΔΨm in cancer cells. JC-1 is a fluorescent dye which accumulates in mitochondria in a potential dependent manner, and is often used for end point analysis of ΔΨm due to its higher fluorescence resolution for ΔΨm compared to TMRM[269,291]. When inside the cytosol, JC-1 remains in its monomeric form and possesses a green fluorescence emission. When ΔΨm is high in healthy mitochondria, JC-1 accumulates inside mitochondria to form J-aggregates, which possess a red fluorescence emission, otherwise JC-1 remains in its monomeric form in the cytosol. The ratio of J-aggregates (red fluorescence) to monomeric JC-1 (green fluorescence) can be calculated and utilised as a quantitative readout of ΔΨm[290]. A decrease in this ratio would indicate depolarisation and injury to ΔΨm, whilst an increase in this ratio would indicate hyperpolarised mitochondria. NSCLC cells were treated with NBS037 for 72 hours and JC-1 fluorescence (green and red) was measured. Ratio of J-aggregates to monomeric JC-1 was calculated (Figure 3.18).

In A549, 72 hours of NBS037 treatment caused a tendency for ΔΨm to decrease towards that of CCCP, a potent uncoupler of ETC acting as a positive control, but failed to reach significance. In contrast, AA was able to significantly decrease ΔΨm to 52% ($p = 0.0204$) of untreated controls. In H460 cells, ΔΨm was decreased with all doses of NBS037, and significant results found with all but 0.5 μM NBS037. 1.5 μM and 2 μM NBS037 were more potent in decreasing ΔΨm than AA, by reducing ΔΨm by 56% and 49% respectively ($p < 0.0001$) compared to the 45% decrease induced by AA ($p = 0.0003$). These results are in line with previous experiments, indicating NBS037 is able to cause injury to OXPHOS and

decrease mitochondrial respiration as a result, with H460 cells more sensitive to the drug than A549 cells.

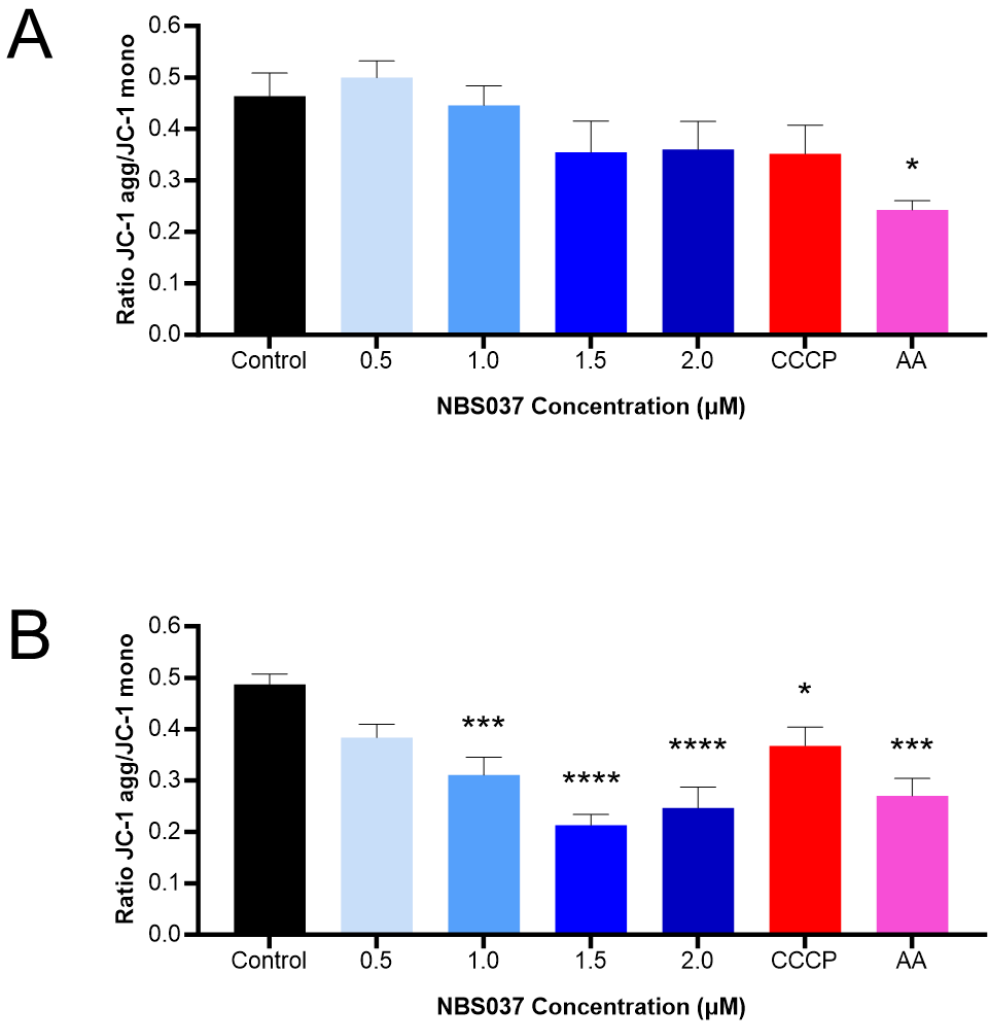

Figure 3.18. Mitochondrial membrane potential in cancer cell lines treated with NBS037. *JC-1 fluorescent dye was used to assess ΔΨm in (A) A549 and (B) H460 NSCLC lines. Cells were treated with NBS037 or DMSO as a vehicle control for 72 hours. CCCP as a positive control or AA, a known OXPHOS inhibitor, were also included. Data represents mean ratio of JC-1 red (aggregates) to green (monomers) fluorescence ± SEM. Statistical analysis was performed by one-way ANOVA with Dunnett's multiple comparisons post hoc tests to compare NBS037 treated cells to untreated controls (*, $p < 0.05$; ***, $p < 0.001$; ****, $p < 0.0001$). N=3.*

3.17 High doses of NBS037 increase ROS generation in H460 cells

ROS are important signalling molecules in cancer and whilst high levels can be toxic, enhanced ROS signalling contributes towards oncogenic signalling pathways for prolonged survival and proliferation[292]. Cancer cells therefore tend to have higher baseline level of ROS than normal cells[293]. For this reason, some anticancer drugs aim to increase ROS levels past the cytotoxic threshold in order to cause apoptosis and cell death[294]. DHE dye was used to assess ROS levels in cancer and non-cancer cells, to investigate whether NBS037 exerts its toxicity through increasing ROS levels significantly. DHE is a fluorescent dye which can permeate through the cell membrane, and is oxidised by superoxide to form 2-hydroxyethidium, or by non-specific oxidation to ethidium[295]. Both products produce a red fluorescence which can be quantified as a readout of ROS present. The DHE assay was carried out on cancer and non-cancer cells after 72 hours of treatment with NBS037, DMSO as a vehicle control, or AA as a comparable OXPHOS inhibitor which generates ROS[289] (Figure 3.19). Fluorescence was normalised to cell number to ensure changes in ROS were not due to changes in cell number, since NBS037 is capable of reducing cell viability.

In A549 cells, DHE fluorescence was decreased to 75% of controls by 0.5 μM NBS037, however as NBS037 dose increased, ROS levels also increased up to 129% of untreated controls with 2 μM NBS037. This was a modest increase compared to AA which resulted in an 160% increase in ROS compared to controls, although any changes observed in A549 did not reach significance. In H460 cells, 0.5 μM NBS037 caused the same fall in ROS as observed in A549 cells, to almost half that of untreated controls; however, ROS levels then increased with increasing NBS037 dose, and were significantly increased with 1.5 μM ($p = 0.0280$) and 2 μM ($p < 0.0001$) NBS037 to approximately 2.5 times greater than untreated controls. AA elicited an 180% increase in ROS in H460 cells, so NBS037 resulted in greater ROS generation than AA.

In MRC-5 cells, NBS037 and AA caused no significant changes in ROS levels, although AA was able to increase ROS by 59% of controls. In ARPE-19 cells, again, no significant changes were observed, however, 2 μM NBS037 was able to increase ROS similar to that of AA which was approximately double that of untreated cells. In this experiment, ROS levels in untreated controls were not significantly different between cancer and non-cancer cell lines.

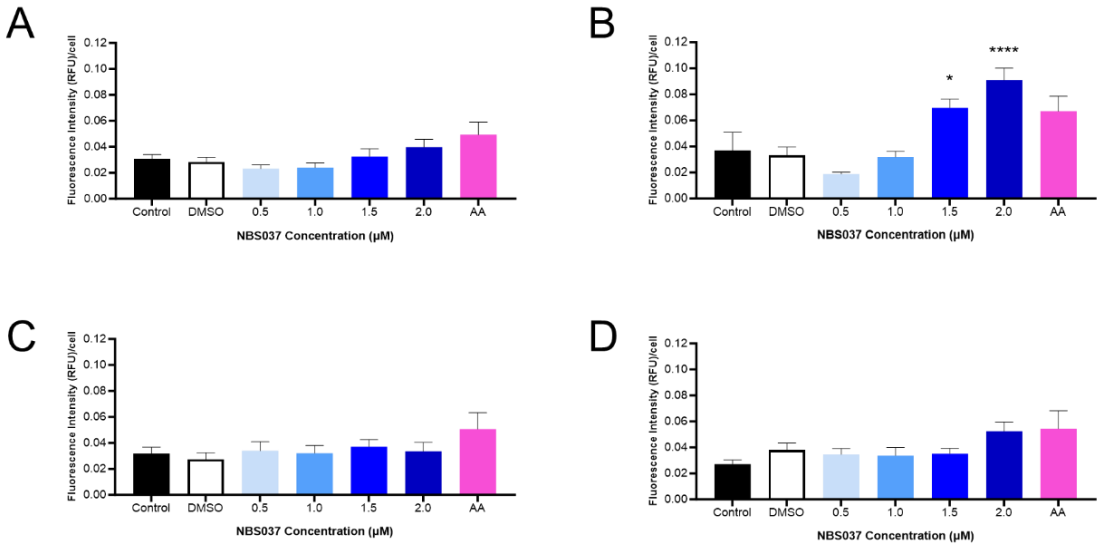

Figure 3.19. ROS generation in cell lines treated with NBS037. *DHE fluorescent probe was used to investigate ROS generation in (A) A549 and (B) H460 NSCLC lines, (C) MRC-5 lung fibroblast, and (D) ARPE-19 retinal epithelial cells. Cells were treated with NBS037, DMSO as a vehicle control, or AA, a known OXPHOS inhibitor for 72 hours. Data represents mean fluorescence corrected for cell number ± SEM. Statistical analysis was performed by one-way ANOVA with Dunnett's multiple comparisons post hoc tests to compare NBS037 treated cells to untreated controls (*, $p < 0.05$; ****, $p < 0.0001$). N=3.*

3.18 NBS037 elicits an increase in SOD2 protein expression in A549, but a decrease in H460 and ARPE-19 lines

Fluctuations in ROS were observed in A549, H460, and ARPE-19 lines, albeit only a significant increase was observed in H460 with NBS037 treatment (Figure 3.19). ROS levels within each

cell are dictated by the combination of production and clearance. The increase in ROS levels observed previously, therefore, may not only be due to an increase in ROS production, which has been linked to OXPHOS inhibition[296], but also could be linked to inhibition of antioxidant systems, a mechanism of cytotoxicity used in some drugs[297]. In order to investigate the effect of NBS037 on antioxidant activity in mitochondria, expression levels of SOD2 were quantified by WB, after 72 hours of treatment with NBS037 or DMSO as the vehicle control (Figure 3.20A). The expression of SOD2 was then normalised to β-actin, the loading control (Figure 3.20B). SOD2 is an antioxidant enzyme localised to the mitochondrial matrix and converts $O2^{\bullet-}$ to H_2O_2 in order to manage the ROS generated from the normal functioning of OXPHOS, and protect against oxidative stress[298].

A549 cells had the lowest naturally occurring SOD2 expression levels, which significantly increased with NBS037 treatment (Figure 3.20B). SOD2 expression doubled with 1 μM NBS037 and was 2.8 times greater than untreated controls with 2 μM ($p = 0.0002$) NBS037. A549 was the only cell line in which NBS037 caused an increase in SOD2 expression levels. In H460, SOD2 expression decreased with higher doses of NBS037, where 2 μM treatment caused a decrease to 46% of untreated controls, although failed to reach significance.

In non-cancer cell lines, MRC-5 showed no significant changes in SOD2 expression, although a modest decrease with NBS037 treatment was observed. In ARPE-19, however, NBS037 caused a significant decrease in SOD2 expression at 0.5 μM ($p = 0.0012$) and 2 μM ($p = 0.0026$) doses. Similar to that of the other cell lines, 2 μM NBS037 caused the largest change in expression, with SOD2 expression decreasing to 43% of untreated controls.

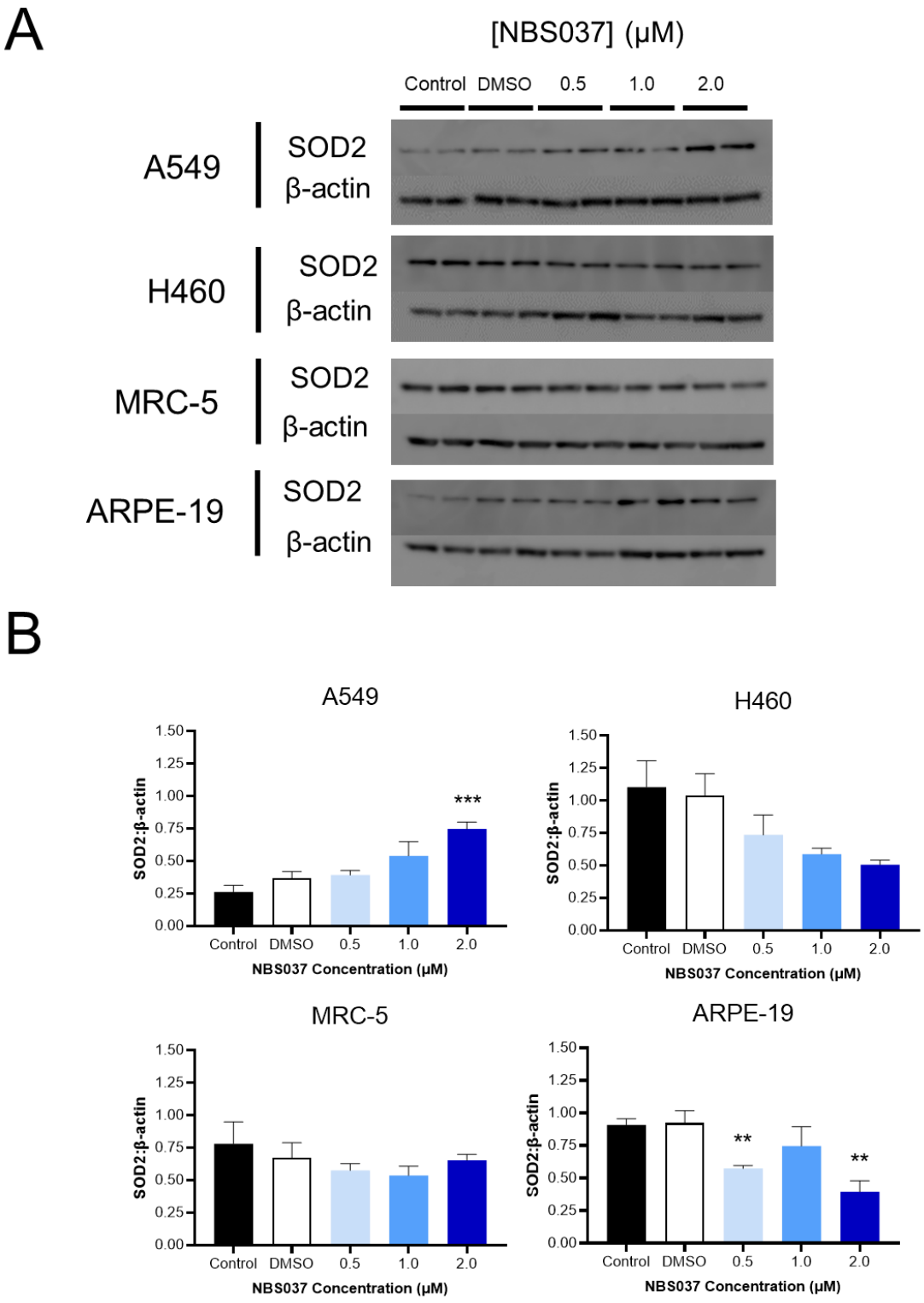

Figure 3.20. SOD2 protein expression in cell lines treated with NBS037. *WB analysis was used to investigate the SOD2 protein expression in A549 and H460 NSCLC lines, MRC-5 lung fibroblast, and ARPE-19 retinal epithelial cells. Cells were treated with NBS037 or DMSO as a vehicle control for 72 hours. (A) shows original blots from cell lysates run in duplicate and (B) represents mean protein expression normalised to β-actin ± SEM, quantified from blots using the G-box software. Statistical analysis was performed by Browne-Forsythe one-way ANOVA with Dunnett's T3 multiple comparisons post hoc tests to compare NBS037 treated cells to untreated controls (*, $p < 0.05$; **, $p < 0.01$; ****, $p < 0.0001$). N=3.*

3.19 Aconitase expression tends to decrease with NBS037 treatment in H460 and MRC-5, but no significant effects are observed

Aconitase is a key enzyme in the TCA cycle within mitochondria, converting citrate to isocitrate. Aconitase is highly sensitive to oxidation, with oxidative stress causing inhibition of enzyme activity[299]. To further elucidate effects of NBS037 on antioxidant status in cell lines, aconitase expression was also analysed by WB after 72 hours of treatment with NBS037 or DMSO as the vehicle control (Figure 3.21A). The expression of aconitase was then normalised to β-actin, the loading control (Figure 3.21B).

In all cell lines tested, no significant changes in aconitase expression were observed, indicative of no severe oxidative stress within the cells. Again, whilst NBS037 caused a tendency to increase aconitase expression in A549, decreases in expression were observed with H460, MRC-5, and ARPE-19. 2 μM NBS037 elicited the largest decrease in aconitase expression in H460, where expression was decreased by 75% compared to untreated controls, but the same dose only decreased expression by 9% in MRC-5 and 38% in ARPE-19 cells.

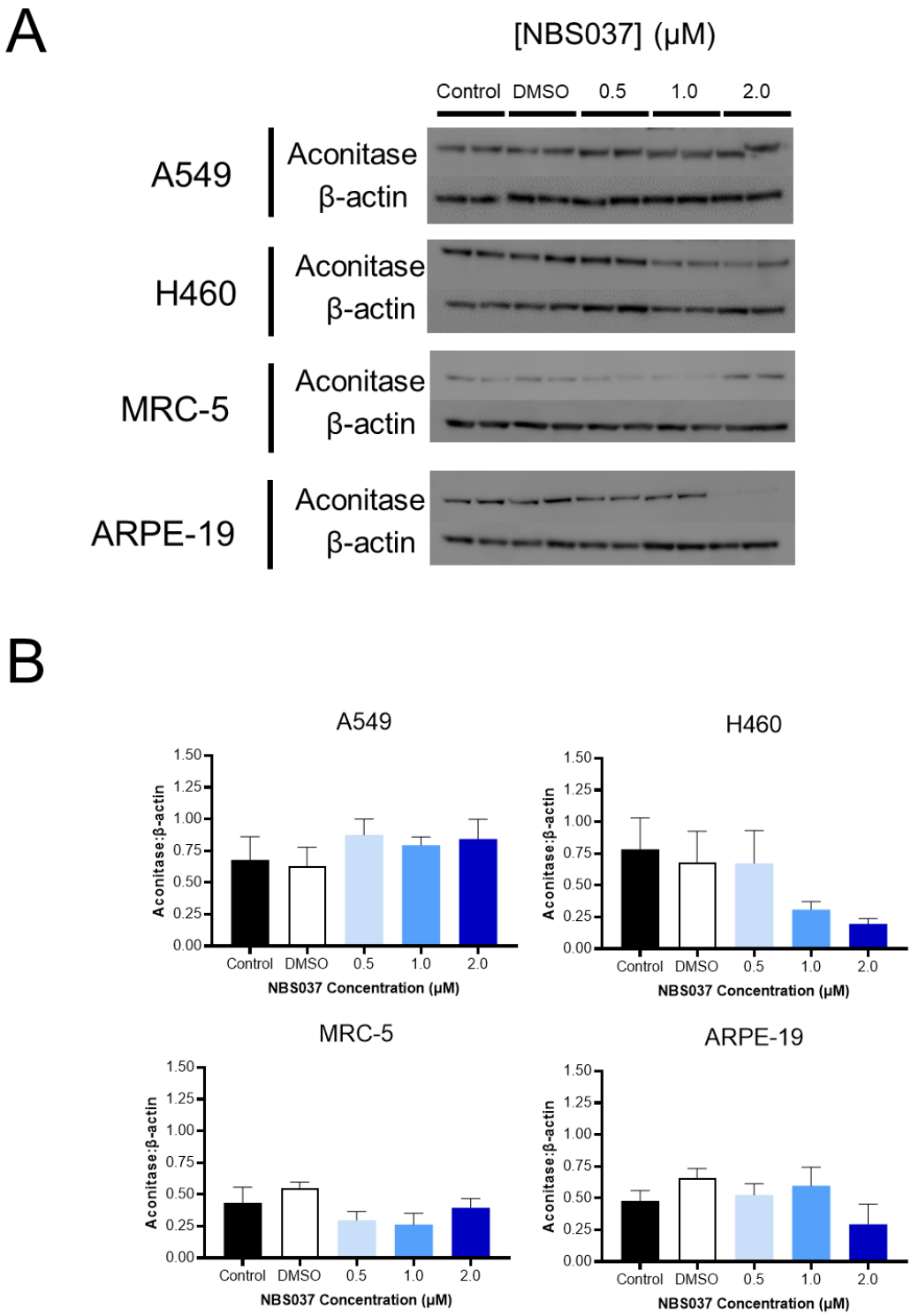

Figure 3.21. Aconitase protein expression in cell lines treated with NBS037. *WB analysis was used to investigate the aconitase protein expression in A549 and H460 NSCLC lines, MRC-5 lung fibroblast, and ARPE-19 retinal epithelial cells. Cells were treated with NBS037 or DMSO as a vehicle control for 72 hours. (A) shows original blots from cell lysates run in duplicate and (B) represents mean protein expression normalised to β-actin ± SEM, quantified from blots using the G-box software. Statistical analysis was performed by one-way ANOVA with Dunnett's multiple comparisons post hoc tests to compare NBS037 treated cells to untreated controls. N=3.*

3.20 Changes in antioxidant protein expression are not due to changes in mitochondrial mass

SOD2 and aconitase are both localised to the mitochondria and therefore changes in expression may be a consequence of changes in mitochondrial mass. SOD2 and aconitase levels, therefore, were normalised to Tom20 expression measured previously (Figure 3.15) to correct for the observed changes in mitochondrial mass (Figure 3.22).

When normalised to mitochondrial mass, significant changes in SOD2 and aconitase were still observed, indicating NBS037 causes changes to these proteins independent of the mitochondrial mass (Figure 3.22A). SOD2 expression in A549 increased with increasing NBS037 dose, with a significant increase of 239% of untreated controls ($p = 0.0016$) observed at 2 μM NBS037. SOD2 expression still decreased with 1 μM and 2 μM NBS037 in H460 cells but this decrease lost its significance. Changes in SOD2 expression in this cell line may therefore be in part due to the decreased mitochondrial mass previously measured (Figure 3.15). MRC-5 showed the same modest decrease in SOD2 expression regardless of the normalisation method, whilst only 2 μM NBS037 caused a decrease in expression (59% of controls) in ARPE-19 cells when taking mitochondrial mass into consideration.

Aconitase expression, when normalised to Tom20, was unchanged by NBS037 treatment in A549, indicating any changes in aconitase expression was more likely due to the upregulation of mitochondrial mass in this cell line (Figure 3.22B). In H460 cells, 1 μM and 2 μM NBS037 caused a 54% decrease in aconitase expression, with 2 μM NBS037 reaching significance ($p = 0.0221$). Interestingly, when corrected for the decreased mitochondrial mass in ARPE-19, aconitase expression approximately doubled with NBS037 treatment compared to untreated controls, until 2 μM NBS037 where expression returned to that of untreated controls. 0.5 μM and 1 μM NBS037 caused aconitase expression to decrease to approximately 40% of

untreated controls in MRC-5, greater than the decrease observed when aconitase was normalised to β-actin (Figure 3.21).

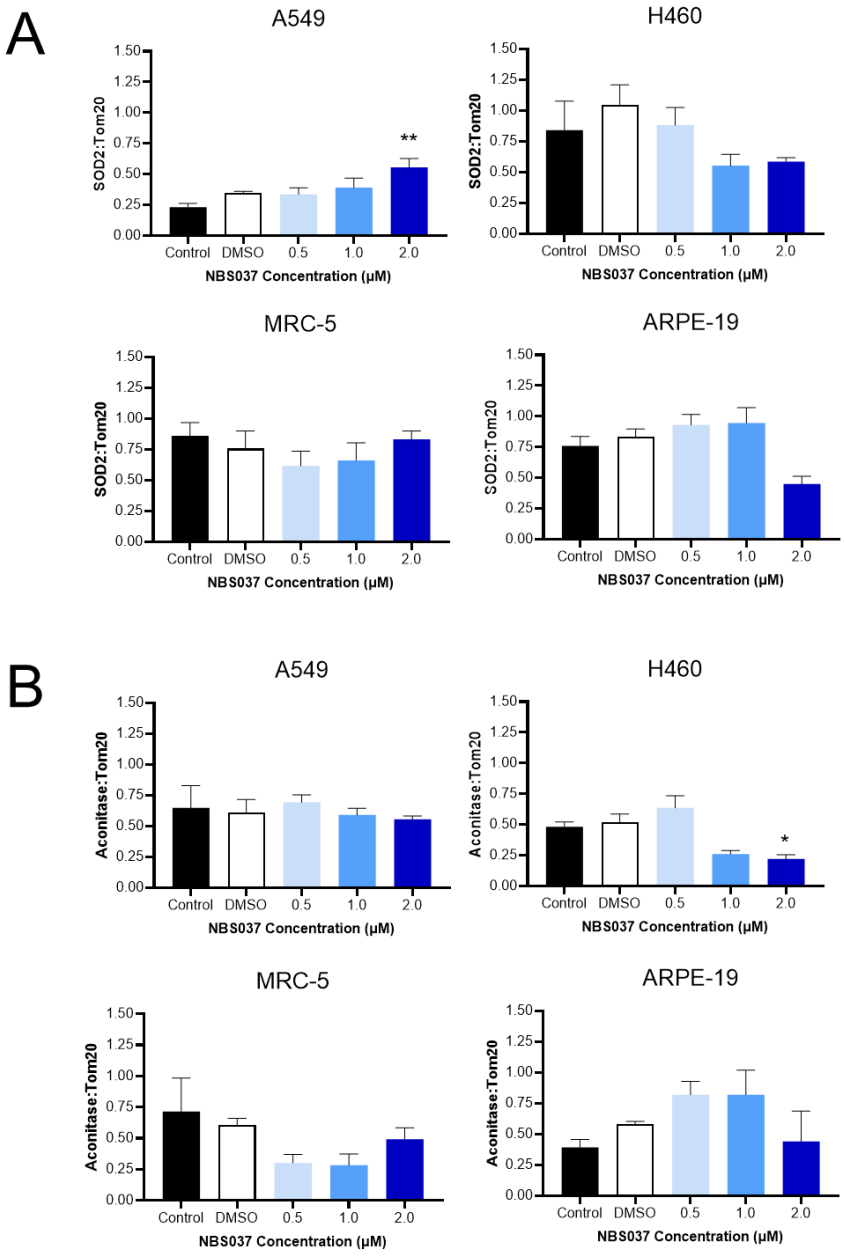

Figure 3.22. Antioxidant protein expression normalised to mitochondrial mass in cell lines treated with NBS037. *WB analysis was used to investigate the SOD2 and aconitase protein expression in A549 and H460 NSCLC lines, MRC-5 lung fibroblast, and ARPE-19 retinal epithelial cells and then normalised to Tom20 expression. Cells were treated with NBS037 or DMSO as a vehicle control for 72 hours. Blots were quantified utilising Gbox software. (A) represents mean protein expression of SOD2 normalised to Tom20 ± SEM and (B) represents mean protein expression of aconitase normalised to Tom20 ± SEM. Statistical analysis was performed by one-way ANOVA with Dunnett's multiple comparisons post hoc tests to compare NBS037 treated cells to untreated controls (*, p < 0.05; **, p < 0.01). N=3.*

3.21 Acute NBS037 treatment increases OCR at high doses

The TPP^+ moiety was found to cause mitochondrial uncoupling as a consequence of increasing lipophilicity[173], so whilst NBS037 was carefully designed to mitigate this, cell lines were tested for evidence of uncoupling. Effects of mitochondrial uncouplers can be observed rapidly after introducing the drug, as quickly as within 20 minutes of treatment in the example of CCCP[300], therefore, oxygen consumption was measured in both cancer and non-cancer cell lines for the first 12 hours of NBS037 treatment (acute treatment). The MitoXpress Xtra probe was used to measure oxygen consumption in real time (Figure 3.23A), and the OCR quantified from the linear increase in oxygen consumption (Figure 3.23B). CCCP is a potent uncoupler of the ETC and is the recommended positive control for assays measuring mitochondrial respiration.

CCCP caused an increase in OCR in all cell lines, as much as double that of untreated controls in H460 ($p < 0.0001$), and indicates the effect uncoupling has on oxygen consumption to compare with NBS037. At the high dose of 10 μM, NBS037 elicited an increase in OCR comparable to CCCP in H460 ($p < 0.0001$), and ARPE-19, whilst significantly increasing OCR in A549 ($p = 0.0002$), and MRC-5 ($p = 0.0065$) less potently than CCCP. 2 μM NBS037 was also able to significantly increase OCR in H460 cells ($p = 0.0041$) and 0.5 μM could elicit a significant increase in OCR in MRC-5 ($p = 0.0484$). Interestingly, this high OCR with 10 μM NBS037, is accompanied by a crash in oxygen consumption within the first six hours of treatment, and oxygen consumption begins to fall towards the trace obtained from AA (Figure 3.23A). AA potently inhibited mitochondrial respiration in all cell lines, indicated by a large decrease in oxygen consumption.

When repeated in 1 mM glucose conditions, the same trends were observed (Figure 3.24), albeit with a universal increase in oxygen consumption when compared to results observed at 11 mM glucose (Figure 3.23). CCCP demonstrated positive uncoupling in A549, H460, and

MRC-5 cell lines, shown by a large increase in OCR (Figure 3.24B), but not in ARPE-19. In H460 cells, NBS037 at 1.5 µM and 2 µM also caused an increase in OCR compared to untreated controls; however, these changes failed to reach significance. With 10 µM NBS037 treatment, the same dropout of oxygen consumption was observed in all cell lines after approximately 2 hours of treatment. A similar dropout was observed in H460 cells after 6 hours of 1.5 µM and 2 µM NBS037 treatment.

From these results, NBS037 has the ability to uncouple mitochondrial respiration at high doses (2 µM and 10 µM) but these high doses cause rapid loss of OXPHOS function. The inhibitory effects of NBS037 observed with 72 hours of treatment (Figure 3.17) are not observed with acute treatment, although oxygen consumption starts to decline below that of untreated controls at around eight hours of treatment in A549, and six hours in H460.

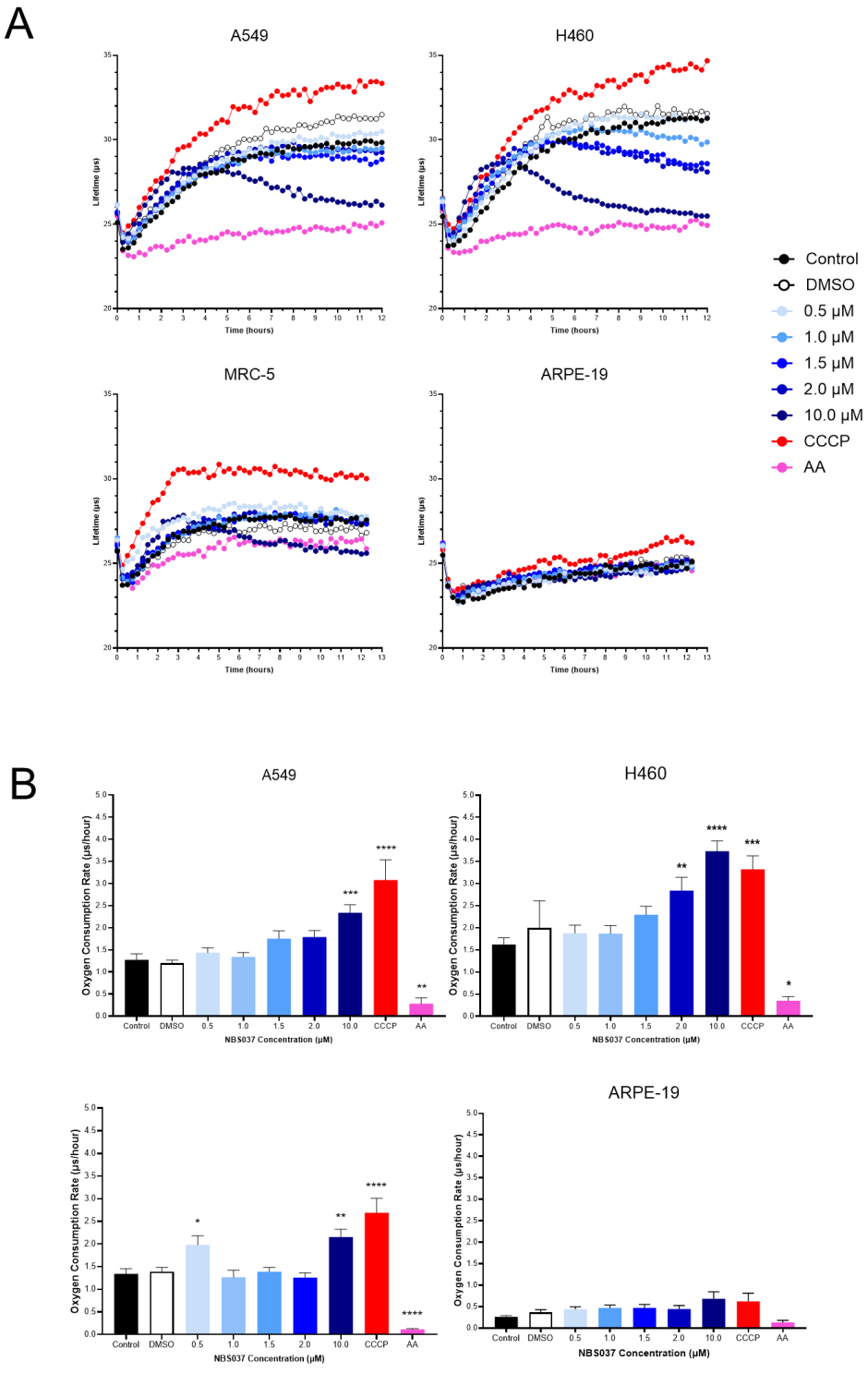

Figure 3.23. Oxygen consumption in cells treated with NBS037 in 11 mM glucose. *MitoXpress Xtra assay was used to assess oxygen consumption for the first 12 hours of NBS037 treatment in A549 and H460 NSCLC, MRC-5 lung fibroblast, and ARPE-19 retinal epithelial cells. MARS software was utilised to calculate (A) mean lifetime of oxygen consumption and (B) mean OCR ± SEM. DMSO was used as a vehicle control, CCCP was used as a positive control, and AA was used as a negative control. Statistical analysis was performed by one-way ANOVA with Dunnett's multiple comparisons post hoc tests to compare NBS037 treated cells to untreated controls (*, $p < 0.05$; **, $p < 0.01$; ***, $p < 0.001$; ****, $p < 0.0001$). N=3.*

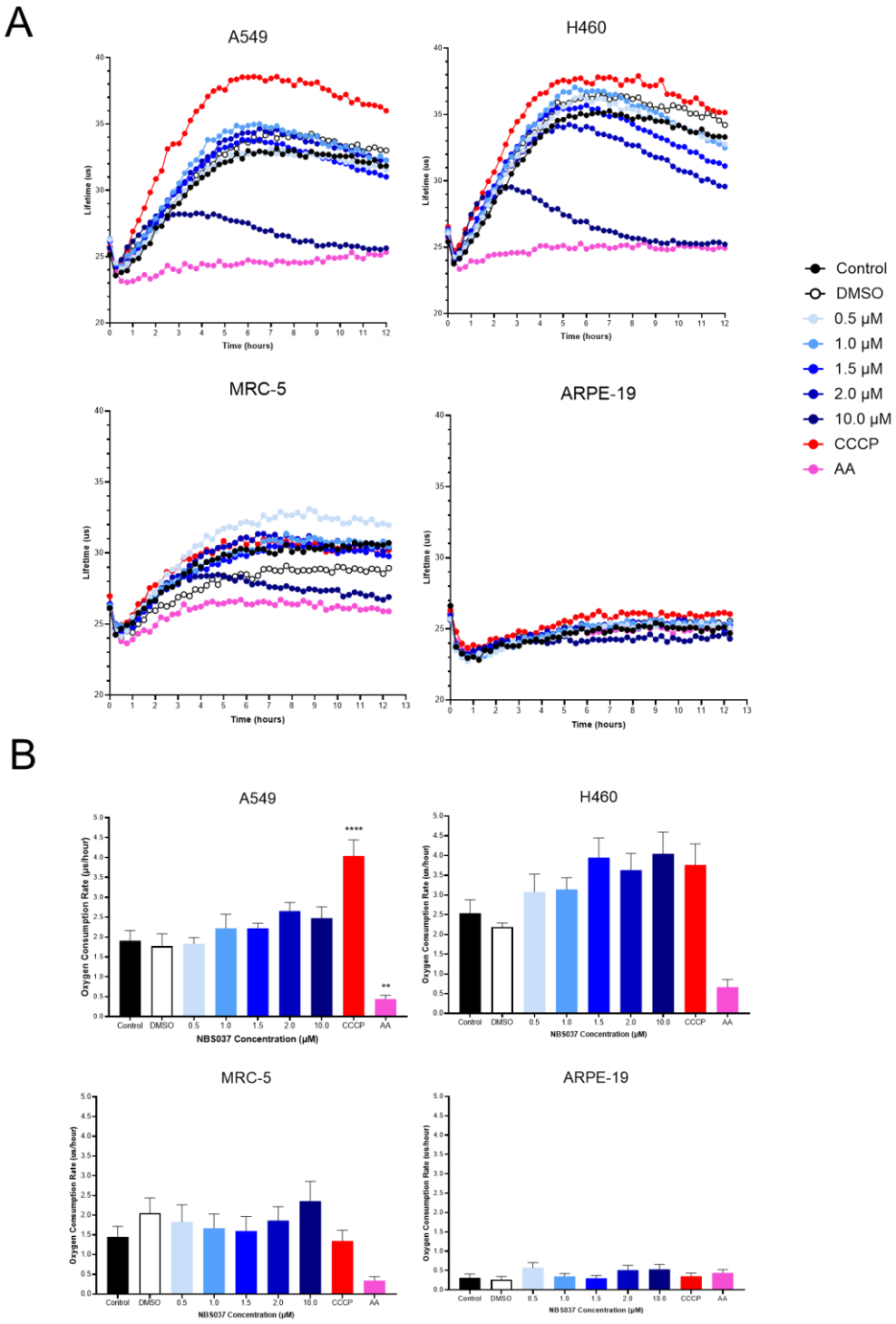

Figure 3.24. Oxygen consumption in cells treated with NBS037 in 1 mM glucose. *MitoXpress Xtra assay was used to assess oxygen consumption for the first 12 hours of NBS037 treatment in A549 and H460 NSCLC, MRC-5 lung fibroblast, and ARPE-19 retinal epithelial cells. MARS software was utilised to calculate (A) mean lifetime of oxygen consumption and (B) mean OCR ± SEM. DMSO was used as a vehicle control, CCCP was used as a positive control, and AA was used as a negative control. Statistical analysis was performed by one-way ANOVA with Dunnett's multiple comparisons post hoc tests to compare NBS037 treated cells to untreated controls (*, $p < 0.05$; **, $p < 0.01$; ***, $p < 0.001$; ****, $p < 0.0001$). N=3.*

3.22 Acute NBS037 treatment has little effect on ROS generation

OXPHOS is a major source of mitochondrially generated ROS, therefore uncoupling OXPHOS and impairing its function would naturally lower ROS levels. In this manner, mild uncoupling can act as a natural negative feedback mechanism to balance ROS levels if production becomes excessive[301]. In order to further elucidate any uncoupling effects, and test any acute effects in ROS production, DHE dye was utilised again to quantify ROS levels in real time during the first 12 hours of NBS037 treatment (Figure 3.25A and B). ROS levels were then quantified at two, four, and ten hours of treatment to identify any significant effects (Figure 3.25C-E). NBS037 treatment was compared to the potent uncoupler CCCP, the OXPHOS inhibitor AA, and the potent ROS generator, menadione. Menadione, known as vitamin K, has been utilised *in vitro* for its anti-cancer effects through increased ROS generation[302].

Menadione proved to be a potent ROS generator in all cell lines tested, with ROS levels significantly increased in A549 ($p = 0.0011$), H460 ($p = 0.0023$), MRC-5 ($p = 0.0002$), and ARPE-19 ($p = 0.002$) in only 2 hours of treatment (Figure 3.25E). AA largely increased ROS in cancer lines from 2 hours of treatment although failing to reach significance. At 4 hours of treatment, 2 μM and 10 μM NBS037 raised ROS levels in H460 cells, which further increased at 10 hours. 10 μM NBS037 significantly increased ROS levels in H460 cells to double that of untreated controls at 10 hours ($p = 0.0188$). 10 μM NBS037 treatment also resulted in a small increase in ROS in the other cell lines tested but failed to reach significance. Interestingly, lower doses of NBS037 caused a small decrease in ROS, the opposite of that observed in H460 cells.

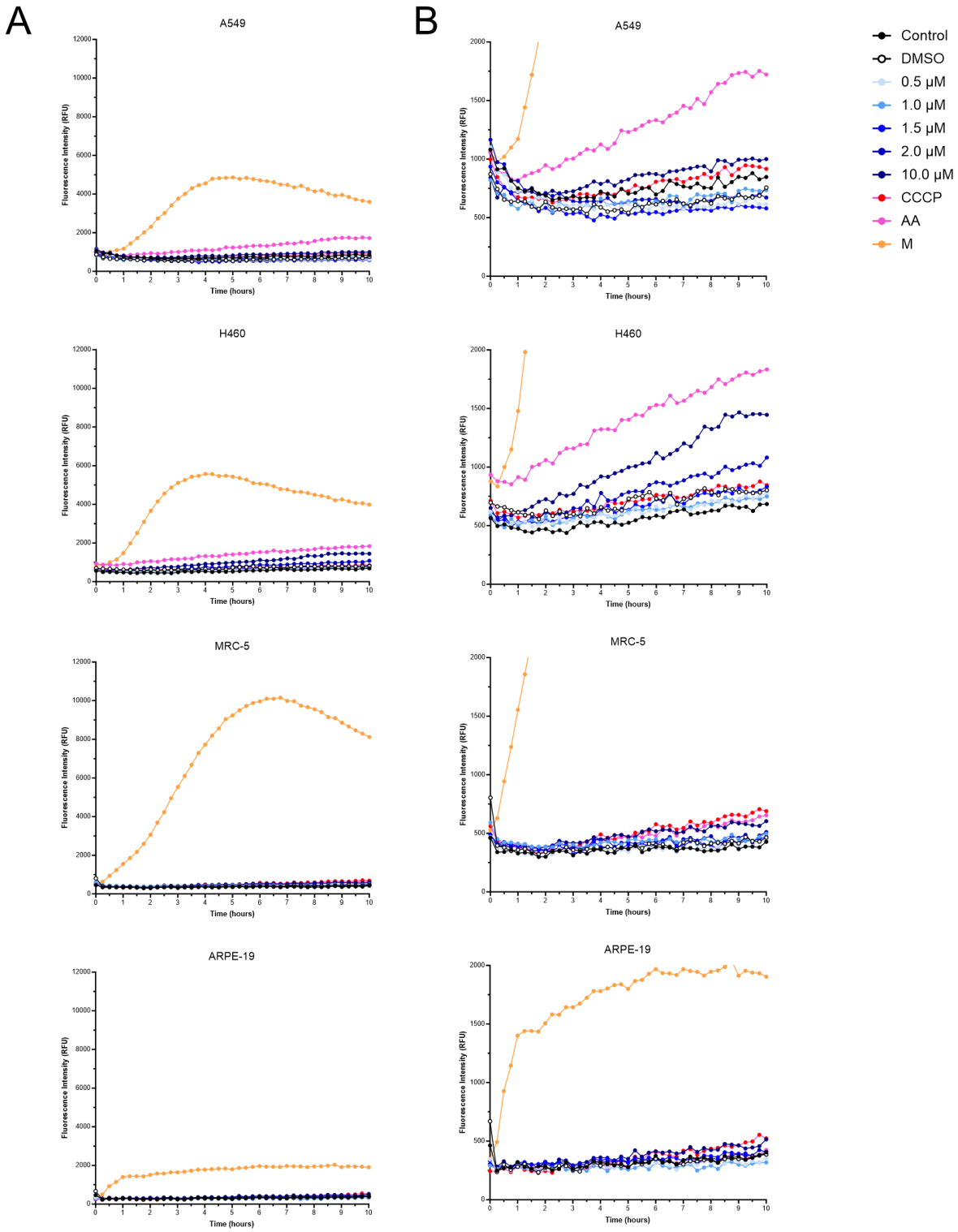
A
B
A549
H460
MRC-5
ARPE-19
Fluorescence Intensity (RFU)
Time (hours)
Control
DMSO
0.5 µM
1.0 µM
1.5 µM
2.0 µM
10.0 µM
CCCP
AA
M

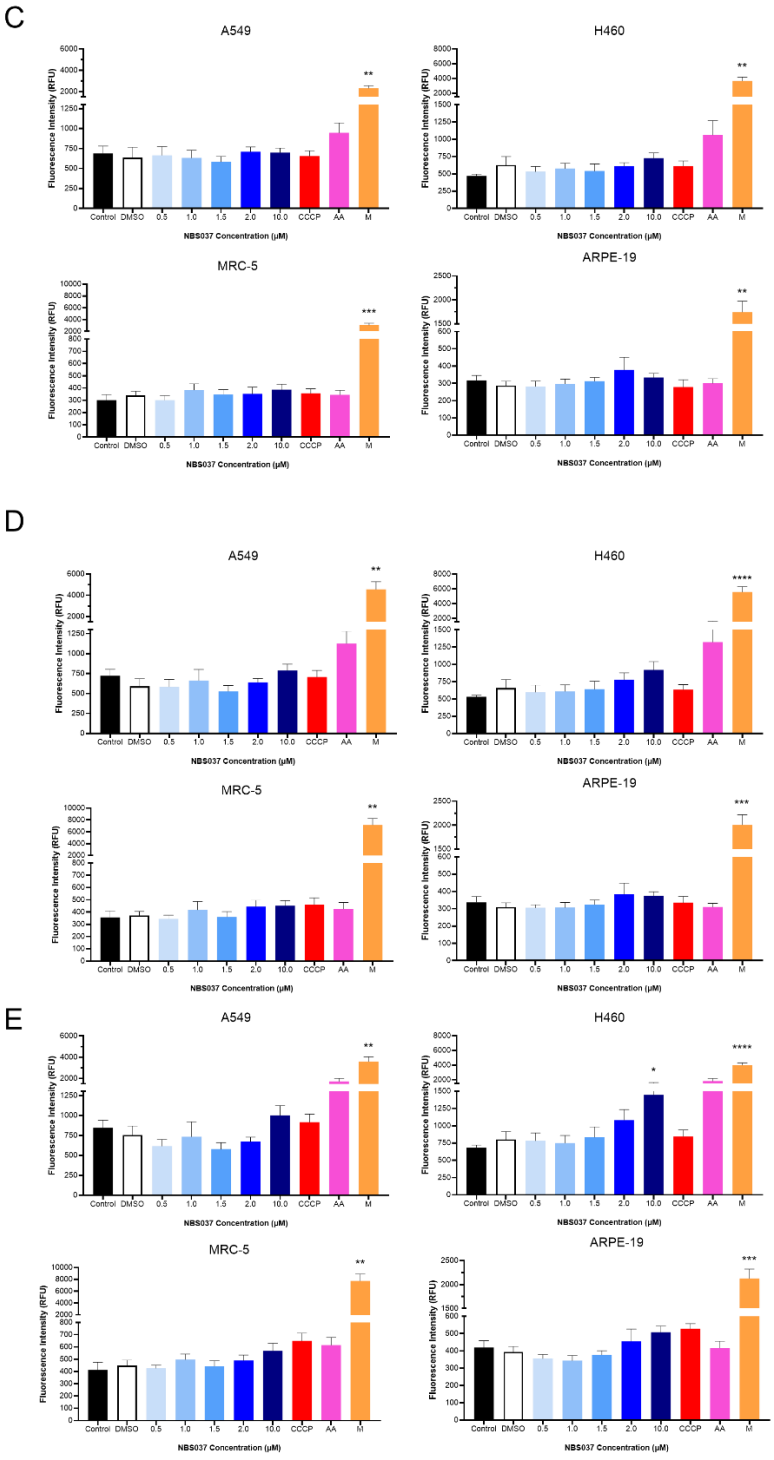

Figure 3.25. ROS levels in cell lines with acute NBS037 treatment. *DHE fluorescent probe was used to investigate ROS levels in A549 and H460 NSCLC lines, MRC-5 lung fibroblast, and ARPE-19 retinal epithelial cells. Cells were treated with NBS037 or DMSO as a vehicle control and fluorescence read immediately for 10 hours. CCCP, a potent uncoupler, AA, a known OXPHOS inhibitor, and menadione (M), a potent ROS generator were also included. (A) Data represents mean fluorescence over 10 hours with full axis and (B) magnified axis. Bars represents mean fluorescence intensity with (C) 2, (D) 4, or (E) 10 hours of drug treatment ± SEM. Statistical analysis was performed by Browne-Forsythe one-way ANOVA with Dunnett's T3 multiple comparisons post hoc tests to compare NBS037 treated cells to untreated controls (**, $p < 0.01$; ***, $p < 0.001$; ****, $p < 0.0001$). N=3.*

3.23 When used in combination with 2DG, NBS037 decreases cell viability further than when used as a single agent

NBS037 was shown to have effects not only on nuclear encoded proteins, but also in non-cancer controls, therefore, if a smaller dose can be utilised for the same effects, this may improve tolerability. 2DG is an analogue to deoxy-D-glucose, the form of glucose that can be used by the body for cellular processes. Unlike deoxy-D-glucose, 2DG has a hydrogen molecule in the place of the 2-hydoxyl group which prevents its conversion into G6P and therefore inhibits further glycolysis. Using a glycolysis inhibitor in combination treatment may prevent compensatory use of glycolysis upon NBS037 induced OXPHOS inhibition, and therefore cause increased cancer cell death. The PI assay was used to investigate the effect of 2DG and NBS037 combination treatment on cell viability in cancer and non-cancer cell lines. Cells were grown for seven days with drug treatment, with DMSO as a vehicle control, and utilising 20 mM of 2DG, the concentration used previously *in vitro* to completely inhibit glycolysis[303–305] (Figure 3.26).

At the concentration of 20 mM, 2DG proves to be toxic to cells, with the cell viability falling from day one in 2DG treated cells (Figure 3.26A), rather than increasing with cell growth as observed in untreated cells in previous experiments (Figure 3.2). After 72 hours of treatment, in H460 cells NBS037 was able to significantly decrease cell viability further then 2DG alone, from 33% of 2DG treated cells with 0.5 μM NBS037 ($p = 0.0189$), to 7% of 2DG treated cells with 2 μM NBS037 ($p = 0.0037$) (Figure 3.26B). In A549 cells, decreases in cell viability compared to 2DG were only found at the highest dose of NBS037. In MRC-5, low doses of NBS037 caused a tendency for increased cell viability although failed to reach significance. In ARPE-19, 1 μM and 2 μM NBS037 was able to significantly increase cell viability ($p = 0.0391$ and $p = 0.0303$ respectively) but 5 μM caused a significant decrease in viability when compared to 2DG treated cells ($p < 0.0001$).

By seven days of treatment, NBS037 was able to elicit significance decreases in cell viability between 1 - 5 μM in A549 cells, whilst only 5 μM NBS037 was capable of significantly reducing cell viability in H460 beyond that of 2DG treated cells (Figure 3.26C). NBS037 was capable of significantly reducing cell viability in ARPE-19 cells at 2 μM ($p = 0.0043$) and 5 μM ($p = 0.0003$), compared to using 2DG alone. 5 μM NBS037 also caused a significant decrease in cell viability in MRC-5 ($p = 0.0274$).

When comparing the effects of NBS037 as a single agent (Figure 3.3 and 3.6) and NBS037 in combination with 2DG (Figure 3.26), combination treatment was more effective in reducing cell viability in all cell lines. Lower doses of NBS037 in combination had the largest changes. Combination treatment utilising 0.5 μM + 2DG caused a 91% lower cell viability in A549 and 97% lower cell viability in H460 compared to the cell viabilities with 0.5 μM NBS037 alone at seven days (Figure 3.3). Non-cancer cell lines were also highly impacted, with 0.5 μM NBS037 in combination decreasing cell viability by 55 - 85% of that recorded with NBS037 alone (Figure 3.6). This much larger reduction in cell viability with combination treatment, however, may be a consequence of the high dose of 2DG used, which was able to potently decrease cell viability without the addition of NBS037 (Figure 3.26A).

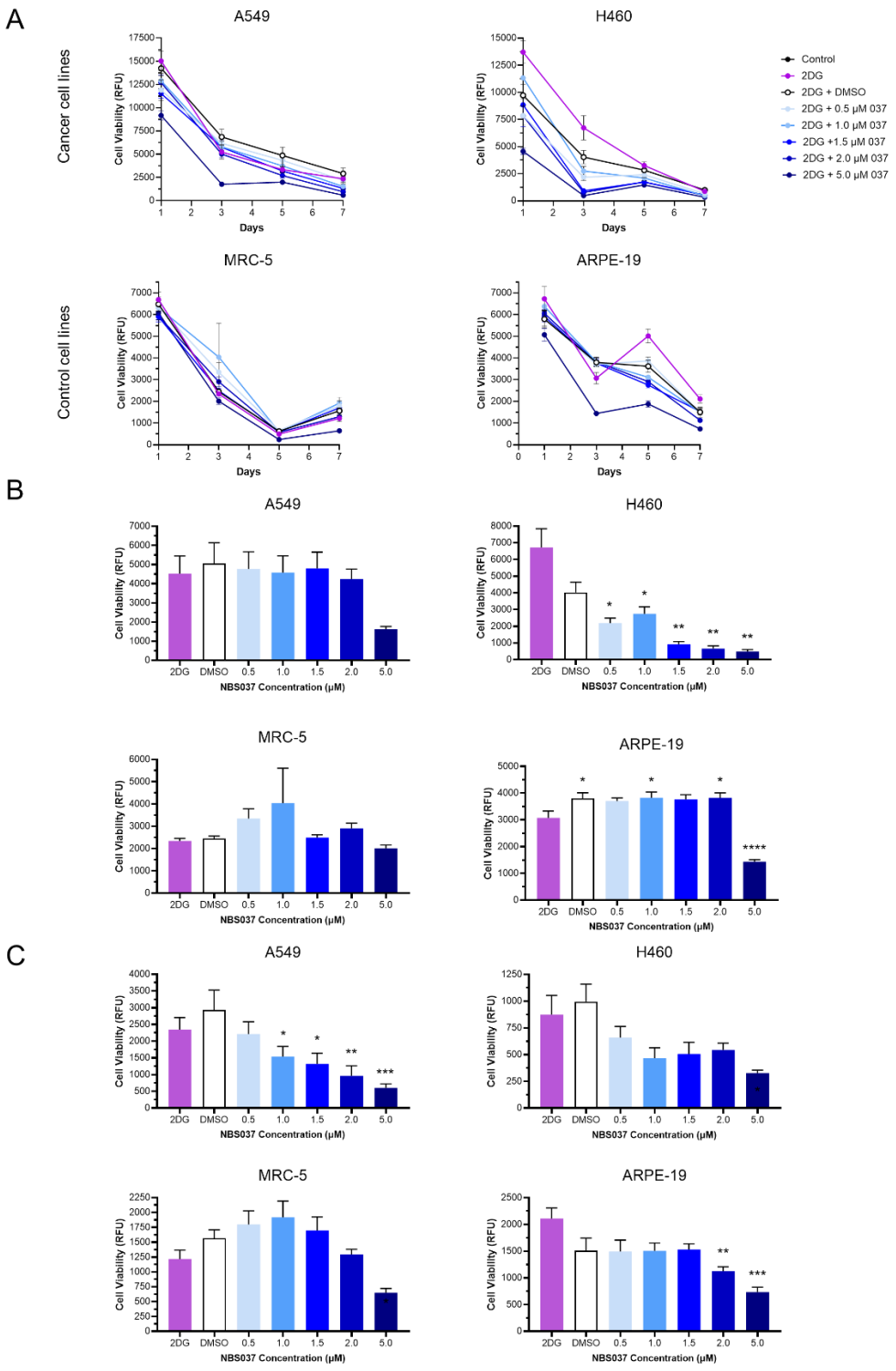

Figure 3.26. Growth curves of cancer cell lines with a combination of NBS037 and 2DG treatment. *PI was used to assess cell viability with NBS037and 20 mM 2DG treatment over seven days in A549 and H460 NSCLC, MRC-5 lung fibroblast, and ARPE-19 retinal epithelial cells in 11 mM glucose. DMSO was used as a vehicle control. Media was replaced daily to maintain glucose levels. (A) Data represents mean cell viability ± SEM over seven days of treatment, (B) represents mean cell viability ± SEM at 72 hours of treatment and (C) seven days of treatment. Statistical analysis was performed by Browne-Forsythe one-way ANOVA with Dunnett's T3 multiple comparisons post hoc tests to compare each treatment group with 2DG treated cells (*, p < 0.05; **, p < 0.01; ***, p < 0.001; ****, p < 0.0001). N=3.*

3.24 High doses of 2DG deplete ATP

High doses of 2DG are often utilised to wholly inhibit glycolysis and at the 20 mM dose, cell viability decreased between one and seven days of treatment in all cell lines tested (Figure 3.26). To explain the decrease in cell viability, the CellTiter-Glo® 2.0 assay was utilised to test the extent of ATP depletion as a result of 2DG treatment in both 11 mM and 1 mM glucose, with measurements corrected for cell number (Figure 3.27). 20 mM 2DG potently decreased ATP in all cell lines, particularly in the cancer cell lines, and non-cancer lines in low glucose. 0.5 mM 2DG was still able to elicit a decrease in ATP but may prove less toxic to cells, and therefore may be a better dose to use for combination treatment.

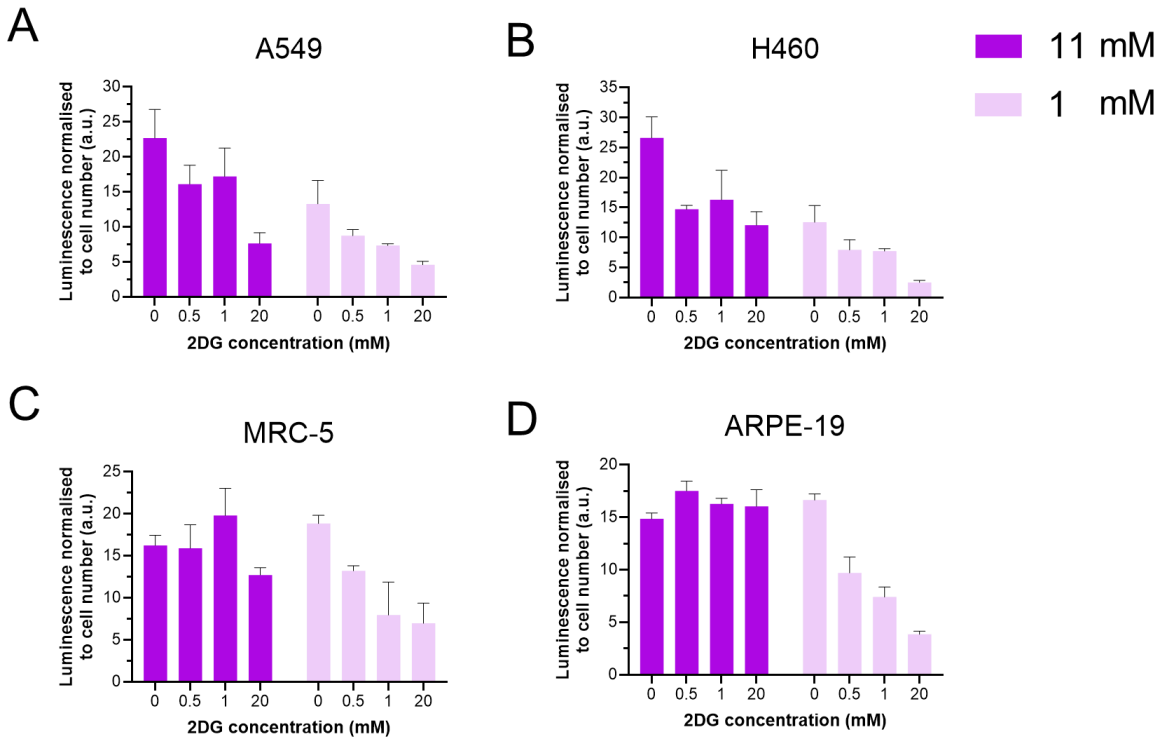

Figure 3.27. ATP levels in cell lines with 2DG treatment. *The CellTiter-Glo® 2.0 assay (Promega) was utilised to measure ATP in cells, with luminescence normalised to viable cell number as determined by PI assay. Cells were plated in triplicate and pretreated with 2DG at 0.5 mM, 1 mM, or 20 mM overnight in both 11 mM and 1 mM glucose media. Data represents mean luminesce normalised to cell number (relative ATP) ± SEM in (A) A549 and (B) H460 NSCLC, (C) MRC-5 lung fibroblast and (D) ARPE-19 retinal epithelium cells. N=1.*

3.25 When used in combination with plasma concentrations of 2DG, NBS037 decreases cell viability in cancer and non-cancer lines

For many *in vitro* studies, high doses of 2DG are used to inhibit glycolysis, however, when tested *in vivo* in mice, plasma concentrations attainable were far lower than the previous 20 mM concentration tested[305,306]. Initial tests on the effect of 2DG on ATP levels showed potent ATP depletion with 20 mM 2DG (Figure 3.27) which resulted in a potent decrease in cell viability in all cell lines (Figure 3.26). In order to test if 2DG and NBS037 combination treatment can produce effects at a much lower dose than when used as single agents, the PI assay was repeated but with combination treatment of 500 μM 2DG and/or NBS037 in concentrations between 0.0625 μM and 1 μM. Cells were treated for seven days in 11 mM (Figure 3.28) or 1 mM (Figure 3.29) glucose and cell viability calculated at each time point to compare treatments.

After 72 hours of treatment, A549 and MRC-5 cells proved to be sensitive to 500 μM 2DG, with significant decreases in cell viability observed with 2DG alone, and with NBS037 in combination (Figure 3.28B). Whilst significant decreases in cell viability are observed in these lines with much lower doses than found with NBS037 alone, these results do not significantly differ from the use of 2DG alone and therefore, the seemingly enhanced potency of NBS037 in combination is more likely due to cell line sensitivity to 2DG. H460 and ARPE-19 cells appeared less sensitive to 2DG, with only 1 μM NBS037 combination treatment able to result in a significant decrease in cell viability compared to untreated controls, but these results were also significantly reduced compared to 2DG alone. Whilst this shows NBS037 is more efficacious in these cell lines, this does not differ from results found previously as 0.5 - 5 μM NBS037 was highly potent in H460 cells as a single agent (Figure 3.2).

With seven days of drug treatments, combination treatment proved to reduce the effect of NBS037 (Figure 3.28C). No significant effects on cell viability were observed in A549 with NBS037 treatment, despite NBS037 as a single agent previously causing a significant decrease in viability at 1 μM (Figure 3.2). Similarly, whilst ARPE-19 was highly sensitive to NBS037 as a single agent, with 2DG in combination, only 1 μM NBS037 produced a significant decrease to 71% of untreated controls ($p = 0.0043$). In H460 cells, whilst 1 μM NBS037 with 2DG produced a 50% reduction in cell viability, lower doses were not capable of inducing effects on cell viability.

In previous experiments, cell lines proved to be more sensitive to NBS037 in 1 mM glucose, when they were pushed towards a more OXPHOS phenotype. Cell viability was measured again but instead in 1 mM glucose conditions to investigate if lower concentrations of NBS037 may be effective (Figure 3.29). With treatment in 1 mM glucose, the most notable difference in cell viability was an increase in sensitivity in ARPE-19 where all treatments caused a significant decrease in cell viability, and by seven days, A549 and MRC-5 lines had significantly lower viability with all drug treatments (Figure 3.29). However, NBS037 in combination with 2DG did not produce significant effects compared to 2DG alone, therefore effects in these cell lines are more likely due to 2DG treatment.

In H460 cells, 1 μM NBS037 is the only combination treatment to produce a significant effect in 72 hours when compared to untreated controls ($p = 0.0036$) and when compared to 2DG treatment ($p = 0.0010$). In seven days of treatment, only 0.5 μM and 1 μM NBS037 treatment resulted in a significant decrease in cell viability when compared to controls and 2DG alone, whereas under high glucose, only 1 μM was significantly different. 1 μM NBS037 in combination with 2DG more potently decreased cell viability in 1 mM glucose where cell viability was 3% of untreated controls ($p < 0.0001$) compared to 50% of controls in 11 mM glucose ($p < 0.0001$).

Overall, 2DG alone potently decreased cell viability in A549, MRC-5, and ARPE-19 cells, so these cell lines proved highly sensitive to glycolysis inhibition. The response to 2DG and NBS037 in combination was not significantly different from 2DG alone so NBS037 did not show improved potency with combination treatment. In the H460 line, only in 1 mM glucose after seven days of treatment did the cells become more sensitive to a lower dose of NBS037 (0.5 μM) in combination with 2DG compared to previously observed with NBS037 alone, but no smaller doses yielded any significant effects.

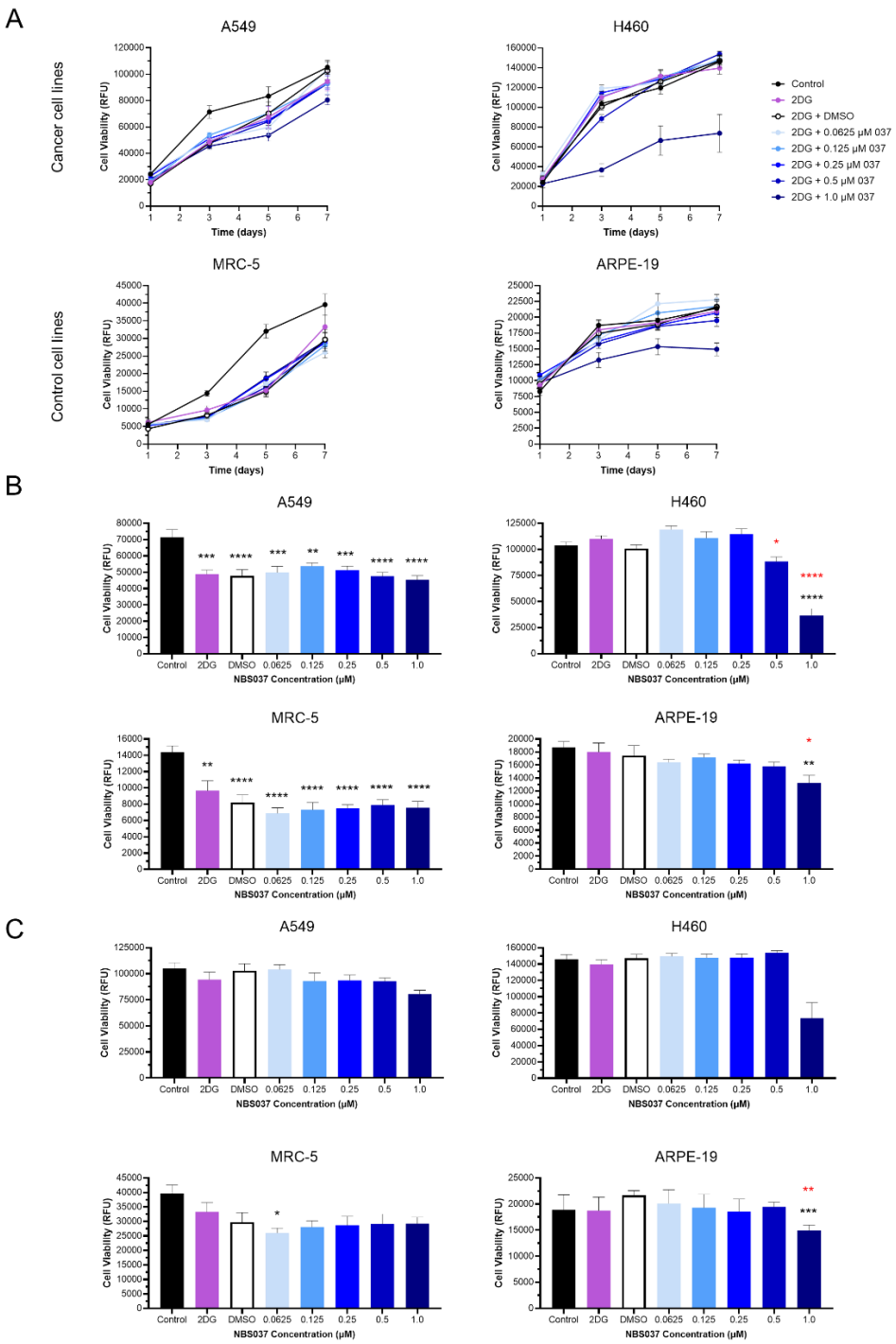

Figure 3.28. Growth curves of cancer cell lines with a combination of NBS037 and 2DG treatment in 11 mM glucose. *PI was used to assess cell viability with NBS037and 500 µM 2DG treatment over seven days in A549 and H460 NSCLC, MRC-5 lung fibroblast, and ARPE-19 retinal epithelial cells in 11 mM glucose. DMSO was used as a vehicle control. Media was replaced daily to maintain glucose levels. (A) Data represents mean cell viability ± SEM over seven days of treatment, (B) represents mean cell viability ± SEM at 72 hours of treatment and (C) seven days of treatment. Statistical analysis was performed by one-way ANOVA with Dunnett's multiple comparisons post hoc tests to compare each treatment group with untreated controls (black asterisks) or 2DG treated cells (red asterisks) (*, $p < 0.05$; **, $p < 0.01$; ***, $p < 0.001$; ****, $p < 0.0001$). N=3.*

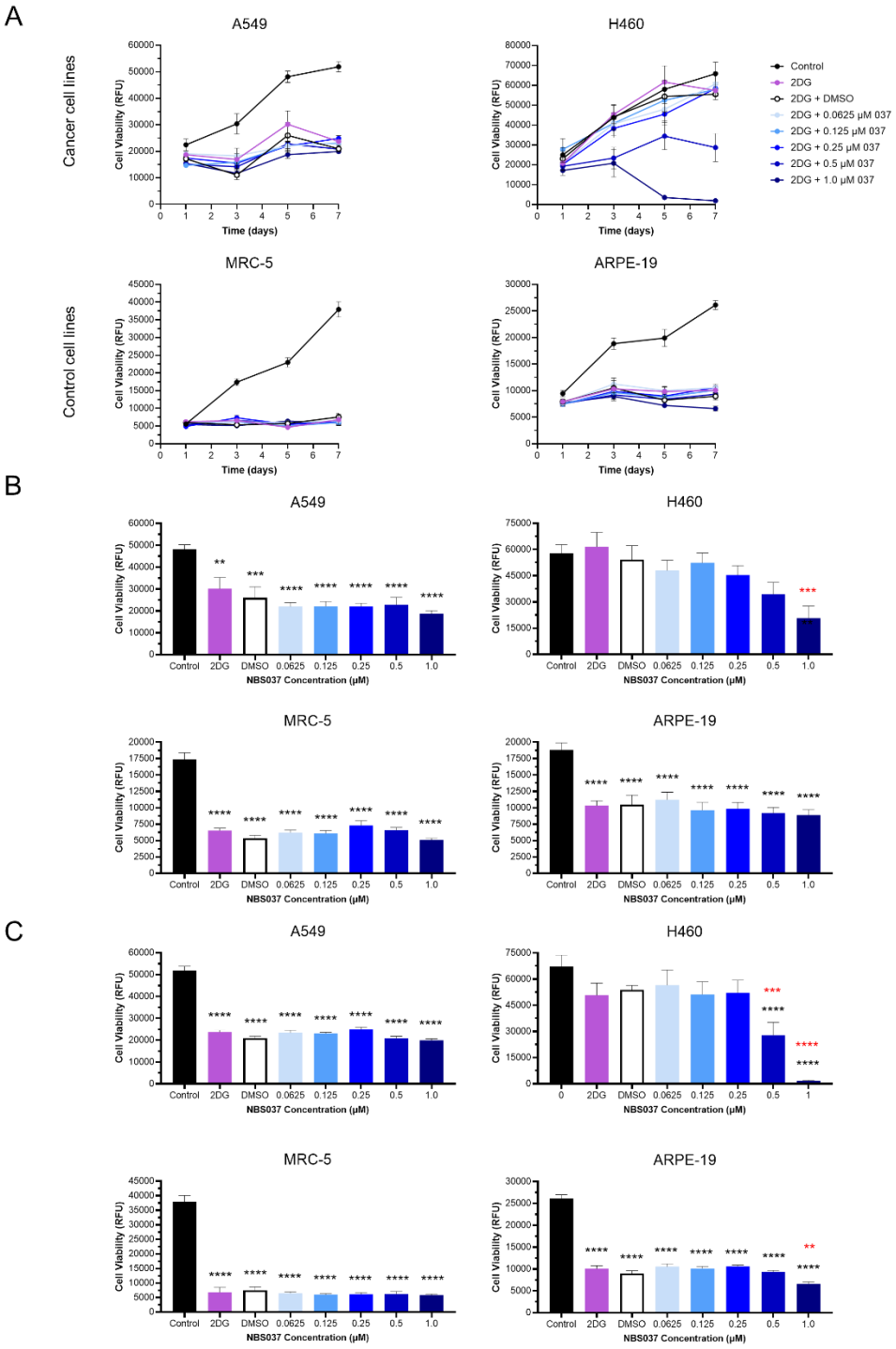

Figure 3.29. Growth curves of cancer cell lines with a combination of NBS037 and 2DG treatment in 1 mM glucose. *PI was used to assess cell viability with NBS037and 500 µM 2DG treatment over seven days in A549 and H460 NSCLC, MRC-5 lung fibroblast, and ARPE-19 retinal epithelial cells in 1 mM glucose. DMSO was used as a vehicle control. Media was replaced daily to maintain glucose levels. (A) Data represents mean cell viability ± SEM over seven days of treatment, (B) represents mean cell viability ± SEM at 72 hours of treatment and (C) seven days of treatment. Statistical analysis was performed by one-way ANOVA with Dunnett's multiple comparisons post hoc tests to compare each treatment group with untreated controls (black asterisks) or 2DG treated cells (red asterisks) (*, $p < 0.05$; **, $p < 0.01$; ***, $p < 0.001$; ****, $p < 0.0001$). N=3.*

3.26 Discussion

The work carried out in this chapter serves as evidence that NBS037 has promising anti-cancer effects when tested *in vitro*, with some effects in non-cancer control lines also.

3.26.1 Choice of cancer cell lines

To investigate the effects of NBS037 *in vitro*, appropriate cell lines were first selected from data provided by Dr Jon Lees. He analysed various cell lines and was able to apply a gene rank score to each, indicating the importance of mitochondrial genes in these lines, with the rank scores for complex I shown in Appendix A. Cell lines with higher rank scores are thought to have higher dependence on OXPHOS and therefore would be a good candidate for NBS037 treatment. From this data mining, H520 NSCLC, Cal51 breast carcinoma and FaDu hypopharyngeal carcinoma were identified as high OXPHOS cancer lines which may be responsive to NBS037. A549 NSCLC cells were selected to validate if a lower gene rank score within the same type of cancer correlated with a lower sensitivity to OXPHOS inhibition. The NSCLC line H460 was also included, which has useful applications in creating xenograft models, and allows *in vivo* work to be carried out later in project[276,277]. With differential OXPHOS dependence in NSCLC lines, these cancer cell lines were the key focus for the majority of the project.

3.26.2 Sensitivity to NBS037

3.26.2.1 Sensitivity of cancer cell lines

A cell viability screen utilising PI showed NBS037 potently decreased cell viability in cancer cell lines (Figure 3.2). Whilst the MTT (3-[4,5-dimethylthiazol-2-yl]-2,5-diphenyltetrazolium bromide) assay is thought of as the gold standard for cytotoxicity assay in drug development,

this assesses cell metabolic activity in order to indicate cell viability[307]. Since NBS037 is a drug which causes changes to metabolism which are yet to be elucidated, an assay independent of metabolism was preferential and likely a clearer viability assay. The PI assay has been used previously for monitoring the growth of human tumour cells *in vitro* as well as testing of cytotoxic compounds[308]. Cell viability was significantly decreased in Cal51, FaDu, H520, A549, and H460 cells with NBS037 within 72 hours of treatment (Figure 3.3), with the NSCLC lines having differential sensitivity to the drug. The sensitivity to NBS037 at 11 mM glucose did not match the gene rank order provided by Dr Lees since Cal51 was not as sensitive as expected, but as glucose was lowered to 1 mM this was rectified . A549 was the least sensitive of the cancer cell lines, with the highest IC50 and H460 the most sensitive with the lowest IC50 (Table 3.2). These findings are in agreement with previous studies testing the use of respiratory chain inhibitors which decrease cell viability and proliferation *in vitro*[237,240]. When tested *in vitro*, Mito-ATQ analogues had an IC50 of 0.18-3 μM[237] and Mito-Met with an IC50 of 1.1 μM[239], highlighting NBS037 is just as potent than current OXPHOS inhibitors in development and dependent on the cell line and culture conditions, can be more effective in reducing cell proliferation. However, when interpreting these results, the effect of contact inhibition must be taken into consideration. After day five of treatments, cancer cell growth begins to slow in untreated and DMSO treated cells (Figure 3.2), indicative that cells may start becoming overconfluent and therefore contact inhibition may prevent further proliferation in the culture plates[309]. If contact inhibition is taking place, the magnitude of NBS037 induced inhibition of proliferation may be greater than reported here. Furthermore, the utilising the PI assay as a read-out of cell viability here is a combination of both proliferation and cell death. Further measures would be required in order to elucidate the effects on NBS037 on either. The medium was replaced daily in order to maintain availability of nutrients; however, in doing so, any floating dead cells would have been removed, yielding a larger cell viability than actually present. Therefore, the compounds tested may have had a larger effect on cell viability than quantified here.

To validate if differential sensitivity to NBS037 was due to a difference in OXPHOS reliance, expression of OXPHOS related proteins (Figure 3.10), ECAR, and OCR (Figure 3.9) were measured in two NSCLC lines, A549 and H460. H460 cells had higher oxygen consumption, and a modest increase in expression of complex II and complex V proteins, and mitochondrial mass compared to A549, indicative that H460 may rely more heavily on OXPHOS under standard culture conditions. However, under these conditions other factors impact the bioenergetics of the cell lines due to culture conditions. The Crabtree effect is one such factor, where supraphysiological glucose in cell culture media leads to upregulation of glycolysis an inhibition of OXPHOS, leading to an underrepresentation of OXPHOS reliance[310]. Similarly, high availability of glucose in cell culture media may lead to changes in post translational modifications which alter the bioenergetics of the cell. Whilst post translational modifications of mitochondrial proteins is less well documented than nuclear encoded proteins, studies have shown mitochondrial glycosylation through high glucose treatment was indeed possible and impaired the function of complex I, III, and IV, coupled with lower ATP content[311]. Measurements of OXPHOS and ECAR at "baseline" in this study, under standard cell culture conditions, should therefore take into consideration this may not be truly reflective of the natural "baseline" of NSCLC cells *in vivo*.

A549 cells had a higher ECAR, indicating higher glycolytic metabolism, but A549 maintained OXPHOS capacity, providing further evidence that OXPHOS is highly important in cancer[138,150,196]. Reducing glucose to shift cells towards a more OXPHOS phenotype, shown by small increases in OXPHOS proteins (Figure 3.10) and OCR (Figure 3.9), increased the potency of NBS037 in both cell lines as expected (Figure 3.3). In low glucose, A549 cells also had an increased ECAR (Figure 3.9). A549 cells have been found to have swollen mitochondria and mtDNA clustering under normal culture conditions, normally considered a sign of mitochondrial stress response[312]. With aberrant mitochondria, A549 cells may behave differently to what is expected and maintain a high rate of glycolysis to counteract any intrinsic

mitochondrial deficits. Furthermore, OXPHOS and glycolysis are not mutually exclusive as glycolysis feeds into the TCA cycle, hence ECARs may increase under low glucose such as observed in A549, and explains why H460 cells maintain high ECAR rates. Measuring ECAR in this manner with the pH Xtra assay relies on changes in pH as a readout of glycolysis rate. The changes in pH can be modulated by factors other than the lactate from glycolysis, such as the CO_2 produced in mitochondrial metabolism which is released into the extracellular media. Therefore assessment of glycolysis may be further verified through measuring enzyme activity or protein expression of key enzymes involved in glycolysis such as HK, PFK, and PK.

These two NSCLC lines were selected for further testing due to their differential sensitivities despite both being NSCLC in origin.

3.26.2.2 Sensitivity of non-cancer cell lines

If NBS037 is to become a viable anti-cancer drug, it must have minimal effects on normal tissue so for this reason, NBS037 was tested in MRC-5 lung fibroblast and ARPE-19 retinal pigment epithelial cells as examples of non-cancer cell lines. Both cell lines originate from healthy tissue and have been utilised previously in cancer research as non-diseased controls[313,314]. With NSCLC our main cancer lines of interest, having a control derived from the same tissue is advantageous and MRC-5 provides an appropriate comparison to the normal lung tissue. ARPE-19 is a spontaneously arising, non-transformed, cell line derived from selective trypsinization of RPE cells to form uniform epithelial population which grow rapidly[315]. Inclusion of this line allows the testing of NBS037 in epithelial cells, which are faster growing and differ in metabolism from fibroblasts. These cell lines possessed a higher IC50 than the cancer cell lines, but the drug was still capable of eliciting a potent decrease in cell viability in the ARPE-19 line, and the MRC-5 line at higher doses. Therefore, it is important to elucidate the mechanism of action and determine whether NBS037 affects cell functioning in non-cancer cell lines in the same manner as cancer cells.

Considering the bioenergetic profiles of the cells, MRC-5 maintains a lower metabolic rate and ΔΨm than the other cell lines (Figure 3.9 and 3.11), regardless of glucose concentration, and would be in agreement with the finding that MRC-5 is the least sensitive to NBS037 (Figure 3.5). ARPE-19 on the other hand, is the most glycolytic of the cell lines tested when using ECAR as a measure of glycolysis but maintains a lower OCR than the cancer lines so a clear reliance on OXPHOS does not explain the sensitivity of ARPE-19 cells to the drug. RPE cells, making up the single-cell layer of epithelium at the outermost layer of the retina, are found to be more OXPHOS and FAO dependent *in vivo*, to allow enough glucose to pass through the RPE cell layer into retinal cells where the glucose is required for cell function and sight[316]. Despite maintaining similar levels of ETC proteins and Tom20 to the cancer cell lines tested (Figures 3.12 - 3.15) it is therefore surprising that ARPE-19 did not appear to have high OXPHOS and instead maintained a lower oxygen consumption than A549 and H460 (Figure 3.17). In culture, however, ARPE-19 cells rapidly proliferate and were found to have a doubling time of approximately 24 hours[315], not dissimilar to the doubling time for A549 and H460 cells. This, coupled with supraphysiological glucose in the culture media, may drive higher rates of glycolysis for high rates of cell proliferation in cell culture, whilst the cell line maintains its OXPHOS machinery.

Overall, whilst cancer cells show promising sensitivity to NBS037, the mechanism of action must be fully elucidated to better understand the sensitivity of non-cancer cell lines to the drug, and whether normal tissue toxicity may be present with NBS037 use.

3.26.3 NBS037 Mechanism of action

3.26.3.1 AZM linked to a mitochondrial targeting sequence has enhanced efficacy compared to unconjugated AZM

Antibiotics are currently being tested *in vitro* and in clinical trials for use as an anti-cancer agent, both with and without a mitochondrial targeting sequence. Examples include tigecycline, doxorubicin, and doxycycline[317]. AZM is also being tested as a single agent *in vitro* with some promising data showing a reduction in cancer cell proliferation[317] and potent effects in combination with standard of care treatments in NSCLC patients[318]. To ensure the effects observed with NBS037 were significantly different from effects seen with AZM alone, cell viability was assessed again but only in the presence of AZM at the same concentrations NBS037 had been tested at (Figure 3.7). AZM treatment at these doses caused no decrease in cell viability in any cell line, differing greatly from the effects of NBS037. In previous studies, the dose of AZM used was far higher in order to elicit effects on cancer cells, with doses between 10 μM and 600 μM proving cytotoxic[318,319]. Such doses also elicited a small decrease in mitochondrial encoded proteins[273]. Whilst NBS037 is highly potent in decreasing cancer and ARPE-19 cell viability, AZM alone does not cause the same effect, and in some cases, AZM significantly increased viable cell count. Without the mitochondrial targeting sequence, it is possible AZM can cause a lower-level disruption to mitochondria, and as a result, cause cellular adaptions such as increased mitochondrial biogenesis, which could in turn favour cell growth and enhanced viability. Therefore, it is safe to conclude that findings included in this chapter are a consequence of the drug NBS037 and the conjugation of AZM to a mitochondrial targeting sequence, rather than AZM alone.

3.26.3.2 Membrane dependent specificity

A key feature of NBS037 is its specificity for cancer cell mitochondria due to biological differences in ΔΨm. Due to higher OXPHOS and energetic output, cancer cells have a much greater ΔΨm than normal cells[285] and therefore, NBS037 should accumulate to a greater extent in cancer cell mitochondria. The ΔΨm in cancer cells was found to be higher than that of the non-cancer cells in agreement with the NBS037 theory of selectivity; however, ARPE-19 cells were still affected by NBS037 despite a lower ΔΨm (Figure 3.11). If NBS037 accumulation is ΔΨm dependent, a lower concentration of NBS037 would accumulate in mitochondria of normal tissues. However, some normal tissues may be highly sensitive to inhibition of mitochondrial protein translation (see 3.26.3.3) or OXPHOS inhibition, and the downstream cellular changes which occur as a result. This could explain the decrease in cell viability in ARPE-19 cells. ARPE-19 may be highly sensitive to the drug but not due to a dependence on OXPHOS (see 3.26.3.4), and sensitive enough that even a lower accumulation of NBS037 can induce effects.

Overall, linking increased potency in cancer cells with their higher ΔΨm provides some promising initial evidence that NBS037 may accumulate in mitochondria in a ΔΨm dependent manner; however, to fully validate the drug's selectivity, a means of measuring accumulation in cancer cells compared to normal cells is required.

3.26.3.3 Mitochondrial proteins

Unlike many other OXPHOS inhibitors in development, which focus on inhibition of a singular respiratory complex, NBS037 exerts its effects through AZM inhibition of mitochondrial ribosomes, which would impact all complexes of the ETC with the exception of nuclear encoded complex II. *In vitro*, the findings are not so simple. Mitochondrially encoded MTCO1 from complex IV was reduced in H460, MRC-5, and ARPE-19 cells indicating target

engagement in both cancer and non-cancer cells (Figure 3.12). In A549 cells, a small decrease in MTCO1 expression was observed with low doses of NBS037 but at higher doses, expression recovered, indicative A549 may be better at adapting to mitochondrial deficits. However, SDHA expression also changed in all cell lines with NBS037 treatment (Figure 3.13). Low doses of NBS037 caused upregulation of SDHA in H460 and ARPE-19, and higher doses reduced SDHA expression in H460, MRC-5, and ARPE-19 when normalised to mitochondrial mass (Figure 3.16). It has been previously shown that inhibition of mitochondrially encoded proteins causes an imbalance with nuclear encoded proteins, the mitonuclear protein balance[320]. Tetracyclines promoted this imbalance, and disrupted global cellular transcription profiles. This caused nuclear encoded proteins to diminish to the same extent of mitochondrial encoded proteins, coupled with overall inhibition of mitochondrial function[321]. 72 hours of NBS037 treatment, therefore, may cause the same effects in disrupting global transcription of nuclear and mitochondrial encoded genes. Furthermore, SDH expression increased in mtDNA mutant patients harbouring complex I deficiencies, indicative that SDHA is regulatable and changes in expression can act as a compensatory mechanism to mitochondrial deficits[322]. SDH is also highly sensitive to ROS effects due to its iron-sulphur cluster[323], similar to that of aconitase, and therefore the tendency for ROS to increase in A549, H460, and ARPE-19 cells with 1 μM and 2 μM NBS037 treatment, may have had some influence in the downregulation of SDHA observed (Figure 3.16).

With 72 hours of treatment, NBS037 caused effects on mitochondrial mass, whether through changes in mitochondrial biogenesis or clearance, where H460 and ARPE-19 experienced a decrease in mitochondrial mass and A549 showed a modest increase (Figure 3.15). Many drugs have effects on mitochondria, whether purposely or not, through changing their bioenergetics, biogenesis, network or mtDNA, with some drugs shown to decrease mitochondrial mass as an off-target effect, similar to observed here with NBS037[324]. In order to restore ATP homeostasis, drugs inducing respiratory injury may have the ability to cause

upregulation of mitochondrial biogenesis in order to compensate for respiratory deficits[325]. This may be the case in A549 cells. A heterogenous population of abnormal and swollen mitochondria has recently been reported in A549 cells[326]. This phenotype is often associated with a mitochondrial stress response, but displays enhanced resistance to mitophagy due to swollen mitochondria unable to undergo fission through canonical mechanisms and their large size preventing enclosure by an autophagic vacuole[326]. These aberrant mitochondria may explain why NBS037 causes minimal effects in this cell line, and why no decrease in mitochondrial mass was observed.

With the opposite observed in H460 and ARPE-19, deficits in respiratory machinery may cause an upregulation of mitophagy to remove the dysfunctional mitochondria, an effect observed with other drug treatments, and would support the decreased mitochondrial mass observed[327,328]. When mitochondrial proteins are normalised to Tom20 expression, a decrease in mitochondrial encoded MTCO1 expression was still observed in H460 but also MRC-5 and ARPE-19, with no significant changes in A549 cells (Figure 3.16). The effects in non-cancer controls require further understanding. Downregulation of mitochondrial proteins in these lines may be a result of NBS037 acting in a nonspecific manner and accumulating in all cells independent of $\Delta\Psi m$, to cause mitochondrial translation effects. Otherwise, if NBS037 does accumulate to a lesser extent in non-cancer cells, other mechanisms may impact expression of mitochondrial proteins. At high doses, AZM was found to be toxic to fibroblasts and epithelial cells with increased ROS and DNA damage. This was accompanied by a marked increase in HIF1-α stabilisation and a shift in metabolism to higher rates of glycolysis[329]. Although the doses tested here were not toxic, a small dose of AZM may still cause an compensatory shift to glycolysis in these cell lines, which may be coupled with a downregulation of mitochondrial OXPHOS proteins which is observed here.

3.26.3.4 OXPHOS capacity

Changes in mitochondrial proteins led to a dose dependent decrease in oxygen consumption in NSCLC cells but no change in non-cancer cells. H460, proven as the highest OXPHOS cell line tested, had the largest fall in oxygen consumption as expected, with NBS037 causing OXPHOS inhibition similar to that of AA (Figure 3.17). With H460 cells more reliant on OXPHOS, successful target engagement and decreased oxygen consumption could lead to ATP depletion to cause the potent decrease in cell viability observed in this cell line.

Minimal changes to mitochondrial protein expression was observed in A549, but a dose dependent decrease in OCR was still observed with NBS037. WB analysis of subunits from complex II and complex IV showed successful translation with higher doses of NBS037 but the lowest dose (0.5 μM) caused a decrease in MTCO1 expression, albeit failing to reach significance (Figure 3.12). With A549 displaying lower OXPHOS than H460, NBS037 effects would be less deleterious than in H460, and A549 may be superior at overcoming mitochondrial deficits, as indicated by an upregulation of mitochondrial mass (Figure 3.15) and recovery of MTCO1 expression (Figure 3.12). Furthermore, the expression of proteins does not always correlate to activity. For example, whilst the OXPHOS proteins may all be expressed, incorrect assembly of the respiratory complex may occur. Complex IV includes 14 subunits, 11 being nuclear encoded and three mitochondrial encoded, whilst complex I consists of 45 subunits, seven of which are encoded by the mitochondrial genome[330]. Any deficits in these mitochondrial proteins may hinder the respiratory protein assembly, as these proteins display a complex assembly involving multiple subunits and cofactors. This would hinder the OCR as observed in A549. Post translational modifications may also affect the subsequent activity of the complex, even with little change in protein expression. For example, many of the respiratory protein subunits are phosphorylated to regulate OXPHOS, and maintain complex stability and activity[331].

Despite NBS037 induced changes to mitochondrial mass and protein expression in MRC-5 and ARPE-19, both cell lines had no significant effects on oxygen consumption with NBS037 after 72 hours of treatment. This is likely due to a threshold effect. These cell lines had lower reliance on OXPHOS, and therefore may tolerate a downregulation of OXPHOS protein expression before any impact on cell metabolism is observed. This would also explain why NBS037 was less potent in decreasing cell viability in these cell lines, despite a downregulation of mitochondrial proteins. AA treatment indicates the proportion of oxygen consumed by the mitochondria in ATP coupled respiration but had no effect in MRC-5 and ARPE-19. This suggests the oxygen consumption measured could be non-mitochondrial or due to proton leak[332], and hence is unaffected by NBS037 induced downregulation of respiratory proteins. Proton leak can be indirectly determined by the subtraction of basal respiration from maximal respiratory capacity, measured by CCCP treatment. Extra mitochondrial oxygen consumption could be due to excessive ROS production and pro-oxidant enzymes[332,333]; however, no such effects were observed with NBS037. When OCR was measured with acute treatment of NBS037 (Figure 3.23), some uncoupling effects were observed with NBS037 in high doses in these lines, but their ETC requirement may be so low that lower doses of NBS037 used in chronic treatment caused no effects on OCR.

Unsurprisingly, since ΔΨm is dictated by mitochondrial health and energetic output, with high ΔΨm an indicator of functional OXPHOS[290], inhibition of OXPHOS in these cancer cell lines also resulted in a decrease in ΔΨm, of which was significant in H460 cells (Figure 3.18). Such depolarisation can also indicate apoptosis, suggesting the decreased cell viability in H460 cells could be due to increased cell death and apoptosis with NBS037 treatment[290]. Depolarisation of the mitochondrial membrane would also drive increased mitophagy, and the need for cells to produce more mitochondria to compensate for deficits. The depolarisation observed was similar to the levels achieved with CCCP and AA, but poses the issue that if NBS037 is ΔΨm dependent in cancer lines, less NBS037 would be able to accumulate inside

mitochondria as treatment duration continues. In order to combat this, different treatment regimens could be explored, with treatments given in cycles to allow for the ΔΨm to recover between treatments.

3.26.3.5 Redox mechanisms

Studies have found that cancer cells have higher levels of ROS in comparison to normal cells, as these molecules promote tumorigenesis through ROS mediated signalling pathways such as EGFR, for cancer cell proliferation and survival[334]. This results in cancer cells being more prone to apoptosis than somatic cells if ROS levels increase further. Many anticancer drugs, such as menadione (vitamin K3)[335], aim to do this - increase ROS levels further to push cancer cells above the cytotoxic threshold whilst normal cells manage these levels. Previous studies show the OXPHOS inhibitor AA increases ROS and depletes the antioxidant glutathione[336,337]. This is due to its inhibition of complex III, which subsequently prevents the oxidation of cytochrome *b* haem groups. The resulting election build up on the cytochrome *b* haem groups allows sufficient time for electrons to react with oxygen to form ROS[338]. Significantly higher levels of ROS were only observed with higher doses of NBS037 in H460 cells, so increasing ROS levels alone is likely not the mechanism of action of NBS037 (Figure 3.19). In agreement with this finding, inhibition of complex IV has previously been found to inhibit complex III generated ROS due to depletion of cytochrome *c*[339]. Generating ROS through compromising the ETC would require very low levels of OXPHOS proteins to be reached, therefore ROS effects are only observed in the cell line which is the most sensitive to NBS037 induced OXPHOS inhibition.

As overall ROS levels are a combination of both production and degradation, any increases in ROS production from NBS037 may be masked by a compensatory increase in antioxidant capacity to bring balance back to baseline ROS levels. In A549 cells, NBS037 caused a

significant increase in SOD2 when normalised to Tom20 (Figure 3.22A), in response to a small increase in ROS at higher doses of NBS037 (Figure 3.19). With A549 cells having a lower OCR, these cells would produce less ROS in the ETC and have a lower need for endogenous SOD2 as shown in Figure 3.20. This cell line may therefore be more responsive to small fluctuations in ROS and upregulate SOD2 accordingly. The opposite was observed in H460 and MRC-5 cells at high doses of NBS037, where there was a drug induced decrease in SOD2, a phenomenon which has been observed before in doxorubicin treated breast cancer cells[340] and cardiomycocytes[341]. With OXPHOS a key contributor to mitochondrial ROS production, its inhibition would lead to slowed production of ROS and therefore a smaller requirement for SOD2 ROS scavengers. This may have caused the decrease in SOD2 expression in these cell lines, particularly the more sensitive H460 line. In H460 cells, this decrease in SOD2 and antioxidant capacity may have caused the apparent increase in ROS levels observed rather than reflecting an increase in ROS generation (Figure 3.19). No significant changes in ROS levels were observed in non-cancer cells despite this decreased antioxidant capacity, indicative that ROS generation was low in these cell lines and may be a consequence of the low OCR observed in these lines (Figure 3.17). Aconitase was used as a further marker of oxidative stress, but again, H460 was the only cell line with any significant change where a decrease in protein expression when normalised to Tom20 was observed (Figure 3.22C). Decreased aconitase expression is associated with higher ROS levels and oxidative stress as cells try to downregulate OXPHOS to mitigate excess ROS production, and is rapidly degraded in the presence of ROS[342]. This would be in agreement with the observation that the ROS levels were increased in this cell line with increased NBS037 dose. The same tendency for decreased expression was observed in MRC-5 although failed to reach significance, which was unsurprising given no significant changes in overall ROS levels were observed. ARPE-19 raised aconitase expression in response to lower levels of the drug which may act to compensate for the mitochondrial deficits in OXPHOS.

Overall, the work here suggests ROS effects are minimal with NBS037, particularly at lower doses, which would be more reflective of drug concentrations achieved *in vivo*. Therefore, abolishing of oncogenic ROS signalling or increasing ROS production above cytotoxic levels do not contribute to the decreased cell viability observed with NBS037 treatment.

3.26.4 Adverse uncoupling effects

With mitochondrial targeting becoming a popular strategy in novel drug design for targeted drug delivery, the TPP^+ moiety, inclusive of the carbon linker region, has been found to have uncoupling effects[173]. Uncoupling of the ETC is a process in which the respiratory chain is disrupted and the proton motive force is dissociated from ATP generation, causing dissipation as heat[301]. Whilst this is a normal physiological process, increased uncoupling can cause injury to OXPHOS and subsequently ATP deficiency. Therefore, uncoupling is a mechanism in which some drugs cause toxicity such as niclosamide and nitazoxanide[343]; however, uncoupling can be highly toxic as all cells share the same ETC components and many vital tissues require OXPHOS for healthy function. NBS037 was carefully formulated to optimise this TPP^+ moiety and linker region for optimal lipophilicity but without uncoupling effects. To ensure no uncoupling effects were observed, which would be noticed as soon as the first hours of treatment, oxygen consumption was measured for the first 12 hours of NBS037 treatment, and initial OCR calculated by linear regression between approximately one and three hours. Uncoupling can be identified as a large increase in initial OCR as cells boost rates of OXPHOS to maintain the ATP output they require[344]. This was observed at very high doses of NBS037 (10 μM), far above the IC50 of all the cell lines used. However, the time course of oxygen consumption highlights this effect was only observed for the first few hours, as oxygen consumption begins to fall with time. High doses of CCCP have previously been found to cause collapse of $\Delta\psi m$, increased mitochondrial fission, and increased autophagolysosome formation, an event preceding mitophagy and autophagy[345]. Increased mitophagy would

remove respiring mitochondria and subsequently cause oxygen consumption to fall. High doses of NBS037, therefore, may cause the same events and explain the fall in oxygen consumption observed, supported by the depolarisation of Δψm observed with NBS037 treatment (Figure 3.18). With increasing time, translational effects on the mitochondrial proteins will start to take effect, or at very high doses of NBS037, cell death, which would otherwise explain the dropout of oxygen consumption observed.

Measurement of ROS also provides an insight into uncoupling effects as uncoupling is a natural mechanism to reduce ROS production if an excess is being produced[346]. In the first 12 hours of treatment, ROS levels as measured by DHE, had a tendency to increase with NBS937 treatment, as it did with AA (Figure 3.25).This provides an indication that NBS037 causes minimal uncoupling but instead behaves as a potent OXPHOS inhibitor.

3.26.5 NBS037 in combination treatment

NBS037 caused alterations in mitochondrial proteins expression and cell viability in non-cancer cells, which proved to be sensitive to the drug at the concentrations used. Utilising a drug in combination with another is a common method in which groups are able to enhance the effects of each but at a smaller dose than as a single agent[347]. 2DG has been tested both *in vitro* and in Phase I and II clinical trials, as both an anti-cancer and anti-viral agent with promising improvements in a range of cancer and COVID-19 patients[348,349]. In many cases however, use of glycolytic inhibitors cause upregulation of OXPHOS as a compensatory mechanism and vice versa, where OXPHOS inhibitors cause increased glycolysis and lactate production[179,350]. 2DG, a potent inhibitor of glycolysis may therefore be a potential compound to test in combination with NBS037 to block both glycolysis and OXPHOS. Combined with doses of 2DG used *in vitro* according to previous literature, NBS037 was able to potently decrease cell viability significantly more than 2DG. The combination of 20 mM 2DG and

NBS037 was also able to decrease cell viability to a greater extent than NBS037 alone; however, the cells did not grow well with 20 mM 2DG, with 20 mM 2DG causing a large depletion in ATP (Figure 3.27).

At concentrations of 2DG achievable in plasma (500 μM), NBS037 concentrations lower than 0.5 μM were tested to assess if combination treatment could enhance the efficacy of both compounds. Doses of NBS037 lower than 0.5 μM were not able to elicit any further significant decreases in cell viability when compared to 2DG, so effects on viability were likely due to 2DG treatment rather than combination treatment. In 1 mM glucose, 500 μM 2DG potently decreased the cell viability of non-cancer controls, so 2DG even at the lower dose may remain unacceptably toxic, and not a viable choice for combination treatment, albeit better tolerated at 11 mM glucose. 2DG also inhibits protein N-glycosylation, subsequently causing endoplasmic reticulum related apoptosis in cancer cells *in vitro*, which may contribute to the large decrease in cell viability observed here[351–353].

3.27 Future directions

Conducting cancer research *in vitro* will always be limited by the poor recapitulation of the tumour environment in cultured cells. Standard culture conditions, in which most experiments take place, utilise atmospheric oxygen and nutrient rich medias, carefully formulated for optimised growth. On the other hand, the tumour environment operates at harsh conditions with cells subjected to hypoxia (<1% O_2) and poor availability of nutrients (~0.1 mM glucose) due to irregular vascularisation. This environment can change greatly even within the same tumour[354]. Therefore, going forward, it would be beneficial to recapitulate these features as much as possible as such environments could impact the cell metabolism and the response to NBS037. Whilst optimising tumour conditions *in vitro* could be another thesis in itself, measuring the oxygen and the nutrient levels in the cell monolayer *in vitro*, and changing this

to recapitulate the tumour microenvironment as much as possible, could help in better understanding mechanisms of action of the drug before having to test in animals. NBS037 is more potent in lower glucose conditions, conditions more reflective of *in vivo* glucose levels, so enhanced toxicities could have been missed before testing in animals.

ARPE-19 cells proved highly sensitive to the drug *in vitro*, with some effects also observed in MRC-5. These lines were used as non-cancer controls; however, utilisation of primary cell lines, those which have been cultured directly from the tissue of origin, would have been a beneficial control. MRC-5 and ARPE-19 cell lines have been cultured for many generations[270], and whilst most characteristics are preserved, some characteristics may deviate from their original tissue of origin. This may cause cells to behave in different ways and alter the cell metabolism, which is highly important for the way in which they respond to NBS037. Whilst primary cell lines are more challenging and expensive to grow, these would give a more accurate view of the effect of NBS037 on normal cells.

This work found that sensitivity to NBS037 was not due to differences in ΔΨm as theorised with the TPP^+ group, as ARPE-cells maintained a low ΔΨm but were still affected by the drug (Figure 3.11). It would be useful, therefore, to understand how much of the drug is entering cells, where it is localised, and the concentration of NBS037 which accumulates inside the mitochondria. Techniques such as Raman spectroscopy, later detailed in this thesis, provides a means of studying these features of NBS037 and would allow us to identify if NBS037 is accumulating at the same concentration inside non-cancer cells as the cancer cell lines to cause the effects seen. If NBS037 accumulates to a lesser extent inside non-cancer cells, the ΔΨm would be validated and effects of NBS037 observed in ARPE-19 and MRC-5 would be due to intrinsic sensitivity.

The work in this project indicates that NBS037 did not cause a downregulation of only mitochondrially encoded proteins, but also changes to mitochondrial mass and nuclear encoded ETC proteins. It would be of interest to expand the range of outputs for this work to include all five of the respiratory complexes, whether by measuring their expression or activity, to further elucidate exact effects on the ETC. Investigating effects on mtDNA and mitochondrial biogenesis, mitochondrial degradation (mitophagy), and transcriptomics for nuclear encoded and mitochondrial encoded proteins alike may also prove beneficial. Further work can be carried out in identifying the cause of decreased cell viability, whether it be increased apoptosis, ATP depletion, or slower cell proliferation. Furthermore, it would be of interest to observe the compensatory mechanisms at play such as rates of glycolysis or FAO during NBS037 treatment, which may allow cancer cell survival.

To best understand the mechanisms of action of NBS037, the drug will need to be tested *in vivo*, where cells are under natural conditions and receive the doses of NBS037 which can be achieved after drug metabolism and dispersal. Animal models provide heterogeneous tumours and normal tissues so the specificity of NBS037 to tumour cells can be truly tested and any adverse effects investigated (see Chapter 4).

Overall, there is still much work which can be carried out in optimising cell models and investigating the effects of NBS037, but the mechanism of action will be far better understood from *in vivo* models, where the correct environment and interactions between cells are in place.

3.28 Chapter summary

Overall, NBS037 showed promising data in effectively decreasing cell viability in cancer cell lines. Successful inhibition of mitochondrial encoded protein translation and OXPHOS in a dose dependent manner was observed, and may contribute to the cytotoxicity of the drug in cancer cell lines. ROS and uncoupling mechanisms proved not to be the mechanism of action of the drug at clinically relevant doses. Effects on mitochondrial mass and nuclear encoded ETC proteins were observed in all cell lines with NBS037 treatment, so further work is required to fully understand the mechanism of action *in vitro*.

4

The Effects of NBS037 *in Vivo*

4.1 Introduction

Whilst cell lines provide an understanding of molecular biology in human cells, they lack an accurate recapitulation of the *in vivo* environment. Mouse models were introduced into laboratories in the early twentieth century and since then have become a vital element of the drug discovery process, allowing the study of drugs and drug targets in the body. As mice share 95% of the human genome, and many anatomical and physiological features[355], drug testing in these models provide a somewhat accurate indication of how these drugs will behave in humans, and are vital for investigating proof of concept mechanisms, tolerability, and efficacy[356].

Many OXPHOS inhibitors currently in development showed promising anti-tumour efficacy *in vivo* in order to allow progression into clinical trials (see Table 1.1). NBS037 has been tested previously in several small-scale mouse studies conducted by Novintum and Evotech in order to test tolerability, efficacy, and maximum tolerated dose (MTD). Following this, Dr James Hulit, University of Oxford, conducted a mouse study to test the effects of NBS037 on tumour growth

(n=12). CD-1 nude mice, an immunodeficient mice line derived from a colony of Swiss mice in 1926[357], were inoculated with H460 NSCLC cells. Mice were treated with 0.1 mL of PBS as a vehicle control, or 3 mg/kg NBS037 through IV tail vein injections. This dosage was deduced from the previous MTD studies. Mice received 15 injections, in three cycles of 3 days on, 1 day off, 2 days on, 1 day off. Treatments were ended at day 20 due to reaching the threshold tumour size of 1000 mm^3. Animals were continually cared for after treatment to observe the effects on the tumour after treatment cessation (Figure 4.1A). Tumour growth delay was observed in NBS037 treated tumours (Figure 4.1B), and NBS037 enhanced the probability of survival (Figure 4.1C), however these findings were not significant. The molecular mechanisms behind such findings, and the effects of NBS037 on cells *in vivo,* are yet to be deduced.

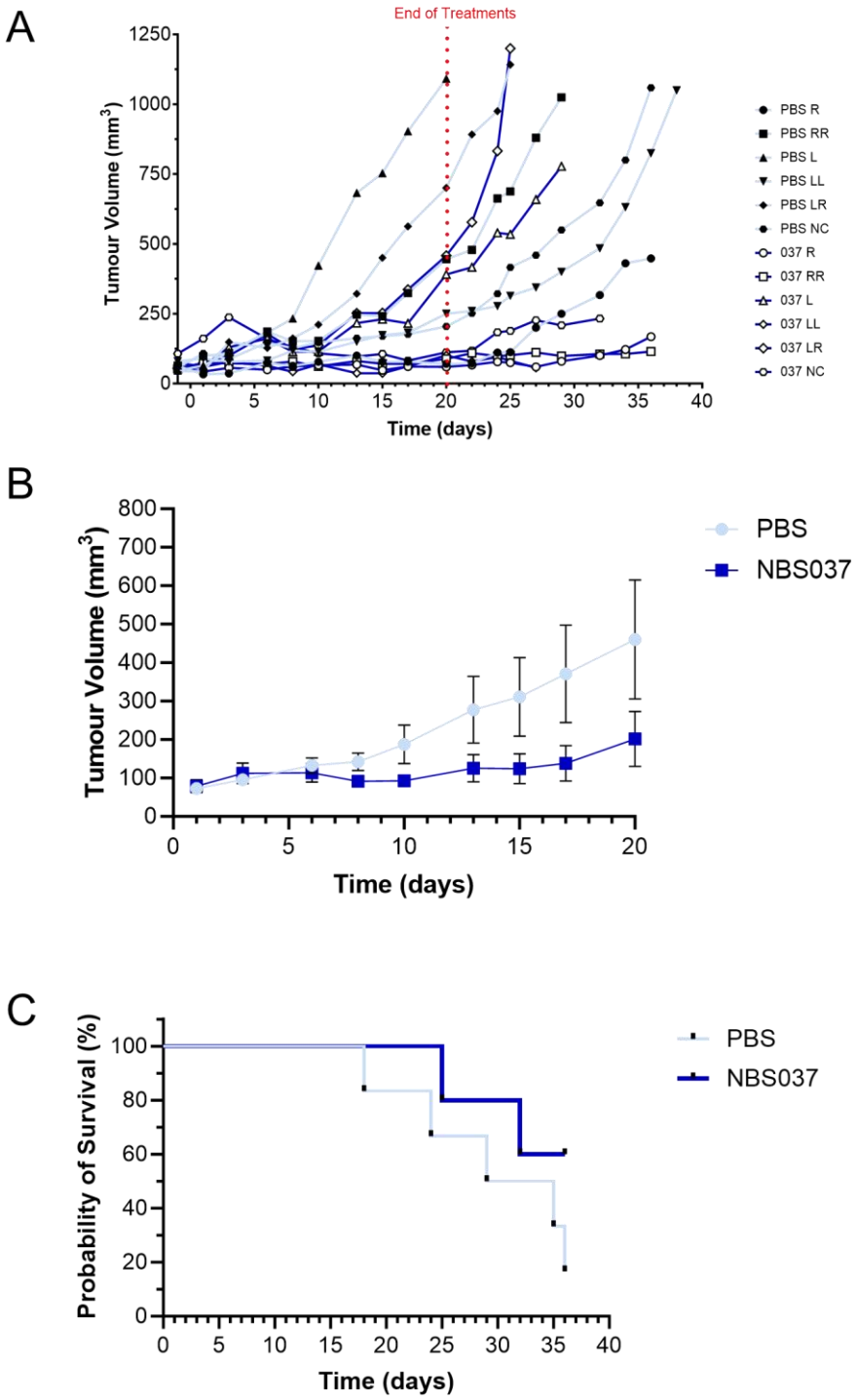

Figure 4.1. The effect of NBS037 on H460 tumour growth in CD-1 mice. *Mice were treated with 0.1 mL PBS (n=6) or 3 mg/kg NBS037 (n=6) in three cycles of 3 days on, 1 day off, 2 days on, 1 day off. Data represents (A) tumour volume in individual PBS and NBS037 treated mice over the experimental period. Treatments were ended at day 20 due to reaching threshold tumour size of 1000 mm^3. Different animals were denoted by clips on the ears: NC (no clip), RR (two right), R (right), LL (two left), L (left), LR (left and right). (B) represents mean tumour volume during the treatment period ± SEM (not significant). (C) represents survival, the time for the tumour to reach 1000 mm^3 (not significant). This work was carried out by Dr James Hulit, University of Oxford.*

4.2 Aims

The specific aims of this chapter are to investigate:

a) NBS037 target engagement
b) Cellular responses to NBS037

in CD-1 mice tissues treated with PBS or NBS037, as part of a small-scale mouse study conducted by Dr James Hulit.

4.3 Tumours successfully grew in nine mice out of twelve

Immunodeficient CD-1 nude mice were inoculated with H460 NSCLC cells and tumours left to grow. When tumour size reached 55 - 65 mm^3, mice were treated with PBS (n=4) or NBS037 (n=5) until mice were culled at threshold tumour size (120-140 mm^3), with the aim of producing tumours of a similar size. Tumour size was measured frequently throughout (Figure 4.2). This work was carried out by Dr James Hulit.

From the 12 mice included in this study, two of those in the PBS treatment arm and one in the NBS037 treatment arm failed to grow tumours larger than 50 mm^3, and therefore did not receive treatment. Animals harbouring these slow growing tumours were still culled at 21 days, but tissues were excluded from any further analysis. Final numbers for further analysis were n=4 for PBS treated tissues and n=5 for NBS037 treated tumours.

The tumours in the NBS037 treatment arm proved to grow quicker than those in the PBS treatment arm, and therefore were culled at day 18 (NC) and 19 (LL, RR, L, LR). In order to achieve similar sizes of tumour, tumours in the PBS treatment arm were allowed to grow for a further two days before mice were culled, with the exception of mouse RR which was culled at day 18 due to a faster growing tumour. Excluding tumours which failed to grow, there was

no significant difference in mean tumour size between PBS and NBS037 treatment groups (Figure 4.2C).

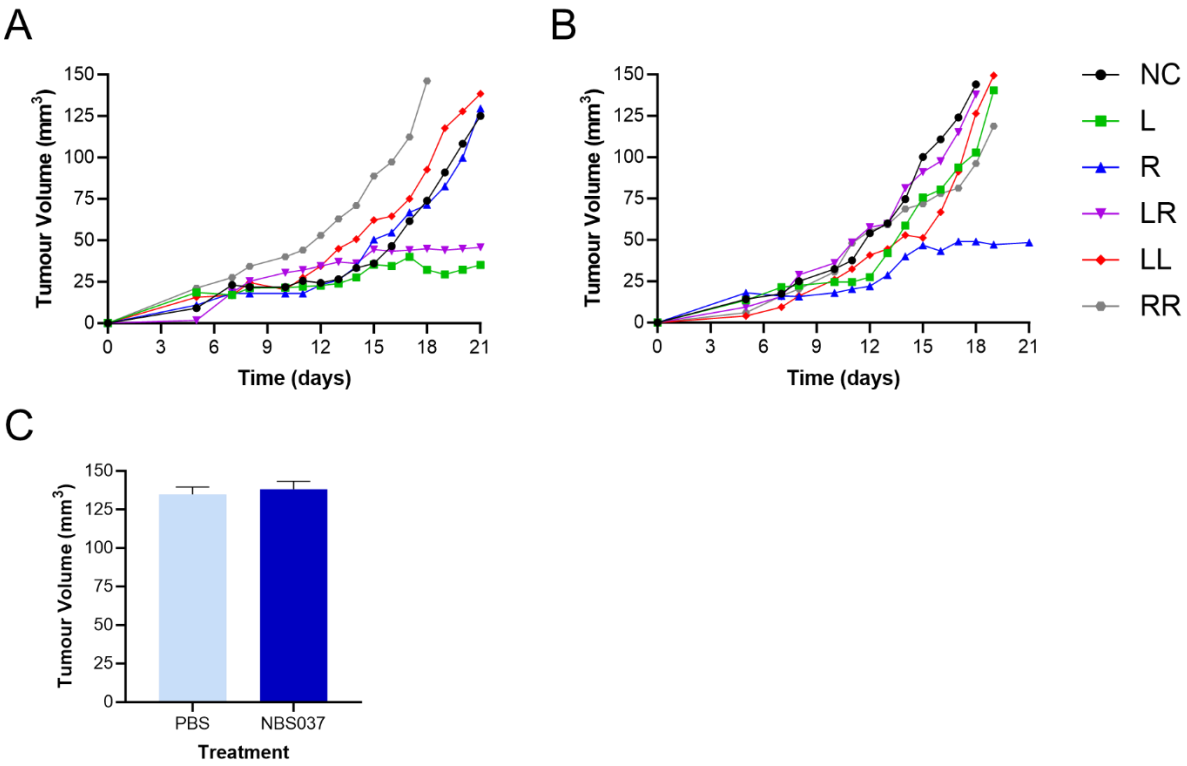

Figure 4.2. H460 tumour growth in CD-1 nude mice treated with PBS or NBS037. *Mice were treated with 0.1 mL PBS or 3 mg/kg NBS037 whe tumour volume exceeded 55 mm^3. Data represents tumour volume in (A) PBS treatment arm, (B) NBS037 treatment arm mice over the experimental period. (C) represents tumour volume when the mice were culled and tissues excised, excluding the tumours which failed to grow larger than 55 mm^3 (PBS n=4, NBS037 n=5). Different animals were denoted by clips on the ears: NC (no clip), RR (two right), R (right), LL (two left), L (left), LR (left and right). Statistical analysis was performed by an unpaired t-test when comparing means. This work was carried out by Dr James Hulit.*

4.4 Notable differences in bodyweight were observed between treatment groups

Tracking of bodyweight is a tool used to monitor the health of the mice and tolerance to the drug. Loss of bodyweight can be a sign of stress and suffering, whether due to handling or treatment, with a 20% drop in bodyweight thought of as a humane endpoint for the animal and cessation of the study[358]. The bodyweights of the mice were measured at least twice a week over the duration of the study and corrected for the injection volume (Figure 4.3). This work was carried out by Dr James Hulit.

Overall, each animal displayed no significant difference in bodyweight between the start and endpoint of the study (Figure 4.3C and D). However, the NBS037 treatment arm had a significantly lower mean bodyweight compared to PBS treated mice ($p = 0.0283$) (Figure 4.3E). PBS treated mice had a mean increase in bodyweight per injection volume of 7.9% whilst NBS037 treated mice had a mean decrease in bodyweight of 1.6% (Figure 4.3F). With the NBS037 group also harbouring faster growing tumours (Figure 4.2), lower bodyweight may be associated with tumour burden, rather than due to any adverse effects of treatment.

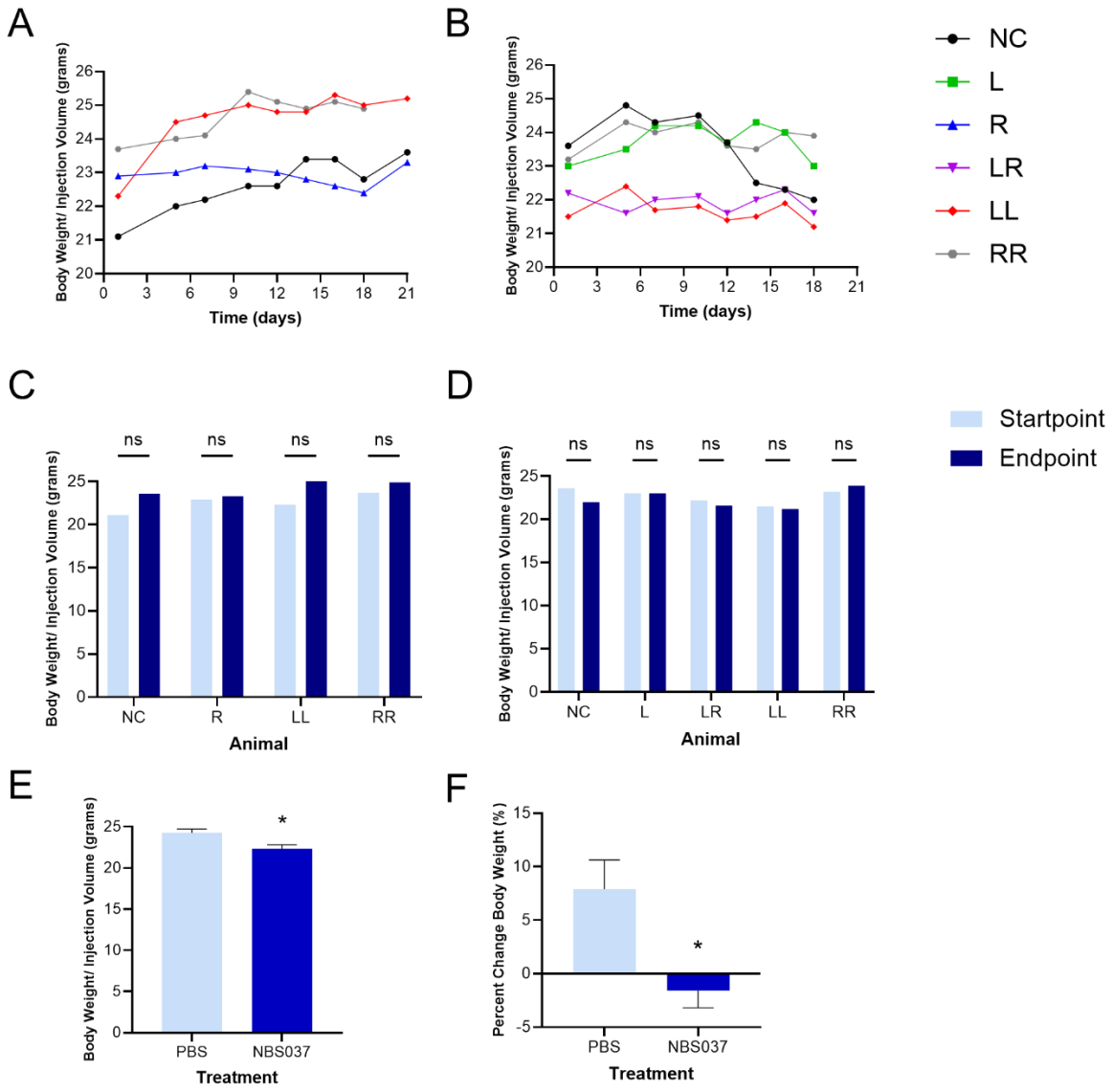

Figure 4.3 Bodyweight of CD-1 nude mice over the experimental period. *The bodyweights of mice treated with 0.1 mL PBS (n=4) or 3 mg/kg NBS037 (n=5) were measured at least twice a week to monitor mouse health. Data represents bodyweight per injection volume in (A) PBS and (B) NBS037 treated mice over the treatment period. Bodyweight per injection volume was compared at start point and endpoint in (C) PBS and (D) NBS037 treated mice. (E) represents mean bodyweight per injection volume ± SEM and (F) represents mean percent change in bodyweight between start and end of study ± SEM. Statistical analysis was performed by an unpaired t-test when comparing mean PBS and NBS037 bodyweights and two-way ANOVA was performed to compare PBS and NBS037 treatments in multiple animals, with Tukey's multiple comparisons test to test differences amongst groups (*, $p < 0.05$). Different animals were denoted by clips on the ears: NC (no clip), RR (two right), R (right), LL (two left), L (left), LR (left and right). This work was carried out by Dr James Hulit.*

4.5 NBS037 has no effect on mitochondrial proteins in brain, heart, and kidney tissue

For NBS037 to be a beneficial drug for patients with high OXPHOS cancers, it must act specifically on cancer cells and have little effects on normal tissue to prevent any adverse side effects. In NBS037 treated mice, minimal changes in mitochondrial proteins in normal tissues are expected, if the TPP^+ targeting group targets cancer mitochondria. Mitochondrial encoded MTCO1 was used as a readout for target engagement, as previously performed in Chapter 3. Brain, heart, kidney, liver, and tumour tissues were extracted from mice which had been treated with PBS (n=4) or NBS037 (n=5). MTCO1 expression in these tissue lysates were determined by WB and quantified from the bands observed. SDHA expression was quantified to show effects on nuclear encoded proteins and Tom20 expression quantified to show changes in mitochondrial mass. Protein expression was normalised to both β-actin, the loading control, and Tom20.

In NBS037 treated animals, no significant effects on mitochondrial proteins or mitochondrial mass were observed in brain (Figure 4.4), heart (Figure 4.5) or kidney (Figure 4.6) tissue as expected but only some small changes were observed. In the heart, MTCO1 levels when normalised to mitochondrial mass, fell by 28% with NBS037 treatment, and SDHA expression increased by 7%. In kidney, MTCO1 expression with NBS037 was 85% that of PBS, but only a 10% decrease in SDHA expression was observed. Whilst these effects are not significant in this treatment period, it would of interest to test if such decreases in MTCO1 are potentiated with extended treatment.

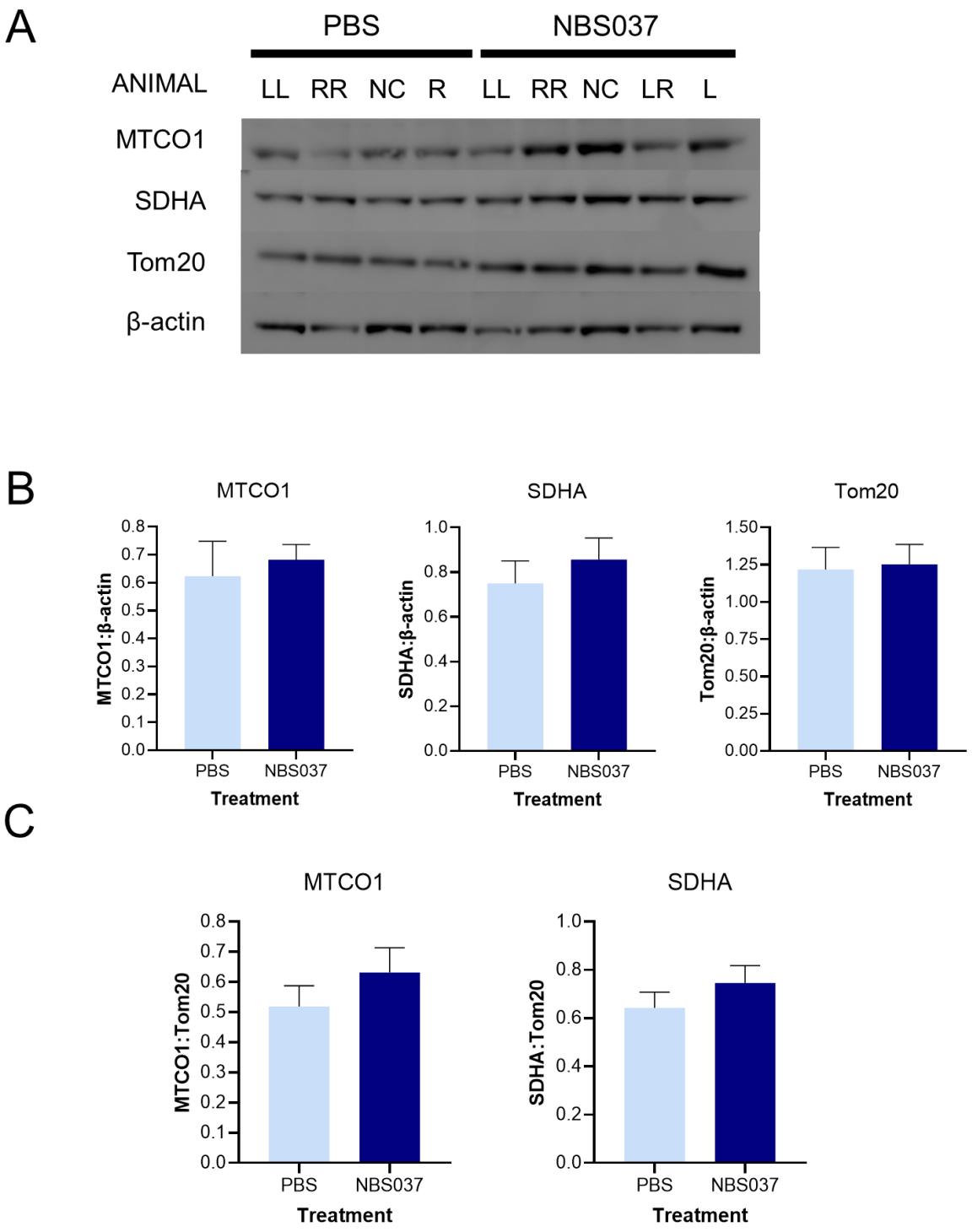

Figure 4.4. Mitochondrial protein expression in brain lysates from PBS and NBS037 treated mice. *WB analysis was used to investigate the mitochondrial protein expression in brain lysates from PBS (n=4) and NBS037 (n=5) treated mice. Data is shown as (A) original blots from tissue lysates, with different animals denoted by clips on the ears: NC (no clip), RR (two right), R (right), LL (two left), L (left), LR (left and right). (B) mean protein expression normalised to β-actin ± SEM, and (C) mean protein expression normalised to Tom20 ± SEM. Protein expression was quantified from blots using the G-box software. Statistical analysis was performed by unpaired t-tests to compare the means of each treatment group. N=3.*

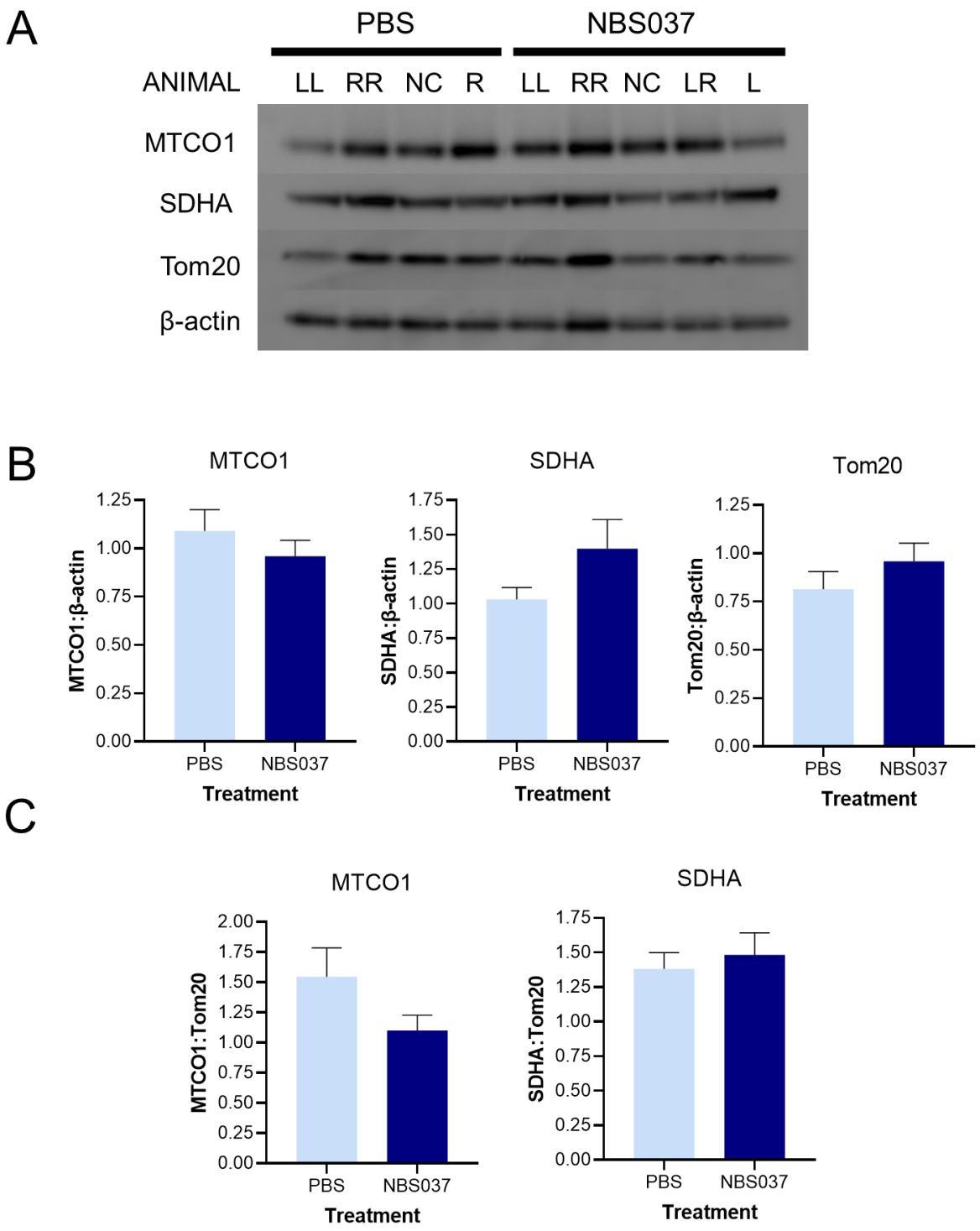

Figure 4.5. Mitochondrial protein expression in heart lysates from PBS and NBS037 treated mice. *WB analysis was used to investigate the mitochondrial protein expression in heart lysates from PBS (n=4) and NBS037 (n=5) treated mice. Data is shown as (A) original blots from tissue lysates, with different animals denoted by clips on the ears: NC (no clip), RR (two right), R (right), LL (two left), L (left), LR (left and right). (B) mean protein expression normalised to β-actin ± SEM, and (C) mean protein expression normalised to Tom20 ± SEM. Protein expression was quantified from blots using the G-box software. Statistical analysis was performed by unpaired t-tests to compare the means of each treatment group. N=3.*

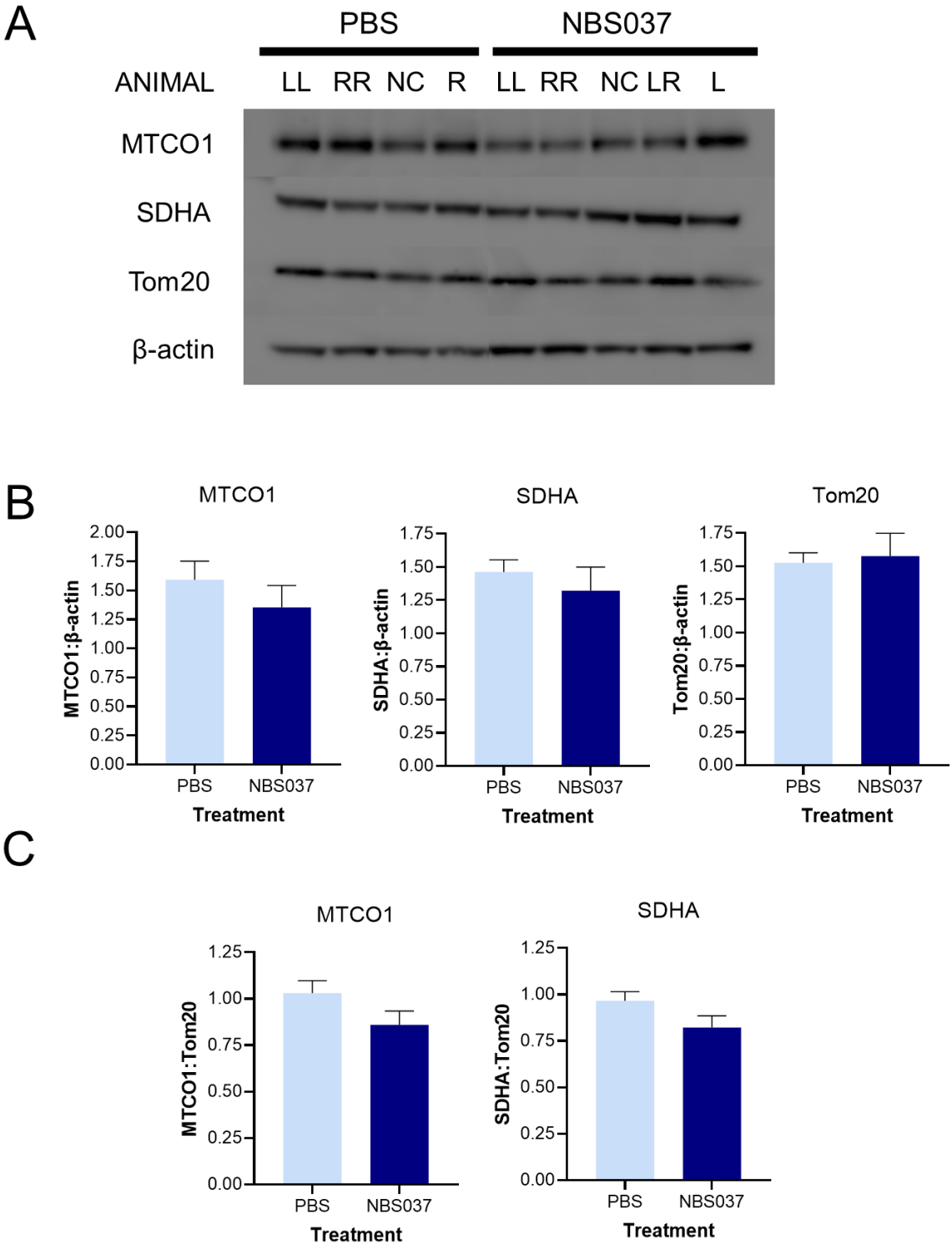

Figure 4.6. Mitochondrial protein expression in kidney lysates from PBS and NBS037 treated mice. *WB analysis was used to investigate the mitochondrial protein expression in kidney lysates from PBS (n=4) and NBS037 (n=5) treated mice. Data is shown as (A) original blots from tissue lysates, with different animals denoted by clips on the ears: NC (no clip), RR (two right), R (right), LL (two left), L (left), LR (left and right). (B) mean protein expression normalised to β-actin ± SEM, and (C) mean protein expression normalised to Tom20 ± SEM. Protein expression was quantified from blots using the G-box software. Statistical analysis was performed by unpaired t-tests to compare the means of each treatment group. N=3.*

4.6 NBS037 reduces mitochondrial protein and mitochondrial mass in liver

Once NBS037 is inside the body, it will be metabolised by the liver, leading to liver tissue having the highest NBS037 exposure of any organ. For this reason, it is especially important to test if NBS037 has any effects on mitochondrial proteins in the liver. MTCO1, SDHA, and Tom20 expression in the liver were quantified by WB from tissue lysates (Figure 4.7).

A significant decrease in MTCO1 ($p = 0.0072$), SDHA ($p = 0.01$), and Tom20 ($p = 0.004$) was observed in liver tissue from NBS037 treated mice; however, when normalised to mitochondrial mass, these significant decreases in MTCO1 and SDHA expression were no longer observed. Instead, there was no change in SDHA, and a 22.6% increase in MTCO1 expression, albeit not significant (Figure 4.7C). Tom20 expression with NBS037 treatment was under half that of PBS treated animals, which therefore lead to a potent overall decrease in mitochondrial localised proteins (Figure 4.7B).

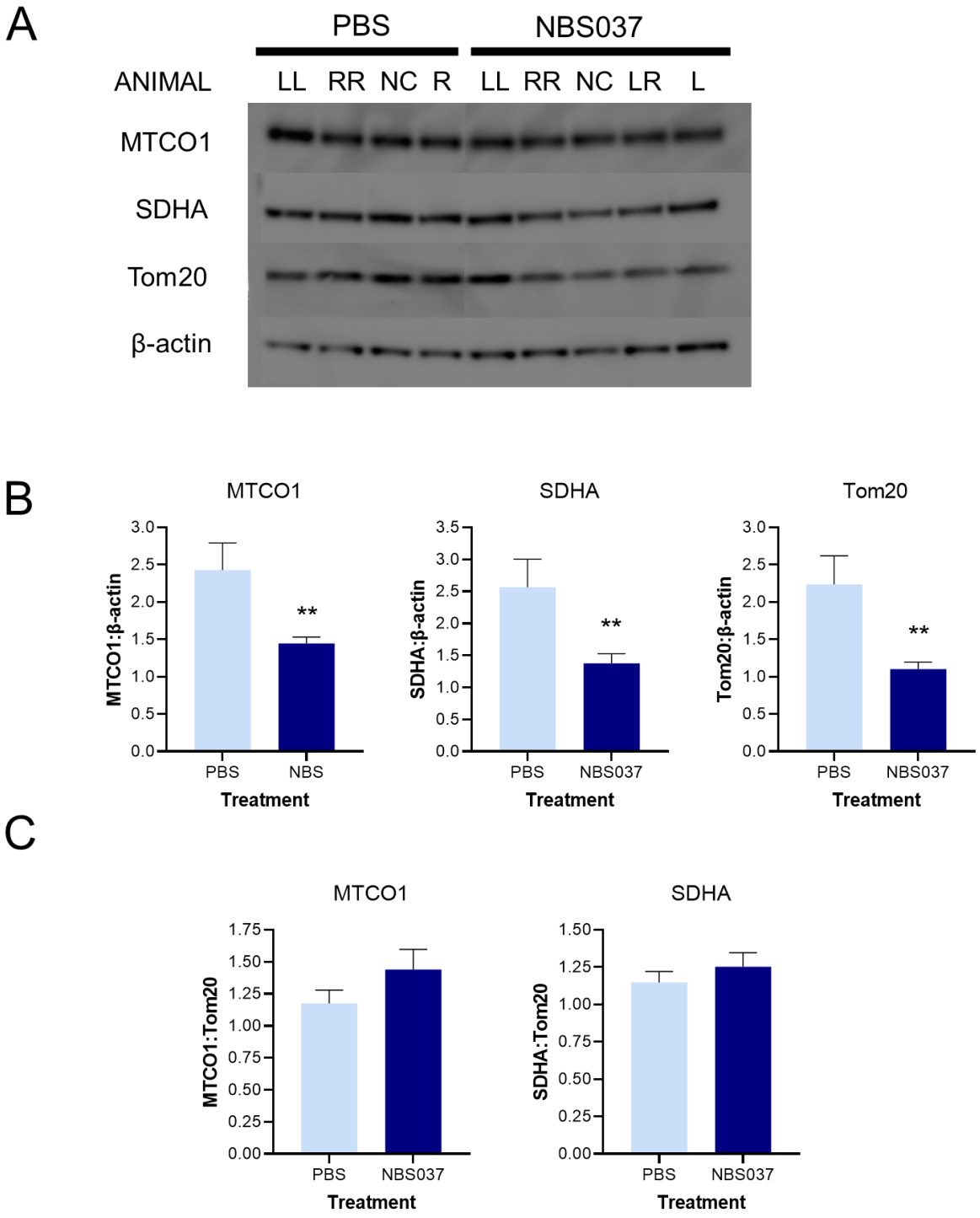

Figure 4.7. Mitochondrial protein expression in liver lysates from PBS and NBS037 treated mice. *WB analysis was used to investigate the mitochondrial protein expression in liver lysates from PBS (n=4) and NBS037 (n=5) treated mice. Data is shown as (A) original blots from tissue lysates, with different animals denoted by clips on the ears: NC (no clip), RR (two right), R (right), LL (two left), L (left), LR (left and right). (B) mean protein expression normalised to β-actin ± SEM, and (C) mean protein expression normalised to Tom20 ± SEM. Protein expression was quantified from blots using the G-box software. Statistical analysis was performed by unpaired t-tests to compare the means of each treatment group (**, p < 0.01). N=3.*

4.7 NBS037 reduces mitochondrial protein and mitochondrial mass in tumour

Due to its structure with a conjugated TPP^+ cation, NBS037 should target tumour cells which have a higher Δψm than normal cells, leading to higher accumulation of drug within tumour cells for successful target engagement. To test is there are any effects on mitochondrial proteins in tumours, MTCO1, SDHA, and Tom20 expression were examined once more by WB but in lysates from tumour tissue (Figure 4.8).

A significant decrease in MTCO1 ($p = 0.0398$) and Tom20 ($p = 0.0048$) expression was observed with NBS037 treatment, with a 34.2% decrease in mitochondrial mass, and MTCO1 levels falling to nearly half that of PBS treated animals. When mitochondrial proteins were normalised to mitochondrial mass, no significant differences were observed, so overall changes in expression were due to falling mitochondrial mass rather than a specific downregulation of MTCO1 alone.

Tumours are known to display vast heterogeneity *in vivo*, therefore grouping animals together and analysing overall means may mask variations between animals. However, in these H460 xenograft models, no such heterogeneity was observed, albeit a small sample size. Mean expression of mitochondrial proteins did have small differences between animals, but no significant differences were found (Figure 4.9).

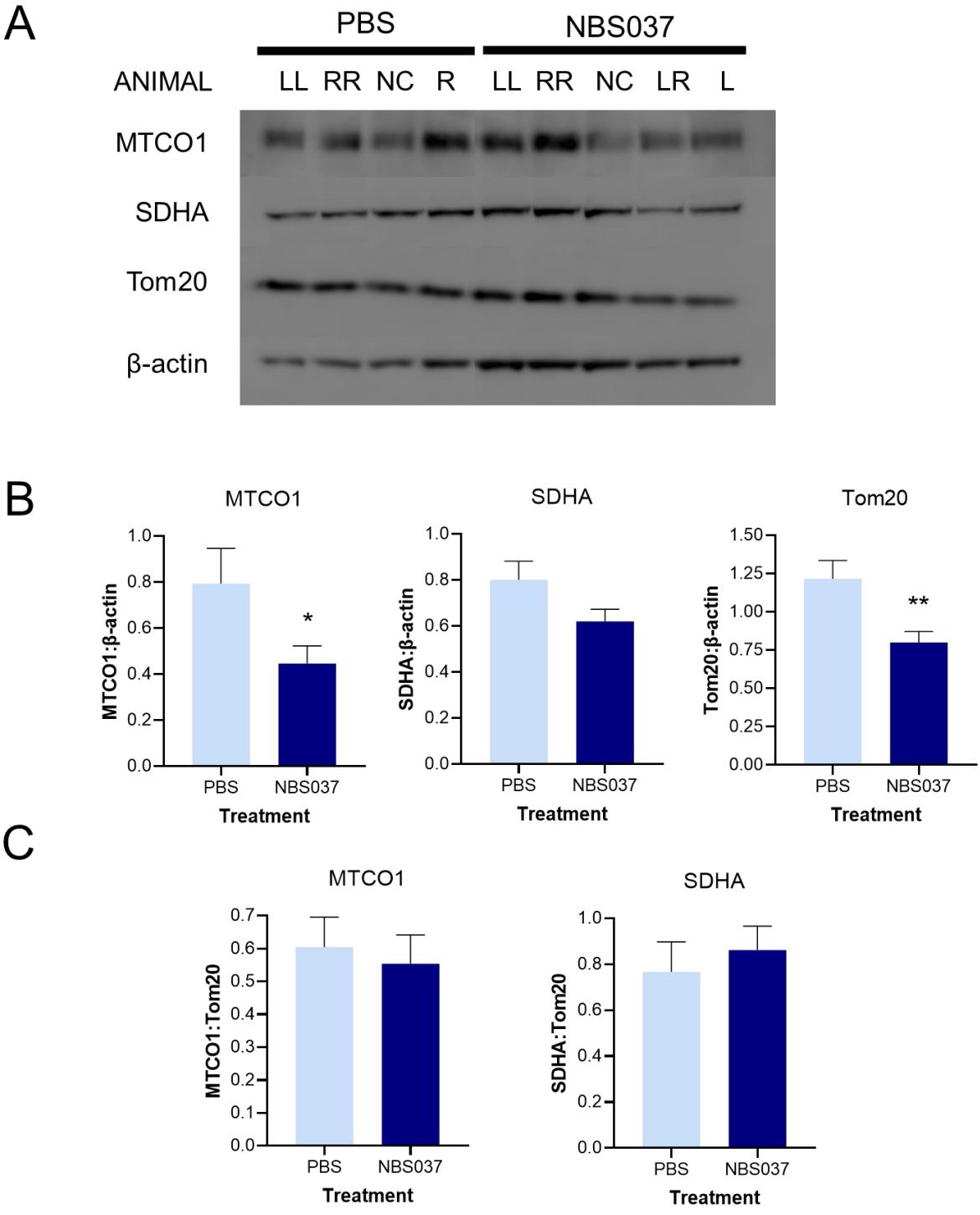

Figure 4.8. Mitochondrial protein expression in tumour lysates from PBS and NBS037 treated mice. *WB analysis was used to investigate the mitochondrial protein expression in tumour lysates from PBS (n=4) and NBS037 (n=5) treated mice. Data is shown as (A) original blots from tissue lysates, with different animals denoted by clips on the ears: NC (no clip), RR (two right), R (right), LL (two left), L (left), LR (left and right). (B) mean protein expression normalised to β-actin ± SEM, and (C) mean protein expression normalised to Tom20 ± SEM. Protein expression was quantified from blots using the G-box software. Statistical analysis was performed by unpaired t-tests to compare the means of each treatment group (*, $p < 0.05$; **, $p < 0.01$). N=3.*

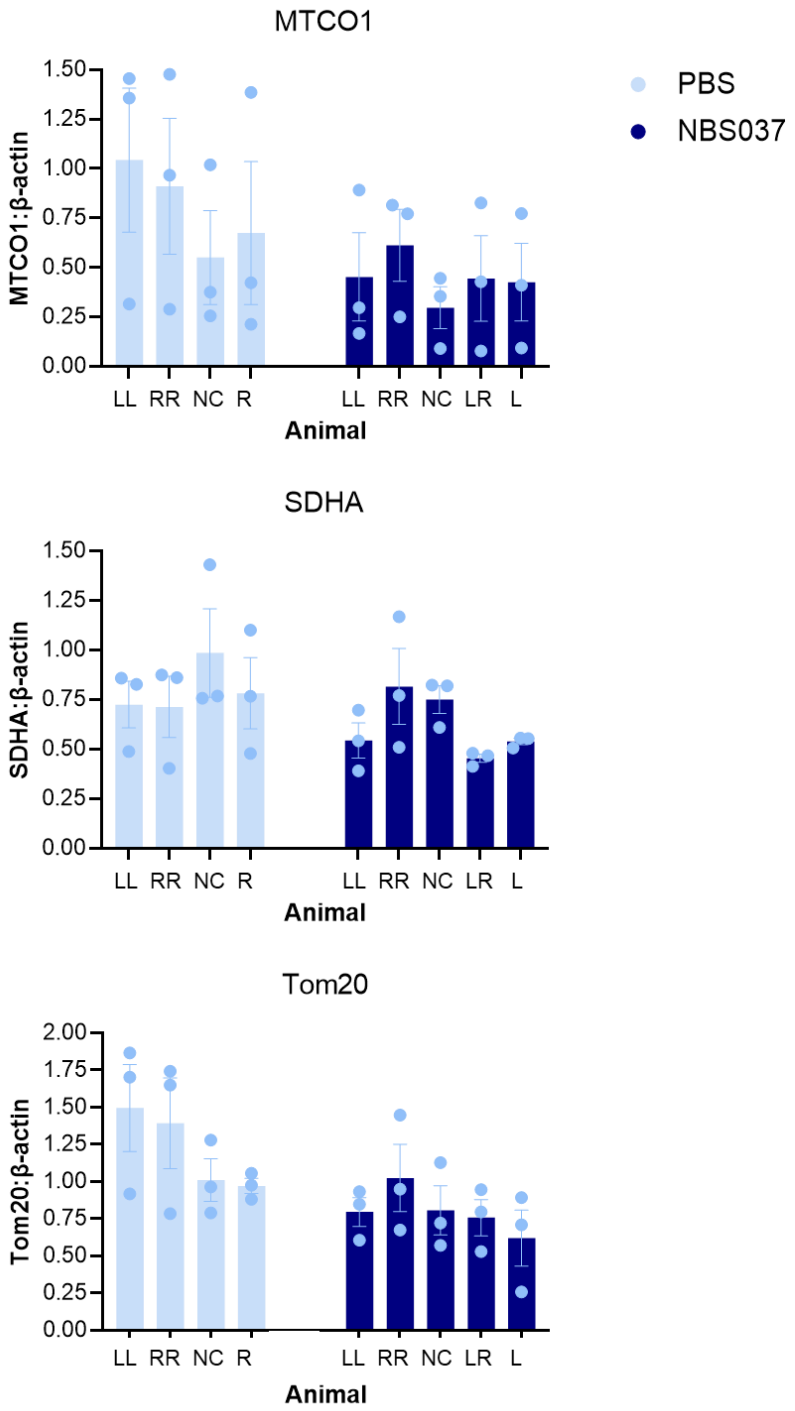

Figure 4.9. Tumours do not display heterogeneity in mitochondrial protein expression between animals. *WB analysis was used to investigate the mitochondrial protein expression in tumour lysates from PBS (n=4) and NBS037 (n=5) treated mice. Different animals were denoted by clips on the ears: NC (no clip), RR (two right), R (right), LL (two left), L (left), LR (left and right). Data is shown as mean protein expression normalised to β-actin ± SEM for each animal tested. Protein expression was quantified from blots using the G-box software. Statistical analysis was performed by two-way ANOVA with Tukey's post hoc multiple comparisons test to compare means between animals. N=3.*

4.8 NBS037 exerts no significant effects on antioxidant protein with the exception of liver

As an indication of REDOX status in the different tissues, SOD2 expression was measured in each tissue by WB (Figure 4.10A). SOD2 expression was quantified by intensity of each band and normalised to β-actin, the loading control (Figure 4.10B), or to mitochondrial mass due to its mitochondrial localisation (Figure 4.10C).

A significant decrease in SOD2 expression was observed in liver lysates from NBS037 treated animals ($p = 0.0016$) where SOD2 was decreased by 40.7% (Figure 4.10B). However, this change in SOD2 expression was proven to be due to the decrease in mitochondrial mass previously observed (Figure 4.7). When normalised to Tom20, SOD2 expression was no longer significantly different between PBS and NBS037 treated animals, and NBS037 treatment caused a 27.9% increase in SOD2 expression instead (Figure 4.10C).

Similarly, a modest increase in SOD2 expression was observed in brain and tumour tissue when normalised to mitochondrial mass (Figure 4.10C), however no changes proved to be statistically significant in any other tissue.

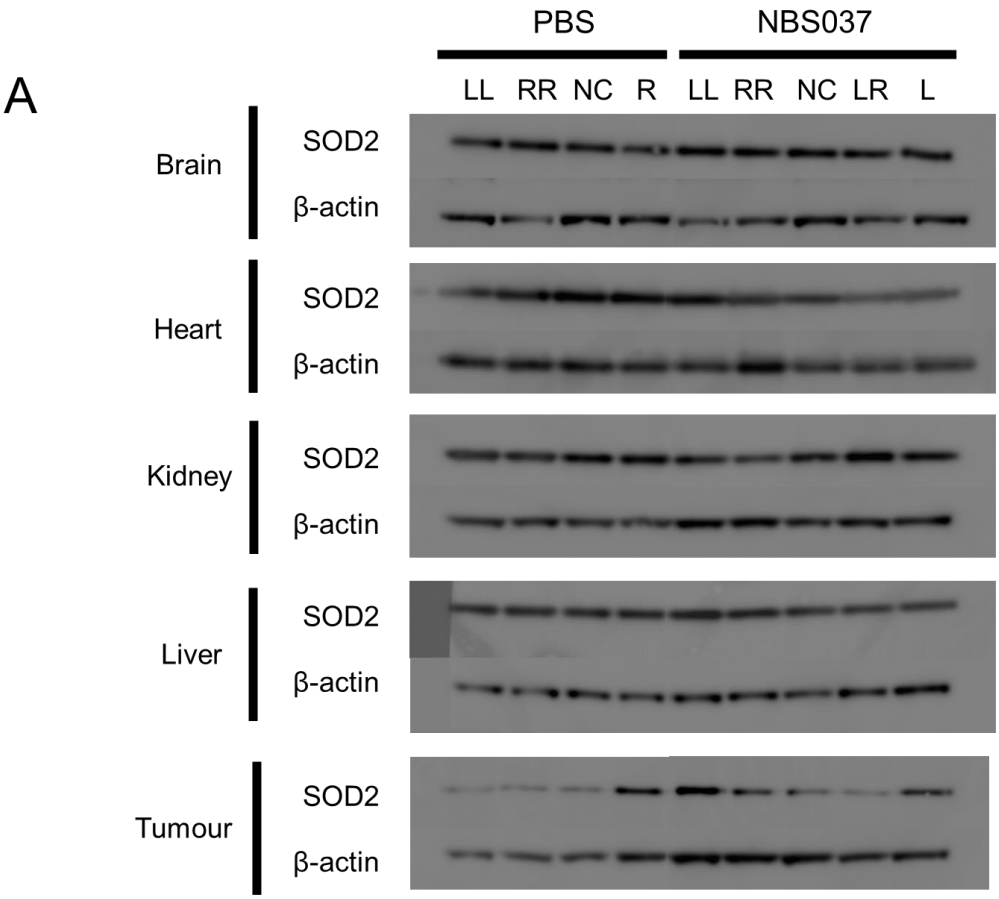
A
PBS
NBS037
LL RR NC R LL RR NC LR L
Brain
Heart
Kidney
Liver
Tumour
SOD2
β-actin

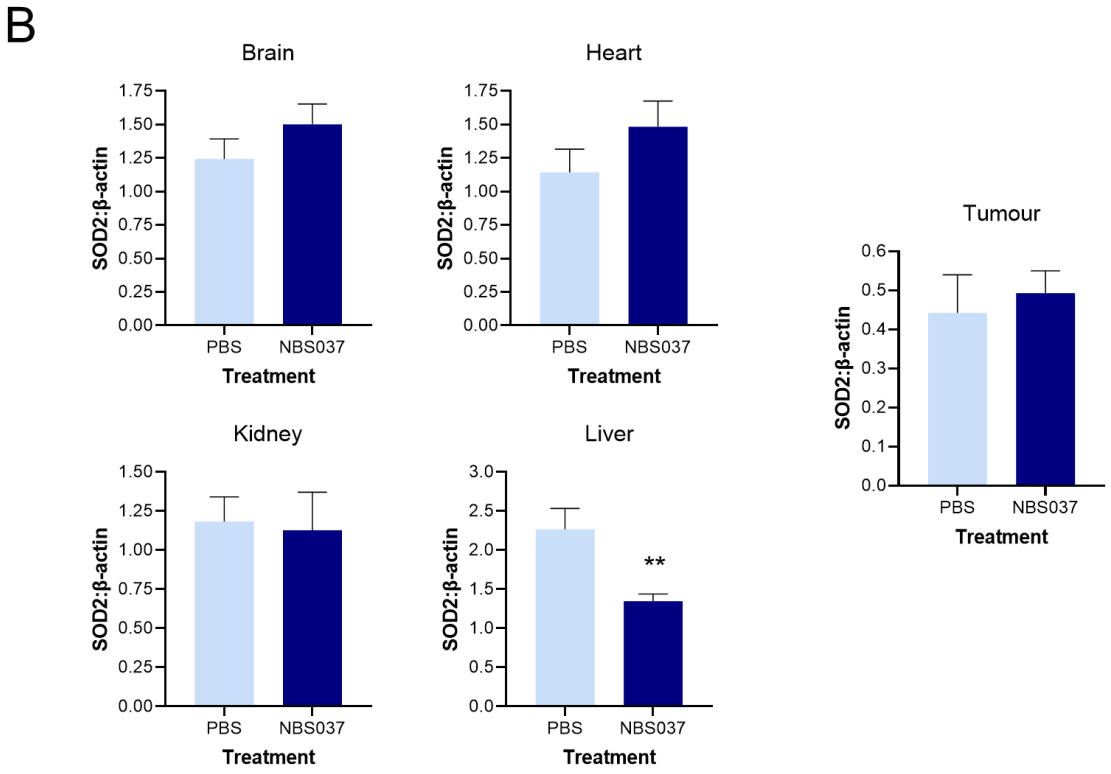
B
Brain
Heart
Kidney
Liver
Tumour
SOD2:β-actin
PBS
NBS037
Treatment
**

C

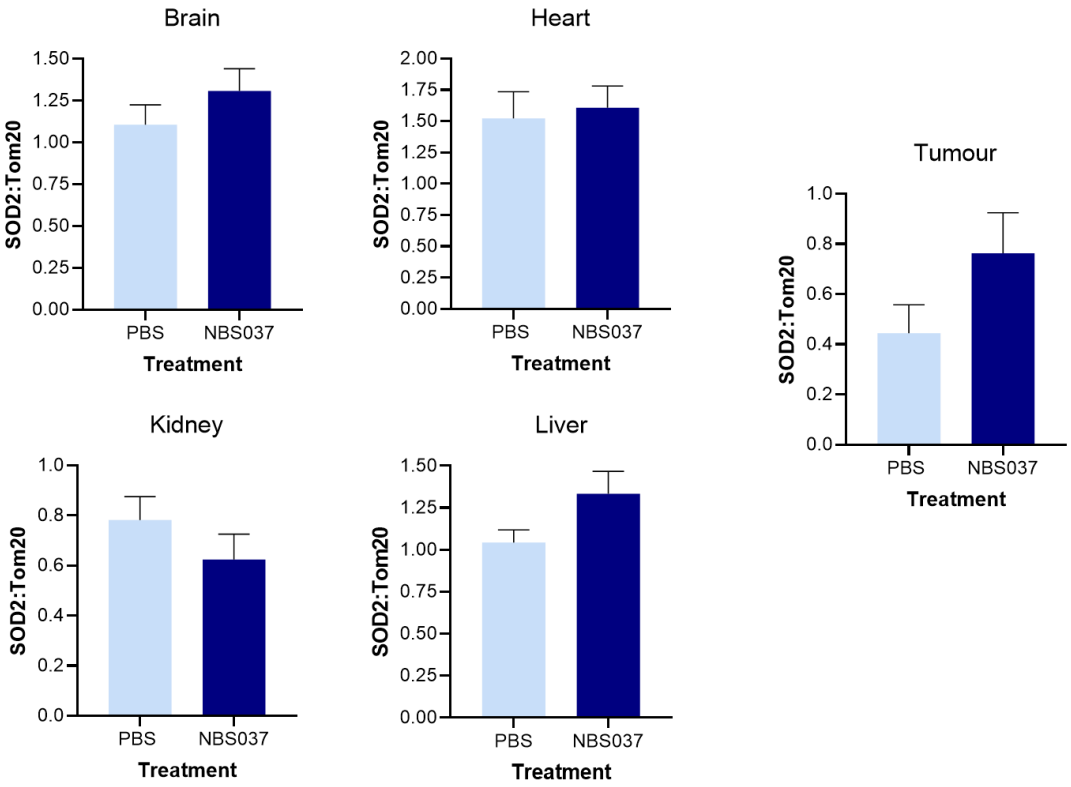

Figure 4.10. SOD2 expression in tissue lysates from PBS and NBS037 treated mice. *WB analysis was used to investigate the SOD2 protein expression in tissue lysates from PBS (n=4) and NBS037 (n=5) treated mice. Data is shown as (A) original blots from tissue lysates, with different animals denoted by clips on the ears: NC (no clip), RR (two right), R (right), LL (two left), L (left), LR (left and right). (B) represents mean SOD2 expression normalised to β-actin ± SEM, and (C) mean SOD2 expression normalised to Tom20 ± SEM. Protein expression was quantified from blots using the G-box software. Statistical analysis was performed by unpaired t-tests to compare the means of different treatment groups (**, p < 0.01). N=3.*

4.9 Normal tissues show no clear evidence of change in cell death with NBS037 treatment

To ensure NBS037 does not cause toxicity in normal tissues, which would lead to adverse effects upon a longer duration of treatment, the TUNEL assay was utilised to stain for cell death. In the late stages of apoptosis, DNA is fragmented and these fragments are able to bind modified dUTPs (EdUTP). Through a copper (I) catalysed reaction between the alkyne group on EdUTP and a fluorophore conjugated azide, DNA fragmentation can be detected through fluorescence. DNAse I acts to fragment the DNA in the sample, and provides a positive control (Figure 4.11A and 4.12A), where positive staining is visualised as bright red punctae which are not always localised to the nucleus of cells.

Heart (Figure 4.11), kidney (Figure 4.12), and liver (Figure 4.13) tissue all showed positive staining for fragmented DNA, indicative of the normal process of apoptosis. Qualitative analysis of images suggest no difference in apoptosis between PBS and NBS037 treated mice in normal tissues.

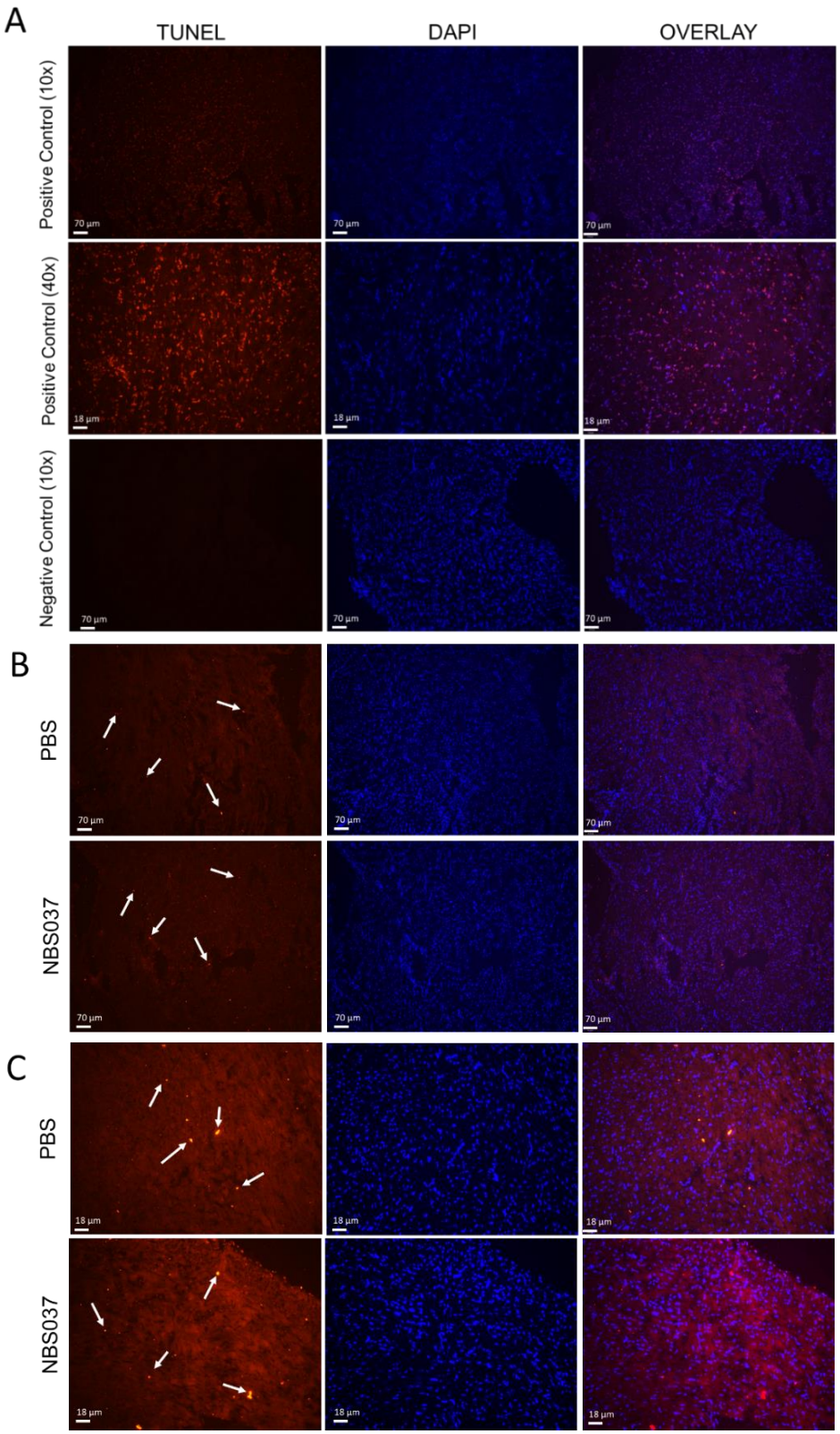

Figure 4.11. TUNEL staining for apoptosis in heart tissue. *The TUNEL assay was utilised to stain for fragmented DNA in the late stages of apoptosis in heart tissue from mice treated with PBS or NBS037 (red). Nuclei were visualised by DAPI present in the mounting media (blue). (A) shows positive controls (DNAse I addition) and negative controls (no primary antibody). Images were taken with a Leica upright microscope at (B) 10x and (C) 40x magnification. All images were subjected to the same exposure. White arrows indicate examples of positive staining (bright red punctae). Data is representative of duplicate sections in one PBS and one NBS037 treated animal.*

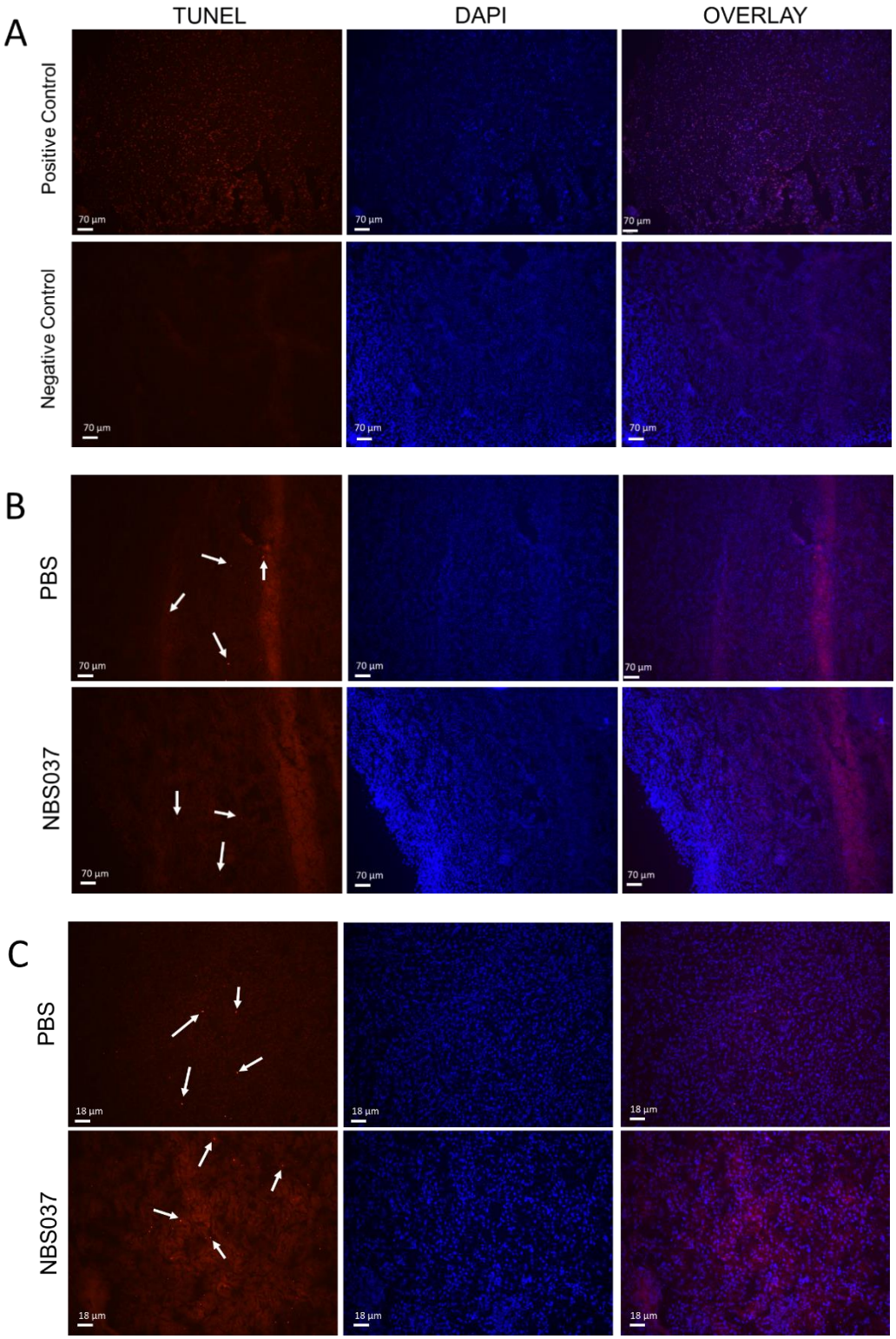

Figure 4.12. TUNEL staining for apoptosis in kidney tissue. *The TUNEL assay was utilised to stain for fragmented DNA in the late stages of apoptosis in kidney tissue from mice treated with PBS or NBS037 (red). Nuclei were visualised by DAPI present in the mounting media (blue). (A) shows positive controls (DNAse I addition) and negative controls (no primary antibody). Images were taken with a Leica upright microscope at (B) 10x and (C) 40x magnification. All images were subjected to the same exposure. White arrows indicate examples of positive staining (bright red punctae). Data is representative of duplicate sections in one PBS and one NBS037 treated animal.*

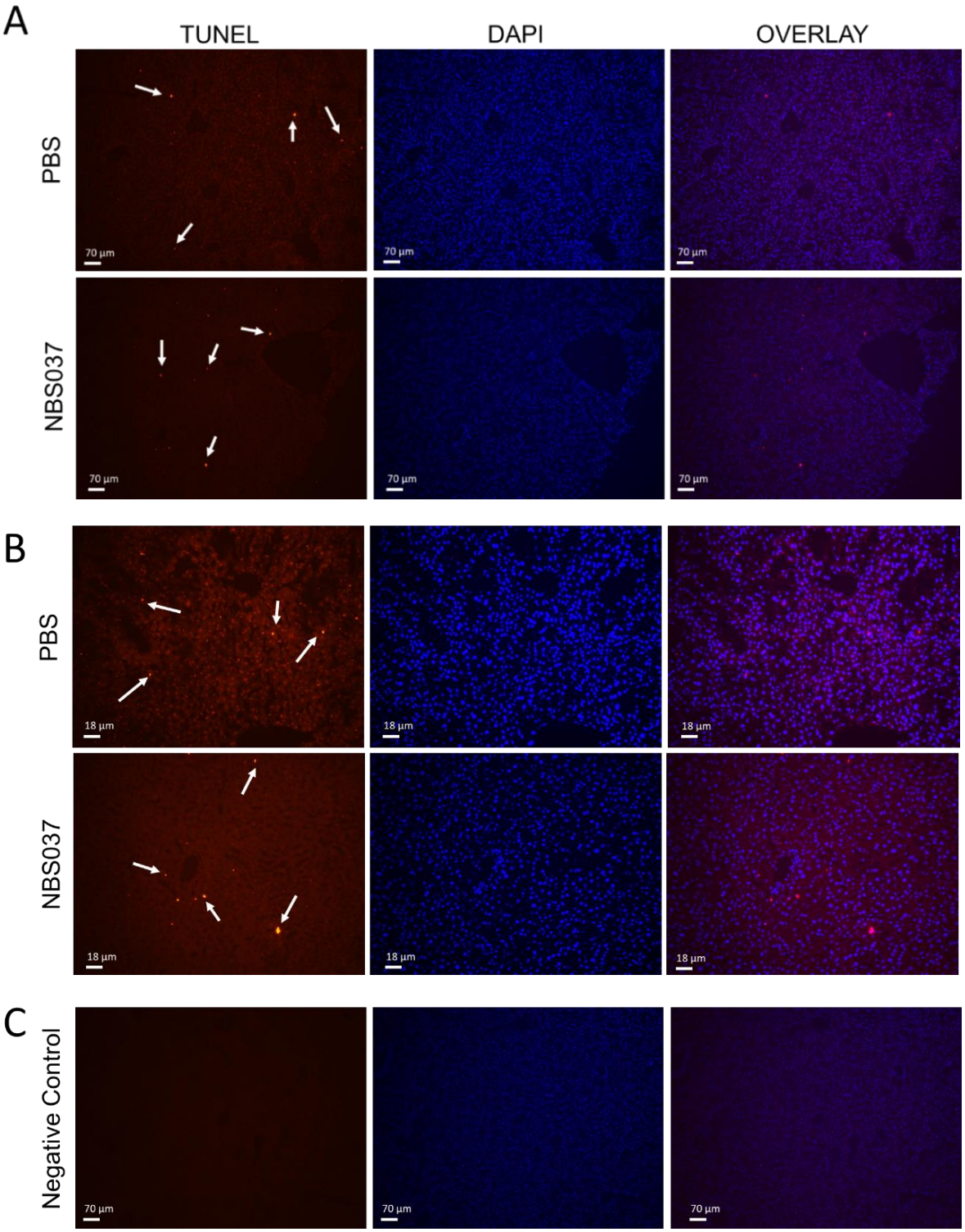

Figure 4.13. TUNEL staining for apoptosis in liver tissue. *The TUNEL assay was utilised to stain for fragmented DNA in the late stages of apoptosis in liver tissue from mice treated with PBS or NBS037 (red). Nuclei were visualised by DAPI present in the mounting media (blue). Images were taken with a Leica upright microscope at (A) 10x and (B) 40x magnification. Negative controls with no primary antibody staining were also included at 10x magnification (C). All images were subjected to the same exposure. White arrows indicate examples of positive staining (bright red punctae). Data is representative of duplicate sections in one PBS and one NBS037 treated animal.*

4.10 Cell death is increased in tumour, with differences observed between periphery and core of tumour

Initial experiments in mouse models by Dr Hulit in showed tumour delay with NBS037 treatment but failed to reach significance. To identify if there were any effects due to cell death, the TUNEL assay was repeated in tumour tissue from both the outer layers of the tumours (Figure 4.14A and B) and the centre of the tumour (Figure 4.14C and D). In the outer tumour sections, no clear difference in apoptosis between PBS and NBS037 tumours were observed; however, there was far greater positive staining in the outer tumour than in normal cells, both greater in intensity and area covered. Under 40x magnification, this was shown by bleaching of the entirety of the cell (Figure 4.14B).

When analysing sections from the centre of the tumour, positive staining was localised in more discreet areas and was not ubiquitously expressed (Figure 4.14C and D). A greater area of positive staining was observed in NBS037 treated sections of central tumour compared to PBS treated tumour (Figure 4.14C). Again, these DNA fragments were not always localised to the nucleus and could be indicative of mtDNA fragments which could be confirmed by quantitative polymerase chain reaction.

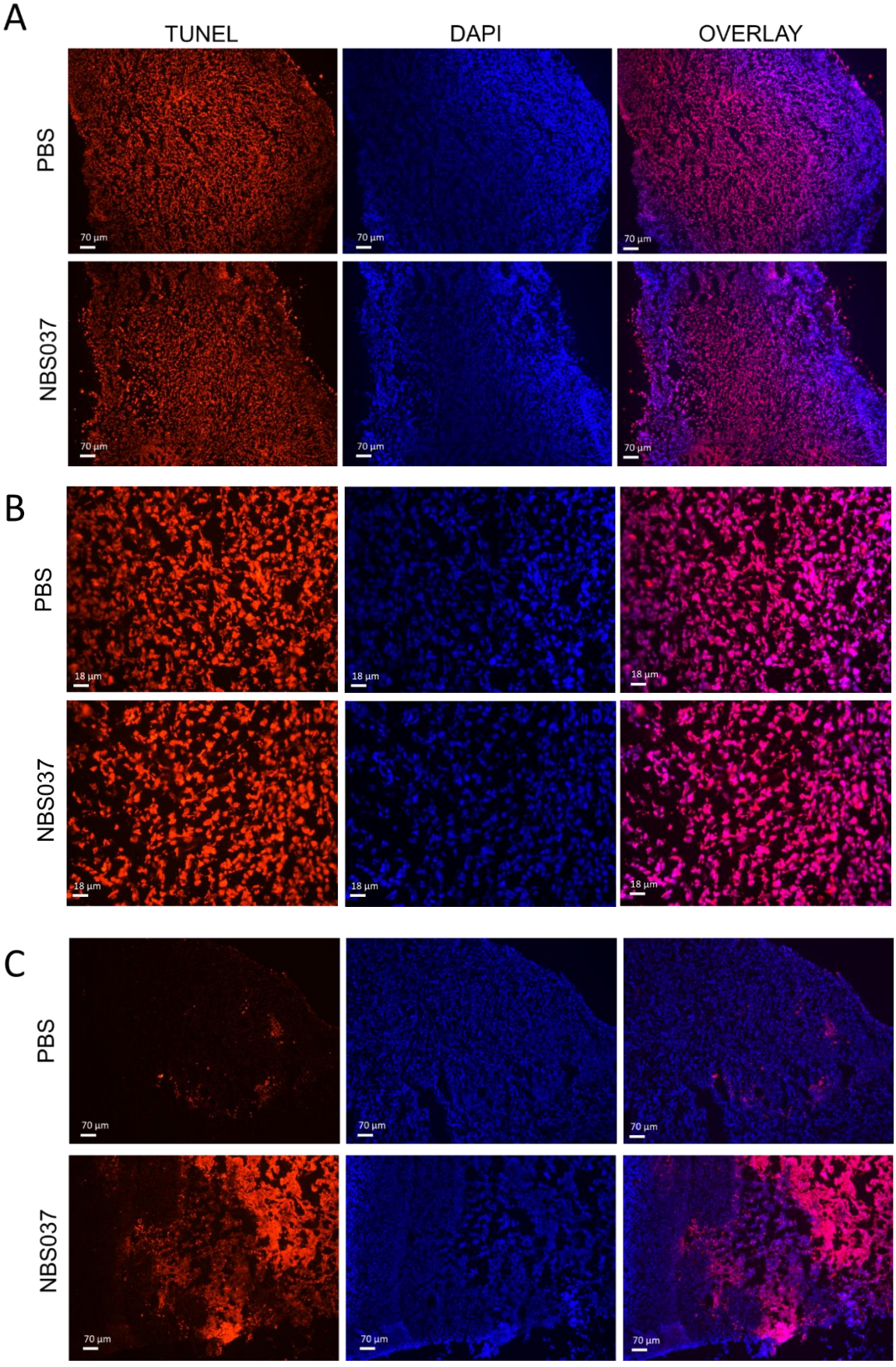
A
TUNEL
DAPI
OVERLAY
PBS
NBS037
70 µm
B
PBS
NBS037
18 µm
C
PBS
NBS037
70 µm

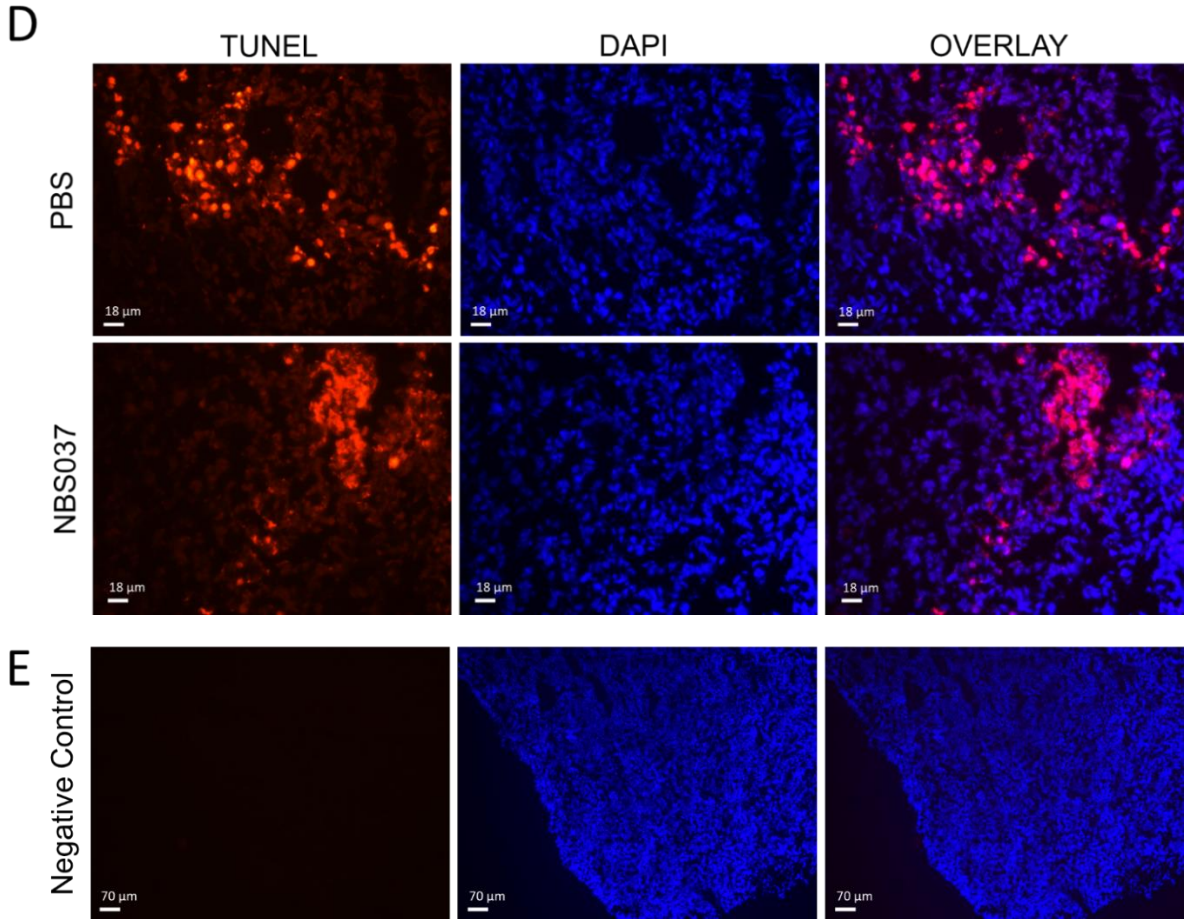

Figure 4.14. TUNEL staining for apoptosis in tumour tissue. *The TUNEL assay was utilised to stain for fragmented DNA in the late stages of apoptosis in tumour tissue from mice treated with PBS or NBS037 (red). Nuclei were visualised by DAPI present in the mounting media (blue). Images were taken with a Leica upright microscope at (A) 10x and (B) 40x magnification in sections from the outer tumour. Images were collected at (C) 10x and (D) 40x magnification in sections from the centre of the tumour. Negative controls with no primary antibody staining were also included at 10x magnification (E). All images were subjected to the same exposure. White arrows indicate examples of positive staining (bright red punctae). Data is representative of duplicate sections in one PBS and one NBS037 treated animal.*

4.11 Normal tissues maintain markers for cell proliferation with NBS037 treatment

To identify any effects NBS037 may have on cell proliferation and tissue growth, immunofluorescence was used to detect Ki67, a nuclear protein involved in cell division and routinely found in actively proliferating cells. Heart (Figure 4.15), kidney (Figure 4.16) and liver (Figure 4.17) tissue all showed limited positive Ki67 staining, indicated by bright green punctae localised to the nuclei. Upon qualitative analysis of images, no difference was observed between tissues treated with PBS and NBS037. Heart tissue had fewer actively proliferating cells whilst kidney tissue had the most, so differences between tissues were observed.

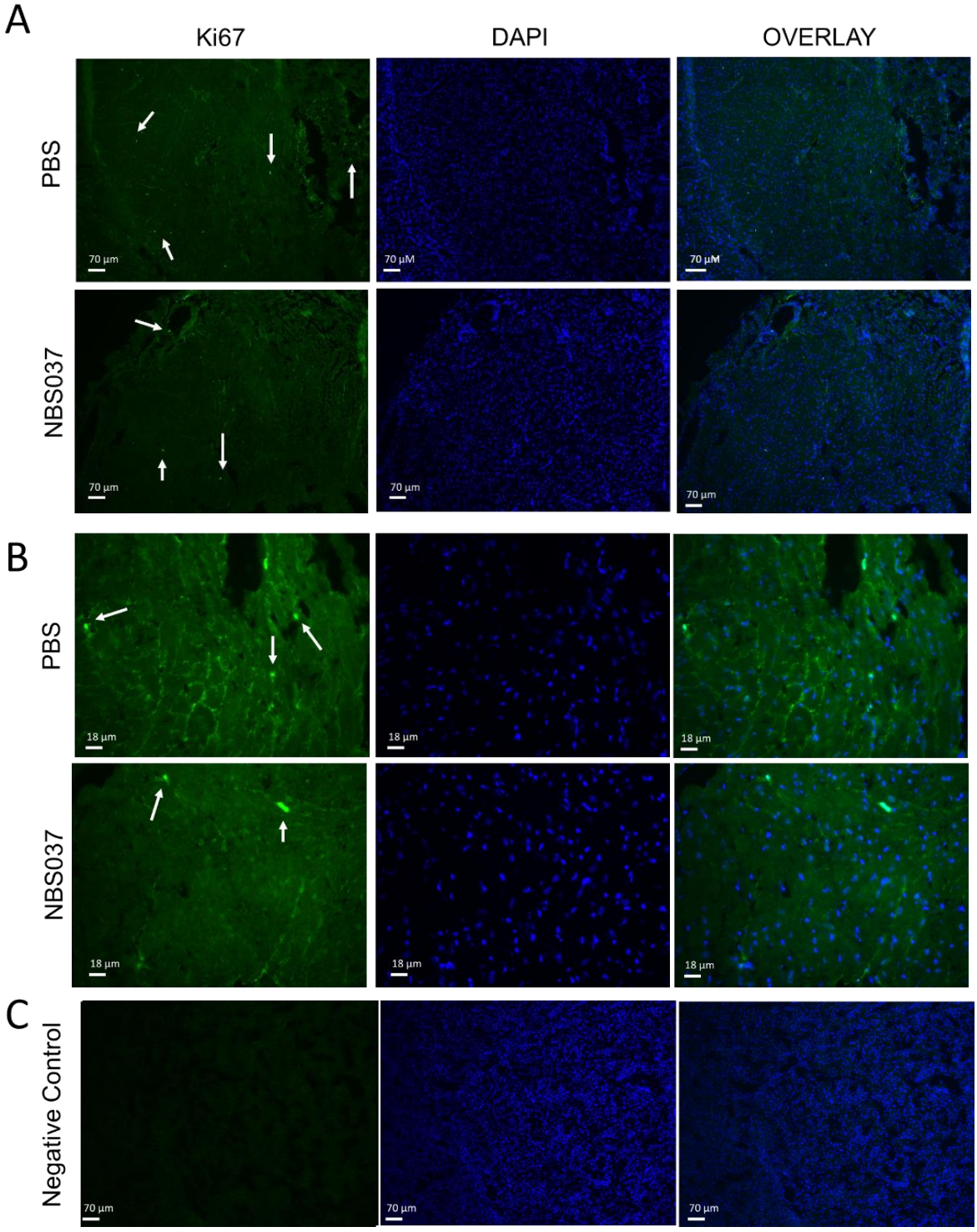

Figure 4.15. Ki67 staining for cell proliferation in heart tissue. *Ki67 was utilised to stain for cell proliferation in heart tissue from mice treated with PBS or NBS037 (green). Nuclei were visualised by DAPI present in the mounting media (blue). Images were taken with a Leica upright microscope at (A) 10x and (B) 40x magnification. Negative controls with no primary antibody staining were also included at 10x magnification (C). All images were subjected to the same exposure. White arrows indicate examples of positive staining (bright green punctae). Data is representative of duplicate sections in one PBS and one NBS037 treated animal.*

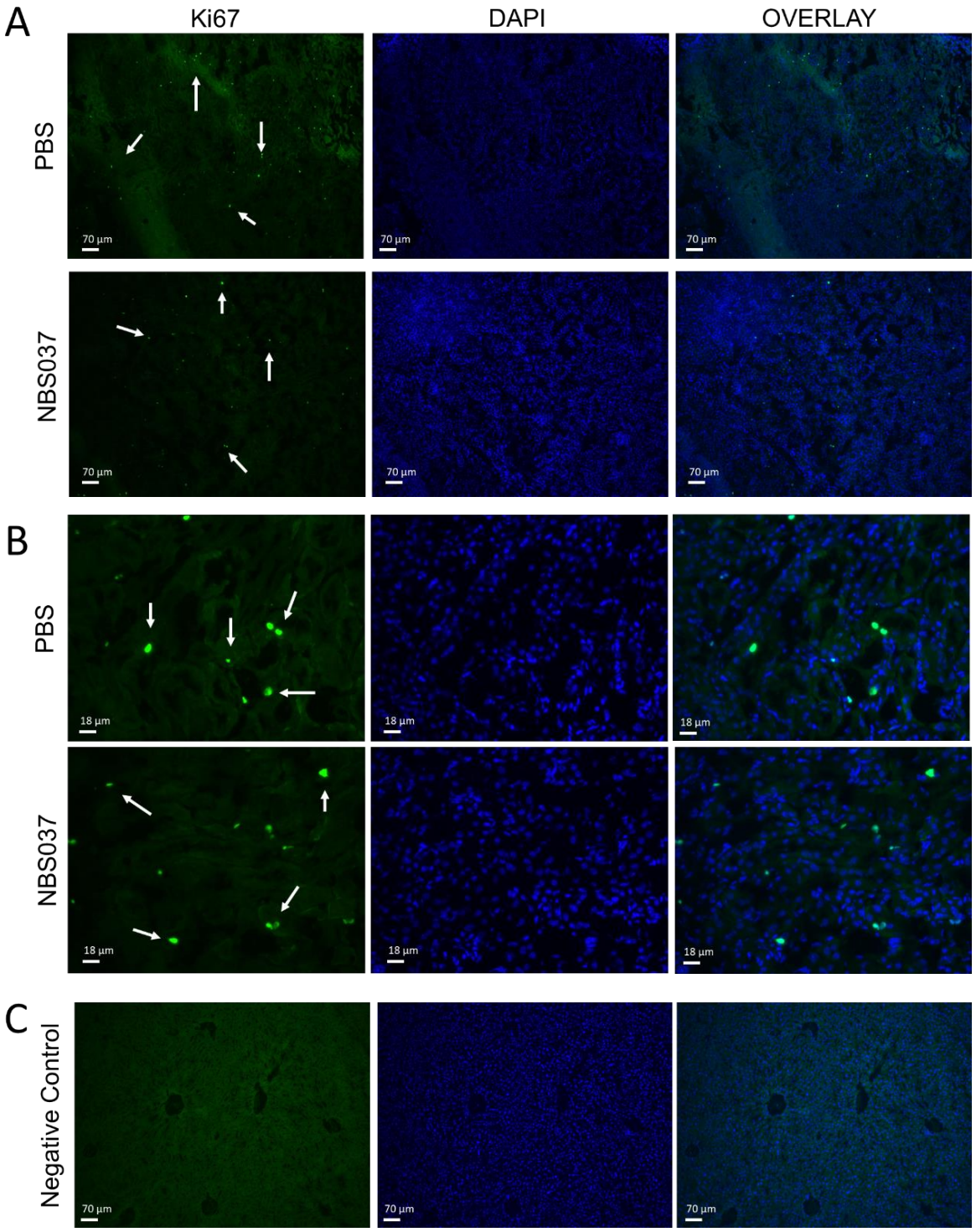

Figure 4.16. Ki67 staining for cell proliferation in kidney tissue. *Ki67 was utilised to stain for cell proliferation in kidney tissue from mice treated with PBS or NBS037 (green). Nuclei were visualised by DAPI present in the mounting media (blue). Images were taken with a Leica upright microscope at (A) 10x and (B) 40x magnification. Negative controls with no primary antibody staining were also included at 10x magnification (C). All images were subjected to the same exposure. White arrows indicate examples of positive staining (bright green punctae). Data is representative of duplicate sections in one PBS and one NBS037 treated animal.*

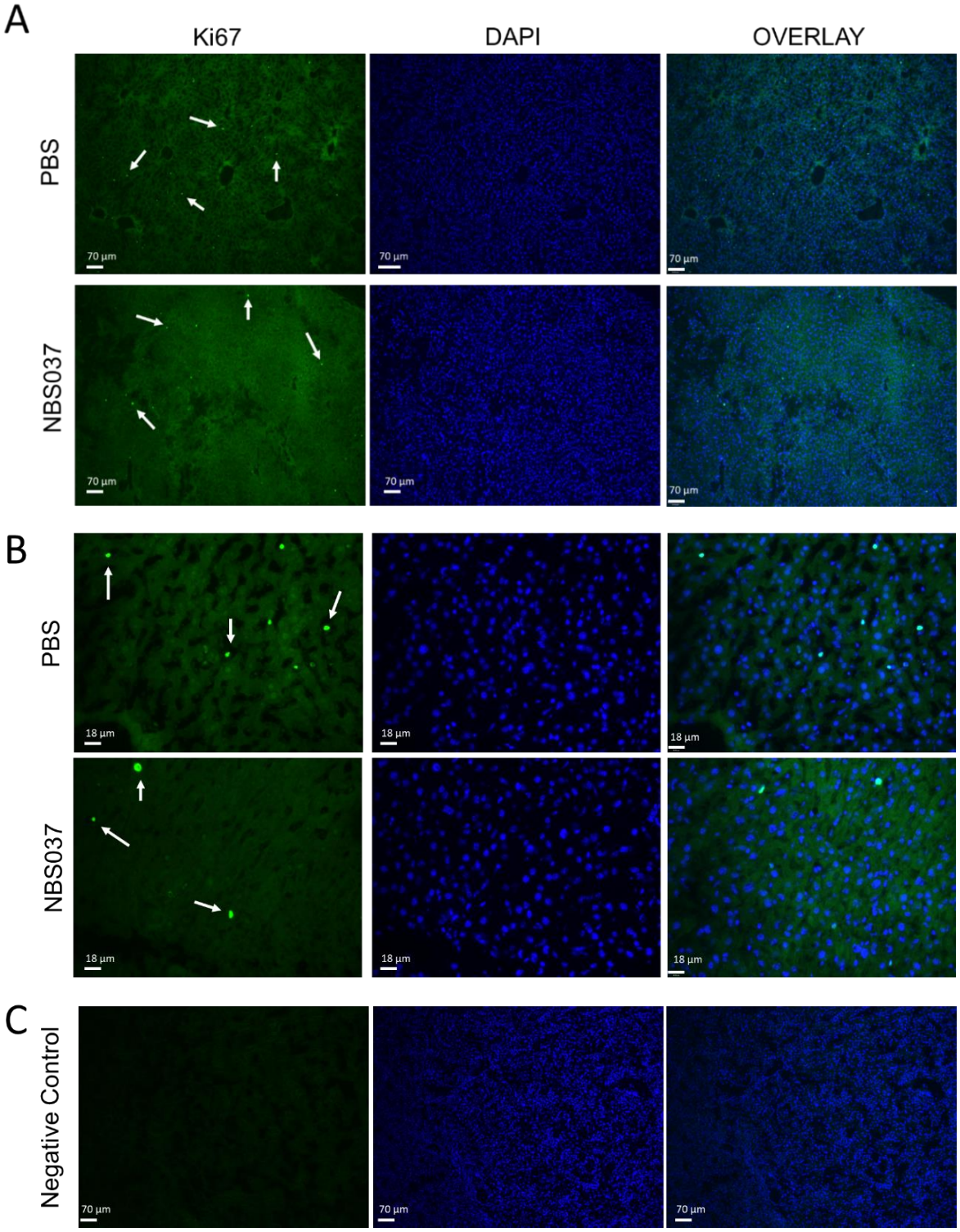

Figure 4.17. Ki67 staining for cell proliferation in liver tissue. *Ki67 was utilised to stain for cell proliferation in liver tissue from mice treated with PBS or NBS037 (green). Nuclei were visualised by DAPI present in the mounting media (blue). Images were taken with a Leica upright microscope at (A) 10x and (B) 40x magnification. Negative controls with no primary antibody staining were also included at 10x magnification (C). All images were subjected to the same exposure. White arrows indicate examples of positive staining (bright green punctae). Data is representative of duplicate sections in one PBS and one NBS037 treated animal.*

4.12 Cell proliferation is upregulated in tumour compared to normal tissues, but is unaffected by NBS037 treatment

Ki67 was examined in tumour tissue from both the outer tumour (Figure 4.18A and B) and centre of the tumour (Figure 4.18C and D). Whilst no visible difference was observed between tissues which received PBS or NBS037, a higher number of cells stained positive for Ki67 compared to normal tissue, regardless of whether tissue was at the periphery or centre of the tumour.

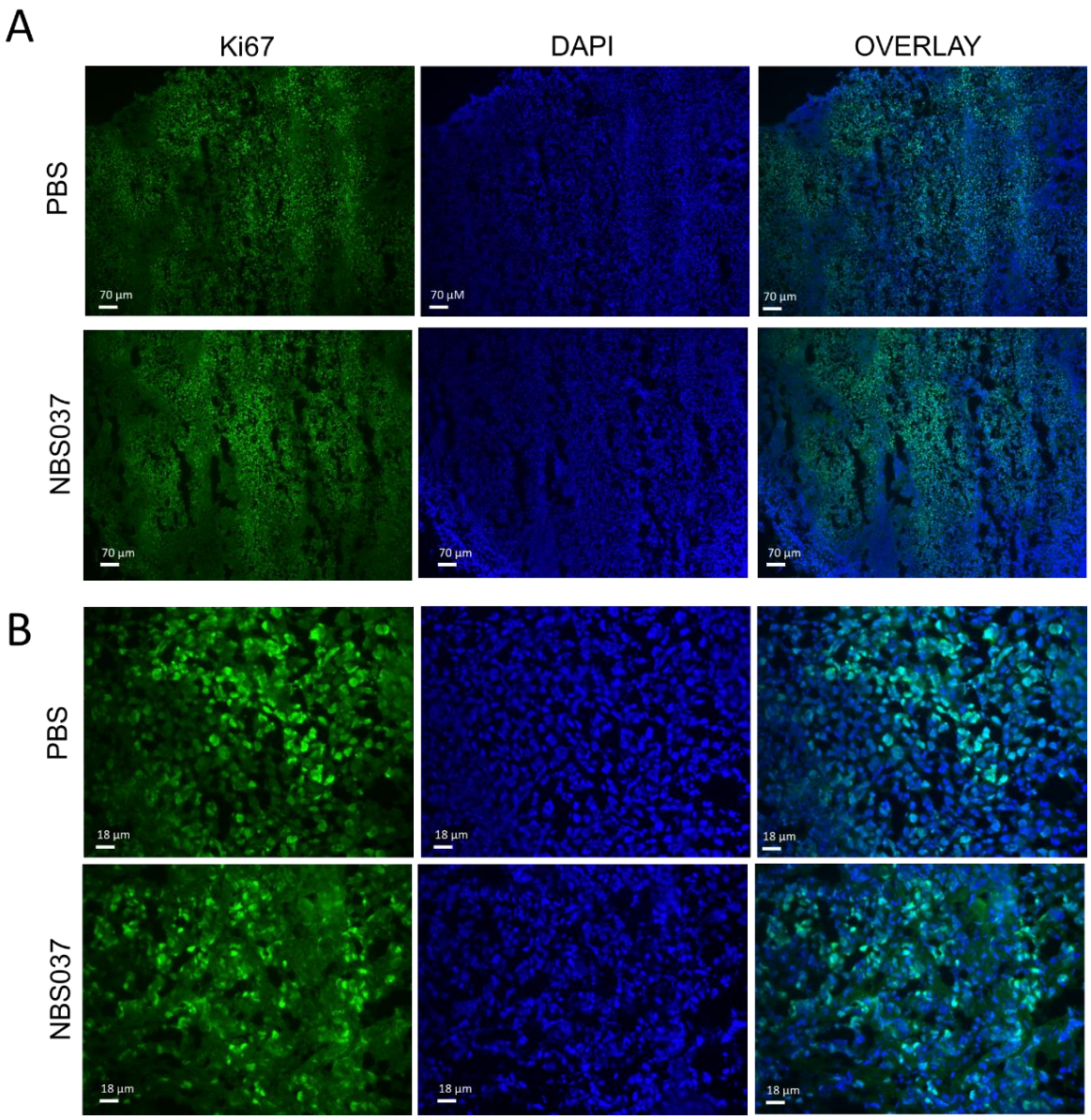

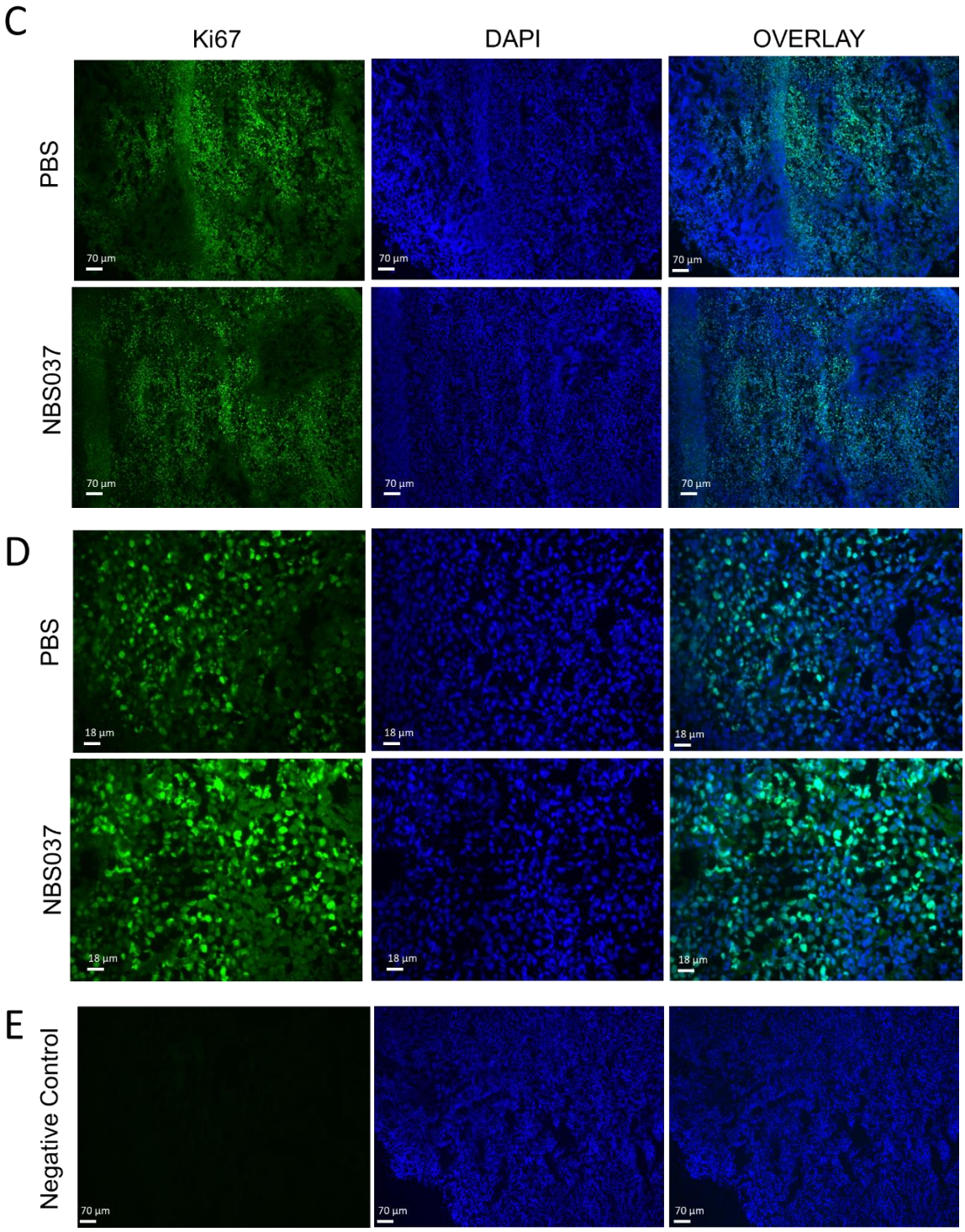

Figure 4.18. Ki67 staining for cell proliferation in tumour tissue. *Ki67 was utilised to stain for cell proliferation in tumour tissue from mice treated with PBS or NBS037 (green). Nuclei were visualised by DAPI present in the mounting media (blue). Images were taken with a Leica upright microscope at (A) 10x and (B) 40x magnification in sections from the outer tumour. Images were collected at (C) 10x and (D) 40x magnification in sections from the centre of the tumour. Negative controls with no primary antibody staining were also included at 10x magnification (E). All images were subjected to the same exposure. White arrows indicate examples of positive staining (bright green punctae). Data is representative of N=3.*

4.13 CD31 staining indicates vasculature is localised around the periphery of the tumour

To investigate whether NBS037 induced effects may be limited by poor vascularisation and poor drug delivery, tissues were stained for CD31, a protein expressed on endothelial cells and a common marker for vasculature differentiation.

In tumour sections from the outer sections of tumour (Figure 4.19 A and B) and inner sections of tumour (Figure 4.19 and D), positive staining for CD31 was observed. A heavier density of positive staining was localised around the periphery of the tumour sections, whilst in the centre of the sections, fewer cells with positive staining were detected (Figure 4.19B). Positive CD31 staining was detected in both PBS and NBS037 treated tissues.

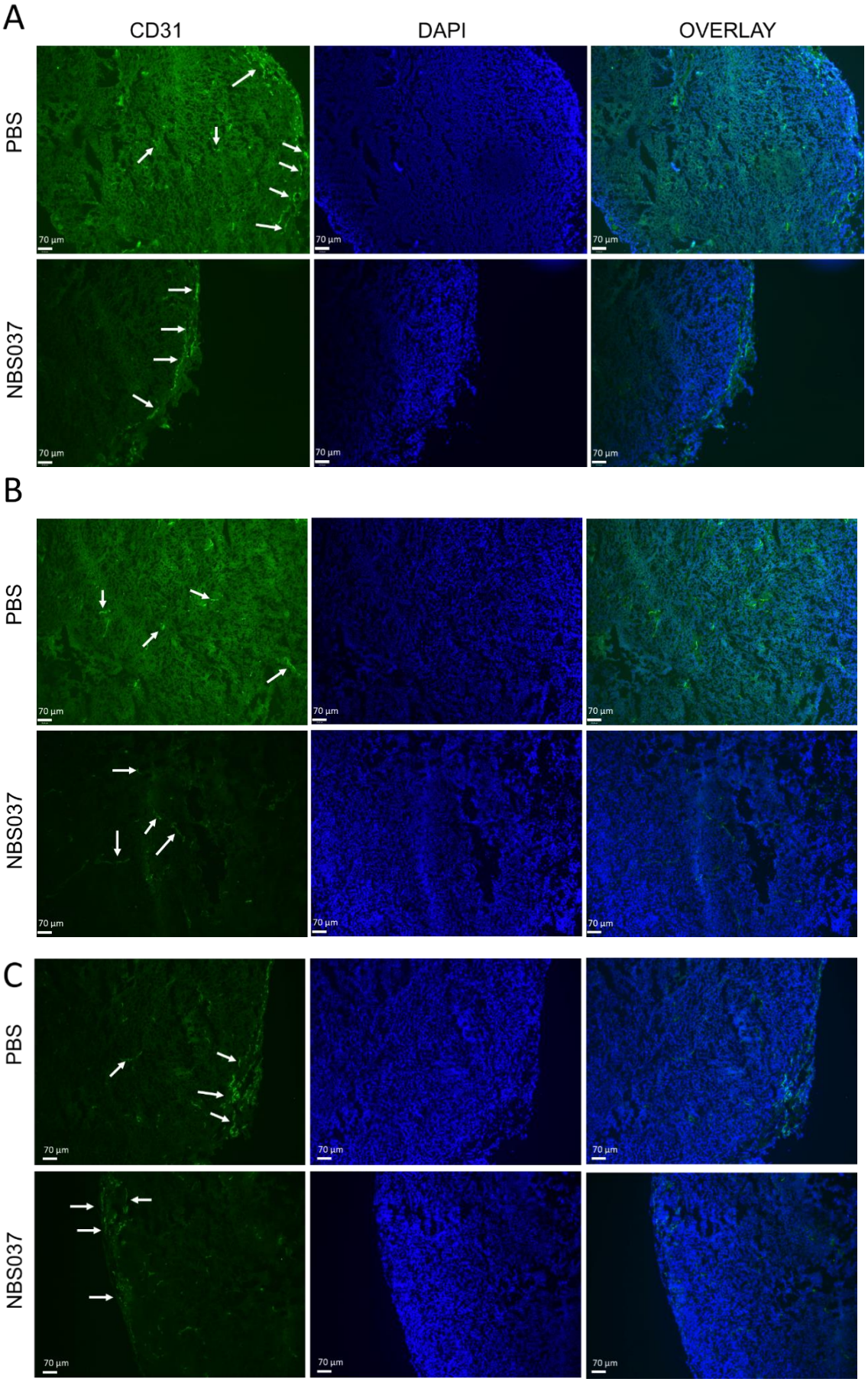
A
CD31
DAPI
OVERLAY
PBS
NBS037
B
PBS
NBS037
C
PBS
NBS037
70 µm

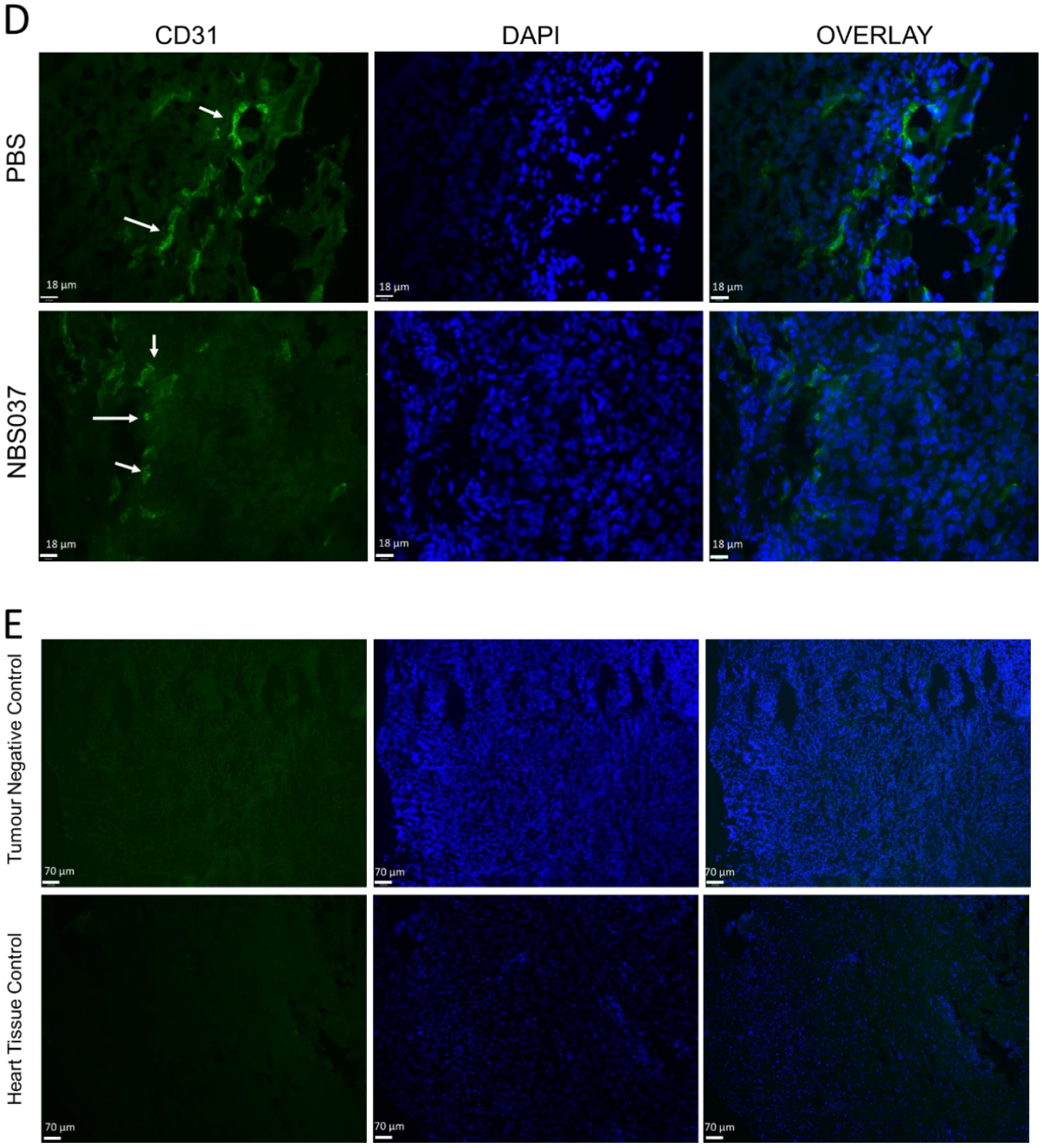

Figure 4.19. CD31 staining for endothelial markers in tumour tissue. *CD31 was utilised to stain for endothelial cells in tumour tissue from mice treated with PBS or NBS037 (green). Nuclei were visualised by DAPI present in the mounting media (blue). Images were taken with a Leica upright microscope at 10x magnification in sections from the outer tumour (A and B). Images were collected at (C) 10x and (D) 40x magnification in sections from the centre of the tumour. Negative controls with no primary antibody staining or negative tissue controls were also included at 10x magnification (E). All images were subjected to the same exposure. White arrows indicate examples of positive staining (bright green areas). Data is representative of N=2.*

4.14 Minimal 8-OHdG staining is observed in normal tissue

To validate that NBS037 has limited ROS generating effects, tissues were stained for 8-hydroxy-2'-deoxyguanosine (8-OHdG), the predominant form of ROS induced oxidative damage in both DNA and mtDNA. To gain a section wide-evaluation of ROS, 10x magnification was utilised; however, no positive staining was detected in heart (Figure 4.20A), kidney (Figure 4.21A), or liver (Figure 4.22A) at this magnification. At 40x magnification, evidence of positive staining was observed in heart (Figure 4.20B), kidney (Figure 4.21B), and liver (Figure 4.21B) through bright punctae in the cytoplasm of cells although the magnification was still limited. There is seemingly no difference between PBS and NBS037 treated kidney and liver tissue. In heart tissue however, NBS037 treated tissue had greater areas of positive staining, indicative this tissue may be experiencing higher levels of ROS.

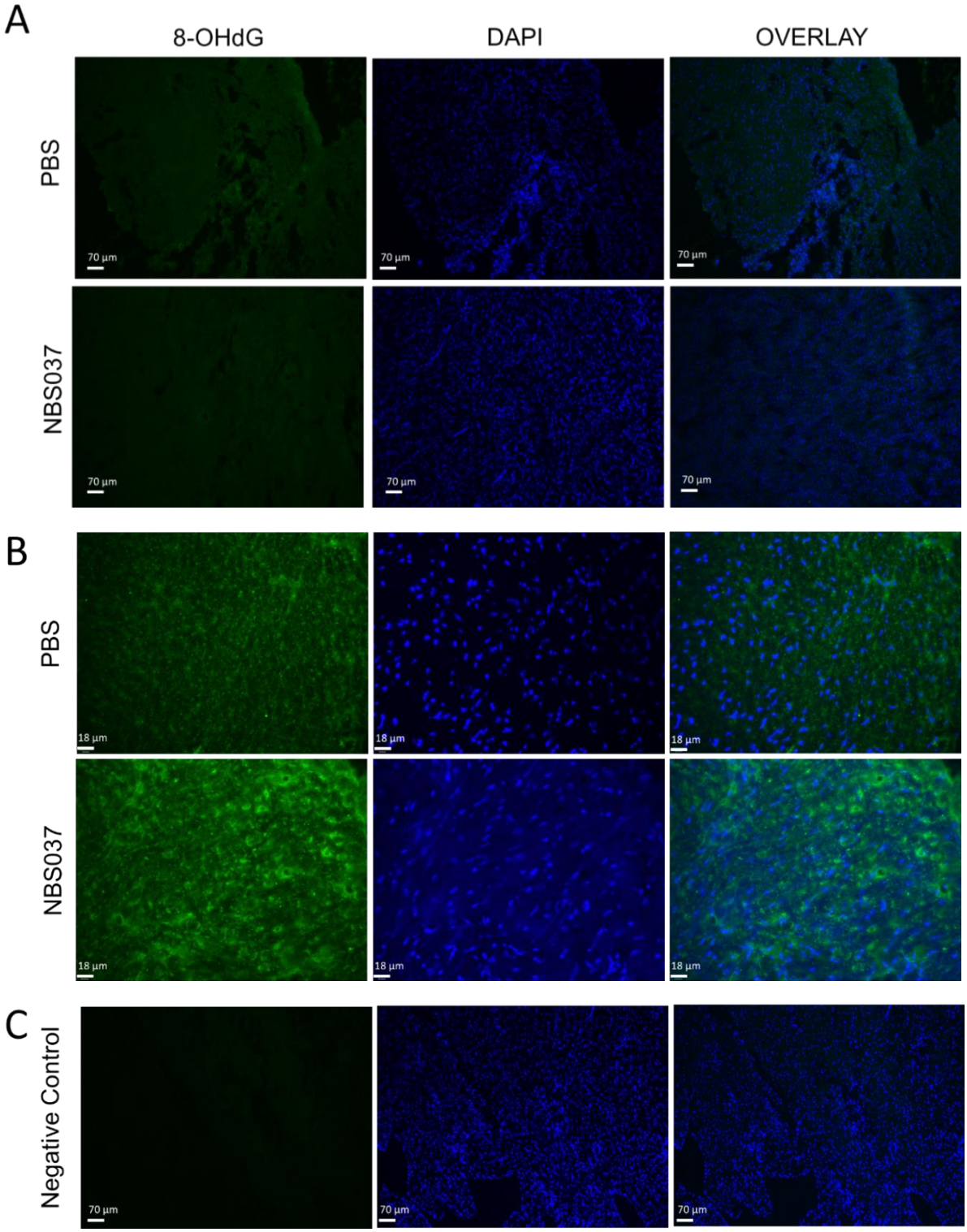

Figure 4.20. 8-OHdG staining for ROS in heart tissue. *8-OHdG was utilised to stain for ROS in heart tissue from mice treated with PBS or NBS037 (green). Nuclei were visualised by DAPI present in the mounting media (blue). Images were taken with a Leica upright microscope at (A) 10x and (B) 40x magnification. Negative controls with no primary antibody staining were also included at 10x magnification (C). All images were subjected to the same exposure. Data is representative of duplicate sections in one PBS and one NBS037 treated animal.*

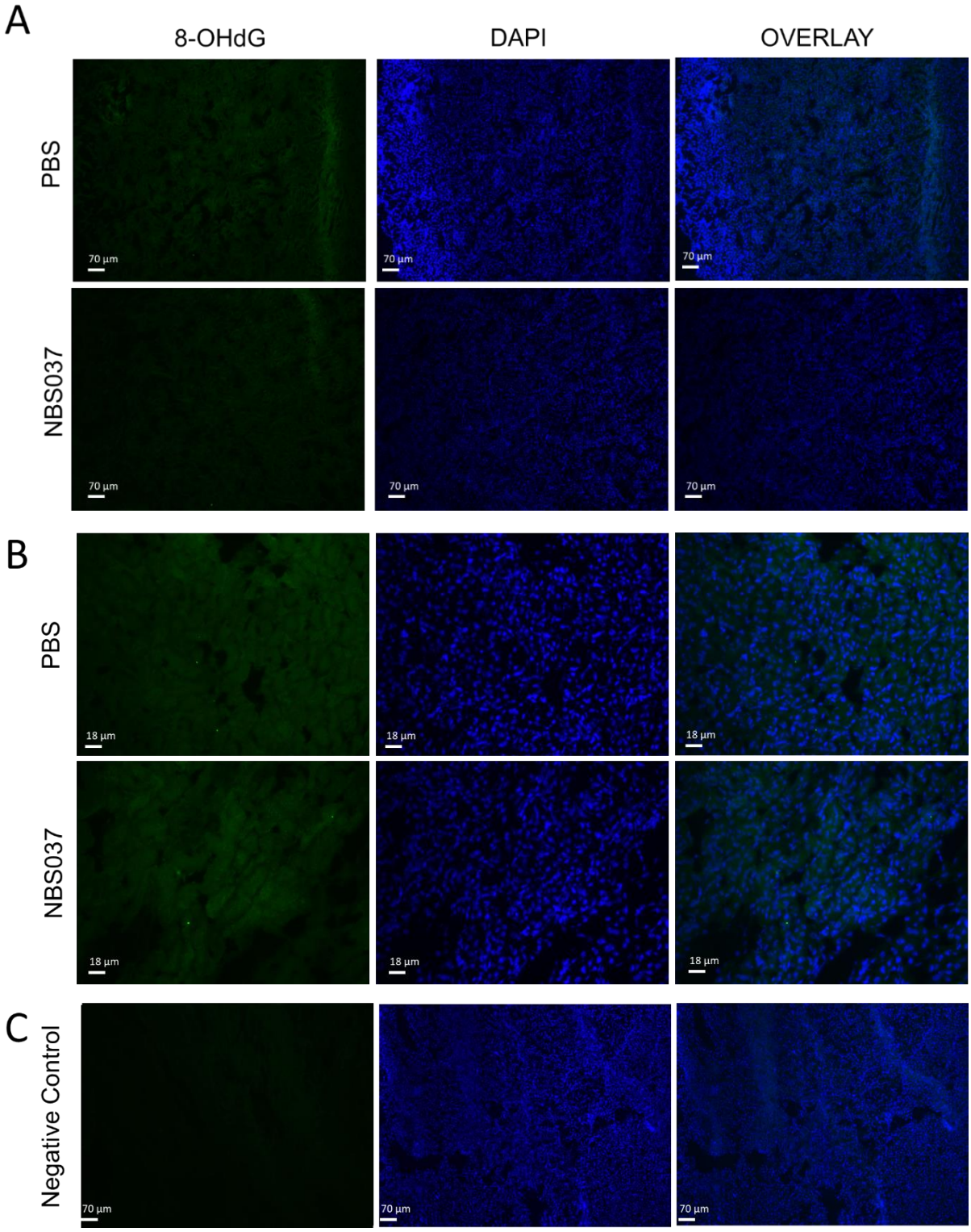

Figure 4.21. 8-OHdG staining for ROS in kidney tissue. *8-OHdG was utilised to stain for ROS in kidney tissue from mice treated with PBS or NBS037 (green). Nuclei were visualised by DAPI present in the mounting media (blue). Images were taken with a Leica upright microscope at (A) 10x and (B) 40x magnification. Negative controls with no primary antibody staining were also included at 10x magnification (C). All images were subjected to the same exposure. Data is representative of duplicate sections in one PBS and one NBS037 treated animal.*

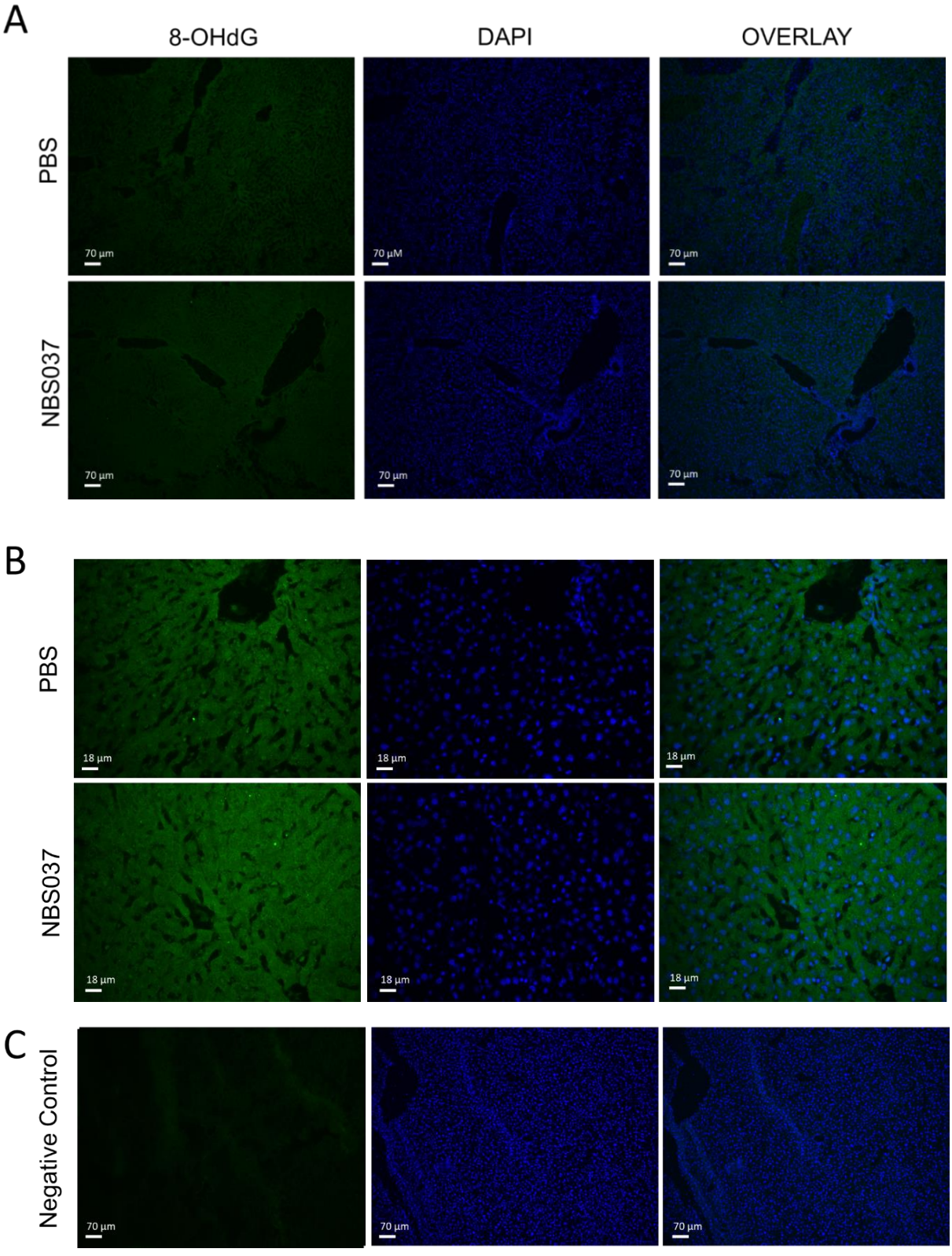

Figure 4.22. 8-OHdG staining for ROS in liver tissue. *8-OHdG was utilised to stain for ROS in liver tissue from mice treated with PBS or NBS037 (green). Nuclei were visualised by DAPI present in the mounting media (blue). Images were taken with a Leica upright microscope at (A) 10x and (B) 40x magnification. Negative controls with no primary antibody staining were also included at 10x magnification (C). All images were subjected to the same exposure. Data is representative of duplicate sections in one PBS and one NBS037 treated animal.*

4.15 Tumours have upregulated ROS compared to normal tissue, but little change is observed with NBS037 treatment

Tumour tissue was stained for 8-OHdG as an indicator of any drug induced changes in ROS or oxidative stress (Figure 4.23). Both PBS and NBS037 treated tumour tissue showed brighter staining than observed with normal tissues, with brighter staining localised to distinct areas within the tumour (Figure 4.23A). At 40x magnification, a brighter background level of staining was observed which was due to higher 8-OHdG and not due to background fluorescence through comparison to the negative control (Figure 4.23B and C). At both 10x and 40x magnification, brighter staining was observed in NBS037 treated tissues, indicative that drug treatment may increase ROS in tumour tissue. However at 40x magnification, positive staining was more ubiquitous in the cell cytosol so this magnification proved not to be sufficient for visualising the 8-OHdG in detail.

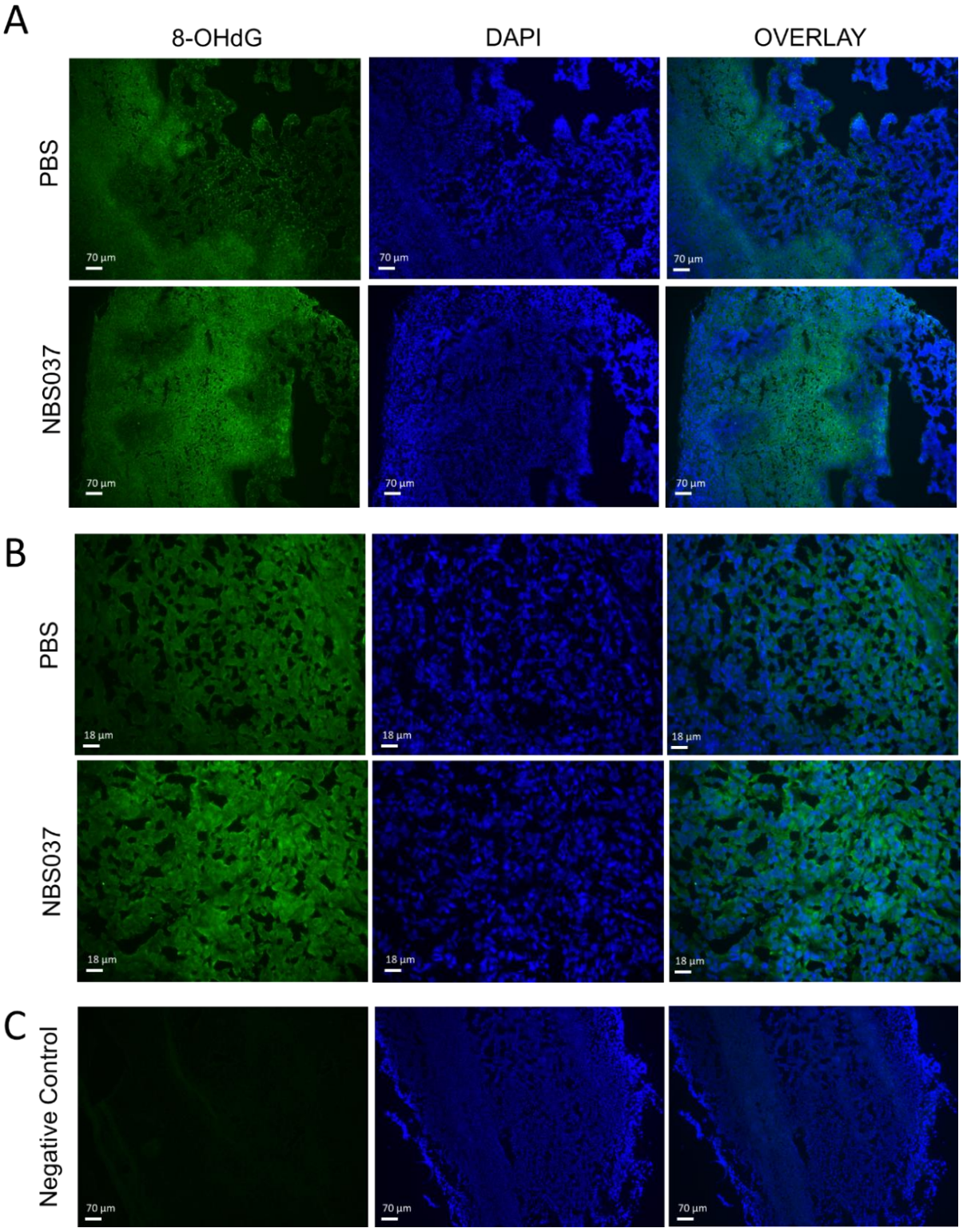

Figure 4.23. 8-OHdG staining for ROS in tumour tissue. *8-OHdG was utilised to stain for ROS in tumour tissue from mice treated with PBS or NBS037 (green). Nuclei were visualised by DAPI present in the mounting media (blue). Images were taken with a Leica upright microscope at (A) 10x and (B) 40x magnification. Negative controls with no primary antibody staining were also included at 10x magnification (C). All images were subjected to the same exposure. Data is representative of N=3.*

4.16 NBS027 treatment decreases CAIX expression

CAIX is a transmembrane protein expressed on cells in hypoxic environments and has therefore become a well-known biomarker for hypoxia within a tumour. Since hypoxia can influence the effect of chemotherapy drugs, the expression of CAIX was tested in tumours treated with PBS compared to those treated with NBS037. WB techniques were used to quantify protein expression in whole tumour lysates normalised to β-actin, the loading control (Figure 4.24). CAIX is known to show twin bands (Figure 4.23A) and when quantified, band 1 showed a significant decrease in CAIX expression in NBS037 treated tumours compared to PBS treated tumours ($p = 0.0025$). Whilst the second band showed a 15.4% decrease in expression in NBS037 treated tumours compared to PBS, this was not significant.

To further investigate any changes in CAIX expression with NBS037 treatment, tumour tissue from the periphery and the core of the tumour were stained with anti-CAIX antibodies (Figure 4.25). Some sections underwent cobalt chloride treatment prior to imaging, as this acts as a hypoxia-mimetic agent and produces a positive control for hypoxia, shown by bright green staining (Figure 4.24E). CAIX is expected to be visualised on the membrane of cells; however, 40x magnification did not provide the resolution required to observe the precise localisation of the protein within cells.

In the periphery of the tumour, the sections on the outside of the tumour which were cut first, localisation of CAIX was observed by distinct areas of brighter green. More of these areas are observed in the PBS treated tumours, with brighter staining observed at 40x magnification in PBS treated tissues compared to NBS037 treated tissues (Figure 4.24B). Such staining patterns are associated with lower CAIX expression in NBS037 treated tumours.

In the centre of the tumour, bright areas of positive CAIX staining are observed in both PBS and NBS037 treated tumours, with NBS037 treated tumours having as much, or more, positive

staining than PBS tumours. At 10x magnification, areas of positive staining are more numerous in the centre of the tumour, accompanied with brighter staining observed at 40x magnification when compared to sections from the periphery of the tumour.

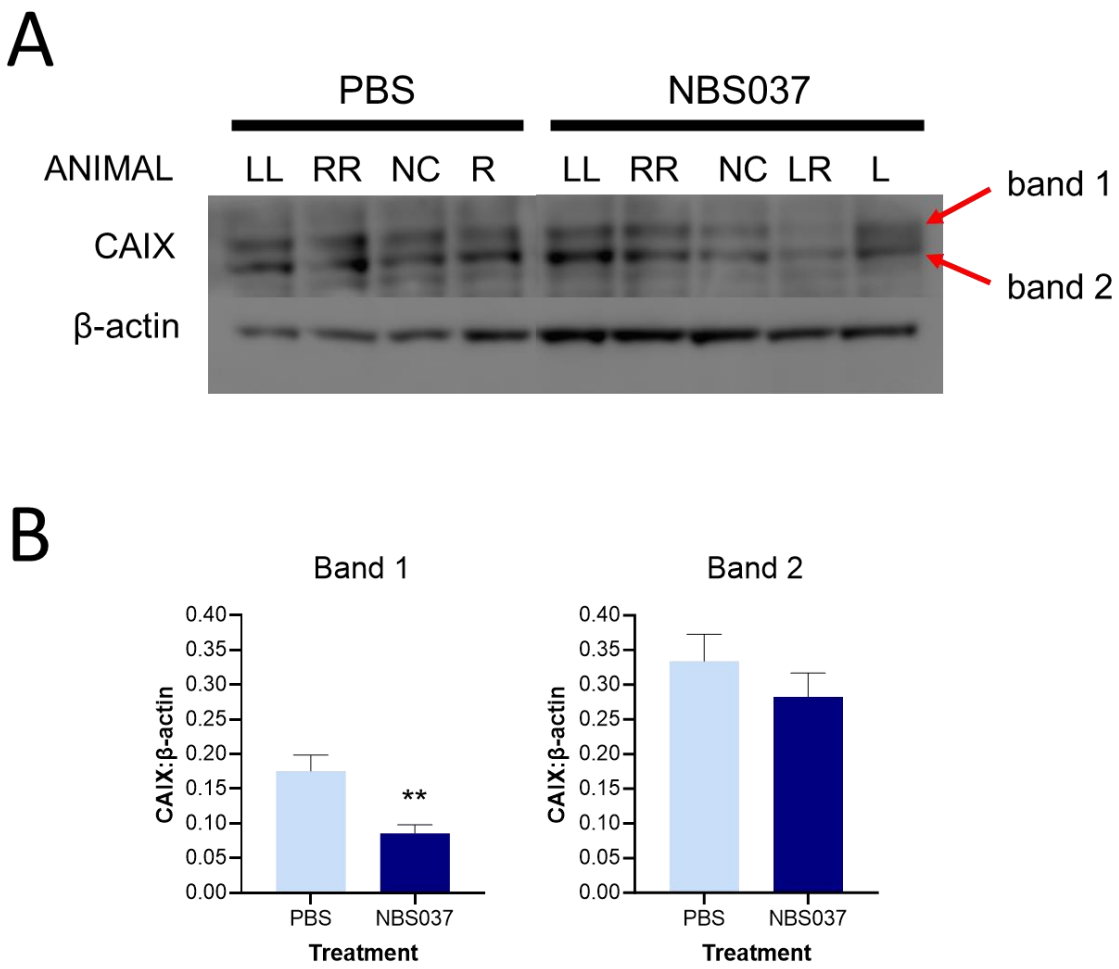

Figure 4.24. CAIX expression in tumour tissue lysates from PBS and NBS037 treated mice. *WB analysis was used to investigate the CAIX protein expression in tumour tissue lysates from PBS (n=4) and NBS037 (n=5) treated mice. Data is shown as (A) original blots from tissue lysates, with different animals denoted by clips on the ears: NC (no clip), RR (two right), R (right), LL (two left), L (left), LR (left and right). (B) mean CAIX expression normalised to β-actin ± SEM. Protein expression was quantified from blots using the G-box software. Statistical analysis was performed by unpaired t-tests to compare means from NBS037 treated mice to PBS treated mice (**, p < 0.01). N=3.*

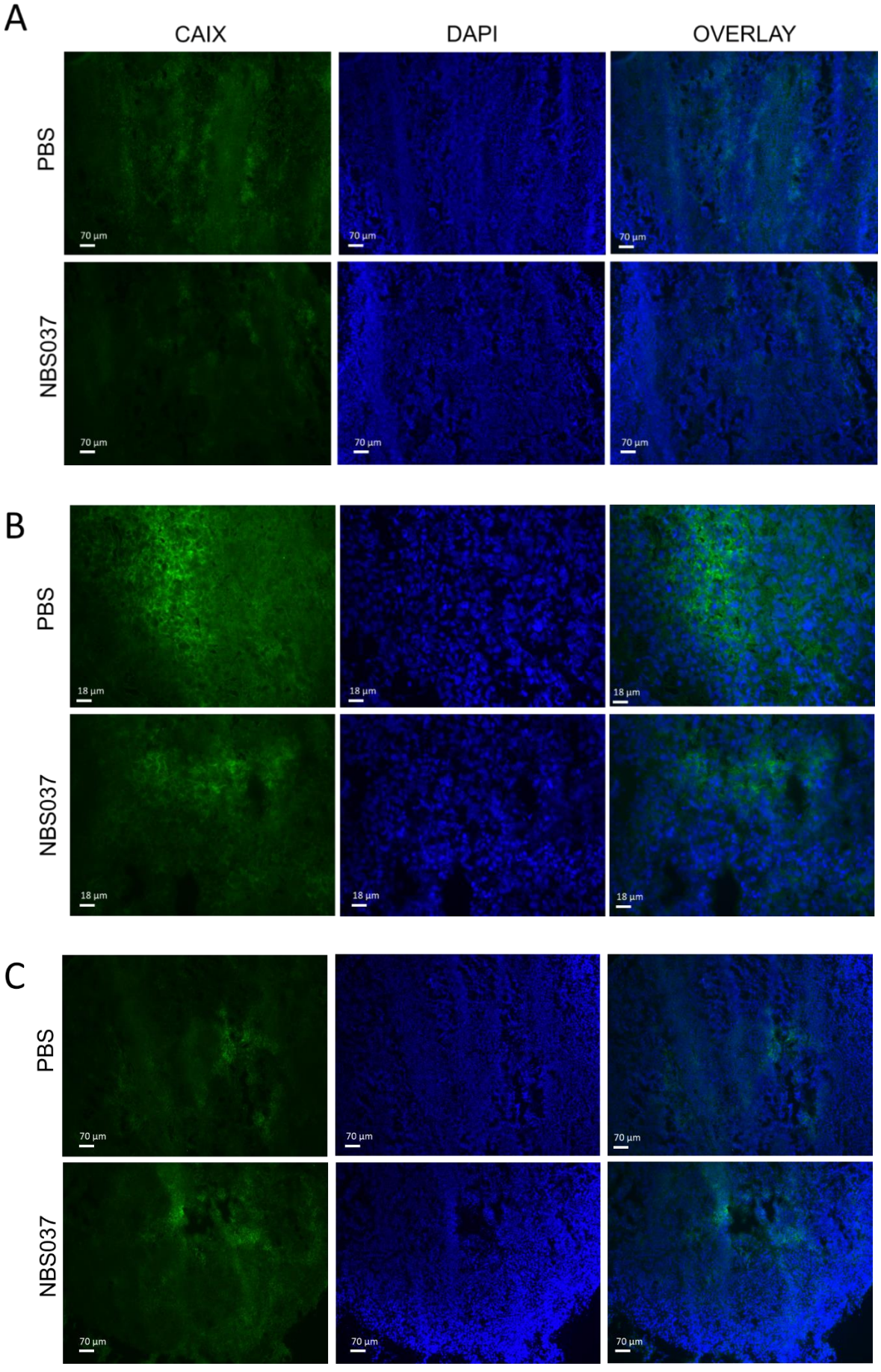
A
CAIX
DAPI
OVERLAY
PBS
NBS037
70 µm
B
PBS
NBS037
18 µm
C
PBS
NBS037
70 µm

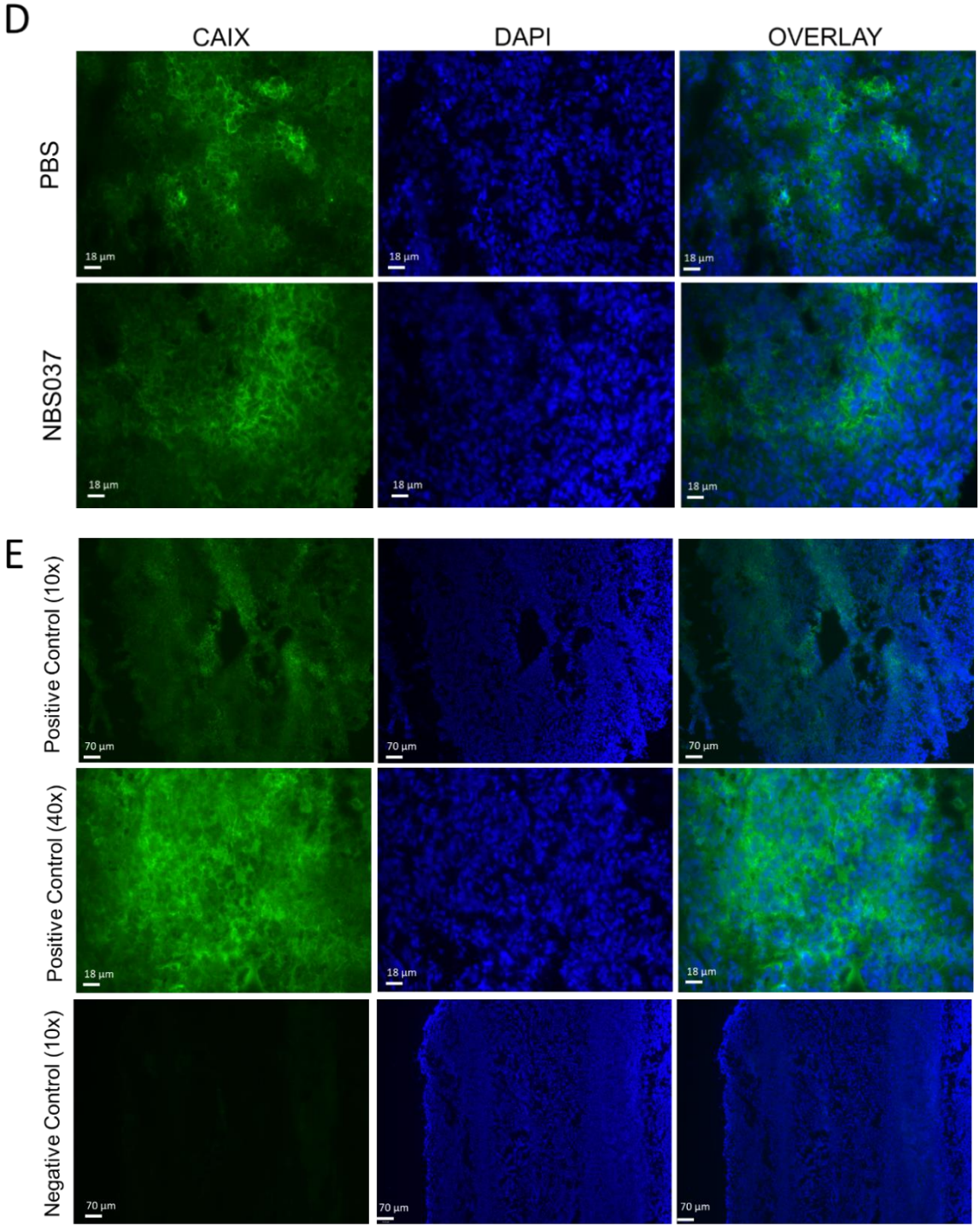

Figure 4.25. CAIX staining for hypoxia in tumour tissue. *CAIX antibodies were utilised to stain for hypoxia in tumour tissue from mice treated with PBS or NBS037 (green). Nuclei were visualised by DAPI present in the mounting media (blue). Sections from the periphery of the tumour were imaged at (A) 10x and (B) 40x magnification. Sections from the core of the tumour were imaged at (C) 10x and (D) 40x magnification. (E) shows positive controls (cobalt chloride addition) and negative controls (no primary antibody). Images were taken with a Leica upright microscope. All images were subjected to the same exposure. Data is representative of N=3.*

4.17 Discussion

4.17.1 NBS037 tolerability

The aims of this chapter were to elucidate the molecular effects of NBS037 *in vivo*, utilising xenograft mouse tissues. Once tumours had grown to an appropriate size (n=9 animals total), mice received NBS037 or PBS in the treatment period (Figure 2.1). Animals were maintained such that tumour size in each treatment arm were the same, proven by no significant difference in tumour mass upon culling (Figure 4.2). Controlling for tumour size in this manner would allow better comparison of PBS to NBS037 treated tumours, since factors such as poor vascularisation and hypoxia associated with larger tumours could influence drug delivery and cellular responses[359]. A larger mouse study completed by Dr James Hulit showed NBS037 treatment caused a small delay tumour growth over a three week treatment period, although this failed to reach significance for the single agent (Figure 4.1). This study focuses more on the cellular responses to NBS037 upon treatment.

Overall, NBS037 was well tolerated in the mice tested. On an individual level, no mouse in this study had a significant change in bodyweight (Figure 4.3) so NBS037 nor treatment administration caused enough stress to the mice to end the study. When the mean bodyweights of mice were compared, mice in the NBS037 treatment arm had a significantly lower bodyweight compared to their PBS treated counterparts, but with only a mean of 1.5% weight decrease compared to the gain in weight in PBS treated mice. Whilst a gain in weight would have been an indicator of a well-tolerated drug, mice in the NBS037 treatment arm also had faster growing tumours. Faster growing tumours may have caused a greater burden on the mice and subsequently a small drop in body weight.

4.17.2 Mechanism of action

4.17.2.1 NBS037 selectivity

Overall, it was promising to observe no significant effects on mitochondrial proteins in brain, heart, or kidney tissue with NBS037 treatment, despite other mitochondrial targeting drugs proving cardiotoxic[180] and neurotoxic[170]; however, NBS037 was able to cause significant effects in liver tissue. The liver is the primary organ for metabolism of pharmacological agents and therefore is exposed to high levels of the drug, and its metabolites as it is metabolised[360,361]. For this reason, hepatotoxicity is a key adverse effect noted with many drugs which have inhibitory effects on OXPHOS, such as the non-steroidal anti-inflammatory drugs nimesulide[362] and diclofenac[363], as well as the antiarrhythmic drug amiodarone[364]. NBS037 may accumulate in the liver to a high enough concentration to cause effects on mitochondria, and could resemble the accumulation experienced inside cancer cells due to the TPP^+ cation. With drug metabolites excreted by the kidney, renal cells may also experience higher levels of drug metabolites[365], which could explain the small but insignificant changes in mitochondrial proteins observed (Figure 4.6). With NBS037 treatment causing changes in mitochondrial proteins, cell death, and hypoxia in the tumour, with little change in normal tissue, this is promising evidence NBS037 possesses selectivity for tumour tissue over normal healthy tissue, but molecular effects require quantitation to be certain.

4.17.2.2 Mitochondrial proteins

To test for any evidence of target engagement, expression levels of MTCO1 were quantified by WB, as previously carried out in Chapter 3. No changes in MTCO1 expression were observed in brain tissue lysates, in keeping with initial toxicology studies of NBS037 which showed no NBS037 in the brain tissue (data not shown) and suggests the inability of NBS037 to cross the blood brain barrier. In heart and kidney tissue, a small but insignificant decrease

in MTCO1 was observed in NBS037 treated animals but in liver and tumour tissue, a significant decrease in MTCO1 was observed. A significant decrease in mitochondrial mass was also observed in both tumour and liver tissue, similar to the effects observed *in vitro* with H460 and ARPE-19 cells (Figure 3.15). When MTCO1 expression was normalised to the changing mitochondrial mass, no significant changes in MTCO1 expression was observed. Similarly, no changes in SDHA expression was observed when normalised to mitochondrial mass, unlike the changes in SDHA observed in cell lines in Chapter 3. This shows the changes in mitochondrial protein expression were due to the change in mitochondrial mass. Upon successful target engagement and inhibition of mitochondria protein translation, mitochondria would become dysfunctional may be cleared by mitophagy, leading to the decrease in mitochondrial mass observed.

Overall, NBS037 treatment caused a decrease in mitochondrial mass in liver and tumour tissue at the dose regime used and length of treatment schedule in this study. This may be an indicator of successful target engagement through inhibition of mitochondrial protein expression and enhanced mitophagy to clear dysfunctional mitochondria. The remaining mitochondria which are not yet depleted of mitochondrial proteins would remain and therefore cause limited changes in mitochondrial protein expression to be observed by WB. Evidence of enhancement of mitophagy has been observed with other OXPHOS inhibitors tested[366,367].

4.17.2.3 Apoptosis and hypoxia

The dysfunctional mitochondria and subsequent decrease in mitochondrial mass may cause the decreased cell viability observed *in vitro* in Chapter 3, due to increased cell death, or apoptosis. The TUNEL assay was used to investigate the amount of fragmented DNA in the tissues, with DNA fragmentation an indicator or late stage apoptosis[368]. Apoptosis is a normal physiological process so it was unsurprising to see evidence of apoptosis, through appearance of bright red punctae, in normal tissues. Evidence of apoptosis did not appear to increase with NBS037 treatment. This was balanced with some, although limited, evidence of cell

proliferation, with Ki67 positive staining in all normal tissues, which again was unaffected by NBS037 treatment, although requires quantification to be certain. Heart, kidney, and liver tissue have low rates of cellular turnover so it is unsurprising that low Ki67 and TUNEL staining were observed in these tissues[369–371], but also provides promising evidence that NBS037 has limited effects in normal tissue.

Tissue from the periphery of the tumour had greater positive TUNEL staining than normal tissue, shown by brighter and more widespread fluorescence (Figure 4.14A). This shows on the periphery of the tumour, there appears to be high rates of apoptosis, but with no clear difference between PBS and NBS037 treated cells. It has been shown that cancer cells still maintain high rates of apoptosis but with cell proliferation faster than cell death in order to grow a tumour[372]. Since the tumours were still growing rapidly and both achieved a similar size, it is unsurprising that high rates of cell death observed with TUNEL staining were balanced with high Ki67 staining (Figure 4.18). A higher proportion of cells stained positive for Ki67 in tumour tissue than normal tissue, regardless of whether tissue was localised at the tumour centre or periphery, and shows the highly dynamic nature of tumours with a fast cell turnover.

In the centre of the tumour, some interesting differences in cell death were observed (Figure 4.14C). PBS treated mice only had positive TUNEL staining in discreet areas of the tumour, however, NBS037 treated tissue had more widespread and brighter staining. This is an indication NBS037 may be causing more cell death within the centre of the tumour compared to PBS. Whilst the core of the tumour is more hypoxic and there is less oxygen available, studies have shown OXPHOS is vital for survival in these harsh conditions[108,111,373], and therefore inhibition of OXPHOS in the centre of the tumour could cause apoptosis and death in these cells.

To confirm the presence of hypoxic areas in the tumour, CAIX antibodies were used to stain for hypoxia[374]. CAIX drives hypoxic adaption due to maintenance of an alkaline intracellular pH and an acidic extracellular pH. This prevents over acidification in cancer cells, and therefore CAIX is overexpressed in hypoxic regions in cancers due to HIF-1α stabilisation. CAIX regulates the reversible conversion of CO_2 into bicarbonate and a proton, and can form transport metabolons with both bicarbonate transporters and MCTs to drive import or export of bicarbonate and lactate respectively[375]. It may be expected that OXPHOS inhibition would cause a compensatory increase in glycolysis and lactate production, further driving acidification and enhanced CAIX expression, however, this was not observed here. CAIX staining was decreased to a small extent in NBS037 treated tissues in the periphery of tumour (Figure 4.25), and when quantified by WB (Figure 4.24), both CAIX bands had decreased expression. This is similar to the findings of van Gisberben et al. (2020), where pharmacological OXPHOS inhibition resulted in a decrease in HIF-1α stabilisation, and its downstream target, CAIX[376]. Mitochondria and mitochondrial oxygen consumption influence the stabilisation of HIF-1α and many studies have shown mitochondrial dysfunction, and increased intracellular oxygen, leads to decreased stabilisation of HIF-1α[377], despite any changes in glycolysis. If OXPHOS is actively inhibited by NBS037, this reduces oxygen consumption and therefore increases oxygenation in the tumour[79,378]. This is the observed with OXPHOS complex inhibitors such as ATQ and IACS-010759. Since hypoxia is often a facilitator of radio- and chemoresistance[379,] these agents act as sensitisers to radio- or chemotherapy due to their effects on tumour oxygenation and alleviation of tumour hypoxia[161,380]. Overall this is evidence that NBS037 may reduce OXPHOS *in vivo,* potentially decreasing CIAX through HIF-1α destabilisation.

Tumours are often poorly vascularised at the centre of the tumour which limits the access to nutrient and drug rich blood[381], driving hypoxia within the centre of the tumour. This would also impact the effect of NBS037 *in vivo* if the drug cannot reach a vast area of the tumour. For this reason, immunofluorescence techniques were used to stain for CD31, an endothelial marker,

to visualise the vasculature of the tumour. As noted by others[382,383], CD31 staining was denser in the surrounding periphery of the tumour, with little positive staining in the middle of each section (Figure 4.19). This indicates a higher density of blood vessels at the periphery of the tumour. This is in agreement with the increased hypoxia observed with CAIX staining in the core of the tumour compared to in the periphery. With some positive CD31 staining in the centre of the tumour still visible, it is plausible that NBS037 can still be delivered, and exert effects on cells which explains the high apoptosis staining observed in the core of the tumour.

Previous literature highlights the importance of mitochondrial function in the process of angiogenesis[384] with evidence that OXPHOS inhibition also inhibits angiogenesis[385,386], however no clear differences in CD31 staining between PBS and NBS037 treated tumours were observed here. Angiogenesis inhibitors currently in use are delivered for at least multiple weeks[387–389], therefore a four day treatment period of NBS037 may not be long enough to observe any effects.

4.17.2.4 Redox mechanisms

With limited changes in ROS, and no clear evidence of oxidative stress observed *in vitro*, markers for oxidative stress were tested again in mouse tissues to observe if the environment *in vivo* environment impacts ROS effects. Expression of SOD2 were measured using WB techniques for each tissue. When expression was compared to housekeeping proteins, NBS037 treatment caused a significant decrease in SOD2 in liver tissue, with little difference between PBS and NBS037 treated animals in any other tissues. However, when SOD2 expression was normalised to mitochondrial mass, NBS037 caused a small increase in SOD2 in liver, tumour, and brain, and slight decrease in expression in kidney, although all changes in expression failed to reach significance.

To validate the minimal ROS mechanisms at play, 8-OHdG was visualised using immunofluorescence techniques. 8-OHdG is an DNA nucleoside which is an oxidative derivative of deoxyguanosine, and therefore commonly used as a readout for oxidative damage to DNA and as a risk factor for carcinogenesis[390,391]. In normal tissue, 10x magnification which was used for a better field of view over the tissue section, failed to distinguish any positive staining for 8-OHdG which would be indicated by bright green fluorescence. Under 40x magnification, heart tissue showed evidence of positive staining, with brighter fluorescence observed in NBS037 treated animals. Such staining was localised to the cytoplasm of cells. Liver also showed evidence of positive staining; however, liver tissue has been known to autofluoresce[392,393]. The fluorescence observed in both heart and liver were not due to autofluorescence, due to lack of signal in the negative controls. Both cardiomyocytes and hepatocytes are reliant on OXPHOS as a predominant energy source, particularly in the heart where a large demand for ATP must be met[394,395]. Higher OXPHOS would result in increased ROS production in these tissues and would explain the brighter staining observed. It is expected that some NBS037 may still enter normal tissue due to attraction to plasma membrane potential, however, given the importance of mitochondrial function in cardiomyocytes, a low dose of NBS037, which threatens mitochondrial deficits, may cause a compensatory increase in OXPHOS in order to maintain energetic output. This would subsequently increase ROS generation and 8-OHdG levels, and may explain the apparent increase in fluorescence observed with NBS037 treatment in heart tissue.

In tumour, brighter staining than in any other tissue was observed, indicative that baseline levels of ROS may be higher than normal tissue as observed by others[72,113,114]. A greater area of positive staining was observed in NBS037 treated tissues, showing the drug may increase levels of ROS in the tissue, similar to findings observed in H460 cells *in vitro* (Figure 3.19). Interestingly, 8-OHdG staining was localised to discrete areas within the tumour tissue. As ROS are produced during OXPHOS, this may indicate areas where the OXPHOS driven

cancer cells are more populous, perhaps linked to the areas closer to tumour vasculature as CD31 staining highlighted some vasculature still existed inside the core of the tumour[84,396,397].

Overall, the findings in this chapter provide initial evidence of changes to mitochondrial mass and proteins in liver and tumour tissues, accompanied by some changes in cell death and CAIX in tumour as determined by IF. However, a number of staining experiments could only be completed in a single PBS and NBS037 treated animal. A lack of animal numbers presents a significant weakness in this work and more reproducible results are required before being able to draw conclusions about NBS037 induced effects in the animal tissues.

4.18 Future directions

Future work can be carried to both improve the work already completed and validate results. To validate the data obtained from the WB, more methods can be applied to analyse the samples. For example, mass spectrometry (MS) can be utilised to identify levels of different metabolites, as well as identify a large number of protein expression levels[398], which can piece together metabolism in these tumours, and any changes NBS037 may cause. However, these techniques require homogenisation of the tumours, losing any spatial resolution of the data, therefore it may beneficial for future work to focus on quantitative imaging techniques.

For imaging work, confocal microscopy may allow for higher resolution of images and higher magnification in order to better observe the target proteins, with both factors a limitation in the current work. For more representative results, the remaining animal tissues would be sectioned and analysed to observe if the effects are observed in all of the animals and not only the small number of samples taken for this thesis Confocal microscopy, coupled with a higher sample number, would allow images to be quantitively analysed through software such

as ImageJ[399], to provide more robust and quantitative results for changes in staining intensity between tumour and normal tissues, and NBS037 treated and untreated tissues.

Future work may also include changes to the mouse study design itself. No effects of NBS037 may have been observed in this study due to low number of doses given and short treatment time frame. Although in cell lines, the drug could take as few as 72 hours to see effects, these cells were in different environments and therefore longer term treatment may be required to see effects *in vivo*. For example, xenograft mouse studies with IACS-010759 utilised daily doses of the drug for 21 days[220], and use of tigecycline peritoneally injected once every alternative day for 30 days[400]. The mouse model used may also be improved. The CD-1 mice used in this study are immunodeficient to allow tumours to be implanted and grown successfully. However this does not truly recapitulate the TME as immune cells and cytokines produced can affect tumour development, behaviour, and therapy response[98,401,402]. The work *in vitro* provided initial insight into NBS037 cytotoxicity and mechanism of action in human cancer cells, however *in vivo* models with a functional immune system would be beneficial for identifying any additional effects from the immune system, or if the drug directly impacts immune cells. Syngeneic models use mouse cancers in a normal mouse so would allow maintenance of a normal immune system and the normal behaviour of tumours to be observed[403,404]. One such cell line which could be used is the B16 melanoma mouse line. An initial screen by Dr Hulit indicated the B16 line had the lowest IC50 out of the mouse lines tested (MC38, LLC, KPC and CT26) (data not shown) and may provide a beneficial secondary model to test both *in vitro,* with similar assays as described in Chapter 3 as well as scratch assays[405], and *in vivo*. Upon subcutaneous injection, B16 cells will form a palpable tumour in five to ten days and has the potential to cause pulmonary metastases[406]. With OXPHOS playing an important role in metastasis, NBS037 also could also be tested in metastatic cells.

With no significant effect on growth delay observed with NBS037 as a single agent (Figure 4.1), future work could test NBS037 in combination with standard of care therapies to enhance

efficacy of both. Dr Hulit tested the effect of NBS037 and standard of care combination treatment on survival in H460 mouse xenograft models (Figure 4.26). CD-1 nude mice were inoculated with H460 cells in order to produce a xenograft tumour and treated for 21 days with PBS (n=12), 3 mg/kg NBS037 (n=11), 20 mg/kg paclitaxel (n=12), 60 mg/kg carboplatin (n=9). A subset of mice received combination treatment of NB037-carboplatin (n=12) or NBS037-paclitaxel (n=8) at the same doses used previously. Whilst NBS037 showed some improvement in survival (based off a tumour threshold size of 1000 mm^3) compared to PBS, carboplatin and paclitaxel, the standard of care treatments for NSCLC were still superior to NBS037 in improving survival probability. However, combination treatment utilising standard of care treatment and NBS037 together, improved the probability of survival greater than any agent used alone. Whether these effects are additive or synergistic are yet to be deduced.

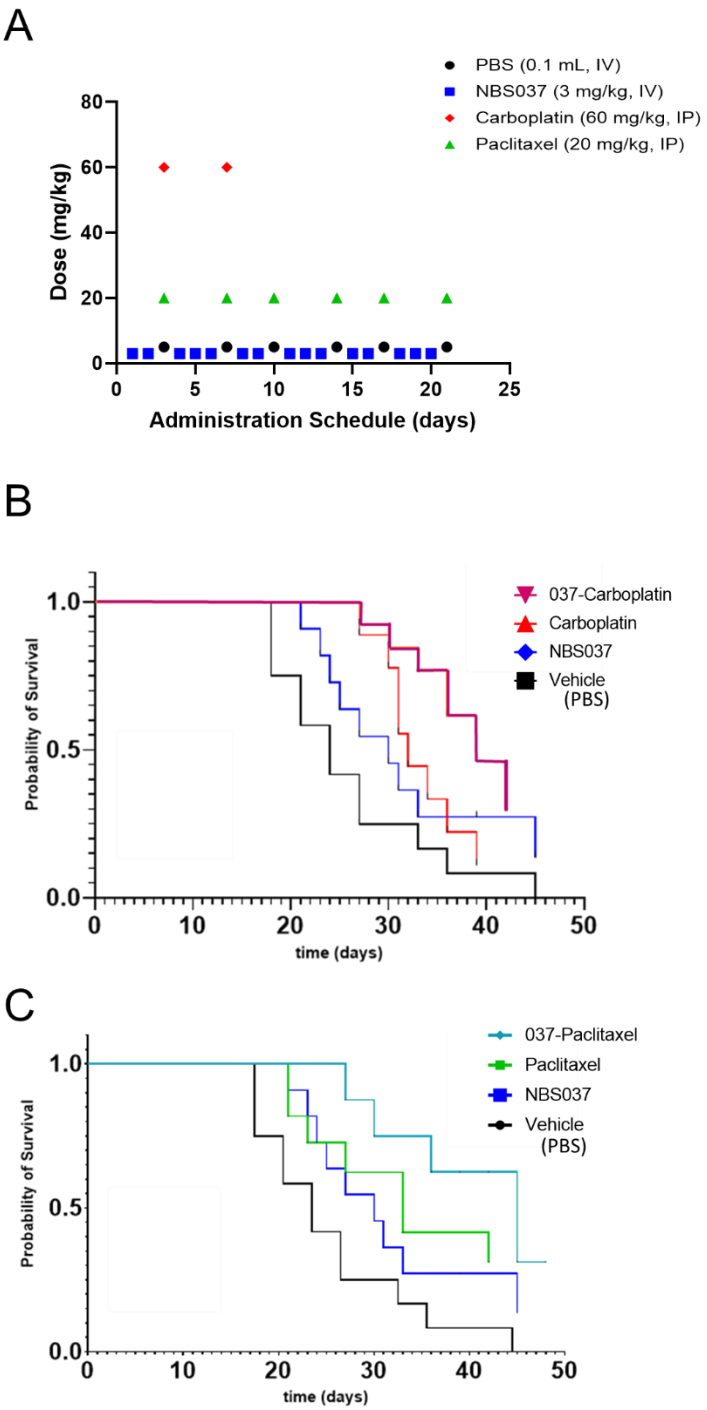

Figure 4.26. The effect of NBS037 and standard of care combination treatment on survival in H460 mouse xenograft models (Hulit). *CD-1 nude mice were innoculated with H460 cells in order to produce a xenograft tumour. Mice were treated for 21 days with PBS (n=12), 3 mg/kg NBS037 (n=11), 20 mg/kg paclitaxel (n=12), 60 mg/kg carboplatin (n=9). A subset of mice received combination treatment of NB037-carboplatin (n=12) or NBS037-paclitaxel (n=8) at the same doses used previously. Treatment schedule is denoted in (A) with IV indicating intravenous administration and IP indicating intraperitoneal injection. (B) represents survival curve with NBS037 and carboplatin treatment, and (C) NBS037 and paclitaxel treatments, based upon a tumour threshold size of 1000 mm^3.*

4.19 Chapter summary

Overall, in initial efficacy experiments by Dr Hulit, NBS037 did not significantly delay tumour growth in xenograft models. When investigating the effect of NBS037 on treated tissues, a decrease in mitochondrial mass was observed in tissues which may be exposed to high concentration of NBS037 (tumour and liver). Subsequently, this resulted in significant effects on mitochondrial localised proteins. The working hypothesis is NBS037 causes a decline in mitochondrial encoded proteins, causing mitochondrial dysfunction, and increased clearance of these mitochondria by mitophagy. Evidence of increased apoptosis was observed in the centre of NBS037 treated tumours but similar to the findings *in vitro*, NBS037 did not exert its apoptotic effects through ROS mechanisms. Analysis of CAIX expression showed promising evidence of alleviation of hypoxia at the centre of tumours with NBS037 treatment, indicative of OXPHOS injury accompanying the decrease in mitochondrial mass, and may explain the cell death observed in tumours. Unlike other OXPHOS inhibitors in development, NBS037 showed no toxicity in normal tissues, with maintenance of mitochondrial proteins and rates of cell proliferation, with the exception of liver tissue in which decreased mitochondrial mass was observed. Despite changes in protein expression in liver, NBS037 was well tolerated, shown by no significant decrease in mouse bodyweight throughout the study.

5

Developing Raman Spectroscopy for Determination of Cell Metabolism

5.1 Introduction

To date, there are various methods to study metabolites within the cell, and how these differ in cancer. ^{13}C tracer analysis[407] and fluorescent probes[408] can allow determination of metabolomic flux and visualisation of metabolites whilst nuclear magnetic resonance (NMR) spectroscopy allows identification of metabolites and their structures[409]. However, MS has remained the gold standard for metabolomics, due to its high sensitivity, extensive metabolite database, and high mass resolving power[410]. In recent years, the Human Metabolome Database has significantly increased its metabolite entries, with 217,920 compounds annotated, and a further 1,581,537 unannotated derivatized metabolite entries as of 2022[411].

Whilst MS is the gold standard for metabolomics, it may only achieve partial coverage of the metabolome, with many metabolites still unidentified[412]. MS is also in development for single cell analysis and for potential in diagnostics but MS requires destructive sample preparation and gives no spatial resolution within a sample[413]. This limits the capabilities of MS for capturing the metabolome in live cells or for analysis of tumour samples which display metabolic heterogeneity within the tumour mass.

Raman spectroscopy is a label-free spectroscopy method increasingly utilised in the biological field due to overcoming the limitations of MS[414]. First observed in 1928, it was observed that upon directing incident light at a sample, most photons will scatter with little difference in energy and return to their fundamental state, named Rayleigh, or elastic, scattering. Some photons, approximately 1 in 10^7, interact with molecules in the sample and either gain or lose energy. This is inelastic scattering[415]. The incident photon may lose energy to the sample molecule, causing the scattered photon to have a longer wavelength than the incident light, which is denoted as Stokes scattering. The opposite may occur when the photon gains energy from the molecule in the sample, and be scattered with a shorter wavelength, known as anti-Stokes scattering. Raman encompasses both Stokes and anti-Stokes scattering, with the former being more common[416] (Figure 5.1). Each molecule will have a different vibrational energy, causing differential polarisation of photons and therefore generate a different Raman 'fingerprint' for each sample. For this reason, Raman has been utilised in the study of biological samples, with Raman bands able to identify important biological macromolecules and metabolites, and distinguish cell types. When coupled with optical microscopy, Raman spectroscopy can also be utilised for analysis at a sub-cellular level, where organelles can be analysed, and accurate localisation of molecules within a cell determined[417,418].

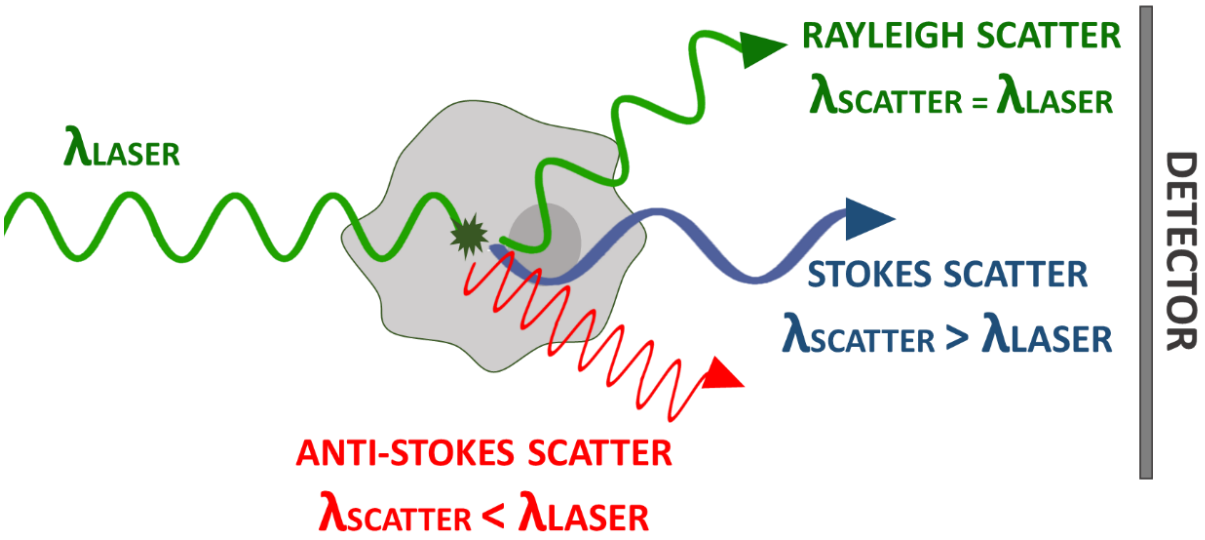

Figure 5.1. Photon scattering patterns in Raman spectroscopy. An incident photon from a laser with wavelength λ_{laser} will interact with a molecule within a sample. Most photons will be scattered with little change in energy, known as Rayleigh scattering, and return to their fundamental state at wavelength λ_{laser}. However some photons will lose energy upon interacting with molecules in the sample and be scattered with a wavelength greater than that of the incident photons, known as Stokes scattering. Photons may also gain energy upon interacting with the sample and scatter with a smaller wavelength than the incident photons, known as anti-Stokes scattering. The scattered photons can be detected and generates a Raman fingerprint for each sample, indicating its molecular make up.

5.2 Aims

The specific aim of this chapter is to investigate if Raman spectroscopy can be utilised to study the metabolic phenotype of cancer cells. Through identifying OXPHOS dependent tumours, we may identify which tumours may be a good candidate for NBS037. This will be achieved by identifying changes in Raman spectra when there are shifts in cell metabolism through:

a) glucose manipulation,

b) use of glycolysis inhibitor 2DG and OXPHOS inhibitor AA,

c) use of NBS037 to inhibit OXPHOS.

Furthermore, the ability of Raman spectroscopy to identify the presence of NBS037 in cells will be investigated.

5.3 Microscopic imaging indicates cellular health under different drug treatments

A549 and H460 NSCLC cell lines were grown for 72 hours in 11 mM or 1 mM glucose media, with or without the addition of drug treatments. The drug treatments included DMSO as a vehicle control, the OXPHOS inhibitors NBS037 or AA, or the glycolysis inhibitor 2DG. Media was replaced daily to maintain glucose levels, and after 72 hours of drug treatments, diluted cell suspensions were dried onto aluminium coated slides for imaging on the HR Evolution confocal Raman microscope (Horiba). During the process, cells were handled with care in order to prevent lysis or rupture due to handling. Multiple fields of view were imaged and representative images shown of cells grown in 11 mM glucose (Figure 5.2).

At baseline and in the presence of DMSO, cells appear healthy and intact, with little evidence of membrane rupture or debris in the extracellular space. Small, dark objects in the field of view may indicate the remnants of dead cells. After treatment with 0.5 μM NBS037, A549 cells show evidence of some membrane rupture with more debris in the extracellular space which is exacerbated with 1 μM NBS037 (indicated by arrows in Figure 5.2). With 1 μM NBS037, the plasma membrane is irregular in some cells, with a similar appearance to a blebbing plasma membrane. Similarly, in H460 cells, there is some evidence of cell membrane rupture with NBS037 at both concentrations. However, with NBS037 treatment, dark spots cover the cells, indicating poor cellular health.

In A459 cells, 10 μM AA treatment was better tolerated than 1 μM NBS037, with less evidence of cell rupture but cell volume often appeared reduced compared to untreated cells. In H460 cells, cell volume also appeared reduced with AA treatment; however, greater evidence of cell rupture was observed than in A549, with much more debris in the extracellular space (indicated by arrows in Figure 5.2). It is interesting to note that the appearance of H460 cells with NBS037 and AA treatment were very different despite both being OXPHOS inhibitors.

Inhibiting glycolysis with 2DG also appeared to have large effects on H460 cells, with increased cell debris released into the extracellular space (indicated by arrows in Figure 5.2). Surprisingly, 2DG caused a greater detriment to cellular health in H460 than A549, with A549 being a more glycolytic line so should have greater sensitivity to detrimental effects of 2DG.

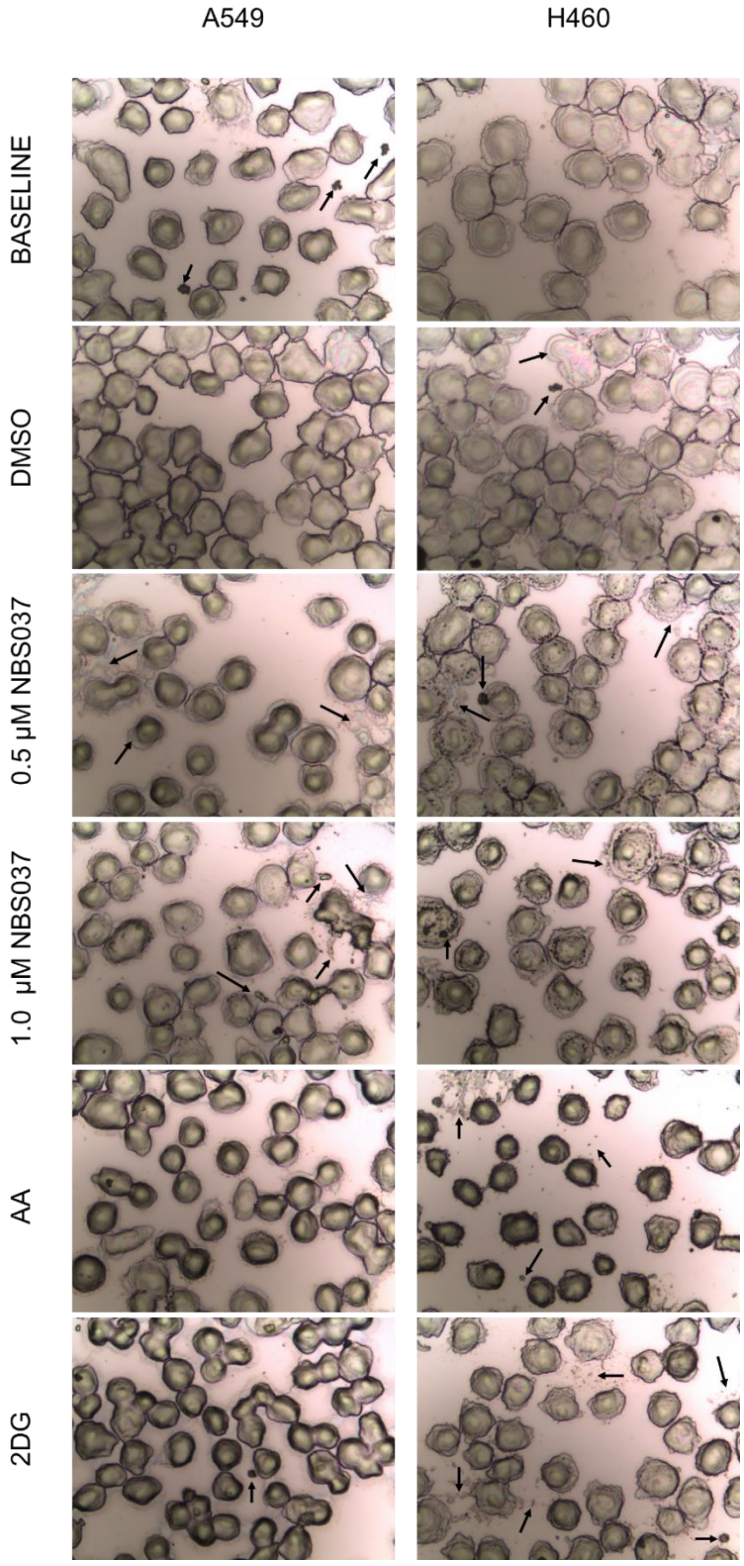

Figure 5.2. Imaging of two NSCLC cell lines under various metabolism inhibitors. *NSCLC cell lines A549 and H460 were treated for 72 hours with DMSO (vehicle), 0.5 µM or 1 µM NBS037, 10 µM AA, or 500 µM 2DG in 11 mM glucose. Media was replaced each day to maintain glucose levels. Cells were suspended in solution and dried onto aluminium coated slides for imaging with an HR Evolution confocal Raman microscope (Horiba). Images were collected at 50x. Black arrows indicate evidence of cell lysis and debris in the extracellular space. Images are representative of N=1.*

5.4 Spectral acquisition

For this pilot study, 10 spectra per cell and ~35 cells per treatment group were collected to create representative results from this biological replicate. 10 specified treatments were included: untreated, DMSO, 0.5 μM or 1 μM NBS037, 10 μM AA, and 500 μM 2DG in 11 mM and 1 mM glucose media. H460 cells failed to grow well in 1 mM glucose with DMSO, 1 μM NBS037, and AA, so due to inadequate numbers of viable cells for analysis, these samples were excluded. Overall, a total of 7200 spectra were included in analysis. Spectra were collected between the wavelengths of 300 cm^{-1} to 3400 cm^{-1} and pre-processed to minimise the effects of external disturbances during data collection[419]. Pre-processing of spectra included a) removal of cosmic rays, b) normalisation by area, and c) baseline correction through shifting to zero, in order to compare the various spectra. Wavenumbers 400-1800 cm^{-1} are thought of as the biological fingerprint regions, with 1800-2700 cm^{-1} indicating the silent region[420] (Figure 5.3). Spectra in the region of 2700-3500 cm^{-1} originate from stretch vibrations of -CH, -NH, and -OH groups, but with peaks often overlapping in this region, they are less informative than those in the fingerprint region[421].

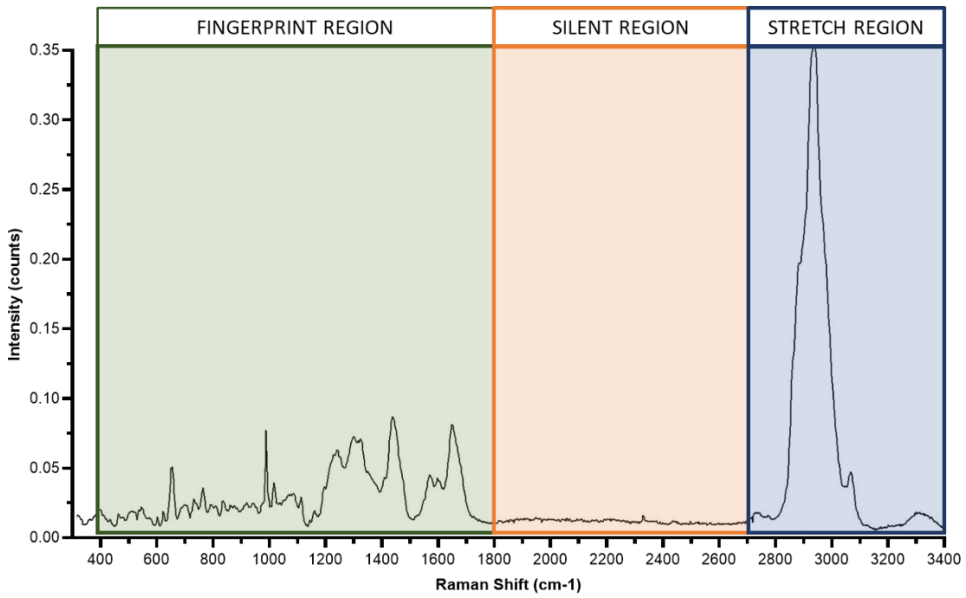

Figure 5.3. Key regions in Raman spectra. *Regions within a Raman spectra reflect different areas of interest. 400-1800 cm^{-1} is known as the fingerprint region, with 1800-2700 cm^{-1} indicating the silent region and peaks between 2700-3500 cm^{-1} originating from stretch vibrations of -CH, -NH, and -OH groups.*

5.5 Glucose manipulation creates distinct phenotypes in A549 and H460 cells

To confirm the OXPHOS capacity of each cell line in 11 mM and 1 mM glucose, a MitoXtress Xtra assay was performed on A549 and H460 cells which were grown in different glucose conditions for 72 hours. As observed in previous chapters, H460 cells had a higher OCR than A549 cells in both 11 mM and 1 mM glucose; however, lowering the glucose resulted in a small increase in OCR in A549 (122%), and a larger increase in H460 cells (134%) (Figure 5.4B). This indicates that lowering the glucose increases OXPHOS capacity in these cancer cell lines, with H460 cells in 1 mM glucose having the greatest OCR and having the highest OXPHOS, significantly differing from both A549 at 11 mM ($p = 0.0192$) and 1 mM glucose ($p = 0.039$).

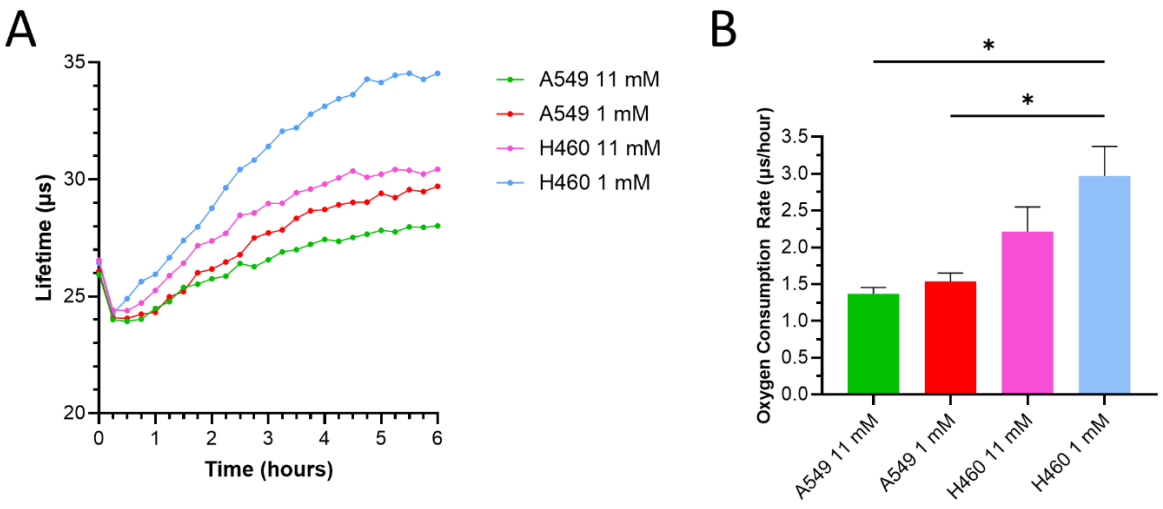

Figure 5.4. The effect of glucose in cell culture media on oxygen consumption in A549 and H460 NSCLC cells. *A549 and H460 NSCLC cells were grown in 11 mM and 1 mM glucose for 72 hours, with daily media changes to maintain glucose availability. A MitoXpress Xtra assay was performed to assess the oxygen consumption over a period of 6 hours. The lifetime fluorescence and OCR was calculated in MARS software. Data represents (A) mean lifetime fluorescence and (B) mean OCR ± SEM. Statistical analysis was performed by Browne-Forsythe one-way ANOVA with Dunnett's T3 multiple comparisons post hoc tests to compare groups (*, $p < 0.05$). N=3.*

Upon confirmation that lowering glucose levels in the cell culture media can produce an enhanced OXPHOS phenotype in A549 and H460 cells, Raman spectroscopy was performed on A549 and H460 cell lines which had been grown in 11 mM or 1 mM glucose for 72 hours. After pre-processing, Raman spectra for each cell in a sample were analysed by PCA (unsupervised) and LDA (supervised) in an R environment. The PCA showed clear separation of H460 cells in the 1 mM group from the other groups (Figure 5.4A). Whilst some cells in the H460 11 mM glucose group showed some separation from A549 cells, the majority were unable to be distinguished from one another and larger scatter was observed. The LDA proved to give superior separation of groups, with H460 cells in 1 mM glucose still having large separation from other groups on LD1 but less overlap between the remaining groups due to improved separation on LD2 (Figure 5.5). Interestingly, whilst there was some overlap still between H460 at 11 mM glucose and A549 cells, H460 and A549 cells in 11 mM glucose had the best separation, with the A549 in 1 mM glucose group falling between the two high glucose groups. This indicates the phenotype of A549 cells at 1 mM glucose, begins to shift similar to that of H460 cells.

From the LDA plot generated, the wavelengths contributing the most towards separation on LD1 or LD2 could be identified (Figure 5.6). For separation on LD1, which highly separates the H460 1 mM phenotype from the other three groups, the largest contributors were peaks corresponding to different amino acids which included tryptophan (1618 cm^{-1}), phenylalanine (621 cm^{-1}), proline (933 cm^{-1}), and hydroxyproline (876 cm^{-1}) . LD1 separation also flagged peaks which are associated with amides and nucleotides (1656 cm^{-1}) and cytosine (781 cm^{-1}), indicating some differences in nucleotide metabolism. Other important compounds included phosphatidylserine (530 cm^{-1}), and glycogen (481 cm^{-1}). Whilst specific compounds were identified as contributors to LD1 separation, peaks at 3060 cm^{-1} indicating aromatic stretching, and peaks associated with stretching vibrations in the CH region were also contributors.

LD2 separated the groups H460 11 mM, A549 11 mM, and A549 1 mM, albeit with some overlap between the three. Top contributors to this separation again lie in the -OH stretching region (3300 cm^{-1}), and aromatic stretching (3059 cm^{-1}). Changes in DNA (1094 cm^{-1}), nucleic acids (810 cm^{-1}), and lipids (1738 cm^{-1}) including phosphatidylserine (530 cm^{-1}) were also detected. Peaks corresponding to some amino acids also showed significant contributions to LD2 which included tryptophan (573 cm^{-1}) tyrosine (855 cm^{-1}), and proline (933 cm^{-1}).

As well as considering the key contributing peaks to group separation, key molecules involved in energy metabolism were quantified in each group through integration of Raman bands. In H460 cells in 1 mM glucose, a universal and significant decrease in amino acids, lipids, carbohydrates, and DNA was observed, with a significant increase in stretching vibrations and amides observed when compared to the other groups (Figure 5.6). Few significant differences were observed between A549 cells in 11 mM glucose and 1 mM glucose but a significant decrease in lipids at 1738 cm^{-1} ($p = 0.0445$) and increase in proline/tyrosine at 855 cm^{-1} ($p = 0.0174$) in A549 1 mM cells follows the trend of H460 cells in 11 mM, a more OXPHOS phenotype. In high glucose H460 cells, there was a tendency for significantly higher amino acids and DNA, and a decrease in glycogen at 481 cm^{-1} ($p = 0.0011$) when compared to A549 high glucose cells, but otherwise no significant differences were observed between the groups. Overall, H460 cells in 1 mM glucose displayed potent changes in key biomolecules involved in metabolism which reflected the clear separation from the other groups on the LDA.

Peaks identified as those corresponding to cytochrome *c* molecules in the mitochondria were also analysed. Key peaks at 750 cm^{-1} and 1583 cm^{-1} were significantly decreased in H460 low glucose cells (both $p < 0.0001$) compared to the other groups. However, cytochrome *c* peaks at 750 cm^{-1} and 1311 cm^{-1} (Appendix B) were significantly increased in H460 high glucose cells compared to A549 cells, so a lowering of cytochrome peak intensity is not reflective of OXPHOS rate alone.

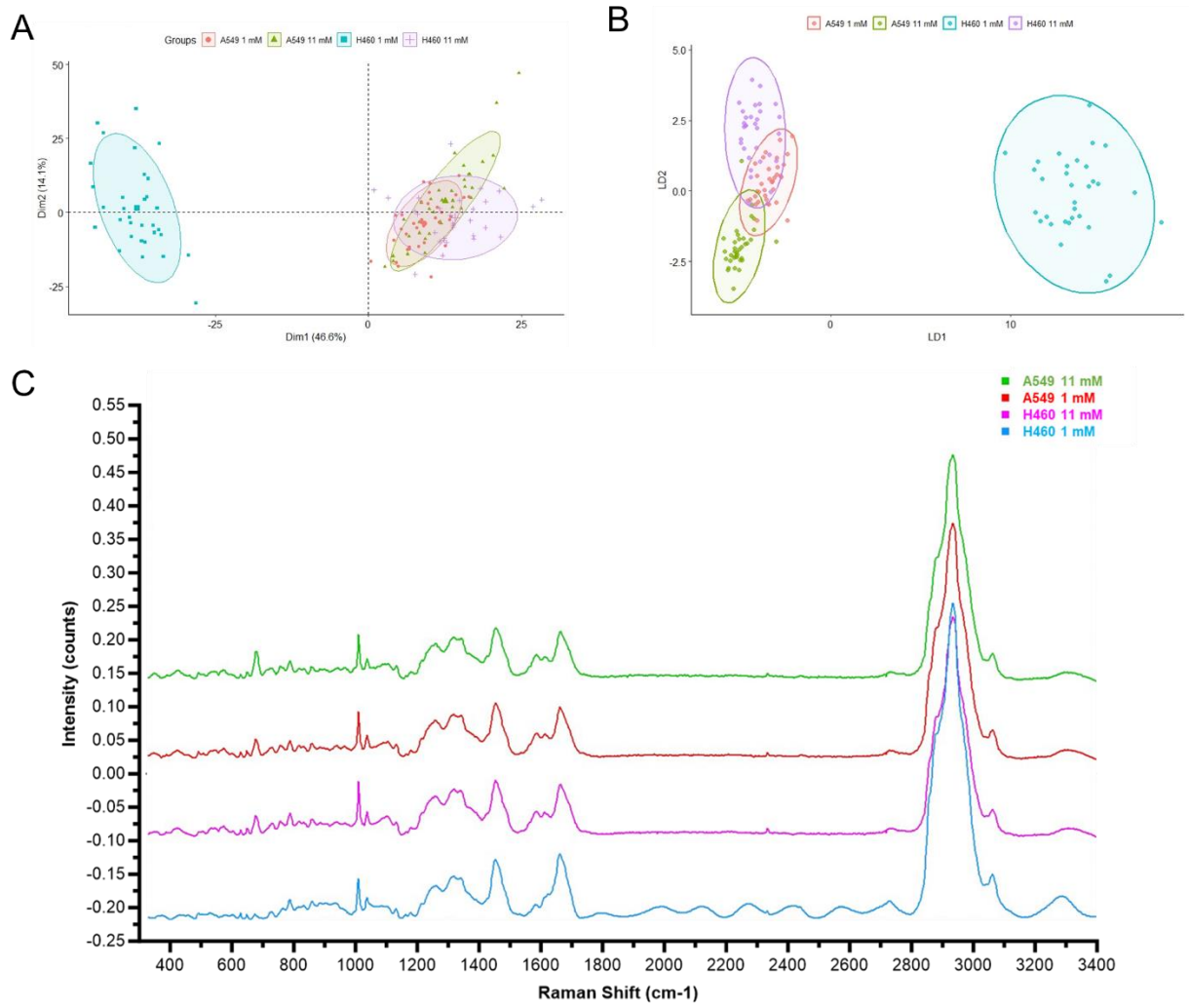

Figure 5.5. The effect of glucose manipulation on Raman spectra in A549 and H460 NSCLC cells. *NSCLC cells were grown in 11 mM or 1 mM glucose media for 72 hours with daily media replenishment. Cells were suspended in solution and dried onto aluminium coated slides for spectral acquisition with an HR Evolution confocal Raman microscope (Horiba). 10 spectra per cell and ~35 cells per sample were collected. Spectra underwent pre-processing and average spectra per sample plotted in an R environment. (A) PCA and (B) LDA plots were calculated to compare the sample groups, with different colours to denote different groups. (C) represents averaged spectra. N=1 of 35 replicate cells per group.*

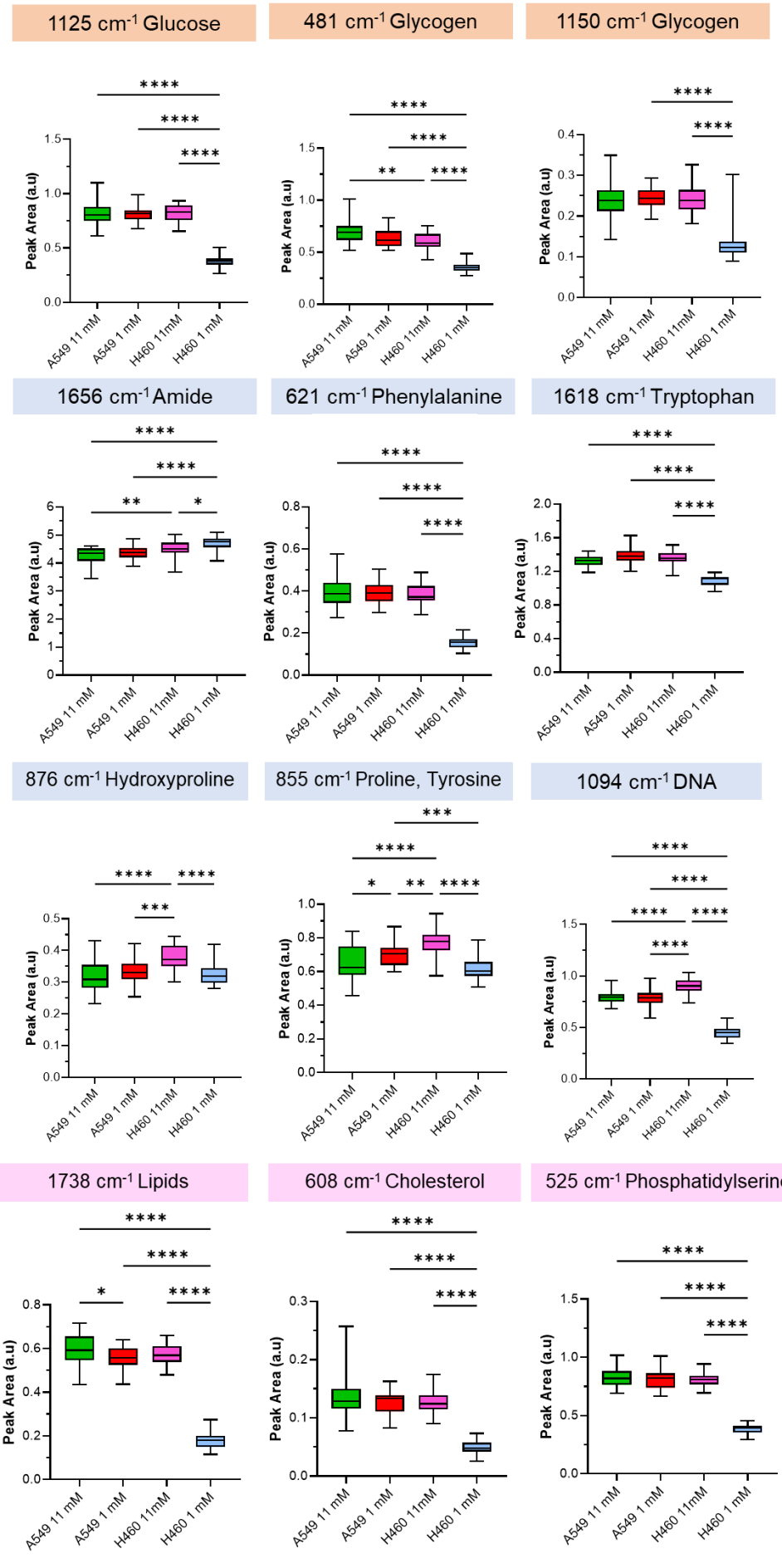
1125 cm-1 Glucose
481 cm-1 Glycogen
1150 cm-1 Glycogen
1656 cm-1 Amide
621 cm-1 Phenylalanine
1618 cm-1 Tryptophan
876 cm-1 Hydroxyproline
855 cm-1 Proline, Tyrosine
1094 cm-1 DNA
1738 cm-1 Lipids
608 cm-1 Cholesterol
525 cm-1 Phosphatidylserine
Peak Area (a.u)
A549 11 mM
A549 1 mM
H460 11mM
H460 1 mM

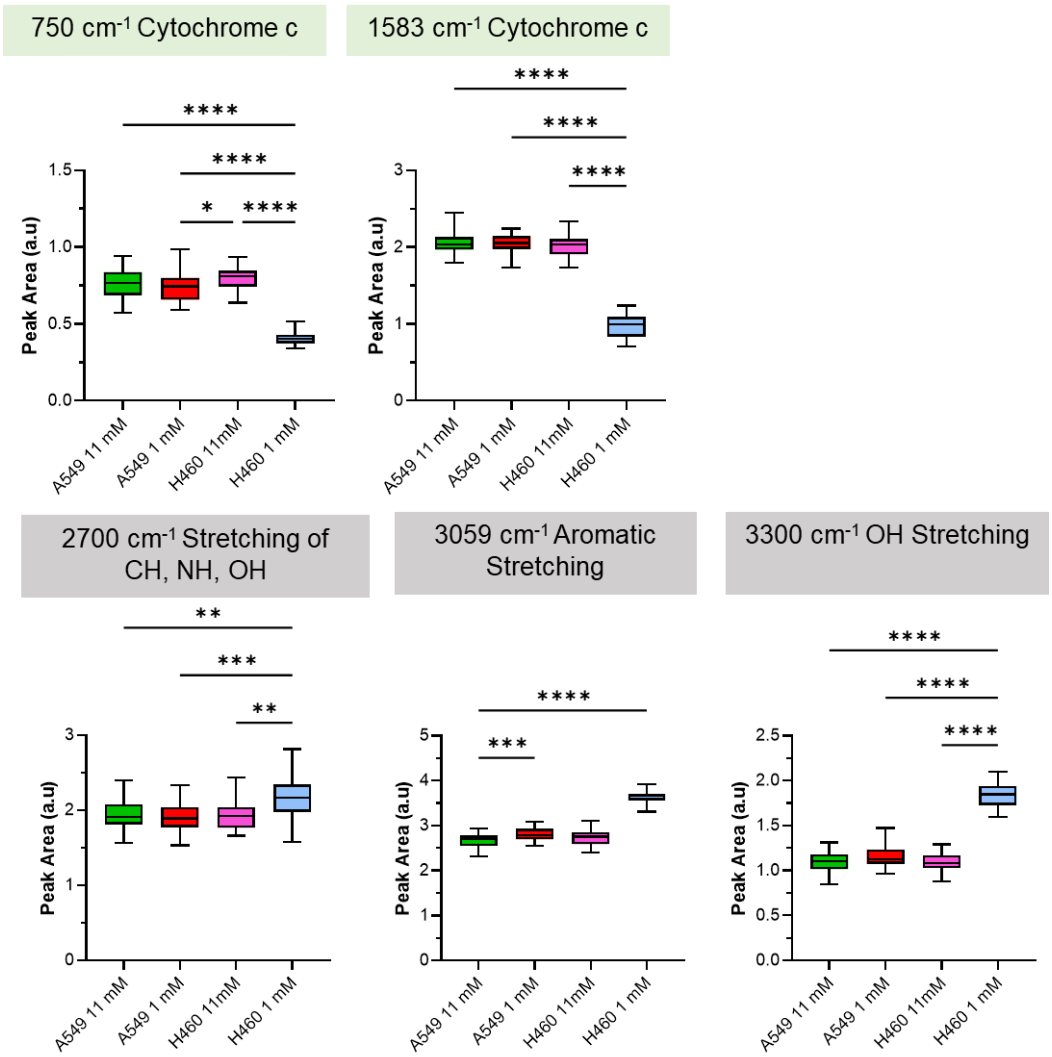

Figure 5.6. The effect of glucose manipulation on biomolecules in A549 and H460 cells. *A549 and H460 cells were grown in 11 mM or 1 mM glucose media for 72 hours with daily media replenishment. Cells were suspended in solution and dried onto aluminium coated slides for spectral acquisition with an HR Evolution confocal Raman microscope (Horiba). 10 spectra per cell and ~35 cells per sample were collected. Spectra underwent pre-processing and average spectra per sample plotted in an R environment. LDA was performed and top contributing peaks to separation on LD1 or LD2 were quantified by peak area. Data is represented as mean ± min/max. Statistical analysis was carried out by one-way ANOVA with Tukey's post hoc multiple comparisons test to compare the means in each group. When SDs were unequal, Brown-Forsythe ANOVA with Dunnett's T3 multiple comparisons test was used to compare the means in each group (*, $p < 0.05$; **, $p < 0.01$; ***, $p < 0.001$; ****, $p < 0.0001$). N=1 of 35 replicate cells per group.*

5.6 Use of metabolism inhibitors create distinct phenotypes in A549 and H460

With evidence that different metabolic phenotypes can be generated through glucose manipulation, the capabilities of Raman spectroscopy to detect robust differences in metabolism through drug effects was tested. A549 and H460 cells were treated for 72 hours with 2DG or AA in high and low glucose in order to inhibit glycolysis and OXPHOS respectively. The MitoXpress Xtra and pH Xtra assay were utilised to calculate the OCR and ECAR respectively as a readout of the drug effects on metabolism. Raman spectroscopy was performed on A549 and H460 cells, and spectra analysed by LDA to identify if the different metabolism modifying drugs cause differential groupings as expected.

In A549 cells, AA caused the OCR to decrease with significant changes in 1 mM glucose ($p = 0.0022$) (Figure 5.7A) which was accompanied by a significant increase in ECAR in 11 mM glucose ($p = 0.0002$) and a small increase in ECAR in 1 mM glucose (Figure 5.7B). Both indicate AA causes an inhibition of OXPHOS and increase in glycolysis to compensate, as expected. 2DG caused a significant increase in OCR in both 11 mM ($p = 0.0092$) and 1 mM ($p = 0.0049$) glucose; however no decrease in ECAR was observed as would be expected from a glycolysis inhibitor, despite a seemingly compensatory increase in OXPHOS.

Analysis of Raman spectra showed that drug treated cells had a distinct phenotype from untreated cells, shown by clear group separation by LDA (Figure 5.7D). A more glycolytic phenotype would be expected to be similar to A549 11 mM samples; however the AA treated cells did not group toward these cells. Likewise, a more OXPHOS phenotype would be expected to group towards the H460 1 mM glucose group, the most OXPHOS of the samples. 2DG treated samples grouped close to H460 1 mM samples, with little separation between the two on LD1, however 2DG treated cells were separated well on LD2 from the high OXPHOS H460 1 mM and possessed some overlap with the AA group. It is plausible that the

presence of the drugs inside the cells cause the two groups to be similar despite having different metabolic phenotypes.

In H460 cells, a similar trend was observed. AA caused a decrease in OCR, which proved significant in 1 m\M glucose ($p = 0.0018$) (Figure 5.8A), and a significant increase in ECAR (Figure 5.8C) in 11 mM ($p = 0.0268$) and 1 mM ($p = 0.0039$) glucose, indicative of a more glycolytic phenotype. This should group closely with A549 11 mM on the LDA plot. 2DG did not cause any significant changes in OCR but unexpectedly increased ECAR, of which was significant in 1 mM glucose ($p = 0.0005$). LDA showed A549 and H460 in 11 mM closely grouped together but were separated well from treated cells due to differences on LD1 (Figure 5.8D). 2DG and AA had separate groupings from one another based on differences in LD2, with spectra from 2DG treated cells and high OXPHOS H460 1 mM cells highly associated with one another.

Overall, in both A549 and H460 cells, use of AA and 2DG does create distinct phenotypes which can be separated by LDA; however, the cells treated with drug closely group together.

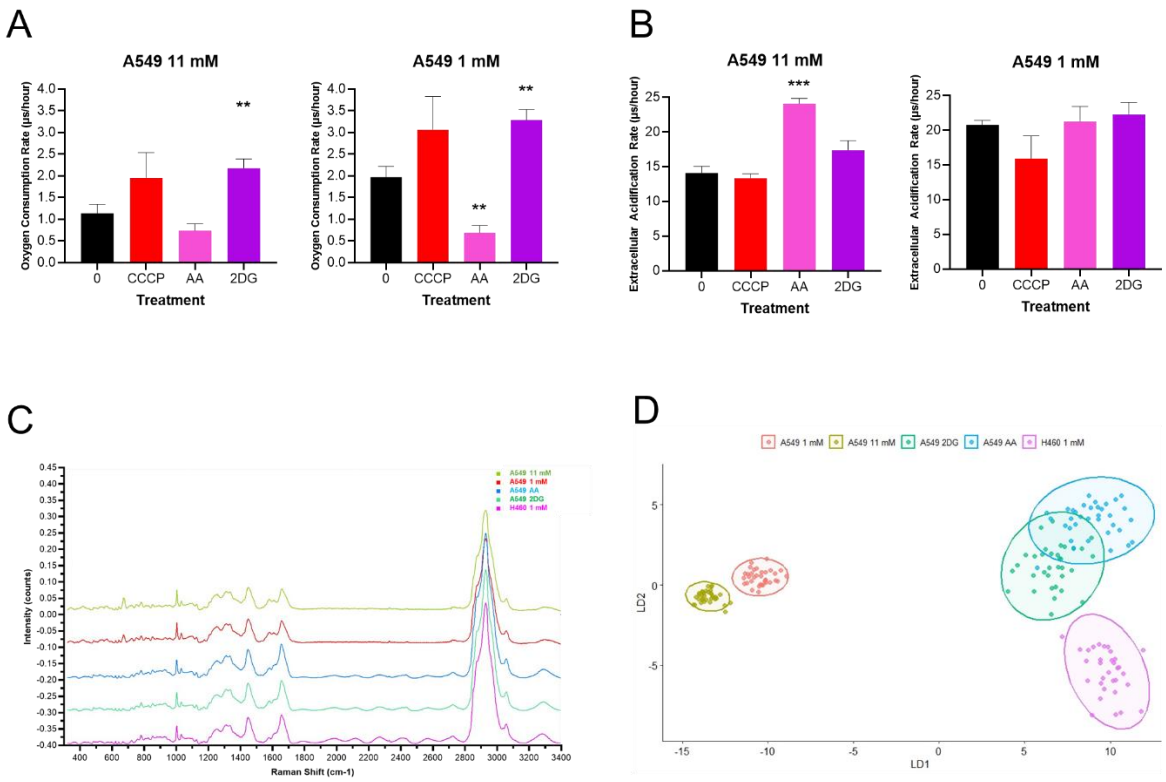

Figure 5.7. The effect of metabolism targeting drugs on Raman spectra in A549 cells. *A549 cells were grown in 11 mM or 1 mM glucose media including CCCP, AA, or 2DG for 72 hours with daily media replenishment. Cells were suspended in solution and dried onto aluminium coated slides for spectral acquisition with an HR Evolution confocal Raman microscope (Horiba). 10 spectra per cell and ~35 cells per sample were collected. Spectra underwent pre-processing and average spectra per sample plotted in an R environment. The MitoXpress Xtra and pH Xtra assays were utilised to measure oxygen consumption and extracellular acidification in live cells. MARS software was utilised to calculate OCR and ECAR. (A) represents mean OCR ± SEM and (B) mean ECAR ± SEM. (C) represents averaged Raman spectra for each sample and (D) LDA plot of sample groups, with different colours to denote different groups. Statistical analysis was performed by one way ANOVA with Dunnett's post hoc multiple comparisons test to compare means to that of untreated controls. When SDs were unequal, Browne-Forsythe one-way ANOVA with Dunnett's T3 multiple comparisons post hoc tests to compare treated cells to untreated controls (**, $p < 0.01$; ***, $p < 0.001$). N=3 for OCR and ECAR analysis and N=1 of 35 replicate cells per group for Raman analysis.*

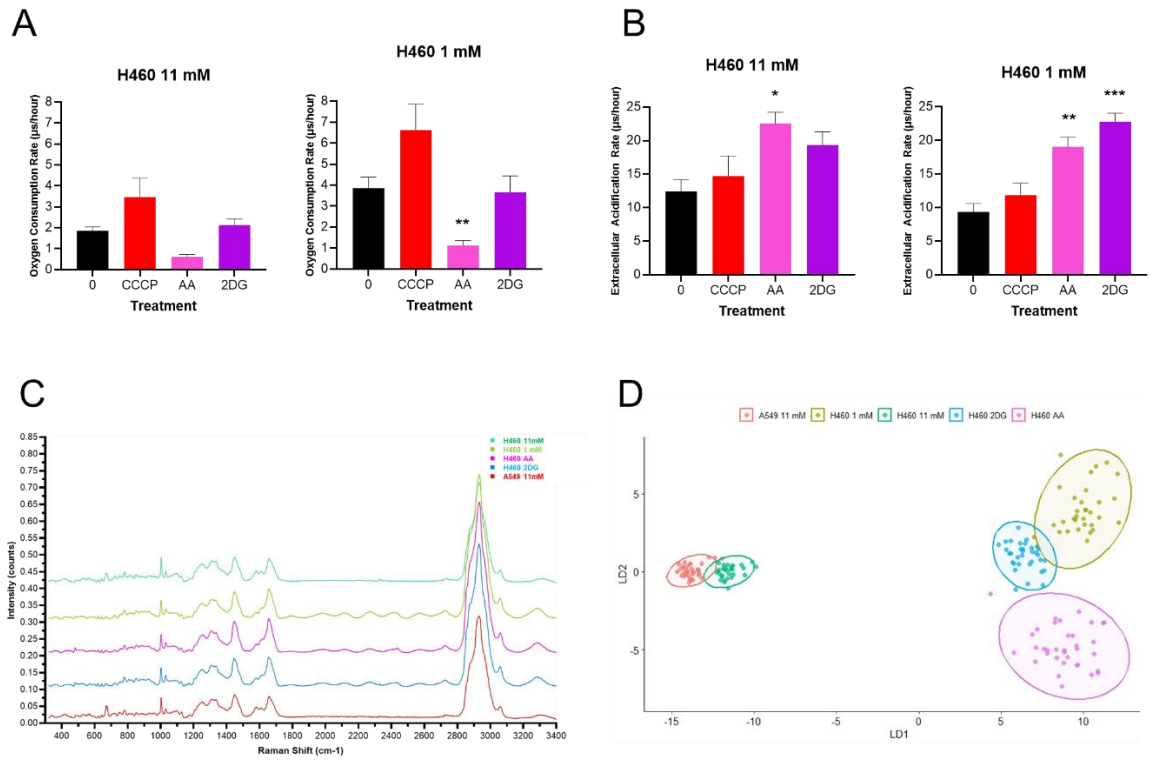

Figure 5.8. The effect of metabolism targeting drugs on Raman spectra in H460 cells. *H460 cells were grown in 11 mM or 1 mM glucose media including CCCP, AA, or 2DG for 72 hours with daily media replenishment. Cells were suspended in solution and dried onto aluminium coated slides for spectral acquisition with an HR Evolution confocal Raman microscope (Horiba). 10 spectra per cell and ~35 cells per sample were collected. Spectra underwent pre-processing and average spectra per sample plotted in an R environment. The MitoXpress Xtra and pH Xtra assays were utilised to measure oxygen consumption and extracellular acidification in live cells. MARS software was utilised to calculate OCR and ECAR. (A) represents mean OCR ± SEM and (B) mean ECAR ± SEM. (C) represents averaged Raman spectra for each sample and (D) LDA plot of sample groups, with different colours to denote different groups. Statistical analysis was performed by one way ANOVA with Dunnett's post hoc multiple comparisons test to compare means to that of untreated controls. When SDs were unequal, Browne-Forsythe one-way ANOVA with Dunnett's T3 multiple comparisons post hoc tests to compare treated cells to untreated controls (*, $p < 0.05$; **, $p < 0.01$; ***, $p < 0.001$). N=3 for OCR and ECAR analysis and N=1 of 35 replicate cells per group for Raman analysis.*

5.7 Treatment with NBS037 creates distinct phenotypes similar to that of antimycin A in A549 cells

Prior experiments, carried out by Sarah Hutchinson, produced the average Raman spectra from solid NBS037. LabSpec 6 software was utilised to find the local intensity maxima, the highest intensity peaks in the spectrum, which could be compared to Raman spectra obtained from cells treated with NBS037 (Figure 5.9).

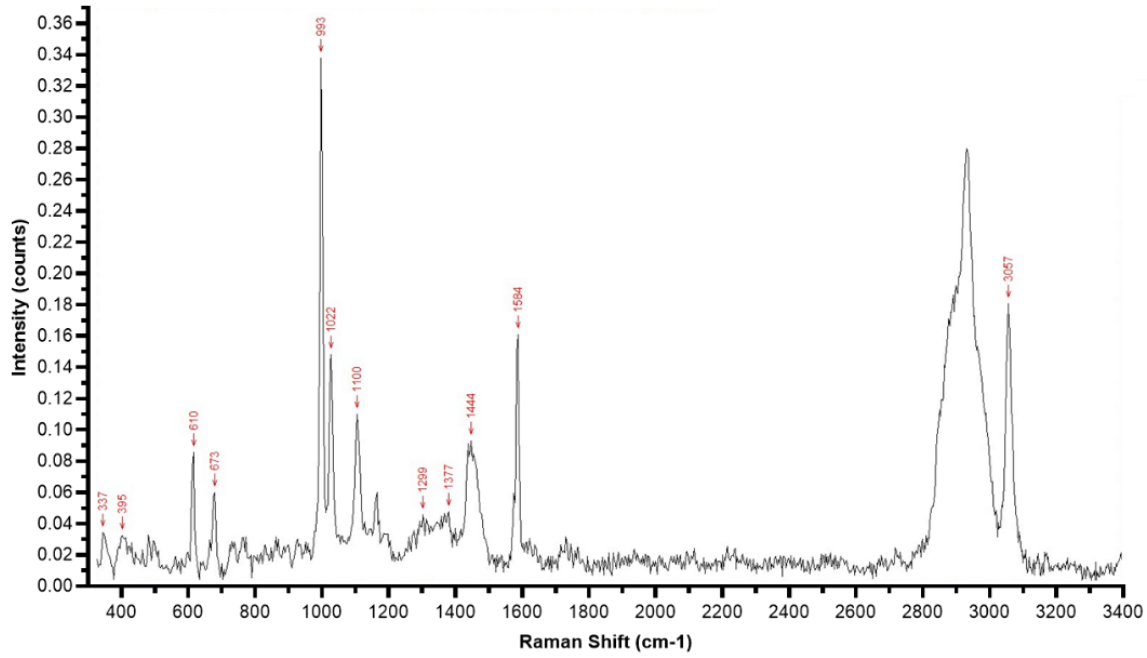

Figure 5.9. Average spectral profile of NBS037 (Hutchinson). *Powdered NBS037 was analysed by Raman spectroscopy (Horiba) and highest intensity peaks labelled. N=3.*

To test the effects of NBS037 on the Raman spectra observed, A549 and H460 cells were grown in 11 mM and 1 mM glucose, with the addition of 0.5 μM, 1 μM NBS037 or AA, for 72 hours. Media was changed daily to maintain glucose levels. Raman spectra were pre-processed and analysed by LDA, with peaks correlating to significant differences in LD1 or LD2 identified and areas of such peaks quantified.

In A549 cells, in both glucose conditions, untreated cells had clear separation from 0.5 μM NBS037, 1 μM NBS037 and AA (Figure 5.10). Untreated cells and 0.5 μM NBS037 separate well from one another on LD1 and LD2, particularly in 11 mM glucose. Untreated cells and 0.5 μM NBS037 cells were separated well from 1 μM NBS037 and AA on LD1. 1 μM NBS037 and AA show close grouping with some overlap; however more separation on LD2 is observed between these groups in 1 mM glucose (Figure 5.10C).

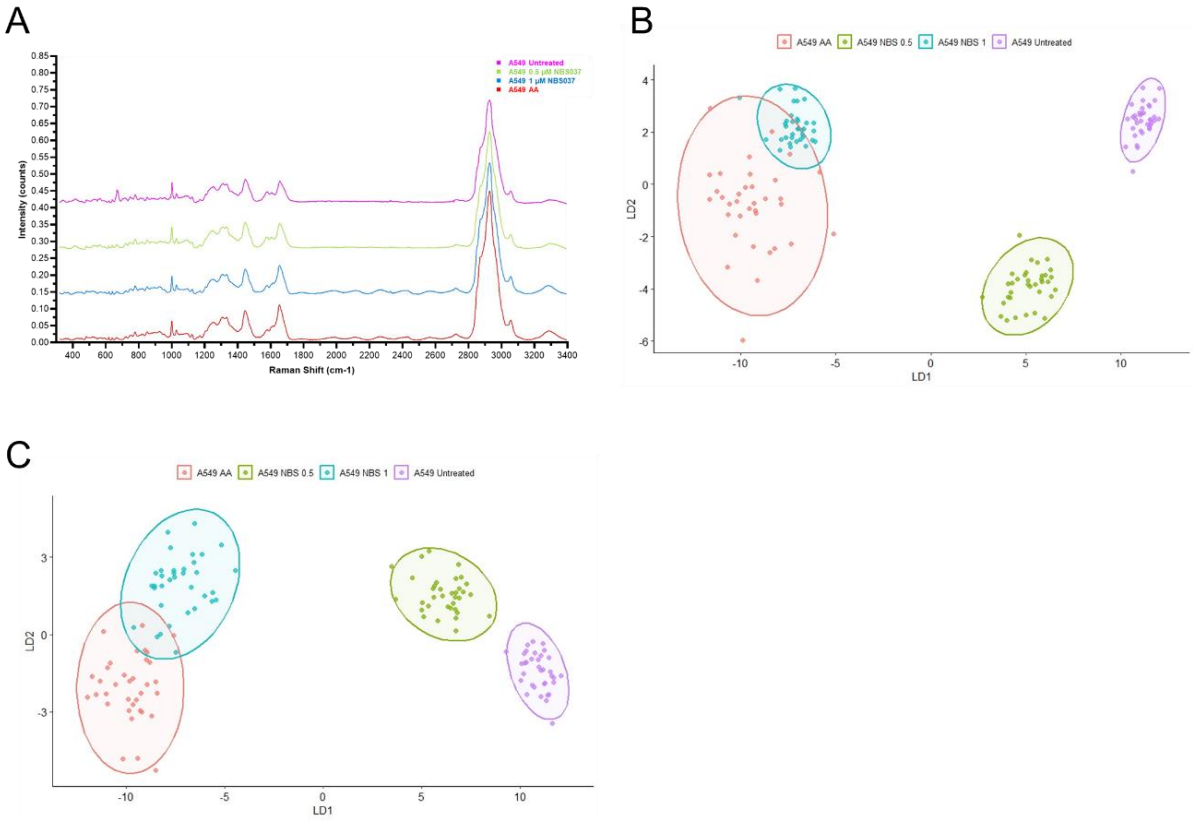

Figure 5.10. The effect of OXPHOS inhibition on Raman spectra in A549 cells. *A549 cells were grown in 11 mM or 1 mM glucose media for 72 hours with daily media replenishment. Cells were suspended in solution and dried onto aluminium coated slides for spectral acquisition with an HR Evolution confocal Raman microscope (Horiba). 10 spectra per cell and ~35 cells per sample were collected. Spectra underwent pre-processing and average spectra per sample plotted in an R environment. (A) represents averaged spectra in 11 mM glucose and LDA plots showing group separation were calculated and plotted for (B) 11 mM glucose and (C) 1 mM glucose, with different colours to denote different groups. N=1 of 35 replicate cells per group.*

Key contributors to separation on LD1, which gave clear separation of untreated cells and low dose of NBS037 from AA and higher dose of NBS037, included amino acids such as tryptophan (1618 cm^{-1}) and tyrosine (1558 cm^{-1}), lipids and phospholipids such as phosphatidylserine (1716 cm^{-1}) and phosphatidylinositol (576 cm^{-1}) and DNA bases (see Appendix C). Amino acids, DNA bases, and lipids were all significantly increased with 0.5 μM NBS037 compared to untreated ($p < 0.0001$) and 1 μM NBS037 treated cells (Figure 5.11). Whilst AA treated cells had significantly decreased lipid ($p < 0.0001$) and adenine levels ($p < 0.0001$) compared to untreated cells, tryptophan and guanine were significantly increased ($p < 0.0001$ and $p = 0.001$ respectively); however, 1 μM NBS037 did not always follow the same trend as AA.

Separation of groups on LD2 included contributions from polyhydroxybutyrate (357 cm^{-1}), carbohydrates such as glucose (1125 cm^{-1}) and glycogen (481 cm^{-1}), DNA bases, and cholesterol (490 cm^{-1}) (see Appendix C). Similar to the trends observed with other biological molecules, glucose was significantly increased in 0.5 μM NBS037 treated cells compared to other treatment groups ($p < 0.0001$) but glycogen was decreased significantly compared to untreated ($p < 0.0001$) and 1 μM NBS037 treated cells ($p < 0.0001$). Significantly decreased glycogen was also observed in AA treated cells compared to untreated cells ($p < 0.0001$).

Many molecules proved to contribute to differences in LD1 and LD2, including the amino acids tyrosine and cysteine, cholesterol, stretching vibrations, and in peaks from NBS037 at 337 cm^{-1} and 395 cm^{-1}. Whilst these NBS037 peaks, and the peak at 993 cm^{-1} corresponding to NBS037, were significantly increased in 0.5 μM NBS037 treated cells compared to untreated ($p < 0.0001$) and decreased in AA treated cells ($p < 0.0001$), there was no significant difference with 1 μM NBS037 compared to untreated cells. Therefore, whilst some NBS037 associated bands corresponded to separation of groups, quantification of these peaks could not be utilised as a clear test for NBS037 presence in these cells in this sample.

Changes in cytochrome *c* bands were also analysed to investigate any differences in REDOX balance with NBS037 use. Compared to untreated cells, 0.5 μM NBS037 caused a significant increase in reduced cytochrome *c* at both 750 cm^{-1} ($p < 0.0001$) and 1583 cm^{-1} ($p < 0.0001$). 1 μM NBS037, however, caused no significant changes in cytochrome *c* compared to untreated cells. AA caused a significant decrease in cytochrome *c* bands at 750 cm^{-1} compared to untreated ($p < 0.0001$) and 1μM NBS037 ($p < 0.0001$) treated cells; however a significant increase in peak intensity at 1583 cm^{-1} for cytochrome *c* was observed with AA when compared to untreated ($p = 0.0321$) and 1 μM NBS037 ($p = 0.0321$) treated cells.

407 cm^{-1} Glucose

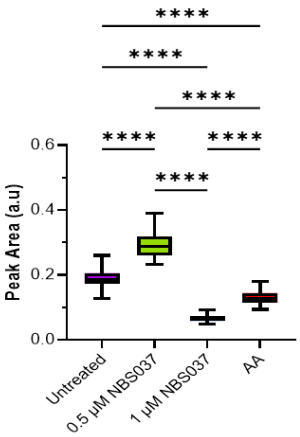

1125 cm^{-1} Glucose

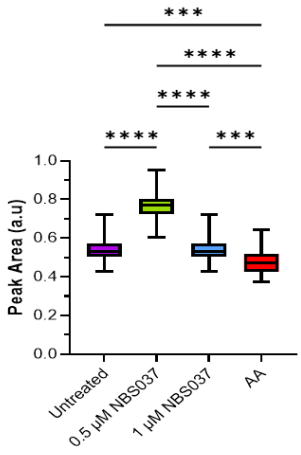

481 cm^{-1} Glycogen

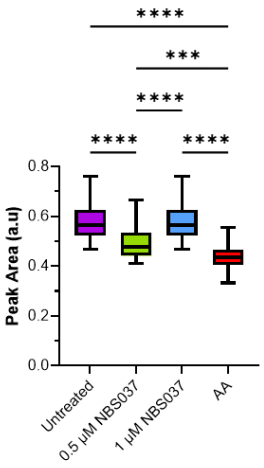

1558 cm^{-1} Tyrosine

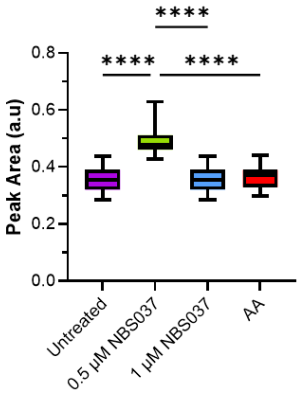

1618 cm^{-1} Tryptophan

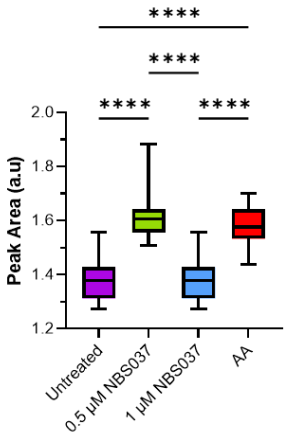

720 cm^{-1} Adenine

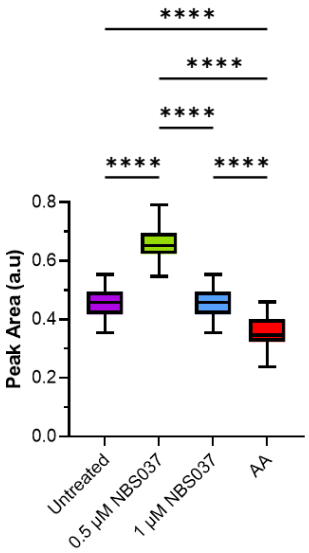

1575 cm^{-1} Guanine

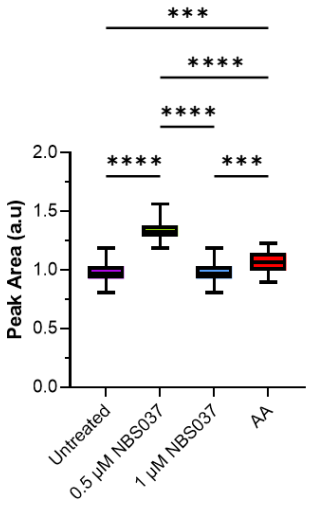

1738 cm^{-1} Lipids

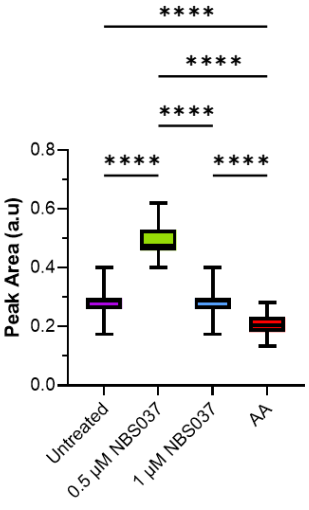

525 cm^{-1} Phosphatidylinositol

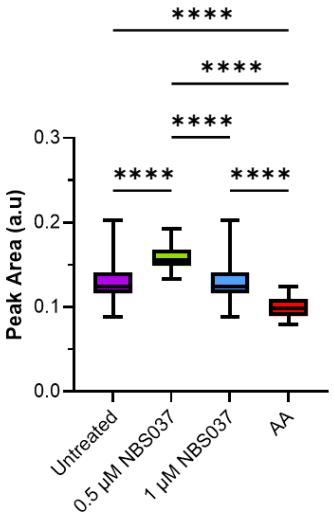

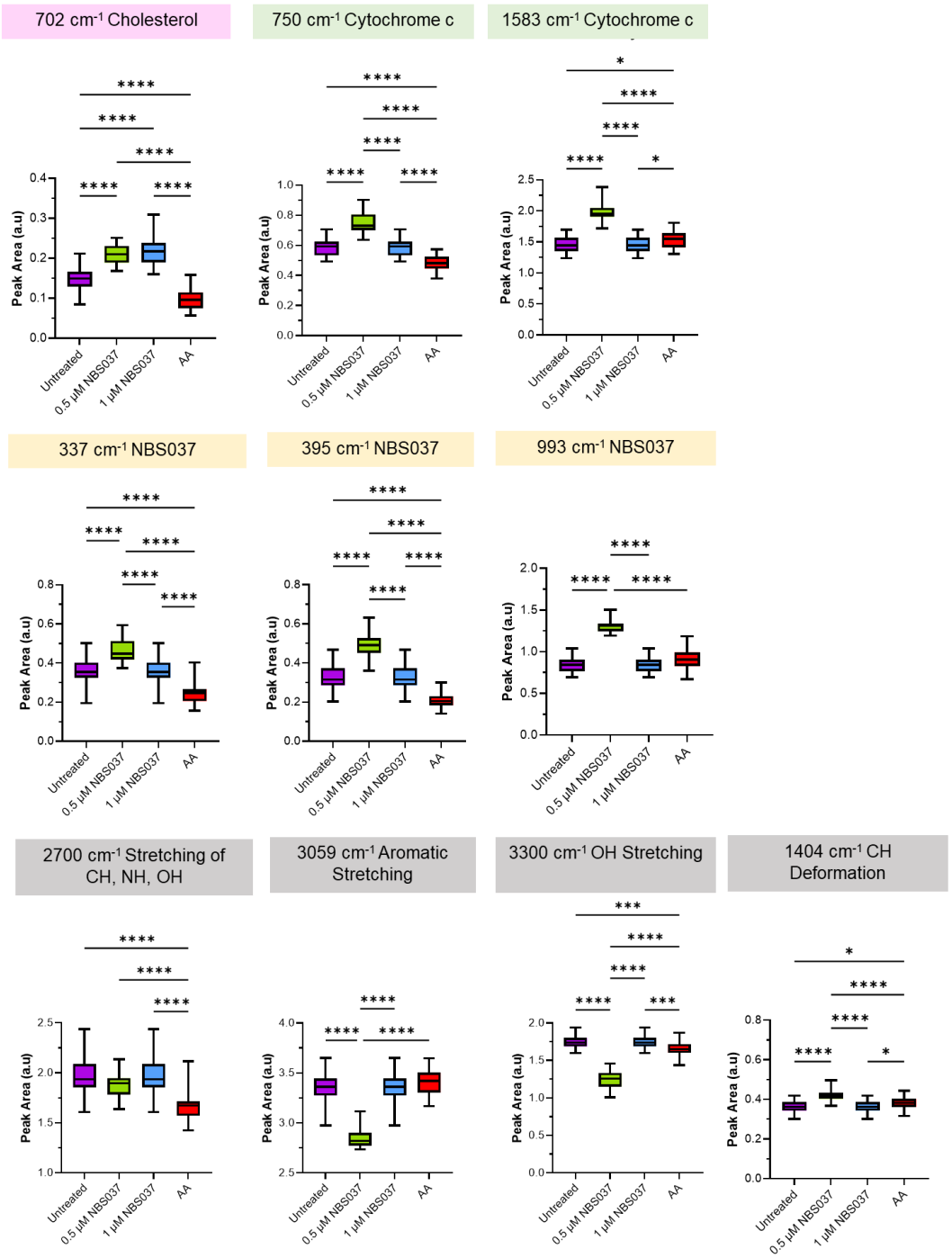

Figure 5.11. The effect of OXPHOS inhibition on biomolecules in A549 cells. *A549 cells were grown in 11 mM glucose media for 72 hours with daily media replenishment. Cells were suspended in solution and dried onto aluminium coated slides for spectral acquisition with an HR Evolution confocal Raman microscope (Horiba). 10 spectra per cell and ~35 cells per sample were collected. Spectra underwent pre-processing and average spectra per sample plotted in an R environment. LDA was performed and top contributing peaks to separation on LD1 or LD2 were quantified by peak area. Data is represented as mean ± min/max. Statistical analysis was carried out by one way ANOVA with Tukey's post hoc multiple comparisons test to compare the means in each group. When SDs were unequal, Brown-Forsythe ANOVA with Dunnett's T3 post hoc multiple comparisons test to compare the means in each group (*, $p < 0.05$; **, $p < 0.01$; ***, $p < 0.001$; ****, $p < 0.0001$). N=1 of 35 replicate cells per group.*

5.8 Treatment with NBS037 creates distinct phenotypes similar to that of antimycin A in H460 cells

In H460 cells, distinct group separation by LDA was also observed (Figure 5.12). Untreated H460 and A549 cells formed distinct groups from one another and were well separated from treated cells based on contributions on LD1. The cells treated with OXPHOS inhibitors did not group closely to the more glycolytic A549 line so a clear glycolytic phenotype was not observed based on grouping alone. The NBS037 and AA treated cells grouped closely together with some separation on LD2 distinguishing the groups, albeit with some overlap. Large overlap is observed with 1 μM NBS037 and AA, indicating that 1 μM NBS037 may cause a similar OXPHOS inhibition effect as AA. 0.5 μM NBS037 as a weaker OXPHOS inhibitor was grouped further away from AA as expected.

Multiple compounds led to the separation of untreated versus treated groups on LD1, including glucose (913 cm^{-1}), glycerol (589 cm^{-1}), amino acids such as tryptophan (1618 cm^{-1}) and phenylalanine (621 cm^{-1}), DNA bases and nucleic acids (1054 cm^{-1}), and amide bonds (1637 cm^{-1}). Interestingly, the OXPHOS inhibitors had a tendency to significantly decrease glucose levels towards that observed in A549 (glycolytic) cells but with the exception of 0.5 μM NBS037 which caused a significant increase in glucose compared to untreated H460 cells ($p = 0.0133$). Glycerol and lipids were also significantly decreased in drug treated cells compared to untreated H460 and A549 cells, but no difference between H460 and A549 cells was observed.

Analysis of amino acids showed different trends dependent on the compound, with phenylalanine, proline, tryptophan, and nucleic acids all significantly decreased with 1 μM NBS037 and in some cases, AA treatment. Tyrosine and amide bonds had a significant increase in peak intensity with AA and NBS037 induced OXPOS inhibition ($p < 0.0001$).

Separation on LD2 was largely driven by changes in proline (855 cm^{-1}) and hydroxyproline (815 cm^{-1}), with nucleic acids (810 cm^{-1}) and tryptophan (573 cm^{-1}) also contributing, so changes in amino acids were highly significant in H460 cells.

Glycogen (481 cm^{-1} and 1150 cm^{-1}), and stretching vibrations also displayed key changes in LD1 and LD2. Glycogen was significantly decreased in drug treated cells compared to untreated H460 cells and untreated A549 cells, but was significantly increased in glycolytic A549 cells when compared to untreated H460 cells ($p = 0.0019$).

Similar to the findings in A549, peaks corresponding to NBS037 were significantly decreased in cells treated with OXPHOS inhibitors compared to untreated A549 and H460 cells ($p < 0.0001$). In A549 cells however, cytochrome *c* peaks were significantly lowered with all doses of NBS037 as well as AA when compared to untreated H460 cells (all $p < 0.0001$) and untreated A549 cells (all $p < 0.0001$), indicative of a decrease in levels of reduced cytochromes. In most of the molecules analysed, trends followed by NBS037 and AA treated cells were unlike that of untreated A549 cells which are highly glycolytic, so no clear association with increased glycolysis was observed with OXPHOS inhibition from this data.

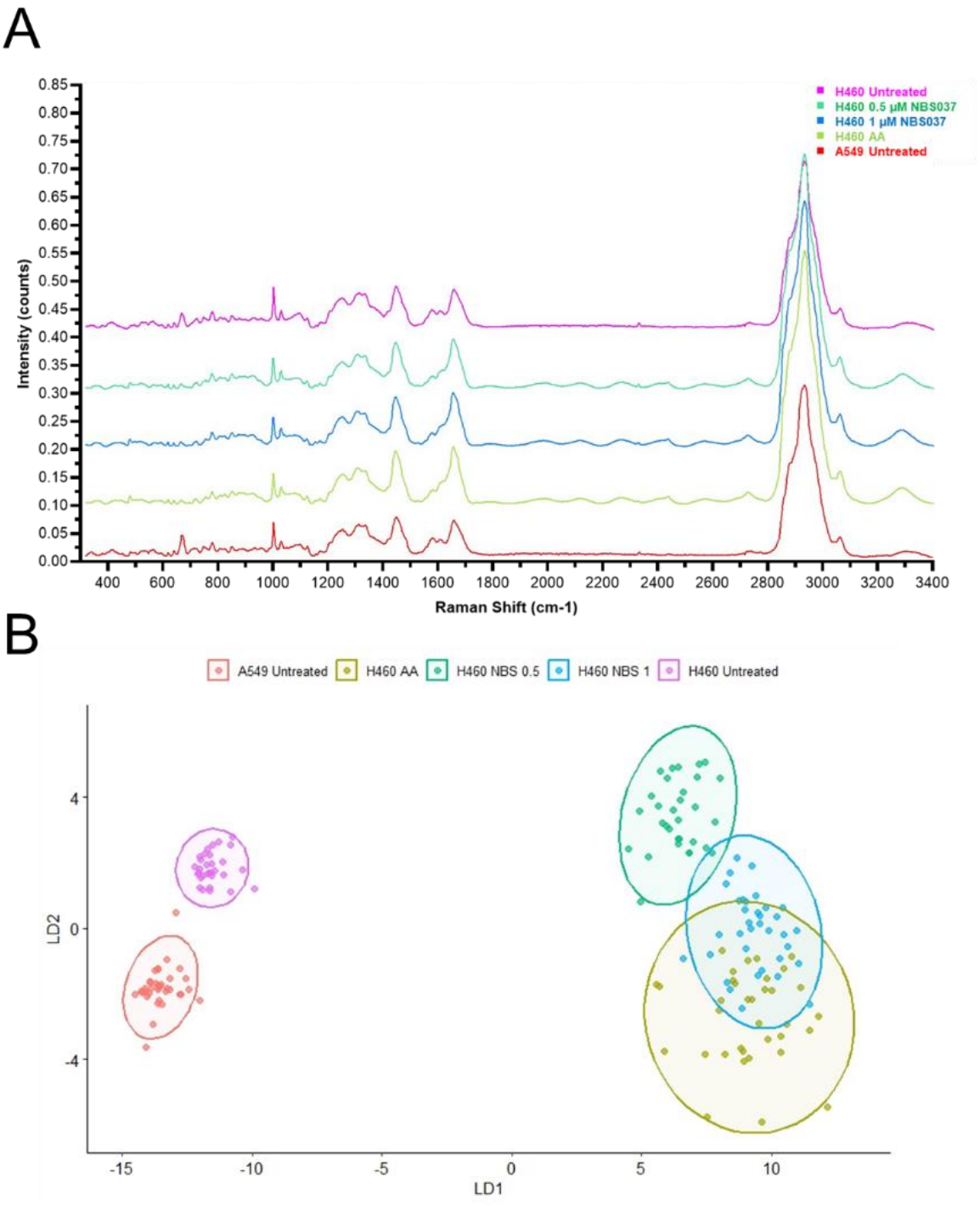

Figure 5.12. The effect of OXPHOS inhibition on Raman spectra in H460 cells. *H460 cells were grown in 11 mM or 1 mM glucose media for 72 hours with daily media replenishment. Cells were suspended in solution and dried onto aluminium coated slides for spectral acquisition with an HR Evolution confocal Raman microscope (Horiba). 10 spectra per cell and ~35 cells per sample were collected. Spectra underwent pre-processing and average spectra per sample plotted in an R environment. (A) represents averaged spectra and (B) LDA plots showing group separation were calculated and plotted, with different colours to denote different groups. N=1 of 35 replicate cells per group.*

913 cm^{-1} Glucose

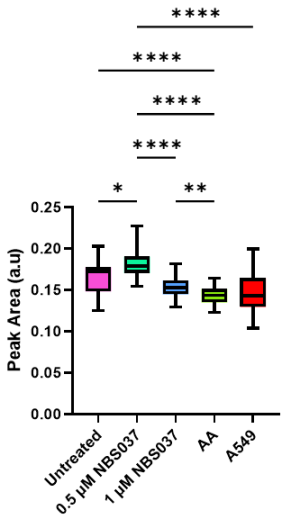

481 cm^{-1} Glycogen

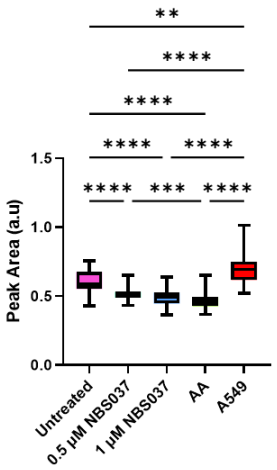

1150 cm^{-1} Glycogen

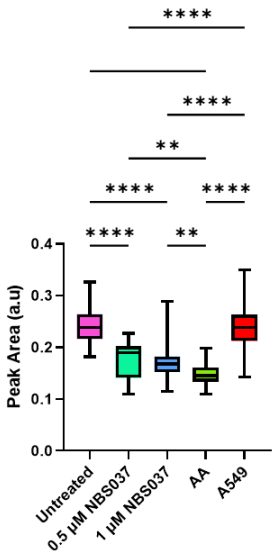

621 cm^{-1} Phenylalanine

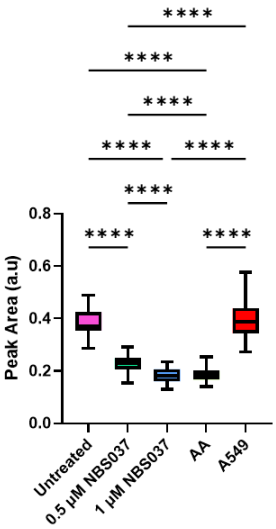

828 cm^{-1} Tyrosine

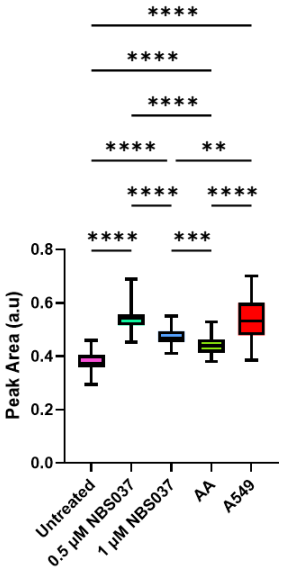

810 cm^{-1} Nucleic Acids

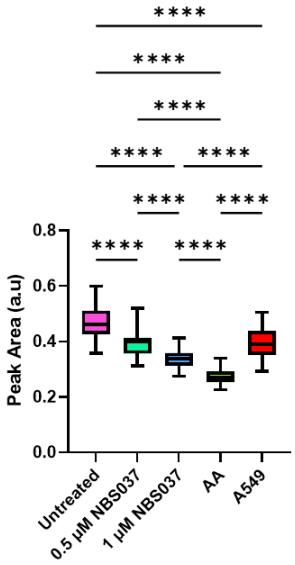

933 cm^{-1} Proline

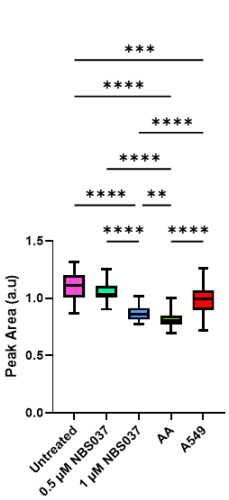

1618 cm^{-1} Tryptophan

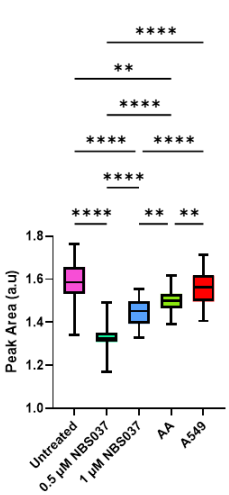

1637 cm^{-1} Amide I

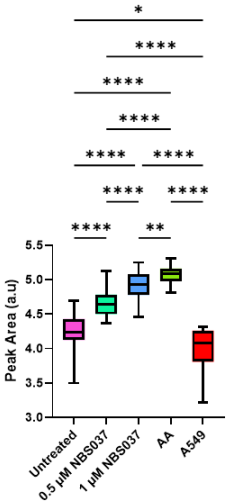

933 cm^{-1} Proline

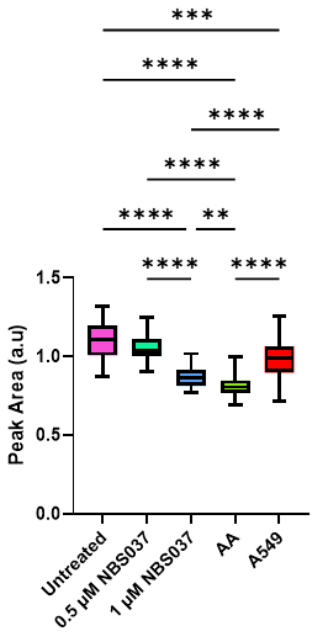

1618 cm^{-1} Tryptophan

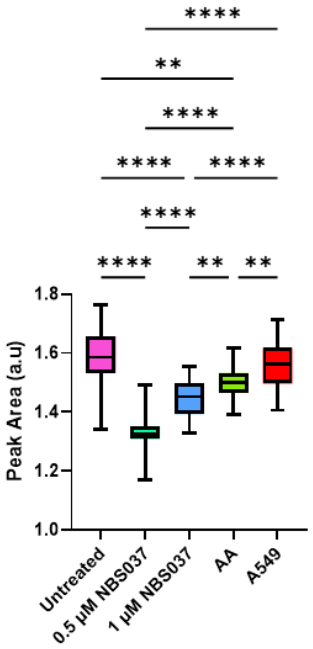

1637 cm^{-1} Amide I

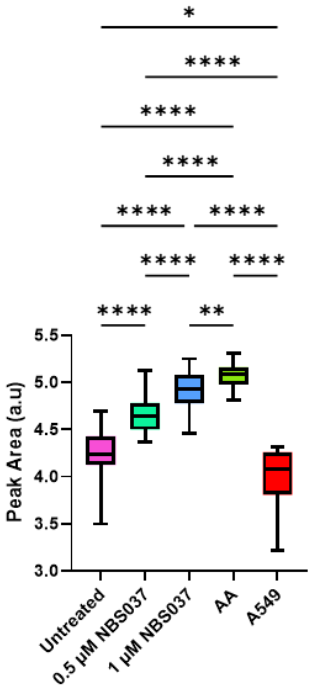

589 cm^{-1} Glycerol

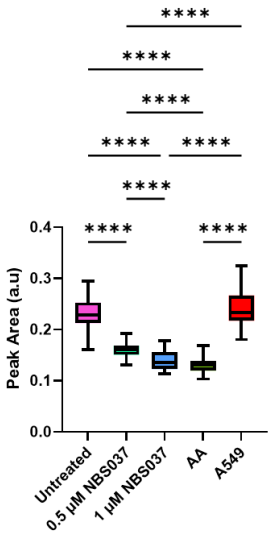

1168 cm^{-1} Lipids

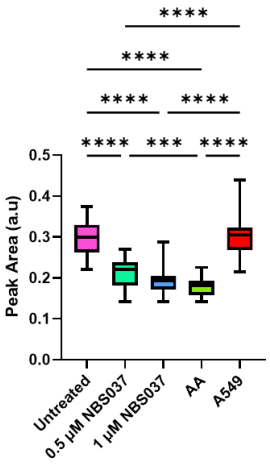

750 cm^{-1} Cytochrome c

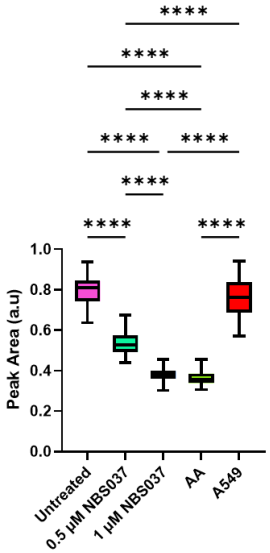

1583 cm^{-1} Cytochrome c

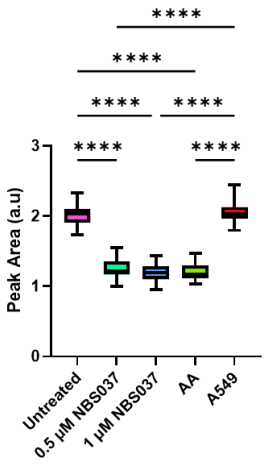

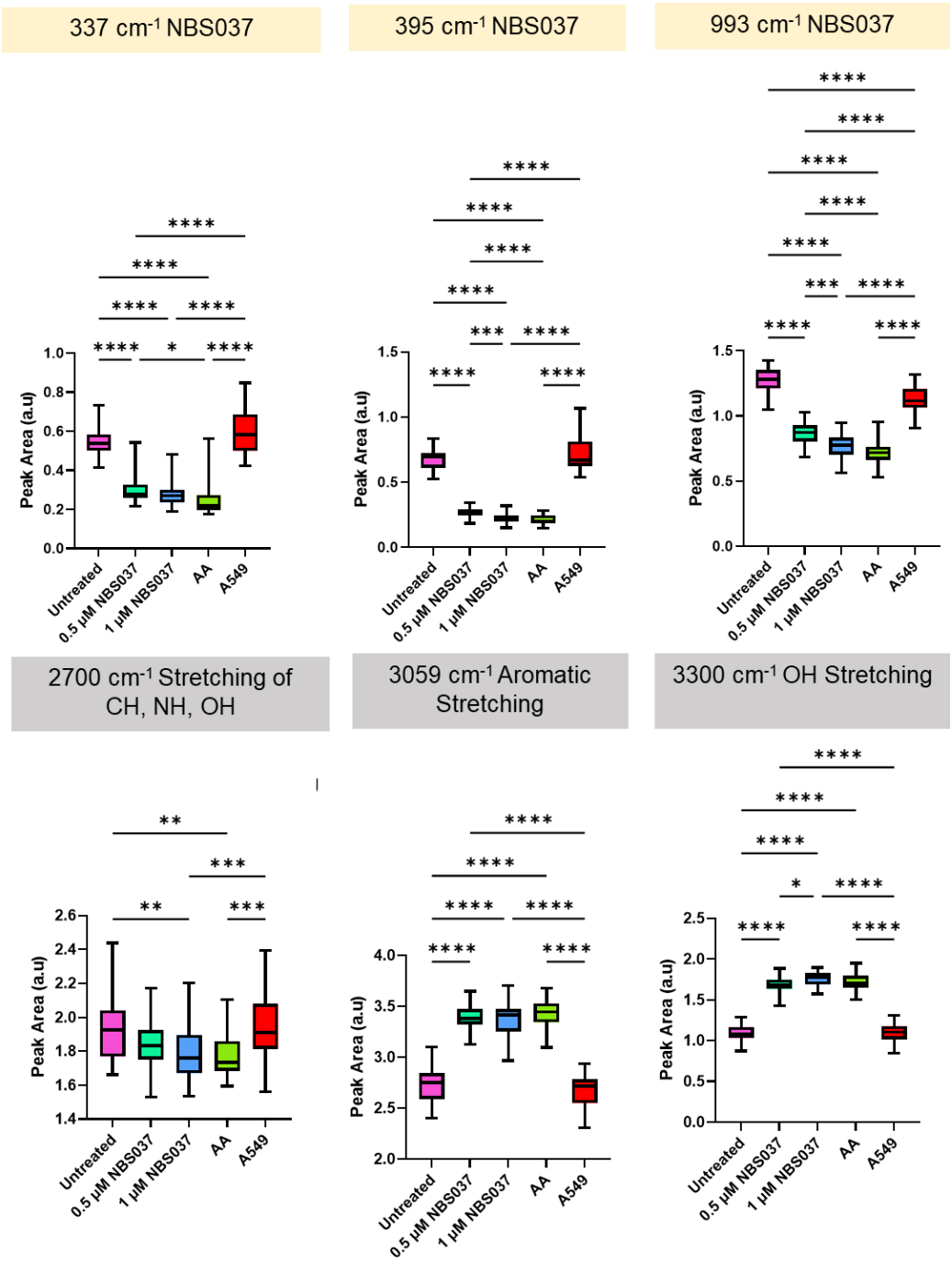

Figure 5.13. The effect of OXPHOS inhibition on biomolecules in H460 cells. *H460 cells were grown in 11 mM glucose media for 72 hours with daily media replenishment. Cells were suspended in solution and dried onto aluminium coated slides for spectral acquisition with an HR Evolution confocal Raman microscope (Horiba). 10 spectra per cell and ~35 cells per sample were collected. Spectra underwent pre-processing and average spectra per sample plotted in an R environment. LDA was performed and top contributing peaks to separation on LD1 or LD2 were quantified by peak area. Data is represented as mean ± min/max. Statistical analysis was carried out by one way ANOVA with Tukey's post hoc multiple comparisons test to compare the means in each group. When SDs were unequal, Brown-Forsythe ANOVA with Dunnett's T3 multiple comparisons test was utilised to compare the means in each group (*, $p < 0.05$; **, $p < 0.01$; ***, $p < 0.001$; ****, $p < 0.0001$). N=1 of 35 replicate cells per group.*

5.9 Discussion

5.9.1 Generation of metabolic phenotypes

The aim of this work was to investigate if Raman spectroscopy can be utilised to detect a specific metabolic signature in cancer cells which is associated with a high OXPHOS or high glycolysis phenotype. To achieve this, cell lines which have high rates of OXPHOS or high glycolysis were first established through manipulation of glucose in the cell culture media. It is well documented that high glucose in culture media supresses mitochondrial respiration and causes an over reliance on glycolysis and therefore produces a more glycolytic phenotype[422]. A549 and H460 cells were grown in standard culture media containing high glucose (11 mM) or low glucose (1 mM) media for 72 hours to allow cells to adapt. The MitoXpress Xtra assay confirmed that H460 cells have a higher OCR, and therefore higher OXPHOS rate than A549 cells, and that decreasing the glucose in the media does have a tendency to increase OXPHOS in cells, albeit more so in H460 than A549 (Figure 5.4).

Use of drugs to modulate metabolism was also tested through the OXPHOS inhibitor AA and glycolysis inhibitor 2DG. When faced with metabolism inhibitors, it would be expected that cells would upregulate other metabolic pathways in order to maintain ATP production as observed with the OXPHOS inhibitors in Table 1.1. When treated with AA, this effect is observed. In both cell lines, treatment with AA caused a decrease in OCR and significant increase in ECAR in all but A549 at low glucose in which no change in ECAR was observed (Figure 5.7 and 5.8). This is indicative that AA can cause an upregulation of glycolysis in these conditions, which has been previously observed by others, and therefore AA treated cells may produce a Raman spectra of a more glycolytic phenotype[423]. With inhibition of glycolysis by 2DG, a compensatory upregulation of OXPHOS would be expected in order to maintain ATP levels, as noted in previous literature[424,425]. At the dose used of 500 μM , 2DG did not inhibit glycolysis in any cell line and instead caused an increase in ECAR and OCR (Figure 5.7 and 5.8). 2DG exerts its effects through inhibiting HK, but with glycolysis preceding OXPHOS, 2DG

would therefore impact both metabolic pathways[426]. At 500 μM, 2DG may weakly inhibit glycolysis, subsequently impact OXPHOS, and cause a compensatory upregulation of both in order to compensate for ATP deficits. The ATP assay highlighted the dose of 500 μM did cause a decrease in ATP levels but not at the same extent as 20 mM, in which glycolysis was completely inhibited (Figure 3.27). Furthermore, as discussed previously (see 3.26.2), 2DG does not impact only glycolysis, but glycosylation also[351] and the pH Xtra assay may be limited in its ability to detect lactate from glycolysis rather than total extracellular acidification which may have contributions from CO_2 produced. Therefore use of 2DG to alter metabolism did not result in a clear OXPHOS or glycolytic phenotype.

Overall, this work proved glucose manipulation was effective in generating different metabolic phenotypes, pushing cells towards higher OXPHOS in low glucose or higher glycolysis in high glucose. To some extent metabolism inhibitors could achieve some changes in metabolic signatures as clearly observed with AA, but inhibiting glycolysis with 2DG proved challenging as the drug would also affect OXPHOS since they are not mutually exclusive.

5.9.2 Separation of treated groups based off Raman spectra

Raman spectroscopy was utilised on cells grown in both high and low glucose, as well as with AA and 2DG to investigate if differences in Raman spectra are observed in cells with differential rates of OXPHOS and glycolysis. The statistical tools PCA and LDA were implemented to find how well the different sample groups separate based off the Raman spectra obtained. LDA is a supervised statistical tool, where sample group assignments are known prior to grouping the Raman spectra, whilst PCA is unsupervised and sample assignments remain unknown[427]. Since the aim of this work is to determine if an OXPHOS or glycolysis signature could be detected at all, LDA was utilised to reduce the dimensions of the data and clearly define the different groups, if any differences are found, such that the important features of the Raman spectra could be extracted and identified. LDA performed

better than PCA at group separation so was used for the later analyses in this chapter (Figure 5.5).

LDA showed clear separation of H460 cells in low glucose conditions from the rest of the groups, in agreement with the previous observation that these cells harbour the highest rate of OXPHOS (over double that of A549 cells) (Figure 5.4). The remaining groups showed some extent of overlap with A549 and H460 on high glucose most separated on LD2, and A549 on low glucose group situated between these two groups. This would be in agreement with what would be expected based on the different metabolism the cells exhibit, with A549 in low glucose showing higher OXPHOS, and behaving more similarly to H460 cells in high glucose.

Previously, only AA could produce a clear metabolic shift of OXPHOS to glycolysis. When testing if metabolism inhibitors also caused clear grouping, distinct groups were observed in treated versus untreated cells but any grouping supporting changes in metabolism was not observed (higher glycolysis with AA). In A549, 11 mM glucose and 1 mM glucose untreated cells were separated well on LD1, with treated groups very clearly separated from untreated groups. LD1 also separated H460 low glucose cells (as a high OXPHOS comparison) from AA and 2DG treated A549 cells, but with both drug treated groups overlapping (Figure 5.7). In H460 cells, untreated H460 and A549 in high glucose separated but had some overlap, whilst low glucose H460 and treated cells had clear separation from untreated controls on LD1 (Figure 5.8). The 2DG treated group was more closely associated with H460 low glucose samples, with the higher OXPHOS phenotype, in agreement with the observation that 2DG treatment also caused an increase in OCR (Figure 5.7 and 5.8). However, in both cell lines, AA treated cells were clearly separated away from A549 cells on high glucose, the most glycolytic of the samples, and was more closely associated with 2DG so the groupings did not indicate a clear OXPHOS or glycolysis divide. The increase in ECAR with 2DG was similar to that of AA, which may be a reason for both drugs grouping closely together if both drugs lead to similar changes in glycolysis or overall metabolism (Figure 5.6).

Overall, LDA was able to successfully separate high OXPHOS cells (H460 1 mM glucose) from cells in other glucose conditions, with some separation between cells which have varying OXPHOS rates (H460 11 mM glucose, A549 11 mM glucose, and A549 1 mM glucose). LDA was not able to distinguish such clear groupings based off metabolism when cells were treated with metabolism inhibitors, and instead clearly separated untreated and treated cells. Treated cells may group more closely together due to cellular stresses, with AA causing ATP depletion and 2DG with partial ATP depletion and glycosylation effects. These cellular stresses could be observed from the confocal microscopy of treated cells (Figure 5.2), where treatment caused a change in cell morphology.

5.9.3 Key biomolecules separating groups with differences in metabolism

In Raman spectroscopy, peak intensities for a biomolecule directly correlate to its concentration, until a point in which detection may be saturated and linearity between peak intensity and molecule concentration is no longer possible[428]. Peaks contributing to differences in LD1 and LD2, as well as a variety of biological molecules relevant in metabolism were quantified and found to be significantly different with changes in glucose concentration in the media. In H460 cells in low glucose, significant decreases in carbohydrates, amino acids, and lipids were all observed when compared to the other sample groups. Intracellular changes in these biomolecules can act as an indication of substrates utilised so with high rates of OXPHOS, it is unsurprising carbohydrates, lipids, and amino acids are all impacted as these are all potential substrates for oxidation in mitochondrial metabolism[28,46]. In H460 low glucose cells, the peak at 1656 cm^{-1} for amide bonds and peaks associated with stretching vibrations significantly increased (Figure 5.6). With amides the most prevalent bond in biomolecules, namely included in proteins, peptides, and DNA, increases in amide bonds could be indicative of increased protein content associated with higher OXPHOS, for example enhanced expression of respiratory machinery. The stretching vibrations are more linked to the –CH3,

–CH2, and C–H functional groups in lipids and amino acid side chains of proteins and carbohydrates[429], so whilst the Raman spectra in this region may be less useful in quantifying specific molecules, changes in stretching vibrations may help identify an overall signature for a high OXPHOS phenotype.

There was no clear relationship between the changes in biological molecules observed and the rates of OXPHOS. This is demonstrated by H460 cells in high glucose, the treatment group with the second highest rate of OXPHOS, which did not always follow the same trend as H460 cells on low glucose. Previous bioenergetic profiling of these cell lines revealed in 11 mM glucose, H460 cells did maintain rates of ECAR similar to that of A549 cells, however on 1 mM glucose the bioenergetic profiles of these cells differed greatly (Figure 3.9). Therefore, whilst no clear trend in biomolecules was observed between least OXPHOS to most OXPHOS cells, clear differences between highly glycolytic (A549 11 mM) and highly OXPHOS (H460 1 mM) were consistently observed and may help discriminate highly OXPHOS and highly glycolytic cells in future.

5.9.4 Detection of NBS037 inside cells

Whilst the key aim in this study was to investigate if signatures of an OXPHOS or glycolytic phenotype could be detected by Raman spectroscopy, a secondary aim was to investigate if the presence of NBS037 could be detected inside cells. The Raman spectra from pure, solid NBS037 was obtained by Sarah Hutchinson and key peaks with local intensity maxima identified (Figure 5.9). First, key peaks from the solid NBS037 were compared to the spectra of cells treated with NBS037 to test if these key NBS037 peaks have higher intensity in cells treated with NBS037 compared to untreated cells, as a readout for NBS037 inside the cells. Interestingly, two of these NBS037 associated peaks at 337 cm^{-1} and 395 cm^{-1} were key contributors to untreated vs treated group separation on LD1 and LD2 in A549 cells, with both peaks significantly higher than untreated cells with 0.5 μM NBS037 (both $p < 0.0001$) but not

1 μM NBS037. In A549 cells this trend was observed with various other peaks associated with NBS037 treatment; however, in H460 cells, with the exception of the peak at 3057 cm^{-1} for NBS037, all NBS037 peaks were significantly decreased compared to untreated cells. Higher intensity of NBS037 associated peaks was therefore not a readout of NBS037 inside the treated cells. This may have been due to measuring Raman spectra from the whole cell. NBS037 should accumulate inside the mitochondria at a much higher concentration than in the cytosol, so we may not observe a profile for NBS037 without looking specifically inside the mitochondria. Obtaining spectra from isolated mitochondria may give us a better readout for the concentration of NBS037 in cells. Since Raman peaks associated with NBS037 were not universally increased compared to untreated cells nor increased in intensity with a higher NBS037 concentration, it is likely the peaks measured here may indicate an alternative compound rather than NBS037 itself.

Many of the high intensity peaks observed with solid NBS037 lay in the fingerprint region of the Raman spectra (Figure 5.14), which may overlap with peaks of known biological molecules in the cell sample and therefore may not provide a viable readout for NBS037[430]. Only peaks which are unique to NBS037 could be used as a reliable readout for presence of the drug. Few peaks have been characterised in the region below 400 cm^{-1} (Figure 5.14), but some peaks associated with NBS037 which proved to be significant by LDA were localised in this region below 400 cm^{-1} and therefore may be a better readout for NBS037 inside the cells. For detection of NBS037, reporters can also be added. These reporters have bonds which generate peaks in the silent region of the spectra, such as the triple bonds of alkyne, cyanide, and nitrile groups, and may be useful in identifying the presence of NBS037[431]. Furthermore, the decrease in peak intensity of NBS037 associated peaks in treated cells could indicate it's successful metabolism, therefore drug metabolites could also be utilised as a readout for NBS037 in these cells to give a positive correlation between peak intensity and presence of the drug.

Finally, the detection of NBS037 inside cells is complex as the Raman spectral profiles also provide a biological fingerprint of the effect of NBS037 on the cells, including effects such as response to OXPHOS inhibition or cell death. Raman spectroscopy has potential to not only measure the concentrations of NBS037 inside cells but also show the resulting effect of treatment on cells. This could be a useful tool in detecting early response to the drug and whether the drug is effective in an individual, preceding symptom onset.

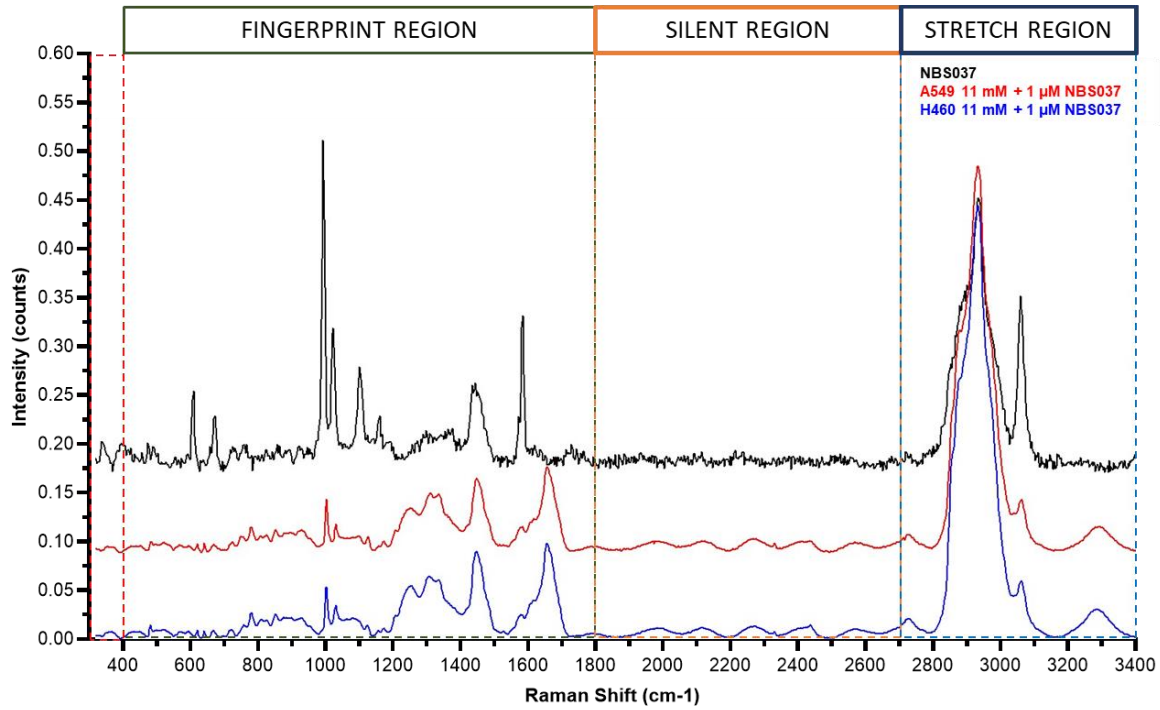

Figure 5.14. Raman spectral profile of NBS037 and NBS037 treated NSCLC cells. *Raman spectra were obtained from pure, solid NBS037 and A549 and H460 NSCLC cells treated with 1 µM NBS037 for 72 hours in 11 mM glucose with daily media replenishment. Cells were suspended in solution and dried onto aluminium coated slides for spectral acquisition with an HR Evolution confocal Raman microscope (Horiba). 10 spectra per cell and ~35 cells per sample were collected. NBS037 spectra were obtained from three batches. The different regions of the Raman spectra are labelled.*

5.9.5 Effects of NBS037 treatment on Raman spectra

After elucidating the effects of NBS037 on NSCLC cells *in vitro* in Chapter 3, next the effects of NBS037 on the Raman spectra of these cells was investigated. Inhibition of OXPHOS by NBS037 should cause changes in metabolism similar to that of AA, and create a distinct metabolic signature to be detected. After 72 hours of treatment with 0.5 μM NBS037, 1 μM NBS037, or 10 μM AA, Raman spectra were obtained from A549 or H460 cells in low or high glucose. In A549, sample grouping by LDA did not differ much between low and high glucose whilst H460 cells failed to grow in low glucose with treatment so could not be tested. Similar to the results observed with AA and 2DG previously, clear separation of untreated versus treated sample groups was observed in both A549 and H460 cells. In A549 cells, samples from 1 μM NBS037 and AA grouped closely together but well separated on LD1 from 0.5 μM NBS037 and untreated cells (Figure 5.10). In H460 cells, treated cells groups clustered closely together, with 0.5 μM NBS037 samples separated from the AA group but 1 μM NBS037 samples sharing overlap between the two (Figure 5.12). These were all distinctly separated from untreated cells on LD1, however cells treated with OXPHOS inhibitors did not group closely with untreated A549 line which would have been expected if NBS037 caused a shift to a higher glycolysis phenotype. Overall, a clear divide between treated and untreated cells was observed with NBS037 treatment, with NBS037 cells grouping closely to AA treated groups. This indicates some similarities in the Raman spectra exist between the two groups. A clear grouping based on metabolism features alone, whether more OXPHOS or more glycolytic, could not be distinguished.

In A549 cells, key molecules leading to separation of untreated and NBS037 treated cells on LD1 included changes in lipids, the amino acids tyrosine and tryptophan, as well as the DNA bases guanine and cytosine (Figure 5.11). Compared to untreated cells, 0.5 μM NBS037 caused a significant increase in the forementioned molecules (all $p < 0.0001$) but no significant changes with 1 μM NBS037. On the contrary, AA caused a significant decrease in lipids

($p < 0.0001$) and DNA bases ($p < 0.0001$) but a significant increase in tryptophan ($p < 0.0001$). Differences in LD2, which largely separated the treatment groups from one another, included carbohydrates and the DNA bases adenine and cytosine. Again, 0.5 μM NBS037 treated cells showed a significant increase in glucose ($p < 0.0001$) and DNA bases ($p < 0.0001$) when compared to untreated cells and other treatment groups, but this was the opposite effect than observed in 1 μM NBS037. This is a phenomenon observed throughout this work. For example, in Chapter 3, 0.5 μM NBS037 in H460 cells caused an increase in MTCO1 and SDHA (Figure 3.16), SOD2 and aconitase (Figure 3.22) when normalised to mitochondrial mass, and decrease in ROS (Figure 3.19), all being the opposite effects than observed with 1 μM NBS037. Metabolic hormesis describes the phenomenon where inhibitory agents cause favourable effects on metabolism when used in a low dose range[432], and may explain the effects observed with 0.5 μM NBS037, whilst 1 μM NBS037 has an inhibitory effect. This finding has been observed with other mitochondrial inhibitors[433]. Both concentrations of NBS037 differed from the effects observed with AA, with AA causing a decrease in glycogen, adenine and glucose at 1125 cm^{-1}.

H460 cells followed a similar trend as observed in A549 cells, with a clear separation between treated versus untreated groups on LD1 due to differences in glycerol, amino acids such as phenylalanine and tryptophan, glucose, nucleic acids and amide bonds (Figure 5.13). Separation of the treated groups on LD2 was driven by changes in amino acids with tryptophan at 573 cm^{-1}, proline and tyrosine all high ranking contributors. In H460 cells all OXPHOS inhibitors caused similar cellular changes in the same manner, unlike observed with A549 cells. Lipids, carbohydrates, and amino acids (with the exception of tyrosine) had the tendency to decrease in treated cells whilst amide bonds and stretching of -OH and aromatic bonds significantly increased in treated cells compared to untreated.

Interestingly, in cells treated with any of the drugs, small bumps were observed in the silent region of the Raman spectra in both A549 (Figure 5.10) and H460 cells (Figure 5.12). This

was not due to any interference from DMSO, the solvent used for the drugs[434], and instead may indicate noise in the signal as no high intensity peaks are observed in this region. More replicates are needed in order to identify if the changes in the silent region are robust and correspond to cellular responses to the drugs, or if these reflect noise in the spectra.

Overall, NBS037 and AA treatment caused significant changes to biomolecules which led to clear separation of treated and untreated groups by LDA. NBS037 and AA treatment did not always cause the same changes in biomolecules, for example, AA could decrease lipids and DNA bases but the same molecules were increased in NBS037. NBS037 has effects on mitochondrial protein translation and AA specifically inhibits complex III of the ETC, so whilst both potently inhibit OXPHOS, both display different mechanisms of action which may impact the cell, and its makeup, in different manners. The use of Raman spectroscopy for identifying effects of NBS037 on the cell, and biomolecules within it, has been successfully demonstrated, shown by differences observed between untreated and NBS037 treated cells. The exact changes NBS037 causes to these classes of molecules could be another project in itself, but developing Raman spectroscopy for this use is an exciting future prospect upon validation of these initial results through increased biological replicates.

5.9.6 Raman spectroscopy for analysis of cytochromes

Cytochromes are a key REDOX proteins implicated in mitochondrial metabolism, primarily acting as cofactors for electron transfer in the ETC, but with other functions in cellular homeostasis and drug metabolism[435]. The Raman spectra for cytochrome *c* in the ETC has previously been characterised, and peaks which correspond to the protein quantified in various cells. Whilst the band position does not shift in experimental conditions, the bands at 750 cm^{-1} and 1583 cm^{-1} are associated with the reduced form of cytochrome *c*. Increased intensity of these bands indicates reduced cytochrome *c*, and lower intensity of these peaks

indicate oxidised cytochrome *c*[436–438]. In H460 cells in low glucose, these bands for cytochrome *c* were significantly lower compared to the other treatment groups ($p < 0.0001$), indicative of a shift in REDOX state to more oxidised cytochrome *c*. Previous work testing REDOX state of cytochromes with increased respiration induced by ADP and succinate addition, showed an increase in reduced cytochrome *c* and increased oxidation of cytochrome *b*[439] , in agreement with the expectation that increased complex III activity results in greater reduction of membrane bound cytochrome *c*[440]. Whilst these results are the opposite of what was observed in this study, quantification of MTCO1 in complex IV showed the highest expression in H460 on 1 mM glucose (Figure 3.10), indicative complex IV may have increased expression and therefore yield a greater amount of oxidised cytochrome *c* which is what was observed here.

On the contrary, in H460 cells with OXPHOS inhibition via NBS037 and AA, both peaks for cytochrome *c* were also significantly reduced compared to untreated H460 ($p < 0.0001$) and A549 cells ($p < 0.0001$). In A549 cells, a lower dose of NBS037 caused an increase in cytochrome *c* band intensity compared to untreated controls ($p < 0.0001$). Similarly, an increase in the 1583 cm^{-1} band for cytochrome *c* was observed with AA treatment ($p = 0.0321$), but a significant decrease in the 750 cm^{-1} band was also observed with AA ($p < 0.0001$). As a readout for cytochrome c REDOX state, all bands associated with cytochromes should change proportionally with the molecule, which was not observed in this case. With different peaks for cytochrome *c* changing in different ways, these Raman peaks may not be indicative of reduced cytochrome *c*, or part of the molecule has changed chemical environment such that the bond is no longer vibrating at the same energy.

As Raman spectra were obtained for the whole cell, peaks for cytochrome *c* may also reflect cytosolic cytochrome *c,* which is associated with apoptosis. An increase in apoptotic cells may be present in drug treated cells as indicated in Chapter 3 through decreased cell viability in these cell lines. In the mitochondria, ~62% of cytochrome *c* is oxidised but the cytosolic pool of cytochrome is almost fully reduced[441]. Cytochromes in the cytosol may then be oxidised in

order to act as ROS scavengers[442] or during apoptosis through Apaf1 binding[443]. Higher ROS, such as observed with AA treatment (Figure 3.19), may be present with NBS037 treatment and therefore have higher levels of oxidised cytochrome *c* shown here by a decrease in cytochrome *c* peaks. The increase in cytochrome *c* peak intensity observed with 0.5 μM in A549 cells indicates a higher proportion of reduced cytochromes which may be a consequence of disruption to the ETC and an imbalance in electron transfer between respiratory proteins.

Overall, determination of cytochrome *c* REDOX status may be a viable indicator of respiration, ROS, and apoptosis within cells; however with multiple types of cytochrome *c* present (cytosolic, mitochondrial, membrane bound, and within complex III and IV[439]), detection by Raman spectroscopy requires further work to yield a reliable readout for these processes.

5.10 Future directions

The work in this chapter is a small step in developing Raman spectroscopy for the cancer research field. Future work would begin with validation of the findings outlined in this project with biological repeats of the NSCLC cells tested. Future opportunities may include the testing of other cancer cell types and the CD-1 mouse tissues collected in the SP237857 mouse study detailed in Chapter 4. By testing various cell types, a clear metabolic signature for OXPHOS or glycolysis may further be validated, with the hope of generating a predictive model for cell metabolism, exampled by Xu et al. (2023)[444] when developing a predictive model for chronic fatigue syndrome patients. A predictive model uses AI and machine learning to predict a sample group based upon only the Raman spectra. Once a robust metabolic signature can be associated with a more OXPHOS or glycolytic phenotype, these machine learning techniques can be applied to a data set in order to predict which metabolic phenotype that cell may fall under.

Increasing literature demonstrates the potential of Raman spectroscopy in cancer diagnostics[445] but with little work to date utilising Raman spectroscopy for cancer cell metabolism. When used in a clinical setting, determination of cell metabolism in an individual's tumour may better guide which treatment to give, for example if a patient's tumour is highly OXPHOS, then OXPHOS inhibition would be an effective therapeutic strategy and NBS037 could be given. This would enhance the efficacy of treatments given and minimises risk of adverse side effects by only giving a drug a patient will respond to. The patient response to a drug may be more rapidly measured through Raman spectroscopy, as opposed to waiting to measure a reduction of tumour growth which can take longer, so cellular responses very early in the treatment can be measured. For example, through comparing the Raman spectra from untreated and NBS037 treated cells, clear differences in biological molecules were found and show response to treatment. This would allow patients to try a range of therapies if some are not providing clinical benefit. Furthermore, since Raman spectroscopy only requires single cells for analysis, a very low number of cells are required from patient biopsy. This minimises the invasiveness of biopsies currently taken, and with low numbers of cells required, cancer cells in the blood, either those metastasising or form blood cancers or CSCs may also be detected.

Using Raman spectroscopy to identify cellular metabolism on a single-cell level would also highly benefit the cancer research space as a whole. This technology would allow us to visualise the spatial differences in cell metabolism within the tumour and within tumour cells. Spatial visualisation of metabolites has already been achieved through matrix-assisted laser desorption/ionization-mass spectrometry (MALDI-MS) imaging. The resolution utilised was 100 μm when most tumour cells have a diameter of 10 μm, therefore this technique cannot visualise molecules at the single-cell level[446]. Raman spectroscopy overcomes this, and would be a useful tool in understanding the complexities of tumour cell metabolism.

Raman could become a useful tool to identify the localisation and accumulation of a drug on both a tissue and single-cell level. If NBS037 can be located within cells, it becomes possible to elucidate if NBS037 is accumulating inside cancer cells specifically as opposed to normal tissue, and if the drug is reaching its target, the mitochondria. An understanding of the movement of NBS037 may help explain its issues with specificity as observed *in vitro* (Chapter 3), and its effects on liver tissue observed in Chapter 4. Therefore, completing more work on identifying behaviour of NBS037 molecules within the cells may help us better understand its mechanisms of action. Identifying the presence of drugs in live cells with Raman spectroscopy has been described in previous literature; however, it is hard to deduce whether Raman peaks correlating to the drug are in fact due to the drug or are due to drug induced effects so more work is yet to be carried out in this space[430,447].

The Raman data analysis in this thesis is just one of many methods that can be utilised to analyse such data. After first development of Raman spectroscopy, Raman spectra analysis involved quantifying peak intensity and identifying any shifts in wavenumber for identified molecules[448]. More recent studies employ statistical models such as orthogonal projections to latent structures discriminant analysis (OPLS-DA)[445] and partial least squares (PLS)[449] with deep learning techniques[450] in order to better identify the differences in Raman spectra between samples. Future work could be carried out to optimise the statistical test utilised for analysis of our Raman data.

5.11 Chapter summary

This work was conducted as a pilot study to identify if an OXPHOS or glycolytic cell signature could be detected by Raman spectroscopy. LDA modelling of Raman spectra was able to distinguish changes in cell metabolism on a single-cell level, and distinguish drug treated cells from those which have not been treated. Cells with high OXPHOS were shown to have changes in amino acid levels, lipids, carbohydrates, and nucleic acids which could be quantified by integration of Raman peaks. Analysis of mitochondrial cytochromes also shows an increase of oxidised cytochrome *c* in high OXPHOS cells, highlighting the use of Raman in identifying REDOX states which are also implicated in mitochondrial metabolism. Raman spectroscopy has a promising future in cancer metabolism research, cancer diagnosis, and treatment mechanism of action, but more work must be carried out to validate a robust signature for specific metabolic phenotypes.

6

Summary and Future Directions

6.1 Summary

Cancer is a leading cause of death worldwide, with many mechanisms at play to confer its survival in the body, and ability to resist current treatment strategies. It is a multifaceted disease characterised by hallmark behaviours which allow cells to sustain uncontrolled proliferation, host immune evasion, and invasion into healthy tissue. In the 1920s Otto Warburg made the pivotal discovery that cancer tissue upregulated glycolysis, even in the presence of oxygen. Later this metabolic shift was named the Warburg effect, and subsequently shaped our understanding of tumour metabolism for the early half of the twentieth century. However, the Warburg effect has been revisited time and time again in recent years, as our understanding of tumour metabolism advances, and new research shows that functional mitochondrial metabolism is vital for tumour survival and progression in some cancers. This objects to the thinking that mitochondrial metabolism is hindered in cancer, as the Warburg effect first theorised. With changes in glycolysis and OXPHOS found in all cancers, dysregulated cellular metabolism was later included as an emerging hallmark of cancer, and a new focus of potential cancer therapeutics.

Mitochondria have a key role in cancer cell proliferation and survival through a number of mechanisms. OXPHOS confers cancer survival in the acidic and nutrient deplete TME, and facilitates tumour growth, therapy resistance, and metastasis through ROS and oncometabolite induced signalling cascades. With OXPHOS shown to be a key feature of tumorigenesis, recent efforts into developing effective treatment strategies have targeted mitochondria and their metabolism, including inhibition of OXPHOS. This has been achieved with FDA approved compounds as well as mitochondrial targeted drugs and novel small molecule inhibitors (summarised in Table 1.1). Whilst many of these compounds have shown effective anti-cancer properties *in vitro*, and some promising effects in clinical trials, many struggle to balance potency with tolerability. Therefore, there is still an unmet clinical need for a drug which can potently kill cancer cells and act in a specific manner to limit side effects in normal tissue.

We have developed a new OXPHOS inhibitor, NBS037, which consists of the antibiotic AZM linked to a mitochondrial targeting group, a TPP^+ cation. Cancer cells have a higher $\Delta\psi m$ than non-cancer cells and therefore, in theory, more NBS037 would accumulate inside the mitochondria of cancer cells, giving the drug its specificity. Due to the prokaryotic nature of mitochondria and similarities in protein synthesis machinery, AZM causes inhibition of mitochondrial ribosomes, and subsequently prevents the translation of mitochondrial genes. Since many subunits of complex I, III, IV, and V are encoded by mtDNA, AZM causes disruption to respiratory complexes, inhibition of OXPHOS, and a myriad of downstream effects. Such effects may include ATP depletion, dysfunctional ROS signalling, prevention of macromolecule synthesis, and eventually, cell death. NBS037 is a novel drug in the cancer space, making this work highly significant in the field as a novel therapeutic strategy in cancer.

Chapter 3 focused on determining if NBS037 causes cancer cell death *in vitro* and investigating the mechanism of action in practise. Dr Lees (Oxford Brookes University) provided data which ranked different cancer cell lines by their dependency on OXPHOS, from

which a variety of cell lines were taken for testing: Cal51, FaDu, H520, and A549, with each showing high OXPHOS dependency. The NSCLC line H460 was also chosen for testing, to compare to the NSCLC lines already chosen, and due to its success as a xenograft model for testing the drug *in vivo*. All of these cell lines proved highly sensitive to NBS037, with a potent dose dependent decrease in cell viability over a seven day treatment period which was exacerbated by low glucose culture conditions. A549 was the least sensitive to NBS037 and H460 was the most sensitive, in agreement with further testing which suggested H460 cells utilise more OXPHOS than A549 cells. In non-cancer cell lines, MRC-5 lung fibroblasts did not respond to NBS037 until the highest dose used, whilst ARPE-19 cells displayed a dose dependent decrease in viability with the drug. A549 and H460 had a much higher Δψm than the non-cancer lines, but since ARPE-19 was still sensitive to the drug, it was deduced that Δψm alone does not explain the sensitivity to the drug. With some NBS037 evidently entering non-cancer cells, the effects on cell viability may depend on the cell line's dependence on OXPHOS, or its dependence on mtDNA protein synthesis. ARPE-19 had a faster growth rate than MRC-5, similar to that of the cancer cell lines, and may have a higher requirement for mtDNA protein synthesis. This may have rendered these cells sensitive to the drug. With many tissues in the body reliant on OXPHOS, and with some having high rates of cellular turnover and higher demand on mtDNA synthesised proteins[451,452], effects of NBS037 on these tissues must be carefully investigated.

When testing the mechanism of action of NBS037 after 72 hours of treatment, a decrease in MTCO1 (complex IV) expression was observed in H460, MRC-5, and ARPE-19 cells, but little effect in A549, highlighting this cell line may be better at compensating for mitochondrial deficits. SDHA expression (complex II), was also affected so the inhibition of mtDNA translation also impacted the expression of nuclear genes. Mitochondrial mass was affected by NBS037, with expression of Tom20 increasing in A549 and decreasing in H460, MRC-5, and ARPE-19, although the cause for such changes in mitochondrial mass, whether increased mitophagy or decreased mitochondrial biogenesis, is yet to be fully determined. With deficits

in mitochondrial proteins and subsequent mitochondrial dysfunction, it is highly likely these mitochondria will be cleared by mitophagy, to cause the decrease in mitochondrial mass observed and subsequently cause deleterious effects to cancer cell function. This would link the changes to mitochondrial proteins to the decreased cell viability observed with NBS037 treatment. With disruption to OXPHOS observed, other mechanisms contributing to cell death were also explored. ROS production was only increased with high doses of NBS037 in H460 cells, with no significant changes to antioxidant expression, so it is unlikely excessive ROS is causing the NBS037 induced decrease in cell viability. With the TPP^+ cation previously found to cause uncoupling effects in studies by other groups[262], acute effects of NBS037 on OCR was examined and mild uncoupling was only observed with NBS037 doses ten times greater than the IC50 (10 μM). At high doses of NBS037, the OCR is increased when compared to untreated controls but the oxygen consumption begins to fall between four to six hours of NBS037 treatment, which may indicate mtDNA translational effects setting in faster than at lower doses, or a high enough loss of ATP of a long enough period such that cell death occurs[453]

Cancer cells are metabolically plastic and can rewire metabolism between a highly glycolytic and highly OXPHOS phenotype easily, usually when adapting to the TME or to overcome chemotherapies which target one metabolic pathway. For this reason, NBS037 was tested alongside the glycolysis inhibitor 2DG, to observe if combination treatment could give a greater decrease in cancer cell viability than either treatment alone. Furthermore, the ability to lower the dose of both drugs and maintain the efficacy would prove advantageous to limiting any adverse effects on normal tissue. Therefore lower doses of NBS037 were tested in combination with 2DG, to test if combination treatment can yield a similar effect on cell viability on a lower drug dose. 20 mM 2DG, which has been used by other groups *in vitro* when using the drug for glycolysis inhibition[454–456], decreased the cell viability in all cell lines between one and seven days of treatment. A greater reduction in cell viability with NBS037 was observed when added in combination with 20 mM 2DG; however, cell viability of cells treated with 2DG

alone decreased throughout the seven day treatment period, highlighting 2DG at this concentration was toxic. Therefore, a dose of 2DG achievable in plasma (500 μM) was utilised in combination with NBS037. The potency of NBS037 was not substantially improved when used in combination with 500 μM 2DG as doses of NBS037 below 0.5 μM did not give any significant effects on cell viability.

With cell culture conditions highly different from physiological conditions, testing NBS037 *in vivo* would have multiple benefits. Studies *in vivo* would allow a better determination of the mechanism of action of NBS037, and test its specificity for cancer by comparing to normal tissue which has not been manipulated for *in vitro* culture. Dr Hulit generated H460 NSCLC xenograft models in CD-1 mice which received treatment with NBS037 or PBS as a vehicle control prior to culling. The aim of this study was to generate tissues which had received NBS037 alone, and investigate the effects of the drug on cellular function. Dr Hulit studied the effect of NBS037 on tumour growth in a previous study and therefore the work in this thesis focuses on cellular effects rather than its effects on tumour growth. Mitochondrial and antioxidant proteins were relatively unchanged in brain, heart, and kidney tissue, indicating that, *in vivo*, NBS037 may act specifically and have a limited impact on normal tissues. In tumour and liver tissue, mitochondrial proteins were decreased due to a significant decrease in mitochondrial mass. Since the drug is metabolised in the liver, the liver would be exposed to high concentrations of NBS037 and its metabolites, which may cause the effects observed in this tissue. No significant changes in mouse bodyweights between the start and end point of the study were observed, indicating that the changes in liver proteins had no adverse effects on mouse health in this study. With mitochondrial mass heavily decreased in tumour, this indicates successful target engagement on the mitochondrial proteins, as the drug causes mitochondrial dysfunction and clearance. This may have an impact on cell proliferation or cell death, in agreement with the potent decrease in cell viability observed in cancer cell lines *in vitro*.

Upon qualitative analysis of effects of NBS037 on cell death, cell proliferation, and ROS production, no clear difference was observed between PBS and NBS037 treated heart, liver, and kidney tissue, but more obvious effects were observed in tumour tissue. Apoptosis appeared increased in the core of the tumour when treated with NBS037 compared to PBS, which was accompanied by a decrease in hypoxia markers. This may indicate decreased oxygen consumption and hinderance of OXPHOS as expected, in agreement with the previous findings of fewer mitochondria and a decrease in mitochondrial protein content. Tumour vasculature was more dense around the periphery of the tumour, with some evidence of endothelial cells in the core of the tumour, which would allow NBS037 to reach cells in the centre of the tumour and cause the increased apoptosis as observed. Qualitative analysis of 8-OHdG staining suggested increased ROS in NBS037 treated tumour tissue compared to PBS treated tissue but more work is required to quantify such changes.

Raman spectroscopy is a label-free method for analysis of biological molecules within a sample, providing an advantage over conventional MS due to its high resolution on a single-cell level. Here, the ability of Raman spectroscopy to investigate cancer cell metabolism was tested, with the aim of identifying an OXPHOS or glycolytic signature from Raman spectra. Initial work showed that glucose manipulation could produce a more OXPHOS or glycolytic phenotype in A549 and H460 NSCLC cells. Through implementing LDA of Raman spectra, differences in cells grown in different glucose conditions were detected, with LDA showing clear separation between H460 cells in low glucose (more OXPHOS) from the other groups. Some separation was observed between A549 high glucose and H460 high glucose, with A549 low glucose samples proving to be an intermediate between the two. Quantification of molecules contributing to group separation showed a significant decrease in lipids, amino acids, carbohydrates, and DNA in the high OXPHOS H460 1 mM glucose cells. Furthermore, quantification of bands corresponding to mitochondrial cytochromes indicated a shift in REDOX balance in H460 low glucose cells, with lower levels of reduced cytochrome *c* and higher levels of oxidised cytochrome *c*.

Manipulation of metabolism through OXPHOS and glycolysis inhibitors did not provide clear LDA grouping reflective of metabolic signature. Instead, untreated and treated cells separated well from one another. When tested with NBS037, no clear shift in metabolism towards glycolysis, a possible compensatory mechanism, was observed from the Raman spectra but LDA grouping found similarities between NBS037 and AA treated cells, suggesting a similar biological phenotype amongst the cells treated with OXPHOS inhibitors. Again, significant differences in carbohydrates, lipids, amino acids, nucleic acids, and mitochondrial cytochromes were observed between untreated and treated cells, and the different concentrations of NBS037, with 1 μM trending towards results observed with AA. A clear signature for NBS037 could not be found inside the cells; however, LDA of A549 did indicate some significant peaks at 337 cm^{-1} and 395 cm^{-1} which had influence in the separation between treatment groups. These have no associated molecule in the literature but do correspond to peaks found in NBS037. The ability to identify NBS037 and its accumulation in cells or isolated mitochondria would be highly useful in furthering this work.

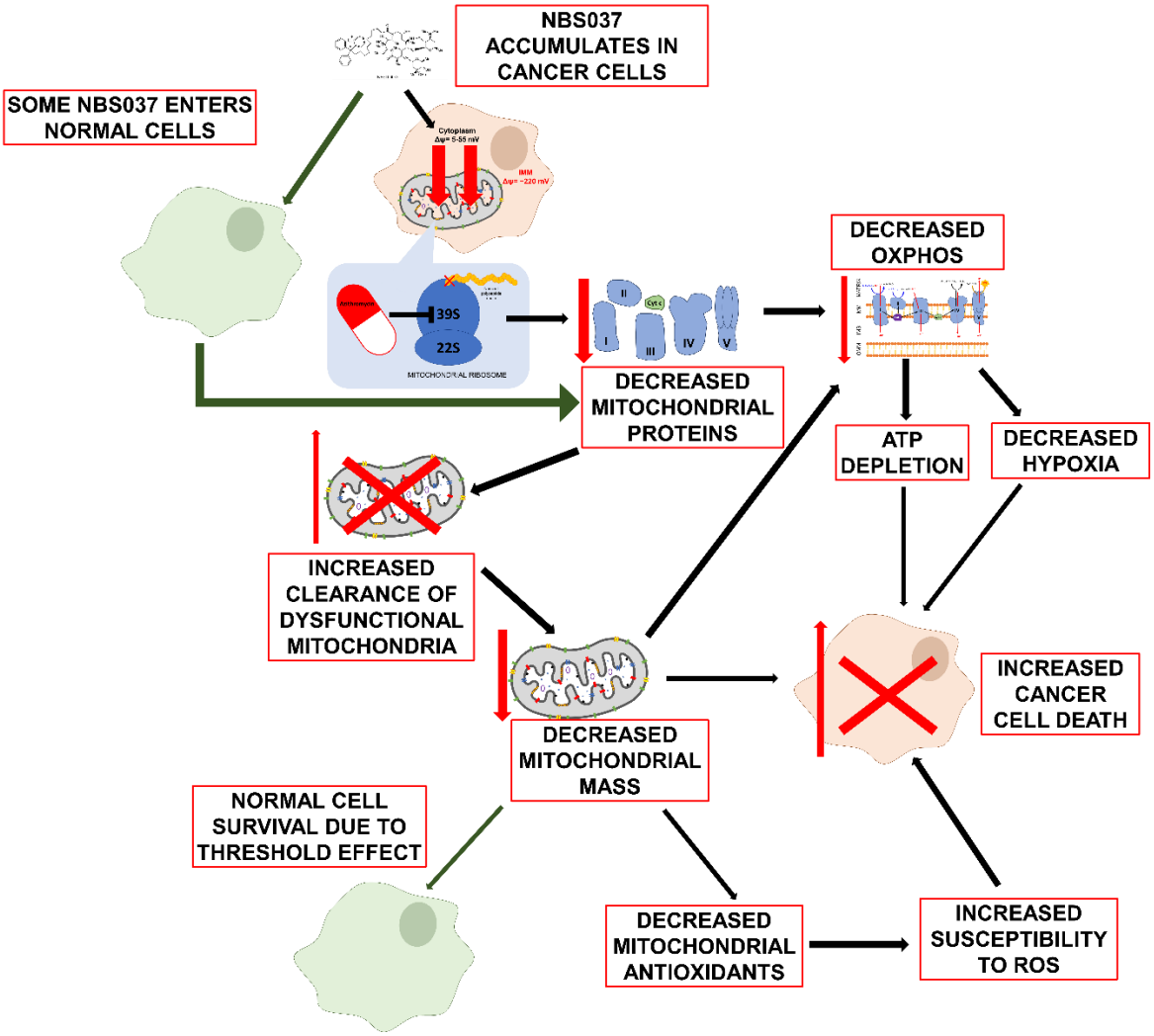

Figure 6.1. The mechanism of action of NBS037 as suggested by this project. *The work in this thesis provides evidence that NBS037 successfully diminishes mitochondrially encoded proteins in the ETC, with subsequent effects on nuclear encoded ETC proteins. This causes a reduction in OXPHOS. Decreased OXPHOS would lead to depleted ATP as cells struggle to meet energetic demands, and subsequently leave cancer cells vulnerable to cell death. A decrease in oxygen consumption would also alleviate hypoxia in the tumour, subsequently causing cell death due to inability to survive in the TME. Dysfunctional mitochondria may lead to increased mitophagy to clear damaged mitochondria, and a decrease in mitochondrial mass which also contributes to cell death in OXPHOS dependent cancer cells. The work in this project also suggests, the decrease in mitochondrial mass also leads to a decrease in mitochondrially localised antioxidants such as SOD2, which may lead to increased susceptibility to ROS induced cell death in cancer cells if ROS levels were to increase. Some NBS037 may enter normal cells, causing small deficits in mitochondrial proteins and mitochondrial mass; however, with a lesser accumulation of the drug inside these cells, the cytotoxic threshold is not reached and normal cells are able to survive.*

6.2 Future directions

The work to date supplies data which provides an insight into the effects of NBS037 *in vitro* and *in vivo*. The aim of this project was to determine the mechanism of action and deduce any off target effects which may limit its success as an anticancer agent. Future work will be focused on increasing the depth of this understanding and expanding upon the work already completed.

6.2.1 NBS037 mechanism of action

In vitro, with ROS and uncoupling effects minimal, more focus can be placed on the exact effect NBS037 has on mitochondrial OXPHOS machinery and how this may cause the reduction in cell viability. This would include expansion of the complexes analysed, measurement of complex activity, and analysis of ATP levels, in a wider variety of cancer cell lines. Testing cell lines with low OXPHOS gene scores in Dr Lees' ranking system would prove if NBS037 is only an effective drug in high OXPHOS cancers when compared to low OXPHOS cancers, and may further aid our understanding of the mechanism of action. Analysis of ATP as an output may help better understand the causes of reduced cell viability if ATP is depleted. If there are no changes to ATP levels, then compensatory mechanisms are assisting cell survival and can be further explored. NBS037 may not have become more potent in combination with 2DG, but it may still synergise well with other chemotherapy or immunotherapy treatments as other avenues to explore.

6.2.2 Improvement of *in vitro* models to test

Utilising MRC-5 and ARPE-19 cells allowed comparison of cancer cell lines to non-cancer controls; however, future work could incorporate primary cell lines as a better indicator of effects of NBS037 on non-cancer cells.

Experimental conditions *in vitro* will always have a large impact on the behaviour of cells. Low oxygen and low glucose cell culture would more closely reflect the environment experienced by these cancer cells *in vivo*, but provide results which are not easily comparable to previous literature in which experiments have been carried out under standard culture conditions. For work with NBS037, it has been useful to compare its potency to other published work on OXPHOS inhibitors which are in development, but the work has also included the use of low glucose in order to appreciate the effect of lowering the glucose and pushing cells towards a more OXPHOS phenotype. Future work can be carried out to further experiment with cell culture conditions used, completing more of the mitochondrial assay work under low glucose, as well as differing oxygen concentrations. With culture conditions not reflective of the physiological environment, the most accurate effect on tumour and normal tissue would be testing the drug *in vivo*, which was achieved in this project, with the help of Dr Hulit in carrying out the mouse study.

6.2.3 Improvements in tissue analysis

The *in vivo* work in this project served as an interesting insight into NBS037 toxicity in normal tissues, as well as cellular responses to the drug in tumour. The aim of the small animal study conducted was to administer PBS and NBS037 to mice with xenograft tumours, and compare the effects of the drug on cells. Loss of mitochondrial mass was observed in the liver, with no obvious effects on cell death or proliferation. As the liver would experience high concentrations of the drug during drug metabolism, future work should keep analysis of the liver a priority in order to ensure longer term exposure to NBS037 has no further effects on the liver. WB analysis was utilised again for analysis of mitochondrial proteins in tissues; however, again, the number of mitochondrial complexes analysed should be expanded in future. Furthermore, methods such as metabolomics may be applied to tissue analysis in order to capture the tissue metabolome, from which OXPHOS inhibition and subsequent effects on metabolism could be more thoroughly deduced.

Immunofluorescence staining gave an initial insight into any changes in cell death, cell proliferation, oxidative damage, tumour vasculature, and hypoxia in NBS037 treated tissues, but image analysis was only qualitative. Future work improving the image resolution, and the sample number of tissues stained would allow completion of quantitative analysis to validate these key initial findings. Key findings to validate would include the potential NBS037 induced cell death in the core of the tumour, as well as alleviation of hypoxia. It is advantageous to use imaging analysis as cell metabolism within the tumour are heterogenous, and imaging allows spatial analysis of NBS037 induced effects.

6.2.4 Future animal studies

Whilst there is copious tissue available from the current mouse study, further studies can be conducted with longer dosing regimens, and in different animal models such as syngeneic mouse models which maintain the host immune system, in order to better recapitulate the response in humans. Furthermore, with OXPHOS a key feature of metastatic disease, future work could test the use of NBS037 treatment in metastatic models such as mouse B16 melanoma[406] and Lewis lung carcinoma cells[457]. However, NBS037 treatment is likely to be more effective in combination with other standard of care treatments, where Dr Hulit has already shown in initial xenograft models that NBS037 in combination with paclitaxel and carboplatin, results in an increased probability of survival when compared to each agent used alone (Figure 4.26). Future testing of NBS037 in combination with standard of care treatments may therefore be an exciting future step in this work. For example, genetically reducing OXPHOS activity by mutating mitochondrial genes improved efficacy of check point inhibitors in cancer cells[458]. Other OXPHOS inhibitors in combination with standard of care treatments have resulted in promising anti-tumour effects[459,460], and highlights the potential for combination therapy in future.

6.2.5 Further development of Raman spectroscopy in cell metabolism studies

The use of Raman spectroscopy for analysis of single-cell or organelle metabolism would be highly beneficial in cancer research and cancer diagnosis. In order to use Raman spectroscopy for such applications, further biological replicates are required to validate the results of this pilot data, and would allow the identification of a robust chemical signature associated with higher OXPHOS or higher glycolysis in cells. Validation of pilot results may be coupled with improved statistical tools for analysing the differences in spectra, and the potential to use AI and machine learning techniques to identify the cell metabolism from any cell spectrum it is given. Such tools could have a significant impact on tumour diagnosis, giving oncologists an insight into which type of drug may best fit an individual, with a high OXPHOS tumour a good candidate to receive NBS037. Detection of NBS037 in cells would also be a useful tool for furthering the work in this project. Identifying the physical presence of NBS037 within cells or mitochondrial would be highly beneficial for indicating if the drug is selective for cancer cells compared to normal cells and determine the quantity of the drug that reaches the cancer cell mitochondria. This would allow validation of the mechanism in which NBS037 accumulates within cells and whether this differs between normal cells and cancer cells.

6.3 Summary statement

Overall, this project provides evidence that NBS037 may be a promising anti-cancer agent, effectively preventing growth of cancer cells *in vitro*. The mechanism of action of NBS037 is shown to be potent inhibition of OXPHOS in sensitive cancer cell lines, shown by a reduction in mitochondrial encoded subunits of respiratory complexes and OCR. This is accompanied by an small increase in ROS and uncoupling effects at high doses of NBS037 but no such effects at low doses. *In vivo*, NBS037 caused a decrease in mitochondrial mass in liver tissue; however, treatment was well tolerated, shown by maintenance of mouse bodyweight throughout treatment duration, so any effects on the liver did not impact the health of the mice.

NBS037 treatment resulted in a decrease in mitochondrial mass in tumour, indicating successful target engagement through causing mitochondrial dysfunction and likely an upregulation of mitophagy as a result. Decreasing the number of functional mitochondria in OXPHOS dependent cells may lead to ATP depletion and the cell death effects observed *in vitro*. There is promising evidence that these changes cause inhibition of OXPHOS in tumour tissue *in vivo*, indicated by a reduction in tumour hypoxia marker. Furthermore, initial data suggests Raman spectroscopy can be utilised to detect differences in cell metabolism corresponding to a more OXPHOS phenotype; however, further work is required in order to characterise the specific signatures associated with OXPHOS or glycolysis. If an OXPHOS signature can be determined, this would give an indication of which tumours may be good candidates for NBS037 treatment in a clinical setting.

Overall, this is exciting work demonstrating our novel OXPHOS inhibitor, NBS037, can cause effects on mitochondrial proteins *in vitro* and *in vivo*, with minimal off-target effects in normal tissue, although further work is required to improve the depth of our understanding of its full mechanism of action.

Bibliography

1. Roger AJ, Muñoz-Gómez SA, Kamikawa R. The Origin and Diversification of Mitochondria. *Current Biology*. 2017;27(21):R1177-R1192. doi:10.1016/j.cub.2017.09.015

2. Cavalier-Smith T. Origin of mitochondria by intracellular enslavement of a photosynthetic purple bacterium. *Proceedings of the Royal Society B: Biological Sciences*. 2006;273(1596):1943-1952. doi:10.1098/rspb.2006.3531

3. Kühlbrandt W. Structure and function of mitochondrial membrane protein complexes. *BMC Biol*. 2015;13(1). doi:10.1186/s12915-015-0201-x

4. Taanman JW. The mitochondrial genome: Structure, transcription, translation and replication. *Biochim Biophys Acta Bioenerg*. 1999;1410(2):103-123. doi:10.1016/S0005-2728(98)00161-3

5. Greber BJ, Ban N. Structure and Function of the Mitochondrial Ribosome. *Annu Rev Biochem*. 2016;85:103-132. doi:10.1146/annurev-biochem-060815-014343

6. Rong Z, Tu P, Xu P, et al. The Mitochondrial Response to DNA Damage. *Front Cell Dev Biol*. 2021;9. doi:10.3389/fcell.2021.669379

7. Druzhyna NM, Wilson GL, LeDoux SP. Mitochondrial DNA repair in aging and disease. *Mech Ageing Dev*. 2008;129(7-8):383-390. doi:10.1016/j.mad.2008.03.002

8. Morio B, Casas F, Pénicaud L. Overview of the cross-talk between hormones and mitochondria. In: *Mitochondria in Obesity and Type 2 Diabetes: Comprehensive Review on Mitochondrial Functioning and Involvement in Metabolic Diseases*. Elsevier; 2019:63-91. doi:10.1016/B978-0-12-811752-1.00003-1

9. Zhou, D., Shao, L., Spitz DR. Reactive Oxygen Species in Normal and Tumor Stem Cells. *Adv Cancer Res*. 2014;122(1):1-67. doi:10.1016/B978-0-12-420117-0.00001-3.Reactive

10. Perillo B, Di Donato M, Pezone A, et al. ROS in cancer therapy: the bright side of the moon. *Exp Mol Med*. 2020;52(2):192-203. doi:10.1038/s12276-020-0384-2

11. Shadel GS, Horvath TL. Mitochondrial ROS Signaling in Organismal Homeostasis. *Cell*. 2015;163(3):560-569. doi:10.1016/j.cell.2015.10.001

12. Collin F. Chemical Basis of Reactive Oxygen Species Reactivity and Involvement in Neurodegenerative Diseases. *Int J Mol Sci*. 2019;20(10):2407. doi:10.3390/ijms20102407

13. He L, He T, Farrar S, Ji L, Liu T, Ma X. Antioxidants Maintain Cellular Redox Homeostasis by Elimination of Reactive Oxygen Species. *Cellular Physiology and Biochemistry*. 2017;44(2):532-553. doi:10.1159/000485089

14. Diebold L, Chandel NS. Mitochondrial ROS regulation of proliferating cells. *Free Radic Biol Med*. 2016;100:86-93. doi:10.1016/j.freeradbiomed.2016.04.198

15. Brillo V, Chieregato L, Leanza L, Muccioli S, Costa R. Mitochondrial dynamics, ros, and cell signaling: A blended overview. *Life*. 2021;11(4). doi:10.3390/life11040332

16. Dakik P, Medkour Y, Mohammad K, Titorenko VI. Mechanisms through which some mitochondria-generated metabolites act as second messengers that are essential contributors

to the aging process in eukaryotes across phyla. *Front Physiol*. 2019;10(APR). doi:10.3389/fphys.2019.00461

17. Martínez-Reyes I, Chandel NS. Mitochondrial TCA cycle metabolites control physiology and disease. *Nat Commun*. 2020;11(1). doi:10.1038/s41467-019-13668-3

18. Tait SWG, Green DR. Mitochondria and cell signalling. *J Cell Sci*. 2012;125(4):807-815. doi:10.1242/jcs.099234

19. Mohanty A, Tiwari-Pandey R, Pandey NR. Mitochondria: the indispensable players in innate immunity and guardians of the inflammatory response. *J Cell Commun Signal*. 2019;13(3):303-318. doi:10.1007/s12079-019-00507-9

20. Duchen MR. Mitochondria and calcium: from cell signalling to cell death. *J Physiol*. 2000;529(1):57-68. doi:10.1111/j.1469-7793.2000.00057.x

21. Berridge MJ, Bootman MD, Roderick HL. Calcium signalling: Dynamics, homeostasis and remodelling. *Nat Rev Mol Cell Biol*. 2003;4(7):517-529. doi:10.1038/nrm1155

22. Wang C, Youle RJ. The role of mitochondria in apoptosis. *Annu Rev Genet*. 2009;43:95-118. doi:10.1146/annurev-genet-102108-134850

23. Bernardi P, Gerle C, Halestrap AP, et al. Identity, structure, and function of the mitochondrial permeability transition pore: controversies, consensus, recent advances, and future directions. *Cell Death Differ*. 2023;30(8):1869-1885. doi:10.1038/s41418-023-01187-0

24. Kinnally KW, Peixoto PM, Ryu SY, Dejean LM. Is mPTP the gatekeeper for necrosis, apoptosis, or both? *Biochim Biophys Acta Mol Cell Res*. 2011;1813(4):616-622. doi:10.1016/j.bbamcr.2010.09.013

25. Judge A, Dodd MS. Metabolism. *Essays Biochem*. 2020;64(4):607-647. doi:10.1042/EBC20190041

26. Deberardinis RJ, Cheng T. Q's next: The diverse functions of glutamine in metabolism, cell biology and cancer. *Oncogene*. 2010;29(3):313-324. doi:10.1038/onc.2009.358

27. Spinelli JB, Haigis MC. The multifaceted contributions of mitochondria to cellular metabolism. *Nat Cell Biol*. 2018;20(7):745-754. doi:10.1038/s41556-018-0124-1

28. Li Q, Hoppe T. Role of amino acid metabolism in mitochondrial homeostasis. *Front Cell Dev Biol*. 2023;11. doi:10.3389/fcell.2023.1127618

29. Moon SJ, Dong W, Stephanopoulos GN, Sikes HD. Oxidative pentose phosphate pathway and glucose anaplerosis support maintenance of mitochondrial NADPH pool under mitochondrial oxidative stress. *Bioeng Transl Med*. 2020;5(3). doi:10.1002/btm2.10184

30. Chandel NS. Glycolysis. *Cold Spring Harb Perspect Biol*. 2021;13(5). doi:10.1101/CSHPERSPECT.A040535

31. Navale AM, Paranjape AN. Glucose transporters: physiological and pathological roles. *Biophys Rev*. 2016;8(1):5-9. doi:10.1007/s12551-015-0186-2

32. Sun X, Peng Y, Zhao J, Xie Z, Lei X, Tang G. Discovery and development of tumor glycolysis rate-limiting enzyme inhibitors. *Bioorg Chem*. 2021;112. doi:10.1016/j.bioorg.2021.104891

33. Zangari J, Petrelli F, Maillot B, Martinou JC. The multifaceted pyruvate metabolism: Role of the mitochondrial pyruvate carrier. *Biomolecules*. 2020;10(7):1-18. doi:10.3390/biom10071068

34. Krebs HA. Rate control of the tricarboxylic acid cycle. *Adv Enzyme Regul*. 1970;8(C):335-353. doi:10.1016/0065-2571(70)90028-2

35. Yoo HC, Yu YC, Sung Y, Han JM. Glutamine reliance in cell metabolism. *Exp Mol Med*. 2020;52(9):1496-1516. doi:10.1038/s12276-020-00504-8

36. Arnold PK, Finley LWS. Regulation and function of the mammalian tricarboxylic acid cycle. *Journal of Biological Chemistry*. 2023;299(2). doi:10.1016/j.jbc.2022.102838

37. Sharma LK, Lu J, Bai Y. *Mitochondrial Respiratory Complex I: Structure, Function and Implication in Human Diseases*.

38. Chaban Y, Boekema EJ, Dudkina N V. Structures of mitochondrial oxidative phosphorylation supercomplexes and mechanisms for their stabilisation. *Biochim Biophys Acta Bioenerg*. 2014;1837(4):418-426. doi:10.1016/j.bbabio.2013.10.004

39. Chandel NS. Mitochondrial complex III: An essential component of universal oxygen sensing machinery? *Respir Physiol Neurobiol*. 2010;174(3):175-181. doi:10.1016/j.resp.2010.08.004

40. LIBERMAN EA, TOPALY VP, TSOFINA LM, JASAITIS AA, SKULACHEV VP. Mechanism of Coupling of Oxidative Phosphorylation and the Membrane Potential of Mitochondria. *Nature*. 1969;222(5198):1076-1078. doi:10.1038/2221076a0

41. Jonckheere AI, Smeitink JAM, Rodenburg RJT. Mitochondrial ATP synthase: Architecture, function and pathology. *J Inherit Metab Dis*. 2012;35(2):211-225. doi:10.1007/s10545-011-9382-9

42. Lee CP, Gu Q, Xiong Y, Mitchell RA, Ernster L. P/O ratios reassessed: Mitochondrial P/O ratios consistently exceed 1.5 with succinate and 2.5 with NAD-linked substrates. *The FASEB Journal*. 1996;10(2):345-350. doi:10.1096/fasebj.10.2.8641569

43. Zhao RZ, Jiang S, Zhang L, Yu Z Bin. Mitochondrial electron transport chain, ROS generation and uncoupling (Review). *Int J Mol Med*. 2019;44(1):3-15. doi:10.3892/ijmm.2019.4188

44. Houten SM, Wanders RJA. A general introduction to the biochemistry of mitochondrial fatty acid β-oxidation. *J Inherit Metab Dis*. 2010;33(5):469-477. doi:10.1007/s10545-010-9061-2

45. Houten SM, Violante S, Ventura F V., Wanders RJA. The Biochemistry and Physiology of Mitochondrial Fatty Acid β-Oxidation and Its Genetic Disorders. *Annu Rev Physiol*. 2016;78:23-44. doi:10.1146/annurev-physiol-021115-105045

46. Kumari A. Beta Oxidation of Fatty Acids. In: *Sweet Biochemistry*. Elsevier; 2018:17-19. doi:10.1016/b978-0-12-814453-4.00004-2

47. Hanahan D, Weinberg RA. Hallmarks of cancer: The next generation. *Cell*. 2011;144(5):646-674. doi:10.1016/j.cell.2011.02.013

48. Hanahan D. Hallmarks of Cancer: New Dimensions. *Cancer Discov*. 2022;12(1):31-46. doi:10.1158/2159-8290.CD-21-1059

49. Natalya N. Pavlova and Craig B. Thompson. Emerging metabolic hallmarks of cancer. *Physiol Behav*. 2018;176(1):139-148. doi:10.1016/j.cmet.2015.12.006.THE

50. Davidson SM, Papagiannakopoulos T, Olenchock BA, et al. Environment impacts the metabolic dependencies of ras-driven non-small cell lung cancer. *Cell Metab*. 2016;23(3):517-528. doi:10.1016/j.cmet.2016.01.007

51. Warburg O, Minami S. Versuche an Überlebendem Carcinom-gewebe. *Klin Wochenschr*. 1923;2(17):776-777. doi:10.1007/BF01712130

52. Warburg O., Wind F. NE. THE METABOLISM OF TUMORS IN THE BODY. *J ournal of General Physiology*. 1927;7(6):519-530. doi:10.1085/jgp.8.6.519

53. Devic S. Warburg Effect - a Consequence or the Cause of Carcinogenesis? *J Cancer*. 2016;7(7):817-822. doi:10.7150/jca.14274

54. Semenza GL. Hypoxia-Inducible Factor 1 (HIF-1) Pathway. *Science's STKE*. 2007;2007(407). doi:10.1126/stke.4072007cm8

55. Tian T, Li X, Zhang J. mTOR signaling in cancer and mtor inhibitors in solid tumor targeting therapy. *Int J Mol Sci*. 2019;20(3). doi:10.3390/ijms20030755

56. Watanabe R, Wei L, Huang J. MTOR signaling, function, novel inhibitors, and therapeutic targets. *Journal of Nuclear Medicine*. 2011;52(4):497-500. doi:10.2967/jnumed.111.089623

57. Conciatori F, Ciuffreda L, Bazzichetto C, et al. mTOR Cross-Talk in Cancer and Potential for Combination Therapy. *Cancers (Basel)*. 2018;10(1):23. doi:10.3390/cancers10010023

58. Dodd KM, Yang J, Shen MH, Sampson JR, Tee AR. mTORC1 drives HIF-1α and VEGF-A signalling via multiple mechanisms involving 4E-BP1, S6K1 and STAT3. *Oncogene*. 2015;34(17):2239-2250. doi:10.1038/onc.2014.164

59. Kalkat M, De Melo J, Hickman K, et al. MYC Deregulation in Primary Human Cancers. *Genes (Basel)*. 2017;8(6):151. doi:10.3390/genes8060151

60. Jaworska M, Szczudło J, Pietrzyk A, et al. The Warburg effect: a score for many instruments in the concert of cancer and cancer niche cells. *Pharmacological Reports*. 2023;75(4):876-890. doi:10.1007/s43440-023-00504-1

61. Nowak N, Kulma A, Gutowicz J. Up-regulation of key glycolysis proteins in cancer development. *Open Life Sci*. 2018;13(1):569-581. doi:10.1515/biol-2018-0068

62. Huang X, Zhao L, Peng R. Hypoxia-Inducible Factor 1 and Mitochondria: An Intimate Connection. *Biomolecules*. 2022;13(1):50. doi:10.3390/biom13010050

63. Zhang C, Liu J, Xu D, Zhang T, Hu W, Feng Z. Gain-of-function mutant p53 in cancer progression and therapy. *J Mol Cell Biol*. 2020;12(9):674-687. doi:10.1093/jmcb/mjaa040

64. Lacroix M, Riscal R, Arena G, Linares LK, Le Cam L. Metabolic functions of the tumor suppressor p53: Implications in normal physiology, metabolic disorders, and cancer. *Mol Metab*. 2020;33:2-22. doi:10.1016/j.molmet.2019.10.002

65. Liberti M V., Locasale JW. The Warburg Effect: How Does it Benefit Cancer Cells? *Trends Biochem Sci*. 2016;41(3):211-218. doi:10.1016/j.tibs.2015.12.001

66. Heiden MGV, Cantley LC, Thompson CB. Understanding the warburg effect: The metabolic requirements of cell proliferation. *Science (1979)*. 2009;324(5930):1029-1033. doi:10.1126/science.1160809

67. Jin L, Zhou Y. Crucial role of the pentose phosphate pathway in malignant tumors (review). *Oncol Lett*. 2019;17(5):4213-4221. doi:10.3892/ol.2019.10112

68. Wang JX, Choi SYC, Niu X, et al. Lactic acid and an acidic tumor microenvironment suppress anticancer immunity. *Int J Mol Sci*. 2020;21(21):1-14. doi:10.3390/ijms21218363

69. Estrella V, Chen T, Lloyd M, et al. Acidity generated by the tumor microenvironment drives local invasion. *Cancer Res*. 2013;73(5):1524-1535. doi:10.1158/0008-5472.CAN-12-2796

70. Liu C, Jin Y, Fan Z. The Mechanism of Warburg Effect-Induced Chemoresistance in Cancer. *Front Oncol*. 2021;11. doi:10.3389/fonc.2021.698023

71. Ge T, Yang J, Zhou S, Wang Y, Li Y, Tong X. The Role of the Pentose Phosphate Pathway in Diabetes and Cancer. *Front Endocrinol (Lausanne)*. 2020;11. doi:10.3389/fendo.2020.00365

72. Nakamura H, Takada K. Reactive oxygen species in cancer: Current findings and future directions. *Cancer Sci*. 2021;112(10):3945-3952. doi:10.1111/cas.15068

73. Chen J, Yang S, Li Y, et al. De novo nucleotide biosynthetic pathway and cancer. *Genes Dis*. 2023;10(6):2331-2338. doi:10.1016/j.gendis.2022.04.018

74. Vaupel P, Schmidberger H, Mayer A. The Warburg effect: essential part of metabolic reprogramming and central contributor to cancer progression. *Int J Radiat Biol*. 2019;95(7):912-919. doi:10.1080/09553002.2019.1589653

75. Kim JW, Dang C V. Cancer's molecular sweet tooth and the warburg effect. *Cancer Res*. 2006;66(18):8927-8930. doi:10.1158/0008-5472.CAN-06-1501

76. Moreno-Sánchez R, Rodríguez-Enríquez S, Marín-Hernández A, Saavedra E. Energy metabolism in tumor cells. *FEBS Journal*. 2007;274(6):1393-1418. doi:10.1111/j.1742-4658.2007.05686.x

77. Christofk HR, Vander Heiden MG, Harris MH, et al. The M2 splice isoform of pyruvate kinase is important for cancer metabolism and tumour growth. *Nature*. 2008;452(7184):230-233. doi:10.1038/nature06734

78. Potter M, Newport E, Morten KJ. The Warburg effect: 80 years on. *Biochem Soc Trans*. 2016;44(5):1499-1505. doi:10.1042/BST20160094

79. Ashton TM, Gillies McKenna W, Kunz-Schughart LA, Higgins GS. Oxidative phosphorylation as an emerging target in cancer therapy. *Clinical Cancer Research*. 2018;24(11):2482-2490. doi:10.1158/1078-0432.CCR-17-3070

80. Zheng J. Energy metabolism of cancer: Glycolysis versus oxidative phosphorylation (review). *Oncol Lett*. 2012;4(6):1151-1157. doi:10.3892/ol.2012.928

81. Kumar PR, Moore JA, Bowles KM, Rushworth SA, Moncrieff MD. Mitochondrial oxidative phosphorylation in cutaneous melanoma. *Br J Cancer*. 2021;124(1):115-123. doi:10.1038/s41416-020-01159-y

82. Whitaker-Menezes D, Martinez-Outschoorn UE, Flomenberg N, et al. Hyperactivation of oxidative mitochondrial metabolism in epithelial cancer cells in situ. *Cell Cycle*. 2011;10(23):4047-4064. doi:10.4161/cc.10.23.18151

83. Schöpf B, Weissensteiner H, Schäfer G, et al. OXPHOS remodeling in high-grade prostate cancer involves mtDNA mutations and increased succinate oxidation. *Nat Commun*. 2020;11(1). doi:10.1038/s41467-020-15237-5

84. Xu Y, Xue D, Bankhead A, Neamati N. Why All the Fuss about Oxidative Phosphorylation (OXPHOS)? *J Med Chem*. 2020;63(23):14276-14307. doi:10.1021/acs.jmedchem.0c01013

85. Lissanu Deribe Y, Sun Y, Terranova C, et al. Mutations in the SWI/SNF complex induce a targetable dependence on oxidative phosphorylation in lung cancer article. *Nat Med*. 2018;24(7):1047-1057. doi:10.1038/s41591-018-0019-5

86. Shackelford DB, Abt E, Gerken L, et al. LKB1 Inactivation Dictates Therapeutic Response of Non-Small Cell Lung Cancer to the Metabolism Drug Phenformin. *Cancer Cell*. 2013;23(2):143-158. doi:10.1016/j.ccr.2012.12.008

87. Zacksenhaus E, Shrestha M, Liu JC, et al. Mitochondrial OXPHOS Induced by RB1 Deficiency in Breast Cancer: Implications for Anabolic Metabolism, Stemness, and Metastasis. *Trends Cancer*. 2017;3(11):768-779. doi:10.1016/j.trecan.2017.09.002

88. Zhao Z, Mei Y, Wang Z, He W. The Effect of Oxidative Phosphorylation on Cancer Drug Resistance. *Cancers (Basel)*. 2022;15(1):62. doi:10.3390/cancers15010062

89. Jin J, Byun JK, Choi YK, Park KG. Targeting glutamine metabolism as a therapeutic strategy for cancer. *Exp Mol Med*. 2023;55(4):706-715. doi:10.1038/s12276-023-00971-9

90. Koundouros N, Poulogiannis G. Reprogramming of fatty acid metabolism in cancer. *Br J Cancer*. 2020;122(1):4-22. doi:10.1038/s41416-019-0650-z

91. Wilde L, Roche M, Domingo-Vidal M, et al. Metabolic coupling and the Reverse Warburg Effect in cancer: Implications for novel biomarker and anticancer agent development. *Semin Oncol*. 2017;44(3):198-203. doi:10.1053/j.seminoncol.2017.10.004

92. Lisanti MP, Martinez-Outschoorn UE, Chiavarina B, et al. Understanding the “lethal” drivers of tumor-stroma co-evolution: Emerging role(s) for hypoxia, oxidative stress and autophagy/mitophagy in the tumor micro-environment. *Cancer Biol Ther*. 2010;10(6):537-542. doi:10.4161/cbt.10.6.13370

93. Liang L, Li W, Li X, et al. ‘Reverse Warburg effect’ of cancer-associated fibroblasts (Review). *Int J Oncol*. 2022;60(6):67. doi:10.3892/ijo.2022.5357

94. Ullah MS, Davies AJ, Halestrap AP. The plasma membrane lactate transporter MCT4, but not MCT1, is up-regulated by hypoxia through a HIF-1α-dependent mechanism. *Journal of Biological Chemistry*. 2006;281(14):9030-9037. doi:10.1074/jbc.M511397200

95. Payen VL, Mina E, Van Hée VF, Porporato PE, Sonveaux P. Monocarboxylate transporters in cancer. *Mol Metab*. 2020;33:48-66. doi:10.1016/j.molmet.2019.07.006

96. Reina-Campos M, Moscat J, Diaz-Meco M. Metabolism shapes the tumor microenvironment. *Curr Opin Cell Biol*. 2017;48:47-53. doi:10.1016/j.ceb.2017.05.006

97. Benny S, Mishra R, Manojkumar MK, Aneesh TP. From Warburg effect to Reverse Warburg effect; the new horizons of anti-cancer therapy. *Med Hypotheses*. 2020;144. doi:10.1016/j.mehy.2020.110216

98. Anderson NM, Simon MC. The tumor microenvironment. *Current Biology*. 2020;30(16):R921-R925. doi:10.1016/j.cub.2020.06.081

99. Yang L V. Tumor microenvironment and metabolism. *Int J Mol Sci*. 2017;18(12). doi:10.3390/ijms18122729

100. Ohta A, Gorelik E, Prasad SJ, et al. *A2A Adenosine Receptor Protects Tumors from Antitumor T Cells*.; 2006. www.pnas.orgcgidoi10.1073pnas.0605251103

101. Neophytou CM, Panagi M, Stylianopoulos T, Papageorgis P. cancers The Role of Tumor Microenvironment in Cancer Metastasis: Molecular Mechanisms and Therapeutic Opportunities. Published online 2021. doi:10.3390/cancers

102. Chen JQ, Russo J. Dysregulation of glucose transport, glycolysis, TCA cycle and glutaminolysis by oncogenes and tumor suppressors in cancer cells. *Biochimica et Biophysica Acta (BBA) - Reviews on Cancer*. 2012;1826(2):370-384. doi:10.1016/j.bbcan.2012.06.004

103. Ahn CS, Metallo CM. Mitochondria as biosynthetic factories for cancer proliferation. *Cancer Metab*. 2015;3(1). doi:10.1186/s40170-015-0128-2

104. Zhao Y, Liu X, Si F, et al. Citrate Promotes Excessive Lipid Biosynthesis and Senescence in Tumor Cells for Tumor Therapy. *Advanced Science*. 2022;9(1). doi:10.1002/advs.202101553

105. Stine ZE, Altman BJ, Hsieh AL, Gouw AM, Dang C V. Deregulation of the Cellular Energetics of Cancer Cells. In: *Pathobiology of Human Disease: A Dynamic Encyclopedia of Disease Mechanisms*. Elsevier Inc.; 2014:444-455. doi:10.1016/B978-0-12-386456-7.01912-2

106. Eniafe J, Jiang S. The functional roles of TCA cycle metabolites in cancer. *Oncogene*. 2021;40(19):3351-3363. doi:10.1038/s41388-020-01639-8

107. Anderson NM, Mucka P, Kern JG, Feng H. The emerging role and targetability of the TCA cycle in cancer metabolism. *Protein Cell*. 2018;9(2):216-237. doi:10.1007/s13238-017-0451-1

108. Fukuda R, Zhang H, Kim J whan, Shimoda L, Dang C V., Semenza GLL. HIF-1 Regulates Cytochrome Oxidase Subunits to Optimize Efficiency of Respiration in Hypoxic Cells. *Cell*. 2007;129(1):111-122. doi:10.1016/j.cell.2007.01.047

109. Fuhrmann DC, Brüne B. Mitochondrial composition and function under the control of hypoxia. *Redox Biol*. 2017;12:208-215. doi:10.1016/j.redox.2017.02.012

110. Michl J, Wang Y, Monterisi S, et al. CRISPR-Cas9 screen identifies oxidative phosphorylation as essential for cancer cell survival at low extracellular pH. *Cell Rep*. 2022;38(10):110493. doi:10.1016/j.celrep.2022.110493

111. Rohani N, Hao L, Alexis MS, et al. Acidification of tumor at stromal boundaries drives transcriptome alterations associated with aggressive phenotypes. *Cancer Res*. 2019;79(8):1952-1966. doi:10.1158/0008-5472.CAN-18-1604

112. Li T, Copeland C, Le A. Glutamine Metabolism in Cancer. In: *The Heterogeneity of Cancer Metabolism. Advances in Experimental Medicine and Biology*. Vol 1311. Springer, Cham; 2021:17-38. http://www.springer.com/series/5584

113. Shah MA, Rogoff HA. Implications of reactive oxygen species on cancer formation and its treatment. *Semin Oncol*. 2021;48(3):238-245. doi:10.1053/j.seminoncol.2021.05.002

114. Liou GY, Storz P. Reactive oxygen species in cancer. *Free Radic Res*. 2010;44(5):479-496. doi:10.3109/10715761003667554

115. Waris G, Ahsan H. Reactive oxygen species: Role in the development of cancer and various chronic conditions. *J Carcinog*. 2006;5:1-8. doi:10.1186/1477-3163-5-14

116. Wei H. *Activation of Oncogenes and/or Inactivation of Anti-Oncogenes by Reactive Oxygen Species*. Vol 8.; 1992.

117. Irani K, Xia Y, Zweier JL, et al. Mitogenic Signaling Mediated by Oxidants in Ras-Transformed Fibroblasts. *Adv Sci*. 2008;275(5306):1649-1652.

118. Heppner DE, van der Vliet A. Redox-dependent regulation of epidermal growth factor receptor signaling. *Redox Biol*. 2016;8:24-27. doi:10.1016/j.redox.2015.12.002

119. Reczek CR, Chandel NS. The two faces of reactive oxygen species in cancer. *Annu Rev Cancer Biol*. 2017;1:79-98. doi:10.1146/annurev-cancerbio-041916-065808

120. Sigismund S, Avanzato D, Lanzetti L. Emerging functions of the EGFR in cancer. *Mol Oncol*. 2018;12(1):3-20. doi:10.1002/1878-0261.12155

121. Ushio-Fukai M, Nakamura Y. Reactive oxygen species and angiogenesis: NADPH oxidase as target for cancer therapy. *Cancer Lett*. 2008;266(1):37-52. doi:10.1016/j.canlet.2008.02.044

122. *Role of Oxidative Stress in Angiogenesis and the Therapeutic Potential of Antioxidants in Breast Cancer*.

123. Ichijo H, Nishida E, Irie K, et al. Induction of Apoptosis by ASK1, a Mammalian MAPKKK That Activates SAPK/JNK and p38 Signaling Pathways. *Science (1979)*. 1997;275(5296):90-94. doi:10.1126/science.275.5296.90

124. Morgan MJ, Liu ZG. Crosstalk of reactive oxygen species and NF-κB signaling. *Cell Res*. 2011;21(1):103-115. doi:10.1038/cr.2010.178

125. Baryła M, Semeniuk-Wojtaś A, Róg L, Kraj L, Małyszko M, Stec R. Oncometabolites—A Link between Cancer Cells and Tumor Microenvironment. *Biology (Basel)*. 2022;11(2):1-18. doi:10.3390/biology11020270

126. Scagliola A, Mainini F, Cardaci S. The tricarboxylic acid cycle at the crossroad between cancer and immunity. *Antioxid Redox Signal*. 2020;32(12):834-852. doi:10.1089/ars.2019.7974

127. Du X, Hu H. The Roles of 2-Hydroxyglutarate. *Front Cell Dev Biol*. 2021;9(March):1-13. doi:10.3389/fcell.2021.651317

128. Stine ZE, Altman BJ, Hsieh AL, Gouw AM, Dang C V. Deregulation of the Cellular Energetics of Cancer Cells. In: *Pathobiology of Human Disease: A Dynamic Encyclopedia of Disease Mechanisms*. Elsevier Inc.; 2014:444-455. doi:10.1016/B978-0-12-386456-7.01912-2

129. Weiss JM. The promise and peril of targeting cell metabolism for cancer therapy. *Cancer Immunology, Immunotherapy*. 2020;69(2):255-261. doi:10.1007/s00262-019-02432-7

130. Galbraith M, Levine H, Onuchic JN, Jia D. Decoding the coupled decision-making of the epithelial-mesenchymal transition and metabolic reprogramming in cancer. *iScience*. 2023;26(1). doi:10.1016/j.isci.2022.105719

131. Tochhawng L, Deng S, Pervaiz S, Yap CT. Redox regulation of cancer cell migration and invasion. *Mitochondrion*. 2013;13(3):246-253. doi:10.1016/j.mito.2012.08.002

132. Bhattacharya D, Scimè A. Metabolic Regulation of Epithelial to Mesenchymal Transition: Implications for Endocrine Cancer. *Front Endocrinol (Lausanne)*. 2019;10. doi:10.3389/fendo.2019.00773

133. Hu Y, Xu W, Zeng H, et al. OXPHOS-dependent metabolic reprogramming prompts metastatic potential of breast cancer cells under osteogenic differentiation. *Br J Cancer*. 2020;123(11):1644-1655. doi:10.1038/s41416-020-01040-y

134. Passaniti A, Kim MS, Polster BM, Shapiro P. Targeting mitochondrial metabolism for metastatic cancer therapy. *Mol Carcinog*. 2022;61(9):827-838. doi:10.1002/mc.23436

135. Lebleu VS, O'Connell JT, Gonzalez Herrera KN, et al. PGC-1α mediates mitochondrial biogenesis and oxidative phosphorylation in cancer cells to promote metastasis. *Nat Cell Biol*. 2014;16(10):992-1003. doi:10.1038/ncb3039

136. Gaude E, Frezza C. Tissue-specific and convergent metabolic transformation of cancer correlates with metastatic potential and patient survival. *Nat Commun*. 2016;7. doi:10.1038/ncomms13041

137. Muralidharan S, Sahoo S, Saha A, et al. Quantifying the Patterns of Metabolic Plasticity and Heterogeneity along the Epithelial–Hybrid–Mesenchymal Spectrum in Cancer. *Biomolecules*. 2022;12(2):297. doi:10.3390/biom12020297

138. Porporato PE, Filigheddu N, Pedro JMBS, Kroemer G, Galluzzi L. Mitochondrial metabolism and cancer. *Cell Res*. 2018;28(3):265-280. doi:10.1038/cr.2017.155

139. Najjar YG, Menk A V., Sander C, et al. Tumor cell oxidative metabolism as a barrier to PD-1 blockade immunotherapy in melanoma. *JCI Insight*. 2019;4(5). doi:10.1172/jci.insight.124989

140. In GK, Ribeiro JR, Yin J, et al. Multi-omic profiling reveals discrepant immunogenic properties and a unique tumor microenvironment among melanoma brain metastases. *NPJ Precis Oncol*. 2023;7(1). doi:10.1038/s41698-023-00471-z

141. Li C, Phoon YP, Karlinsey K, et al. A high OXPHOS CD8 T cell subset is predictive of immunotherapy resistance in melanoma patients. *Journal of Experimental Medicine*. 2022;219(1). doi:10.1084/jem.20202084

142. Zhu X, Chen HH, Gao CY, et al. Energy metabolism in cancer stem cells. *World J Stem Cells*. 2020;12(6):448-461. doi:10.4252/WJSC.V12.I6.448

143. Li Y, Wang Z, Ajani JA, Song S. Drug resistance and Cancer stem cells. *Cell Communication and Signaling*. 2021;19(1). doi:10.1186/s12964-020-00627-5

144. Missiroli S, Perrone M, Genovese I, Pinton P, Giorgi C. Cancer metabolism and mitochondria: Finding novel mechanisms to fight tumours. *EBioMedicine*. 2020;59. doi:10.1016/j.ebiom.2020.102943

145. Jia P, Wu Y, Du H, et al. I-8, a novel inhibitor of mutant IDH1, inhibits cancer progression in vitro and in vivo. *European Journal of Pharmaceutical Sciences*. 2019;140(September):105072. doi:10.1016/j.ejps.2019.105072

146. Stein EM, DiNardo CD, Pollyea DA, et al. Enasidenib in mutant IDH2 relapsed or refractory acute myeloid leukemia. *Blood*. 2017;130(6):722-731. doi:10.1182/blood-2017-04-779405

147. Cassidy-Stone A, Chipuk JE, Ingerman E, et al. Chemical Inhibition of the Mitochondrial Division Dynamin Reveals Its Role in Bax/Bak-Dependent Mitochondrial Outer Membrane Permeabilization. *Dev Cell*. 2008;14(2):193-204. doi:10.1016/j.devcel.2007.11.019

148. Olichon A, Baricault L, Gas N, et al. Loss of OPA1 perturbates the mitochondrial inner membrane structure and integrity, leading to cytochrome c release and apoptosis. *Journal of Biological Chemistry*. 2003;278(10):7743-7746. doi:10.1074/jbc.C200677200

149. Montero AJ, Jassem J. Cellular redox pathways as a therapeutic target in the treatment of cancer. *Drugs*. 2011;71(11):1385-1396. doi:10.2165/11592590-000000000-00000

150. Vasan K, Werner M, Chandel NS. Mitochondrial Metabolism as a Target for Cancer Therapy. *Cell Metab*. 2020;32(3):341-352. doi:10.1016/j.cmet.2020.06.019

151. Kaushik I, Ramachandran S, Prasad S, Srivastava SK. Drug rechanneling: A novel paradigm for cancer treatment. *Semin Cancer Biol*. 2021;68:279-290. doi:10.1016/j.semcancer.2020.03.011

152. Shaw R.J., Lamia K.A., Vasquez D., Koo S.H., Bardeesy N., Depinho R.A., Montminy M. CLC. The Kinase LKB1 Mediates Glucose Homeostasis in Liver and Therapeutic Effects of Metformin. *Science (1979)*. 2005;310(5754):1642-1646. doi:10.1126/science.1120781.The

153. Evans J.M., Donnelly L.A., Emslie-Smith A.M., Alessi D.R. MAD. Metformin and reduced risk of cancer in diabetic patients. *Br Med J*. 2005;330(7503):1303-1304. doi:10.1136/bmj.38393.572188.EB

154. Choi YK, Park KG. Metabolic roles of AMPK and metformin in cancer cells. *Mol Cells*. 2013;36(4):279-287. doi:10.1007/s10059-013-0169-8

155. Keerthana CK, Rayginia TP, Shifana SC, et al. The role of AMPK in cancer metabolism and its impact on the immunomodulation of the tumor microenvironment. *Front Immunol*. 2023;14(February):1-16. doi:10.3389/fimmu.2023.1114582

156. Brown JR, Chan DK, Shank JJ, et al. Phase II clinical trial of metformin as a cancer stem cell–targeting agent in ovarian cancer. *JCI Insight*. 2020;5(11):1-12. doi:10.1172/jci.insight.133247

157. Gulati S, Desai J, Palackdharry SM, et al. Phase 1 dose-finding study of metformin in combination with concurrent cisplatin and radiotherapy in patients with locally advanced head and neck squamous cell cancer. *Cancer*. 2020;126(2):354-362. doi:10.1002/cncr.32539

158. Lord SR, Harris AL. Is it still worth pursuing the repurposing of metformin as a cancer therapeutic? *Br J Cancer*. 2023;128(6):958-966. doi:10.1038/s41416-023-02204-2

159. Fiorillo M, Lamb R, Tanowitz HB, et al. Repurposing atovaquone: Targeting mitochondrial complex III and OXPHOS to eradicate cancer stem cells. *Oncotarget*. 2016;7(23):34084-34099. doi:10.18632/oncotarget.9122

160. Hammond DJ, Burchell JR, Pudney M. Inhibition of pyrimidine biosynthesis de novo in Plasmodium falciparum by 2-(4-t-butylcyclohexyl)-3-hydroxy-1,4-naphthoquinone in vitro. *Mol Biochem Parasitol*. 1985;14(1):97-109. doi:10.1016/0166-6851(85)90109-4

161. Ashton TM, Fokas E, Kunz-Schughart LA, et al. The anti-malarial atovaquone increases radiosensitivity by alleviating tumour hypoxia. *Nat Commun*. 2016;7. doi:10.1038/ncomms12308

162. Coates JTT, Rodriguez-Berriguete G, Puliyadi R, et al. The anti-malarial drug atovaquone potentiates platinum-mediated cancer cell death by increasing oxidative stress. *Cell Death Discov*. 2020;6(1). doi:10.1038/s41420-020-00343-6

163. Skwarski M, McGowan DR, Belcher E, et al. Mitochondrial inhibitor atovaquone increases tumor oxygenation and inhibits hypoxic gene expression in patients with non-small cell lung cancer. *Clinical Cancer Research*. 2021;27(9):2459-2469. doi:10.1158/1078-0432.CCR-20-4128

164. Gao Y, Shang Q, Li W, et al. Antibiotics for cancer treatment: A double-edged sword. *J Cancer*. 2020;11(17):5135-5149. doi:10.7150/jca.47470

165. Vázquez-Laslop N, Mankin AS. How Macrolide Antibiotics Work. *Trends Biochem Sci*. 2018;43(9):668-684. doi:10.1016/j.tibs.2018.06.011

166. Yaghoubi S, Zekiy AO, Krutova M, et al. Tigecycline antibacterial activity, clinical effectiveness, and mechanisms and epidemiology of resistance: narrative review. *European Journal of Clinical Microbiology & Infectious Diseases*. 2022;41(7):1003-1022. doi:10.1007/s10096-020-04121-1

167. Dong Z, Abbas MN, Kausar S, et al. Biological Functions and Molecular Mechanisms of Antibiotic Tigecycline in the Treatment of Cancers. *Int J Mol Sci*. 2019;20(14):3577. doi:10.3390/ijms20143577

168. Reed GA, Schiller GJ, Kambhampati S, et al. A Phase 1 study of intravenous infusions of tigecycline in patients with acute myeloid leukemia. *Cancer Med*. 2016;5(11):3031-3040. doi:10.1002/cam4.845

169. Molina JR, Sun Y, Protopopova M, et al. An inhibitor of oxidative phosphorylation exploits cancer vulnerability. *Nat Med*. 2018;24(7):1036-1046. doi:10.1038/s41591-018-0052-4

170. Yap TA, Daver N, Mahendra M, et al. Complex I inhibitor of oxidative phosphorylation in advanced solid tumors and acute myeloid leukemia: phase I trials. *Nat Med*. 2023;29(1):115-126. doi:10.1038/s41591-022-02103-8

171. Noble RA, Thomas H, Zhao Y, et al. Simultaneous targeting of glycolysis and oxidative phosphorylation as a therapeutic strategy to treat diffuse large B-cell lymphoma. *Br J Cancer*. 2022;(April). doi:10.1038/s41416-022-01848-w

172. Rha SY, Beom SH, Shin YG, et al. Phase I study of IM156, a novel potent biguanide oxidative phosphorylation (OXPHOS) inhibitor, in patients with advanced solid tumors. *Journal of Clinical Oncology*. 2020;38(15_suppl):3590-3590. doi:10.1200/jco.2020.38.15_suppl.3590

173. Kulkarni CA, Fink BD, Gibbs BE, et al. A Novel Triphenylphosphonium Carrier to Target Mitochondria without Uncoupling Oxidative Phosphorylation. *J Med Chem*. 2021;64(1):662-676. doi:10.1021/acs.jmedchem.0c01671

174. Smith RAJ, Porteous CM, Coulter C V., Murphy MP. Selective targeting of an antioxidant to mitochondria. *Eur J Biochem*. 1999;263(3):709-716. doi:10.1046/j.1432-1327.1999.00543.x

175. Zielonka J, Cheng G, Mcallister DM, et al. Mitochondria-targeted chromanol inhibits breast cancer cell energy metabolism and promotes cell death. *Free Radical Research Center and Department of Biophysics*. 2013;13:10.

176. Zinovkin RA, Lyamzaev KG, Chernyak B V. Current perspectives of mitochondria-targeted antioxidants in cancer prevention and treatment. *Front Cell Dev Biol*. 2023;11(March):1-15. doi:10.3389/fcell.2023.1048177

177. Kalyanaraman B, Cheng G, Hardy M, et al. Mitochondria-targeted metformins: Antitumour and redox signalling mechanisms. *Interface Focus*. 2017;7(2). doi:10.1098/rsfs.2016.0109

178. Cheng, G., Zielonka, J., Ouari, O., Lopez, M., McAllister, D., Boyle, K., Barrios, C.S., Weber, J.J., Johnson, B.D., Hardy, M., Dwinell, M.B., Kalyanaraman B. Mitochondria-targeted analogs of metformin exhibit enhanced antiproliferative and radiosensitizing effects in pancreatic cancer cells. *Cancer Res*. 2016;76(13):3904-3915. doi:10.1158/0008-5472.CAN-15-2534.Mitochondria-targeted

179. Xu Y, Xue D, Bankhead A, Neamati N. Why All the Fuss about Oxidative Phosphorylation (OXPHOS)? *J Med Chem*. 2020;63(23):14276-14307. doi:10.1021/acs.jmedchem.0c01013

180. Varga Z V., Ferdinandy P, Liaudet L, Pacher P. Drug-induced mitochondrial dysfunction and cardiotoxicity. *Am J Physiol Heart Circ Physiol*. 2015;309(9):H1453-H1467. doi:10.1152/ajpheart.00554.2015

181. Rana P, Aleo MD, Gosink M, Will Y. Evaluation of in Vitro Mitochondrial Toxicity Assays and Physicochemical Properties for Prediction of Organ Toxicity Using 228 Pharmaceutical Drugs. *Chem Res Toxicol*. 2019;32(1):156-167. doi:10.1021/acs.chemrestox.8b00246

182. Bando K, Ochiai S, Kunimatsu T, et al. Comparison of potential risks of lactic acidosis induction by biguanides in rats. *Regulatory Toxicology and Pharmacology*. 2010;58(1):155-160. doi:10.1016/j.yrtph.2010.05.005

183. Janku F, LoRusso P, Mansfield AS, et al. First-in-human evaluation of the novel mitochondrial complex I inhibitor ASP4132 for treatment of cancer. *Invest New Drugs*. 2021;39(5):1348-1356. doi:10.1007/s10637-021-01112-7

184. Rubiño MEG, Carrillo E, Alcalá GR, Domínguez-Martín A, Marchal JA, Boulaiz H. Phenformin as an anticancer agent: Challenges and prospects. *Int J Mol Sci*. 2019;20(13). doi:10.3390/ijms20133316

185. Kolata GB. The Phenformin Ban: Is the Drug an Imminent Hazard? *Science (1979)*. 1979;203(4385):1094-1096. doi:10.1126/science.424735

186. Saraei P, Asadi I, Kakar MA, Moradi-Kor N. The beneficial effects of metformin on cancer prevention and therapy: A comprehensive review of recent advances. *Cancer Manag Res*. 2019;11:3295-3313. doi:10.2147/CMAR.S200059

187. Whitburn J, Edwards CM, Sooriakumaran P. Metformin and Prostate Cancer: a New Role for an Old Drug. *Curr Urol Rep*. 2017;18(6):1-7. doi:10.1007/s11934-017-0693-8

188. Yap TA, Daver N, Mahendra M, et al. Complex I inhibitor of oxidative phosphorylation in advanced solid tumors and acute myeloid leukemia: phase I trials. *Nat Med*. 2023;29(1):115-126. doi:10.1038/s41591-022-02103-8

189. Rovini A, Heslop K, Hunt EG, et al. Quantitative analysis of mitochondrial membrane potential heterogeneity in unsynchronized and synchronized cancer cells. *FASEB Journal*. 2021;35(1):1-14. doi:10.1096/fj.202001693R

190. Santos-de-Frutos K, Djouder N. When dormancy fuels tumour relapse. *Commun Biol*. 2021;4(1):747. doi:10.1038/s42003-021-02257-0

191. Zong WX, Rabinowitz JD, White E. Mitochondria and Cancer. *Mol Cell*. 2016;61(5):667-676. doi:10.1016/j.molcel.2016.02.011

192. Martinez-Outschoorn UE, Peiris-Pagés M, Pestell RG, Sotgia F, Lisanti MP. Cancer metabolism: A therapeutic perspective. *Nat Rev Clin Oncol*. 2017;14(1):11-31. doi:10.1038/nrclinonc.2016.60

193. Wong AL, Soo RA, Tan DS, et al. Phase I and biomarker study of OPB-51602, a novel signal transducer and activator of transcription (STAT) 3 inhibitor, in patients with refractory solid malignancies. *Annals of Oncology*. 2015;26(5):998-1005. doi:10.1093/annonc/mdv026

194. Tsuji A, Akao T, Masuya T, Murai M, Miyoshi H. IACS-010759, a potent inhibitor of glycolysis-deficient hypoxic tumor cells, inhibits mitochondrial respiratory complex I through a unique mechanism. *Journal of Biological Chemistry*. 2020;295(21):7481-7491. doi:10.1074/jbc.RA120.013366

195. Janku F, LoRusso P, Mansfield AS, et al. First-in-human evaluation of the novel mitochondrial complex I inhibitor ASP4132 for treatment of cancer. *Invest New Drugs*. 2021;39(5):1348-1356. doi:10.1007/s10637-021-01112-7

196. Cadassou O, Jordheim LP. OXPHOS inhibitors, metabolism and targeted therapies in cancer. *Biochem Pharmacol*. 2023;211:115531. doi:10.1016/j.bcp.2023.115531

197. Mitola G, Falvo P, Bertolini F. New Insight to Overcome Tumor Resistance: An Overview from Cellular to Clinical Therapies. *Life*. 2021;11(11):1131. doi:10.3390/life11111131

198. Oliva CR, Markert T, Ross LJ, et al. Identification of Small Molecule Inhibitors of Human Cytochrome c Oxidase That Target Chemoresistant Glioma Cells. *Journal of Biological Chemistry*. 2016;291(46):24188-24199. doi:10.1074/jbc.M116.749978

199. Bastian A, Matsuzaki S, Humphries KM, et al. AG311, a small molecule inhibitor of complex I and hypoxia-induced HIF-1α stabilization. *Cancer Lett*. 2017;388:149-157. doi:10.1016/j.canlet.2016.11.040

200. Jung KH, Song SH, Paik JY, et al. Direct Targeting of Tumor Cell F1F0 ATP-Synthase by Radioiodine Angiostatin In Vitro and In Vivo. *Cancer Biother Radiopharm*. 2007;22(5):704-712. doi:10.1089/cbr.2007.369

201. Salomon AR, Voehringer DW, Herzenberg LA, Khosla C. Apoptolidin, a selective cytotoxic agent, is an inhibitor of F0F1-ATPase. *Chem Biol*. 2001;8(1):71-80. doi:10.1016/S1074-5521(00)00057-0

202. Diepart C, Karroum O, Magat J, et al. Arsenic Trioxide Treatment Decreases the Oxygen Consumption Rate of Tumor Cells and Radiosensitizes Solid Tumors. *Cancer Res*. 2012;72(2):482-490. doi:10.1158/0008-5472.CAN-11-1755

203. Broniarek I, Jarmuszkiewicz W. Atorvastatin affects negatively respiratory function of isolated endothelial mitochondria. *Arch Biochem Biophys*. 2018;637:64-72. doi:10.1016/j.abb.2017.12.003

204. Schöckel L, Glasauer A, Basit F, et al. Targeting mitochondrial complex I using BAY 87-2243 reduces melanoma tumor growth. *Cancer Metab*. 2015;3(1):11. doi:10.1186/s40170-015-0138-0

205. Schöckel L, Glasauer A, Basit F, et al. Targeting mitochondrial complex I using BAY 87-2243 reduces melanoma tumor growth. *Cancer Metab*. 2015;3(1):1-16. doi:10.1186/s40170-015-0138-0

206. Ellinghaus P, Heisler I, Unterschemmann K, et al. BAY 87-2243, a highly potent and selective inhibitor of hypoxia-induced gene activation has antitumor activities by inhibition of mitochondrial complex I. *Cancer Med*. 2013;2(5):611-624. doi:10.1002/cam4.112

207. Ellinghaus P, Heisler I, Unterschemmann K, et al. BAY 87-2243, a highly potent and selective inhibitor of hypoxia-induced gene activation has antitumor activities by inhibition of mitochondrial complex I. *Cancer Med*. 2013;2(5):611-624. doi:10.1002/cam4.112

208. Fiorillo M, Lamb R, Tanowitz HB, et al. Bedaquiline, an FDA-approved antibiotic, inhibits mitochondrial function and potently blocks the proliferative expansion of stem-like cancer cells (CSCs). *Aging*. 2016;8(8):1593-1607. doi:10.18632/aging.100983

209. Biziotis O, Tsakiridis EE, Ali A, et al. Canagliflozin mediates tumor suppression alone and in combination with radiotherapy in non-small cell lung cancer (NSCLC) through inhibition of HIF-1α. *Mol Oncol*. 2023;17(11):2235-2256. doi:10.1002/1878-0261.13508

210. Angelopoulou A, Kolokithas-Ntoukas A, Papaioannou L, et al. Canagliflozin-loaded magnetic nanoparticles as potential treatment of hypoxic tumors in combination with radiotherapy. *Nanomedicine*. 2018;13(19):2435-2454. doi:10.2217/nnm-2018-0145

211. Ju R, Fei K, Li S, et al. Metabolic Mechanisms and a Rational Combinational Application of Carboxyamidotriazole in Fighting Pancreatic Cancer Progression after Chemotherapy. *Journal of Pharmacology and Experimental Therapeutics*. 2018;367(1):20-27. doi:10.1124/jpet.118.249326

212. Ju R, Guo L, Li J, et al. Carboxyamidotriazole inhibits oxidative phosphorylation in cancer cells and exerts synergistic anti-cancer effect with glycolysis inhibition. *Cancer Lett*. 2016;370(2):232-241. doi:10.1016/j.canlet.2015.10.025

213. Nadanaciva S, Bernal A, Aggeler R, Capaldi R, Will Y. Target identification of drug induced mitochondrial toxicity using immunocapture based OXPHOS activity assays. *Toxicology in Vitro*. 2007;21(5):902-911. doi:10.1016/j.tiv.2007.01.011

214. Udeani GO, Gerhauser C, Thomas CF, et al. Cancer chemopreventive activity mediated by deguelin, a naturally occurring rotenoid. *Cancer Res*. 1997;57(16):3424-3428.

215. Kim WY, Chang DJ, Hennessy B, et al. A Novel Derivative of the Natural Agent Deguelin for Cancer Chemoprevention and Therapy. *Cancer Prevention Research*. 2008;1(7):577-587. doi:10.1158/1940-6207.CAPR-08-0184

216. Wilk A, Wyczechowska D, Zapata A, et al. Molecular Mechanisms of Fenofibrate-Induced Metabolic Catastrophe and Glioblastoma Cell Death. *Mol Cell Biol*. 2015;35(1):182-198. doi:10.1128/MCB.00562-14

217. Brunmair B, Lest A, Staniek K, et al. Fenofibrate Impairs Rat Mitochondrial Function by Inhibition of Respiratory Complex I. *Journal of Pharmacology and Experimental Therapeutics*. 2004;311(1):109-114. doi:10.1124/jpet.104.068312

218. Zou Y, Sun Y, Wang Y, et al. Cancer cell-mitochondria hybrid membrane coated Gboxin loaded nanomedicines for glioblastoma treatment. *Nat Commun*. 2023;14(1). doi:10.1038/s41467-023-40280-3

219. Shi Y, Lim SK, Liang Q, et al. Gboxin is an oxidative phosphorylation inhibitor that targets glioblastoma. *Nature*. 2019;567(7748):341-346. doi:10.1038/s41586-019-0993-x

220. Molina JR, Sun Y, Protopopova M, et al. An inhibitor of oxidative phosphorylation exploits cancer vulnerability. *Nat Med*. 2018;24(7):1036-1046. doi:10.1038/s41591-018-0052-4

221. Noble RA, Thomas H, Zhao Y, et al. Simultaneous targeting of glycolysis and oxidative phosphorylation as a therapeutic strategy to treat diffuse large B-cell lymphoma. *Br J Cancer*. 2022;(April). doi:10.1038/s41416-022-01848-w

222. Rha SY, Beom SH, Shin YG, et al. Phase I study of IM156, a novel potent biguanide oxidative phosphorylation (OXPHOS) inhibitor, in patients with advanced solid tumors. *Journal of Clinical Oncology*. 2020;38(15_suppl):3590-3590. doi:10.1200/jco.2020.38.15_suppl.3590

223. Morgan J, Liu Y, Coothankandaswamy V, et al. Kalkitoxin Inhibits Angiogenesis, Disrupts Cellular Hypoxic Signaling, and Blocks Mitochondrial Electron Transport in Tumor Cells. *Mar Drugs*. 2015;13(3):1552-1568. doi:10.3390/md13031552

224. Young CW, Currie VE, Kim JH, O'Hehir MA, Farag FM, Kinahan JE. Phase I and Clinical Pharmacologic Evaluation of Lonidamine in Patients with Advanced Cancer. *Oncology*. 1984;41(1):60-65. doi:10.1159/000225888

225. Amadori D, Frassineti GL, De Matteis A, et al. Modulating effect of lonidamine on response to doxorubicin in metastatic breast cancer patients: Results from a multicenter prospective randomized trial. *Breast Cancer Res Treat*. 1998;49(3):209-217. doi:10.1023/A:1006063412726

226. Nisticò C, Garufi C, Milella M, et al. Weekly epirubicin plus lonidamine in advanced breast carcinoma. *Breast Cancer Res Treat*. 1999;56(3):231-235. doi:10.1023/A:1006213815195

227. Lim SC, Carey KT, Mckenzie M. *Anti-Cancer Analogues ME-143 and ME-344 Exert Toxicity by Directly Inhibiting Mitochondrial NADH: Ubiquinone Oxidoreductase (Complex I)*. Vol 5.; 2015. www.ajcr.us/ISSN:2156-6976/ajcr0003000

228. Zhang L, Zhang J, Ye Z, Townsend DM, Tew KD. Pharmacology of ME-344, a novel cytotoxic isoflavone. In: ; 2019:187-207. doi:10.1016/bs.acr.2019.01.005

229. Gulati S, Desai J, Palackdharry SM, et al. Phase 1 dose-finding study of metformin in combination with concurrent cisplatin and radiotherapy in patients with locally advanced head and neck squamous cell cancer. *Cancer*. 2020;126(2):354-362. doi:10.1002/cncr.32539

230. Saraei P, Asadi I, Kakar MA, Moradi-Kor N. The beneficial effects of metformin on cancer prevention and therapy: A comprehensive review of recent advances. *Cancer Manag Res*. 2019;11:3295-3313. doi:10.2147/CMAR.S200059

231. Brown JR, Chan DK, Shank JJ, et al. Phase II clinical trial of metformin as a cancer stem cell–targeting agent in ovarian cancer. *JCI Insight*. 2020;5(11):1-12. doi:10.1172/jci.insight.133247

232. Whitburn J, Edwards CM, Sooriakumaran P. Metformin and Prostate Cancer: a New Role for an Old Drug. *Curr Urol Rep*. 2017;18(6):1-7. doi:10.1007/s11934-017-0693-8

233. Bridges HR, Jones AJY, Pollak MN, Hirst J. Effects of metformin and other biguanides on oxidative phosphorylation in mitochondria. *Biochemical Journal*. 2014;462(3):475-487. doi:10.1042/BJ20140620

234. Evans J.M., Donnelly L.A., Emslie-Smith A.M., Alessi D.R. MAD. Metformin and reduced risk of cancer in diabetic patients. *Br Med J*. 2005;330(7503):1303-1304. doi:10.1136/bmj.38393.572188.EB

235. Xiong D, Yin Z, Huang M, et al. Mitochondria-targeted atovaquone promotes anti-lung cancer immunity by reshaping tumor microenvironment and enhancing energy metabolism of anti-tumor immune cells. *Cancer Commun*. Published online November 6, 2023. doi:10.1002/cac2.12500

236. Villa-Ruano N, Anaya-Ruiz M, Villafaña-Diaz L, Barron-Villaverde D, Perez-Santos M. Drug repurposing of mito-atovaquone for cancer treatment. *Pharm Pat Anal*. 2023;12(4):143-149. doi:10.4155/ppa-2023-0015

237. Cheng G, Hardy M, Topchyan P, et al. Potent inhibition of tumour cell proliferation and immunoregulatory function by mitochondria-targeted atovaquone. *Sci Rep*. 2020;10(1). doi:10.1038/s41598-020-74808-0

238. Kalyanaraman B, Cheng G, Hardy M, You M. OXPHOS-targeting drugs in oncology: new perspectives. *Expert Opin Ther Targets*. 2023;27(10):939-952. doi:10.1080/14728222.2023.2261631

239. Kalyanaraman B, Cheng G, Hardy M, et al. Mitochondria-targeted metformins: Antitumour and redox signalling mechanisms. *Interface Focus*. 2017;7(2). doi:10.1098/rsfs.2016.0109

240. Cheng, G., Zielonka, J., Ouari, O., Lopez, M., McAllister, D., Boyle, K., Barrios, C.S., Weber, J.J., Johnson, B.D., Hardy, M., Dwinell, M.B., Kalyanaraman B. Mitochondria-targeted analogs of metformin exhibit enhanced antiproliferative and radiosensitizing effects in pancreatic cancer cells. *Cancer Res*. 2016;76(13):3904-3915. doi:10.1158/0008-5472.CAN-15-2534.Mitochondria-targeted

241. Rohlenova K, Sachaphibulkij K, Stursa J, et al. Selective Disruption of Respiratory Supercomplexes as a New Strategy to Suppress Her2 high Breast Cancer. *Antioxid Redox Signal*. 2017;26(2):84-103. doi:10.1089/ars.2016.6677

242. Bielcikova Z, Stursa J, Krizova L, et al. Mitochondrially targeted tamoxifen in patients with metastatic solid tumours: an open-label, phase I/Ib single-centre trial. *EClinicalMedicine*. 2023;57:101873. doi:10.1016/j.eclinm.2023.101873

243. Bajpai A, Desai NN, Pandey S, Shukla C, Datta B, Basu S. Nanoparticle-Mediated Routing of Antibiotics into Mitochondria in Cancer Cells. *ACS Appl Bio Mater*. 2021;4(9):6799-6806. doi:10.1021/acsabm.1c00527

244. Pandya SR, Singh H, Desimone MF, Singh J, George N, Jasani S. Circumventing challenges in mitochondrial targeting for cancer treatment: leveraging nanoplatforms for effective solutions. *Mater Adv*. Published online 2024. doi:10.1039/d3ma00629h

245. Al Assi A, Posty S, Lamarche F, et al. A novel inhibitor of the mitochondrial respiratory complex I with uncoupling properties exerts potent antitumor activity. *Cell Death Dis*. 2024;15(5):311. doi:10.1038/s41419-024-06668-9

246. Baccelli I, Gareau Y, Lehnertz B, et al. Mubritinib Targets the Electron Transport Chain Complex I and Reveals the Landscape of OXPHOS Dependency in Acute Myeloid Leukemia. *Cancer Cell*. 2019;36(1):84-99.e8. doi:10.1016/j.ccell.2019.06.003

247. Liu L, Zhu H, Wu W, et al. Neoantimycin F, a Streptomyces-Derived Natural Product Induces Mitochondria-Related Apoptotic Death in Human Non-Small Cell Lung Cancer Cells. *Front Pharmacol*. 2019;10. doi:10.3389/fphar.2019.01042

248. Ren J, Wang B, Wu Q, Wang G. Combination of niclosamide and current therapies to overcome resistance for cancer: New frontiers for an old drug. *Biomedicine & Pharmacotherapy*. 2022;155:113789. doi:10.1016/j.biopha.2022.113789

249. Jiang H, Li AM, Ye J. The magic bullet: Niclosamide. *Front Oncol*. 2022;12. doi:10.3389/fonc.2022.1004978

250. Wang Z, Ren J, Du J, Wang H, Liu J, Wang G. Niclosamide as a Promising Therapeutic Player in Human Cancer and Other Diseases. *Int J Mol Sci*. 2022;23(24):16116. doi:10.3390/ijms232416116

251. Clementi E, Brown GC, Foxwell N, Moncada S. On the mechanism by which vascular endothelial cells regulate their oxygen consumption. *Proceedings of the National Academy of Sciences*. 1999;96(4):1559-1562. doi:10.1073/pnas.96.4.1559

252. Hickok J, Thomas D. Nitric Oxide and Cancer Therapy: The Emperor has NO Clothes. *Curr Pharm Des*. 2010;16(4):381-391. doi:10.2174/138161210790232149

253. Wang T, Ma F, Qian H li. Defueling the cancer: ATP synthase as an emerging target in cancer therapy. *Mol Ther Oncolytics*. 2021;23:82-95. doi:10.1016/j.omto.2021.08.015

254. Viale A, Pettazzoni P, Lyssiotis CA, et al. Oncogene ablation-resistant pancreatic cancer cells depend on mitochondrial function. *Nature*. 2014;514(7524):628-632. doi:10.1038/nature13611

255. Brambilla L, Lahiri T, Cammer M, Levy DE. STAT3 Inhibitor OPB-51602 Is Cytotoxic to Tumor Cells Through Inhibition of Complex I and ROS Induction. *iScience*. 2020;23(12):101822. doi:10.1016/j.isci.2020.101822

256. Ogura M, Uchida T, Terui Y, et al. Phase I study of <scp>OPB</scp> -51602, an oral inhibitor of signal transducer and activator of transcription 3, in patients with relapsed/refractory hematological malignancies. *Cancer Sci*. 2015;106(7):896-901. doi:10.1111/cas.12683

257. Benej M, Hong X, Vibhute S, et al. Papaverine and its derivatives radiosensitize solid tumors by inhibiting mitochondrial metabolism. *Proceedings of the National Academy of Sciences*. 2018;115(42):10756-10761. doi:10.1073/pnas.1808945115

258. Dong LF, Freeman R, Liu J, et al. Suppression of Tumor Growth In vivo by the Mitocan α-tocopheryl Succinate Requires Respiratory Complex II. *Clinical Cancer Research*. 2009;15(5):1593-1600. doi:10.1158/1078-0432.CCR-08-2439

259. Cochrane EJ, Hulit J, Lagasse FP, et al. Impact of Mitochondrial Targeting Antibiotics on Mitochondrial Function and Proliferation of Cancer Cells. *ACS Med Chem Lett*. 2021;12(4):579-584. doi:10.1021/acsmedchemlett.0c00632

260. Lagler H, Kiesewetter B, Dolak W, et al. Treatment of mucosa associated lymphoid tissue lymphoma with a long-term once-weekly regimen of oral azithromycin: Results from the phase II MALT—A trial. *Hematol Oncol*. 2019;37(1):22-26. doi:10.1002/hon.2555

261. Zielonka J, Cheng G, Mcallister DM, et al. Mitochondria-targeted chromanol inhibits breast cancer cell energy metabolism and promotes cell death. *Free Radical Research Center and Department of Biophysics*. 2013;13:10.

262. Kulkarni CA, Fink BD, Gibbs BE, et al. A Novel Triphenylphosphonium Carrier to Target Mitochondria without Uncoupling Oxidative Phosphorylation. *J Med Chem*. 2021;64(1):662-676. doi:10.1021/acs.jmedchem.0c01671

263. Bagkos G, Koufopoulos K, Piperi C. A new model for mitochondrial membrane potential production and storage. *Med Hypotheses*. 2014;83(2):175-181. doi:10.1016/j.mehy.2014.05.001

264. Forrest MD. Why cancer cells have a more hyperpolarised mitochondrial membrane potential and emergent prospects for therapy. *bioRxiv*. Published online 2015:1-42.

265. Heidary M, Ebrahimi Samangani A, Kargari A, et al. Mechanism of action, resistance, synergism, and clinical implications of azithromycin. *J Clin Lab Anal*. 2022;36(6). doi:10.1002/jcla.24427

266. Böttger EC, Springer B, Prammananan T, Kidan Y, Sander P. Structural basis for selectivity and toxicity of ribosomal antibiotics. *EMBO Rep*. 2001;2(4):318-323. doi:10.1093/embo-reports/kve062

267. ThermoFisher Scientific. Useful Numbers for Cell Culture. https://www.thermofisher.com/uk/en/home/references/gibco-cell-culture-basics/cell-culture-protocols/cell-culture-useful-numbers.html.

268. Agilent. MitoXpress Xtra Oxygen Consumption Assay (HS Method). Published April 2024. Accessed April 16, 2024. https://www.agilent.com/cs/library/usermanuals/public/5991-9328EN_MitoXpress_Xtra_User_Guide.pdf

269. Perry SW, Norman JP, Barbieri J, Brown EB, Gelbard HA. Mitochondrial membrane potential probes and the proton gradient: a practical usage guide. *Biotechniques*. 2011;50(2):98-115. doi:10.2144/000113610

270. Maqsood MI, Matin MM, Bahrami AR, Ghasroldasht MM. Immortality of cell lines: Challenges and advantages of establishment. *Cell Biol Int*. 2013;37(10):1038-1045. doi:10.1002/cbin.10137

271. Ellinghaus P, Heisler I, Unterschemmann K, et al. BAY 87-2243, a highly potent and selective inhibitor of hypoxia-induced gene activation has antitumor activities by inhibition of mitochondrial complex I. *Cancer Med*. 2013;2(5):611-624. doi:10.1002/cam4.112

272. Bajpai A, Desai NN, Pandey S, Shukla C, Datta B, Basu S. Nanoparticle-Mediated Routing of Antibiotics into Mitochondria in Cancer Cells. *ACS Appl Bio Mater*. 2021;4(9):6799-6806. doi:10.1021/acsabm.1c00527

273. Cochrane EJ, Hulit J, Lagasse FP, et al. Impact of Mitochondrial Targeting Antibiotics on Mitochondrial Function and Proliferation of Cancer Cells. *ACS Med Chem Lett*. 2021;12(4):579-584. doi:10.1021/acsmedchemlett.0c00632

274. ATCC. Cell Products. Accessed November 10, 2023. https://www.atcc.org/cell-products#t=productTab&numberOfResults=24

275. Giurgiu M, Reinhard J, Brauner B, et al. CORUM: The comprehensive resource of mammalian protein complexes - 2019. *Nucleic Acids Res*. 2019;47(D1):D559-D563. doi:10.1093/nar/gky973

276. Steiner P, Joynes C, Bassi R, et al. Tumor growth inhibition with cetuximab and chemotherapy in non-small cell lung cancer xenografts expressing wild-type and mutated epidermal growth factor receptor. *Clinical Cancer Research*. 2007;13(5):1540-1551. doi:10.1158/1078-0432.CCR-06-1887

277. Yamori T, Sato S, Chikazawa H, Kadota T. Anti-tumor efficacy of paclitaxel against human lung cancer xenografts. *Japanese Journal of Cancer Research*. 1997;88(12):1205-1210. doi:10.1111/j.1349-7006.1997.tb00350.x

278. Dengler, W.A., Schulte, J., Berge, r D.P., Mertelsmann, R., Fiebig HH. Development of a propidium iodide fluorescence assay for proliferation and cytotoxicity assays. *Anticancer Drugs*. 1995;6(4):522-532. doi:10.1097/00001813-199508000-00005

279. Audzeyenka I, Rachubik P, Typiak M, et al. Hyperglycemia alters mitochondrial respiration efficiency and mitophagy in human podocytes. *Exp Cell Res*. 2021;407(1):112758. doi:10.1016/j.yexcr.2021.112758

280. Kenakin TP. Safety pharmacology. In: *Harmacology in Drug Discovery and Development: Understanding Drug Response*. Second. Elsevier Inc.; 2017:251-273. doi:10.1016/B0-12-369400-0/00859-0

281. Hynes J, Carey C, Will Y. Fluorescence-based microplate assays for in vitro assessment of mitochondrial toxicity, metabolic perturbation, and cellular oxygenation. *Curr Protoc Toxicol*. 2016;2016:2.16.1-2.16.30. doi:10.1002/cptx.3

282. Weissig V, Editors ME. *Mitochondrial Medicine Assessing Mitochondria*. Vol 2.; 2022.

283. Park SH, Lee AR, Choi K, Joung S, Yoon JB, Kim S. TOMM20 as a potential therapeutic target of colorectal cancer. *BMB Rep*. 2019;52(12):712-717. doi:10.5483/BMBRep.2019.52.12.249

284. Wilde L, Roche M, Domingo-Vidal M, et al. Metabolic coupling and the Reverse Warburg Effect in cancer: Implications for novel biomarker and anticancer agent development. *Semin Oncol*. 2017;44(3):198-203. doi:10.1053/j.seminoncol.2017.10.004

285. Begum HM, Shen K. Intracellular and microenvironmental regulation of mitochondrial membrane potential in cancer cells. *WIREs Mechanisms of Disease*. 2023;15(3):1-20. doi:10.1002/wsbm.1595

286. Rovini A, Heslop K, Hunt EG, et al. Quantitative analysis of mitochondrial membrane potential heterogeneity in unsynchronized and synchronized cancer cells. *FASEB Journal*. 2021;35(1):1-14. doi:10.1096/fj.202001693R

287. Sarah Creed MM. *Cancer Metabolism Methods and Protocols Methods in Molecular Biology 1928*. (Haznadar M, ed.).; 2019.

288. Forrest MD. Why cancer cells have a more hyperpolarised mitochondrial membrane potential and emergent prospects for therapy. *bioRxiv*. Published online 2015:1-42.

289. Han, Y.H., Kim, S.H., Kim, S.Z. and Park WH. Antimycin A as a mitochondrial electron transport inhibitor prevents the growth of human lung cancer A549 cells. *Oncol Rep*. 2008;20:689-693. doi:doi.org/10.3892/or_00000061

290. Sivandzade F, Bhalerao A, Cucullo L. Analysis of the Mitochondrial Membrane Potential Using the Cationic JC-1 Dye as a Sensitive Fluorescent Probe. *Bio Protoc*. 2019;9(1):1-13. doi:10.21769/BioProtoc.3128

291. Cho H, Cho YY, Shim MS, Lee JY, Lee HS, Kang HC. Mitochondria-targeted drug delivery in cancers. *Biochimica et Biophysica Acta (BBA) - Molecular Basis of Disease*. 2020;1866(8):165808. doi:10.1016/j.bbadis.2020.165808

292. Perillo B, Di Donato M, Pezone A, et al. ROS in cancer therapy: the bright side of the moon. *Exp Mol Med*. 2020;52(2):192-203. doi:10.1038/s12276-020-0384-2

293. Nakamura H, Takada K. Reactive oxygen species in cancer: Current findings and future directions. *Cancer Sci*. 2021;112(10):3945-3952. doi:10.1111/cas.15068

294. Conklin KA. Chemotherapy-associated oxidative stress: Impact on chemotherapeutic effectiveness. *Integr Cancer Ther*. 2004;3(4):294-300. doi:10.1177/1534735404270335

295. Dikalov SI, Harrison DG. Methods for detection of mitochondrial and cellular reactive oxygen species. *Antioxid Redox Signal*. 2014;20(2):372-382. doi:10.1089/ars.2012.4886

296. Esposito LA, Melov S, Panov A, Cottrell BA, Wallace DC. Mitochondrial disease in mouse results in increased oxidative stress. *Proc Natl Acad Sci U S A*. 1999;96(9):4820-4825. doi:10.1073/pnas.96.9.4820

297. Sznarkowska A, Kostecka A, Meller K, Bielawski KP. Inhibition of cancer antioxidant defense by natural compounds. *Oncotarget*. 2017;8(9):15996-16016. doi:10.18632/oncotarget.13723

298. Kim YS, Vallur PG, Phaëton R, Mythreye K, Hempel N. Insights into the dichotomous regulation of SOD2 in cancer. *Antioxidants*. 2017;6(4):1-25. doi:10.3390/antiox6040086

299. Yan LJ, Levine RL, Sohal RS. Oxidative damage during aging targets mitochondrial aconitase. *Proc Natl Acad Sci U S A*. 1997;94(21):11168-11172. doi:10.1073/pnas.94.21.11168

300. Zhang YQ, Shen X, Xiao XL, et al. Mitochondrial uncoupler carbonyl cyanide m-chlorophenylhydrazone induces vasorelaxation without involving KATPchannel activation in

smooth muscle cells of arteries. *Br J Pharmacol*. Published online 2016:3145-3158. doi:10.1111/bph.13578

301. Demine S, Renard P, Arnould T. Mitochondrial uncoupling: A key controller of biological processes in physiology and diseases. *Cells*. 2019;8(8). doi:10.3390/cells8080795

302. Loor, G., Kondapalli, J., Schriewer, J.M., Chandel, N.S., Vanden Hoek, T.L., Schumacker PT. Menadione triggers cell death through ROS-dependent mechanisms involving PARP activation without requiring apoptosis. *Free Radic Biol Med*. 2010;49(12):1925-1936. doi:10.1016/j.freeradbiomed.2010.09.021

303. Sobhakumari A, Orcutt KP, Love-Homan L, et al. 2-deoxy-D-glucose suppresses the in vivo antitumor efficacy of erlotinib in head and neck squamous cell carcinoma cells. *Oncol Res*. 2016;24(1):55-64. doi:10.3727/096504016X14586627440192

304. Fath MA, Diers AR, Aykin-Burns N, Simons AL, Hua L, Spitz DR. Mitochondrial electron transport chain blockers enhance 2-deoxy-D-glucose induced oxidative stress and cell killing in human colon carcinoma cells. *Cancer Biol Ther*. 2009;8(13):1228-1236. doi:10.4161/cbt.8.13.8631

305. Wokoun U, Hellriegel M, Emons G, Gröndker C. Co-Treatment of breast cancer cells with pharmacologic doses of 2-deoxy-D-glucose and metformin: Starving tumors. *Oncol Rep*. 2017;37(4):2418-2424. doi:10.3892/or.2017.5491

306. Stein M, Lin H, Jeyamohan C, et al. Targeting tumor metabolism with 2-deoxyglucose in patients with castrate-resistant prostate cancer and advanced malignancies. *Prostate*. 2010;70(13):1388-1394. doi:10.1002/pros.21172

307. Van Tonder A, Joubert AM, Cromarty AD. Limitations of the 3-(4,5-dimethylthiazol-2-yl)-2,5-diphenyl-2H-tetrazolium bromide (MTT) assay when compared to three commonly used cell enumeration assays. *BMC Res Notes*. 2015;8(1):1-10. doi:10.1186/s13104-015-1000-8

308. Dengler, W.A., Schulte, J., Berger, D.P., Mertelsmann, R., Fiebig HH. Development of a propidium iodide fluorescence assay for proliferation and cytotoxicity assays. *Anticancer Drugs*. 1995;6(4):522-532. doi:10.1097/00001813-199508000-00005

309. Grimes DR, Fletcher AG. Close Encounters of the Cell Kind: The Impact of Contact Inhibition on Tumour Growth and Cancer Models. *Bull Math Biol*. 2020;82(2):20. doi:10.1007/s11538-019-00677-y

310. Mot AI, Liddell JR, White AR, Crouch PJ. Circumventing the Crabtree Effect: A method to induce lactate consumption and increase oxidative phosphorylation in cell culture. *Int J Biochem Cell Biol*. 2016;79:128-138. doi:10.1016/j.biocel.2016.08.029

311. Hu Y, Suarez J, Fricovsky E, et al. Increased Enzymatic O-GlcNAcylation of Mitochondrial Proteins Impairs Mitochondrial Function in Cardiac Myocytes Exposed to High Glucose. *Journal of Biological Chemistry*. 2009;284(1):547-555. doi:10.1074/jbc.M808518200

312. Nasonovs A, Garcia-Diaz M, Bogenhagen DF. *A549 Cells Contain Enlarged Mitochondria with Independently Functional Clustered MtDNA Nucleoids*. Vol 16.; 2021. doi:10.1371/journal.pone.0249047

313. Chang S, Singh L, Thaker K, et al. Altered Retrograde Signaling Patterns in Breast Cancer Cells Cybrids with H and J Mitochondrial DNA Haplogroups. *Int J Mol Sci*. 2022;23(12). doi:10.3390/ijms23126687

314. Sairi AMM, Ismail SI, Sukor A, et al. Cytotoxicity and Anticancer Activity of Donkioporiella mellea on MRC5 (Normal Human Lung) and A549 (Human Lung Carcinoma) Cells Lines. *Evidence-based Complementary and Alternative Medicine*. 2020;2020. doi:10.1155/2020/7415672

315. DUNN KC, AOTAKI-KEEN AE, PUTKEY FR, HJELMELAND LM. ARPE-19, A Human Retinal Pigment Epithelial Cell Line with Differentiated Properties. *Exp Eye Res*. 1996;62(2):155-170. doi:10.1006/exer.1996.0020

316. Hurley JB. Retina Metabolism and Metabolism in the Pigmented Epithelium: A Busy Intersection. *Annu Rev Vis Sci*. 2021;7:665-692. doi:10.1146/annurev-vision-100419-115156

317. Lamb R, Ozsvari B, Lisanti CL, Tanowitz HB. Antibiotics that target mitochondria effectively eradicate cancer stem cells , across multiple tumor types : Treating cancer like an infectious disease. 6(7).

318. Chu DJ, Yao DE, Zhuang YF, et al. Azithromycin enhances the favorable results of paclitaxel and cisplatin in patients with advanced non-small cell lung cancer. 2014;13(2):2796-2805.

319. Ozkan T, Hekmatshoar Y, Zeynep A, Koc A. Assessment of azithromycin as an anticancer agent for treatment of imatinib sensitive and resistant CML cells. *Leuk Res*. 2021;102(January):106523. doi:10.1016/j.leukres.2021.106523

320. Houtkooper RH, Mouchiroud L, Ryu D, et al. Mitonuclear protein imbalance as a conserved longevity mechanism. *Nature*. 2013;497(7450):451-457. doi:10.1038/nature12188

321. Moullan N, Mouchiroud L, Wang X, et al. Tetracyclines disturb mitochondrial function across eukaryotic models: A call for caution in biomedical research. *Cell Rep*. 2015;10(10):1681-1691. doi:10.1016/j.celrep.2015.02.034

322. Warren C, McDonald D, Capaldi R, et al. Decoding mitochondrial heterogeneity in single muscle fibres by imaging mass cytometry. *Sci Rep*. 2020;10(1):15336. doi:10.1038/s41598-020-70885-3

323. Morten KJ, Ackrell BAC, Melov S. Mitochondrial Reactive Oxygen Species in Mice Lacking Superoxide Dismutase 2. *Journal of Biological Chemistry*. 2006;281(6):3354-3359. doi:10.1074/jbc.M509261200

324. Aminzadeh-Gohari S, Weber DD, Vidali S, Catalano L, Kofler B, Feichtinger RG. From old to new — Repurposing drugs to target mitochondrial energy metabolism in cancer. *Semin Cell Dev Biol*. 2020;98(March 2019):211-223. doi:10.1016/j.semcdb.2019.05.025

325. Nunn AVW, Guy GW, Bell JD. The quantum mitochondrion and optimal health. *Biochem Soc Trans*. 2016;44(4):1101-1110. doi:10.1042/BST20160096

326. Nasonovs A, Garcia-Diaz M, Bogenhagen DF. *A549 Cells Contain Enlarged Mitochondria with Independently Functional Clustered MtDNA Nucleoids*. Vol 16.; 2021. doi:10.1371/journal.pone.0249047

327. Lin Y, Yang B, Huang Y, et al. Mitochondrial DNA-targeted therapy: A novel approach to combat cancer. *Cell Insight*. 2023;2(4):100113. doi:10.1016/j.cellin.2023.100113

328. Zhang C, Liu Z, Bunker E, et al. Sorafenib targets the mitochondrial electron transport chain complexes and ATP synthase to activate the PINK1-Parkin pathway and modulate cellular drug response. *Journal of Biological Chemistry*. 2017;292(36):15105-15120. doi:10.1074/jbc.M117.783175

329. Jiang X, Baucom C, Elliott RL. Mitochondrial Toxicity of Azithromycin Results in Aerobic Glycolysis and DNA Damage of Human Mammary Epithelia and Fibroblasts. *Antibiotics*. 2019;8(3):110. doi:10.3390/antibiotics8030110

330. Signes A, Fernandez-Vizarra E. Assembly of mammalian oxidative phosphorylation complexes I–V and supercomplexes. *Essays Biochem*. 2018;62(3):255-270. doi:10.1042/EBC20170098

331. Castellanos E, Lanning NJ. Phosphorylation of OXPHOS Machinery Subunits: Functional Implications in Cell Biology and Disease. *Yale J Biol Med*. 2019;92(3):523-531.

332. Chacko BK, Kramer PA, Ravi S, et al. The Bioenergetic Health Index: a new concept in mitochondrial translational research. *Clin Sci*. 2014;127(6):367-373. doi:10.1042/CS20140101

333. Quinlan CL, Treberg JR, Brand MD. Mechanisms of Mitochondrial Free Radical Production and their Relationship to the Aging Process. In: *Handbook of the Biology of Aging*. Elsevier; 2011:47-61. doi:10.1016/B978-0-12-378638-8.00003-8

334. Weng MS, Chang JH, Hung WY, Yang YC, Chien MH. The interplay of reactive oxygen species and the epidermal growth factor receptor in tumor progression and drug resistance. *Journal of Experimental and Clinical Cancer Research*. 2018;37(1):1-11. doi:10.1186/s13046-018-0728-0

335. Yamada A, Osada S, Tanahashi T, et al. Novel therapy for locally advanced triple-negative breast cancer. *Int J Oncol*. 2015;47(4):1266-1272. doi:10.3892/ijo.2015.3113

336. Park WH, Han YW, Kim SH, Kim SZ. An ROS generator, antimycin A, inhibits the growth of HeLa cells via apoptosis. *J Cell Biochem*. 2007;102(1):98-109. doi:10.1002/jcb.21280

337. PARK WH, YOU BR. Antimycin A induces death of the human pulmonary fibroblast cells via ROS increase and GSH depletion. *Int J Oncol*. 2016;48(2):813-820. doi:10.3892/ijo.2015.3276

338. Quinlan CL, Gerencser AA, Treberg JR, Brand MD. The Mechanism of Superoxide Production by the Antimycin-inhibited Mitochondrial Q-cycle. *Journal of Biological Chemistry*. 2011;286(36):31361-31372. doi:10.1074/jbc.M111.267898

339. Cobley JN. Mechanisms of Mitochondrial ROS Production in Assisted Reproduction: The Known, the Unknown, and the Intriguing. *Antioxidants*. 2020;9(10):933. doi:10.3390/antiox9100933

340. Pilco-Ferreto N, Calaf GM. Influence of doxorubicin on apoptosis and oxidative stress in breast cancer cell lines. *Int J Oncol*. 2016;49(2):753-762. doi:10.3892/ijo.2016.3558

341. Patintingan CG, Louisa M, Juniantito V, et al. Moringa oleifera Leaves Extract Ameliorates Doxorubicin-Induced Cardiotoxicity via Its Mitochondrial Biogenesis Modulatory Activity in Rats. *J Exp Pharmacol*. 2023;Volume 15:307-319. doi:10.2147/JEP.S413256

342. Han D, Loukianoff S, McLaughlin L. *Oxidative Stress Indices: Analytical Aspects and Significance*. Elsevier B.V.; 2000. doi:10.1016/b978-044482650-3/50017-1

343. Shrestha R, Johnson E, Byrne FL. Exploring the therapeutic potential of mitochondrial uncouplers in cancer. *Mol Metab*. 2021;51(March):101222. doi:10.1016/j.molmet.2021.101222

344. Dmitry P. *Perspectives of Pharmacological Correction and Evaluation of Mitochondrial Dysfunction in Neurodegenerative and Ischemic Brain Lesions*. Vol 69. 1st ed. Elsevier B.V.; 2021. doi:10.1016/B978-0-12-819487-4.00018-5

345. Lombardo T, Folgar MG, Salaverry L, et al. Regulated Cell Death of Lymphoma Cells after Graded Mitochondrial Damage is Differentially Affected by Drugs Targeting Cell Stress Responses. *Basic Clin Pharmacol Toxicol*. 2018;122(5):489-500. doi:10.1111/bcpt.12945

346. Berry BJ, Trewin AJ, Amitrano AM, Kim M, Wojtovich AP. Use the Protonmotive Force : Mitochondrial Uncoupling and Reactive Oxygen Species. *J Mol Biol*. 2018;430(21):3873-3891. doi:10.1016/j.jmb.2018.03.025

347. Stine ZE, Schug ZT, Salvino JM. Targeting cancer metabolism in the era of precision oncology. doi:10.1038/s41573-021-00339-6

348. Pajak B, Siwiak E, Sołtyka M, et al. 2-Deoxy-D-Glucose and its analogs: From diagnostic to therapeutic agents. *Int J Mol Sci*. 2020;21(1). doi:10.3390/ijms21010234

349. Huang Z, Chavda VP, Vora LK, et al. 2-Deoxy-D-Glucose and its Derivatives for the COVID-19 Treatment: An Update. *Front Pharmacol*. 2022;13(April):1-10. doi:10.3389/fphar.2022.899633

350. Zhang Y, Li Q, Huang Z, et al. Targeting Glucose Metabolism Enzymes in Cancer Treatment: Current and Emerging Strategies. *Cancers (Basel)*. 2022;14(19). doi:10.3390/cancers14194568

351. Ahadova A, Gebert J, von Knebel Doeberitz M, Kopitz J, Kloor M. Dose-dependent effect of 2-deoxy-D-glucose on glycoprotein mannosylation in cancer cells. *IUBMB Life*. 2015;67(3):218-226. doi:10.1002/iub.1364

352. Repas J, Zupin M, Vodlan M, et al. Dual Effect of Combined Metformin and 2-Deoxy-D-Glucose Treatment on Mitochondrial Biogenesis and PD-L1 Expression in Triple-Negative Breast Cancer Cells. *Cancers (Basel)*. 2022;14(5):1343. doi:10.3390/cancers14051343

353. Ishino K, Kudo M, Peng WX, et al. 2-Deoxy- d -glucose increases GFAT1 phosphorylation resulting in endoplasmic reticulum-related apoptosis via disruption of protein N -glycosylation in pancreatic cancer cells. *Biochem Biophys Res Commun*. 2018;501(3):668-673. doi:10.1016/j.bbrc.2018.05.041

354. Elia I, Haigis MC. Metabolites and the tumour microenvironment: from cellular mechanisms to systemic metabolism. *Nat Metab*. 2021;3(1):21-32. doi:10.1038/s42255-020-00317-z

355. Elizabeth C. Bryda. The Mighty Mouse: The Impact of Rodents on Advances in Biomedical Research. *Mo Med*. 2013;110(3):207-211.

356. Dudal S, Bissantz C, Caruso A, et al. Translating pharmacology models effectively to predict therapeutic benefit. *Drug Discov Today*. 2022;27(6):1604-1621. doi:10.1016/j.drudis.2022.03.009

357. Manenti G. Outbred CD-1 mice carry the susceptibility allele at the pulmonary adenoma susceptibility 1 (Pas1) locus. *Carcinogenesis*. 2003;24(6):1143-1148. doi:10.1093/carcin/bgg065

358. Talbot SR, Biernot S, Bleich A, et al. Defining body-weight reduction as a humane endpoint: a critical appraisal. *Lab Anim*. 2020;54(1):99-110. doi:10.1177/0023677219883319

359. Sriraman SK, Aryasomayajula B, Torchilin VP. Barriers to drug delivery in solid tumors. *Tissue Barriers*. 2014;2(3):e29528-1-e29528-10. doi:10.4161/tisb.29528

360. Vaja R, Rana M. *Drugs and the Liver*.

361. Corsini A, Bortolini M. Drug-induced liver injury: The role of drug metabolism and transport. *J Clin Pharmacol*. 2013;53(5):463-474. doi:10.1002/jcph.23

362. bio Erminio Mingatto F, Cardozo dos Santos A, Rodrigues T, cio Antonio Pigoso A, rgio Akira Uyemura S, Curti C. *Effects of Nimesulide and Its Reduced Metabolite on Mitochondria*. Vol 131.; 2000. www.nature.com/bjp

363. Syed M, Skonberg C, Hansen SH. Mitochondrial toxicity of diclofenac and its metabolites via inhibition of oxidative phosphorylation (ATP synthesis) in rat liver mitochondria: Possible role in drug induced liver injury (DILI). *Toxicology in Vitro*. 2016;31:93-102. doi:10.1016/j.tiv.2015.11.020

364. Serviddio G, Bellanti F, Giudetti AM, et al. Mitochondrial oxidative stress and respiratory chain dysfunction account for liver toxicity during amiodarone but not dronedarone administration. *Free Radic Biol Med*. 2011;51(12):2234-2242. doi:10.1016/j.freeradbiomed.2011.09.004

365. Masereeuw R, Russel FGM. Mechanisms and clinical implications of renal drug excretion. *Drug Metab Rev*. 2001;33(3-4):299-351. doi:10.1081/DMR-120000654

366. Reisbeck L, Linder B, Tascher G, et al. The iron chelator and OXPHOS inhibitor VLX600 induces mitophagy and an autophagy-dependent type of cell death in glioblastoma cells. *American Journal of Physiology-Cell Physiology*. 2023;325(6):C1451-C1469. doi:10.1152/ajpcell.00293.2023

367. Saito K, Zhang Q, Yang H, et al. Exogenous mitochondrial transfer and endogenous mitochondrial fission facilitate AML resistance to OxPhos inhibition. *Blood Adv*. 2021;5(20):4233-4255. doi:10.1182/bloodadvances.2020003661

368. Walker JM. *M E T H O D S I N M O L E C U L A R B I O L O G Y ™ Series Editor*. http://www.springer.com/series/7651

369. Stanger BZ. Cellular Homeostasis and Repair in the Mammalian Liver. *Annu Rev Physiol*. 2015;77(1):179-200. doi:10.1146/annurev-physiol-021113-170255

370. Fujigaki Y. Different modes of renal proximal tubule regeneration in health and disease. *World J Nephrol*. 2012;1(4):92. doi:10.5527/wjn.v1.i4.92

371. Yutzey KE. Cardiomyocyte Proliferation. *Circ Res*. 2017;120(4):627-629. doi:10.1161/CIRCRESAHA.116.310058

372. Wang RA, Li QL, Li ZS, et al. Apoptosis drives cancer cells proliferate and metastasize. *J Cell Mol Med*. 2013;17(1):205-211. doi:10.1111/j.1582-4934.2012.01663.x

373. Michl J, Wang Y, Monterisi S, et al. CRISPR-Cas9 screen identifies oxidative phosphorylation as essential for cancer cell survival at low extracellular pH. *Cell Rep*. 2022;38(10):110493. doi:10.1016/j.celrep.2022.110493

374. Juhász P, Hasulyó D, Bedekovics J, et al. *Carbonic Anhydrase IX (CAIX) Expressing Hypoxic Micro-Environment Hampers CD8+ Immune Cell Infiltrate in Breast Carcinoma*.; 2022. www.appliedimmunohist.com

375. Becker HM. Carbonic anhydrase IX and acid transport in cancer. *Br J Cancer*. 2020;122(2):157-167. doi:10.1038/s41416-019-0642-z

376. van Gisbergen MW, Offermans K, Voets AM, et al. Mitochondrial Dysfunction Inhibits Hypoxia-Induced HIF-1α Stabilization and Expression of Its Downstream Targets. *Front Oncol*. 2020;10. doi:10.3389/fonc.2020.00770

377. Thomas LW, Ashcroft M. Exploring the molecular interface between hypoxia-inducible factor signalling and mitochondria. *Cellular and Molecular Life Sciences*. 2019;76(9):1759-1777. doi:10.1007/s00018-019-03039-y

378. Coates JT. *Targeting Tumour Hypoxia: Shifting Focus from Oxygen Supply to Demand*.; 2019.

379. Cosse JP, Michiels C. Tumour Hypoxia Affects the Responsiveness of Cancer Cells to Chemotherapy and Promotes Cancer Progression. *Anticancer Agents Med Chem*. 2008;8(7):790-797. doi:10.2174/187152008785914798

380. Rytelewski M, Harutyunyan K, Baran N, et al. Inhibition of Oxidative Phosphorylation Reverses Bone Marrow Hypoxia Visualized in Imageable Syngeneic B-ALL Mouse Model. *Front Oncol*. 2020;10. doi:10.3389/fonc.2020.00991

381. Dewhirst MW, Secomb TW. Transport of drugs from blood vessels to tumour tissue. *Nat Rev Cancer*. 2017;17(12):738-750. doi:10.1038/nrc.2017.93

382. Rajaganeshan R, Prasad R, Guillou PJ, et al. The influence of invasive growth pattern and microvessel density on prognosis in colorectal cancer and colorectal liver metastases. *Br J Cancer*. 2007;96(7):1112-1117. doi:10.1038/sj.bjc.6603677

383. Peterson HI. The microcirculation of tumors. In: Orr F, Buchanan M, Weiss L, eds. *Microcirculation in Cancer Metastasis*. CRC Press Inc.; 1991:277-298.

384. Luo Z, Yao J, Wang Z, Xu J. Mitochondria in endothelial cells angiogenesis and function: current understanding and future perspectives. *J Transl Med*. 2023;21(1). doi:10.1186/s12967-023-04286-1

385. Xiong Y, Liu W, Huang Q, et al. Tigecycline as a dual inhibitor of retinoblastoma and angiogenesis via inducing mitochondrial dysfunctions and oxidative damage. *Sci Rep*. 2018;8(1). doi:10.1038/s41598-018-29938-x

386. Samtani S, Amaral J, Campos MM, Fariss RN, Becerra SP. Doxycycline-mediated inhibition of choroidal neovascularization. *Invest Ophthalmol Vis Sci*. 2009;50(11):5098-5106. doi:10.1167/iovs.08-3174

387. Herbst RS, Heymach J V, O'Reilly MS, Onn A, Ryan AJ. Vandetanib (ZD6474): an orally available receptor tyrosine kinase inhibitor that selectively targets pathways critical for tumor growth

and angiogenesis. *Expert Opin Investig Drugs*. 2007;16(2):239-249. doi:10.1517/13543784.16.2.239

388. Adjei AA, Molina JR, Mandrekar SJ, et al. Phase I trial of sorafenib in combination with gefitinib in patients with refractory or recurrent non - Small cell lung cancer. *Clinical Cancer Research*. 2007;13(9):2684-2691. doi:10.1158/1078-0432.CCR-06-2889

389. Garcia J, Hurwitz HI, Sandler AB, et al. Bevacizumab (Avastin®) in cancer treatment: A review of 15 years of clinical experience and future outlook. *Cancer Treat Rev*. 2020;86. doi:10.1016/j.ctrv.2020.102017

390. VALAVANIDIS A, VLACHOGIANNI T, FIOTAKIS C. 8-hydroxy-2' -deoxyguanosine (8-OHdG): A Critical Biomarker of Oxidative Stress and Carcinogenesis. *Journal of Environmental Science and Health, Part C*. 2009;27(2):120-139. doi:10.1080/10590500902885684

391. Wu LL, Chiou CC, Chang PY, Wu JT. Urinary 8-OHdG: A marker of oxidative stress to DNA and a risk factor for cancer, atherosclerosis and diabetics. *Clinica Chimica Acta*. 2004;339(1-2):1-9. doi:10.1016/j.cccn.2003.09.010

392. Shang L, Hosseini M, Liu X, Kisseleva T, Brenner DA. Human hepatic stellate cell isolation and characterization. *J Gastroenterol*. 2018;53(1):6-17. doi:10.1007/s00535-017-1404-4

393. Croce AC, De Simone U, Freitas I, et al. Human liver autofluorescence: An intrinsic tissue parameter discriminating normal and diseased conditions. *Lasers Surg Med*. 2010;42(5):371-378. doi:10.1002/lsm.20923

394. Grattagliano I, Russmann S, Diogo C, et al. Mitochondria in Chronic Liver Disease. *Curr Drug Targets*. 2011;12(6):879-893. doi:10.2174/138945011795528877

395. Nguyen BY, Ruiz-Velasco A, Bui T, Collins L, Wang X, Liu W. Mitochondrial function in the heart: the insight into mechanisms and therapeutic potentials. *Br J Pharmacol*. 2019;176(22):4302-4318. doi:10.1111/bph.14431

396. Guillaumond F, Leca J, Olivares O, et al. Strengthened glycolysis under hypoxia supports tumor symbiosis and hexosamine biosynthesis in pancreatic adenocarcinoma. *Proc Natl Acad Sci U S A*. 2013;110(10):3919-3924. doi:10.1073/pnas.1219555110

397. Hensley CT, Faubert B, Yuan Q, et al. Metabolic Heterogeneity in Human Lung Tumors. *Cell*. 2016;164(4):681-694. doi:10.1016/j.cell.2015.12.034

398. Zhou W, Liotta LA, Petricoin EF. Cancer metabolism and mass spectrometry-based proteomics. *Cancer Lett*. 2015;356(2):176-183. doi:10.1016/j.canlet.2013.11.003

399. Schneider CA, Rasband WS, Eliceiri KW. NIH Image to ImageJ: 25 years of image analysis. *Nat Methods*. 2012;9(7):671-675. doi:10.1038/nmeth.2089

400. Wang B, Ao J, Yu D, Rao T, Ruan Y, Yao X. Inhibition of mitochondrial translation effectively sensitizes renal cell carcinoma to chemotherapy. *Biochem Biophys Res Commun*. 2017;490(3):767-773. doi:10.1016/j.bbrc.2017.06.115

401. Baghban R, Roshangar L, Jahanban-Esfahlan R, et al. Tumor microenvironment complexity and therapeutic implications at a glance. *Cell Communication and Signaling*. 2020;18(1). doi:10.1186/s12964-020-0530-4

402. Whiteside TL. The tumor microenvironment and its role in promoting tumor growth. *Oncogene*. 2008;27(45):5904-5912. doi:10.1038/onc.2008.271

403. Cook DP, Galpin KJC, Rodriguez GM, et al. Comparative analysis of syngeneic mouse models of high-grade serous ovarian cancer. *Commun Biol*. 2023;6(1). doi:10.1038/s42003-023-05529-z

404. Zeng Z, Wong CJ, Yang L, et al. TISMO: Syngeneic mouse tumor database to model tumor immunity and immunotherapy response. *Nucleic Acids Res*. 2022;50(D1):D1391-D1397. doi:10.1093/nar/gkab804

405. Liang CC, Park AY, Guan JL. In vitro scratch assay: a convenient and inexpensive method for analysis of cell migration in vitro. *Nat Protoc*. 2007;2(2):329-333. doi:10.1038/nprot.2007.30

406. Overwijk WW, Restifo NP. B16 as a Mouse Model for Human Melanoma. *Curr Protoc Immunol*. 2000;39(1). doi:10.1002/0471142735.im2001s39

407. Buescher JM, Antoniewicz MR, Boros LG, et al. A roadmap for interpreting 13C metabolite labeling patterns from cells. *Curr Opin Biotechnol*. 2015;34:189-201. doi:10.1016/j.copbio.2015.02.003

408. Hong S, Pawel GT, Pei R, Lu Y. Recent progress in developing fluorescent probes for imaging cell metabolites. *Biomedical Materials (Bristol)*. 2021;16(4). doi:10.1088/1748-605X/abfd11

409. Moco S. Studying Metabolism by NMR-Based Metabolomics. *Front Mol Biosci*. 2022;9(April):1-12. doi:10.3389/fmolb.2022.882487

410. Duncan KD, Fyrestam J, Lanekoff I. Advances in mass spectrometry based single-cell metabolomics. *Analyst*. 2019;144(3):782-793. doi:10.1039/c8an01581c

411. Wishart DS, Guo A, Oler E, et al. HMDB 5.0: the Human Metabolome Database for 2022. *Nucleic Acids Res*. 2022;50(D1):D622-D631. doi:10.1093/nar/gkab1062

412. Wishart DS. Advances in metabolite identification. *Bioanalysis*. 2011;3(15):1769-1782. doi:10.4155/bio.11.155

413. Xu J, Yu T, Zois CE, et al. Unveiling cancer metabolism through spontaneous and coherent raman spectroscopy and stable isotope probing. *Cancers (Basel)*. 2021;13(7):1-24. doi:10.3390/cancers13071718

414. Raman C V., Krishnan KS. A new type of secondary radiation. *Nature*. 1928;121(3048):501-502. doi:10.1038/121501c0

415. Zhang Y, Hong H, Cai W. Imaging with Raman Spectroscopy. 2011;11(6):654-661.

416. Kauffmann TH, Kokanyan N, Fontana MD. Use of Stokes and anti-Stokes Raman scattering for new applications. *Journal of Raman Spectroscopy*. 2019;50(3):418-424. doi:10.1002/jrs.5523

417. Du J, Su Y, Qian C, et al. Raman-guided subcellular pharmaco-metabolomics for metastatic melanoma cells. *Nat Commun*. 2020;11(1). doi:10.1038/s41467-020-18376-x

418. Shen Y, Yue J, Xu W, Xu S. Recent progress of surface-enhanced Raman spectroscopy for subcellular compartment analysis. *Theranostics*. 2021;11(10):4872-4893. doi:10.7150/thno.56409

419. Mitsutake H, Poppi R, Breitkreitz M. Raman Imaging Spectroscopy: History, Fundamentals and Current Scenario of the Technique. *J Braz Chem Soc*. Published online 2019. doi:10.21577/0103-5053.20190116

420. Mhlanga N, Tetyana P, Nyembe S, Sikhwivhilu L. Application of Raman Spectroscopy in Biomedical Diagnostics. In: *Recent Developments in Atomic Force Microscopy and Raman Spectroscopy for Materials Characterization*. IntechOpen; 2022. doi:10.5772/intechopen.99771

421. Krafft C, Neudert L, Simat T, Salzer R. Near infrared Raman spectra of human brain lipids. *Spectrochim Acta A Mol Biomol Spectrosc*. 2005;61(7):1529-1535. doi:10.1016/j.saa.2004.11.017

422. Golikov M V., Valuev-Elliston VT, Smirnova OA, Ivanov A V. Physiological Media in Studies of Cell Metabolism. *Mol Biol*. 2022;56(5):629-637. doi:10.1134/S0026893322050077

423. Ghosh AK, Sloviter HA. Glycolysis and the Pasteur Effect in Rat Reticulocytes. *Journal of Biological Chemistry*. 1973;248(9):3035-3040. doi:10.1016/S0021-9258(19)44005-2

424. Shiratori R, Furuichi K, Yamaguchi M, et al. Glycolytic suppression dramatically changes the intracellular metabolic profile of multiple cancer cell lines in a mitochondrial metabolism-dependent manner. *Sci Rep*. 2019;9(1):18699. doi:10.1038/s41598-019-55296-3

425. Liu G, Luo Q, Li H, Liu Q, Ju Y, Song G. Increased Oxidative Phosphorylation Is Required for Stemness Maintenance in Liver Cancer Stem Cells from Hepatocellular Carcinoma Cell Line HCCLM3 Cells. *Int J Mol Sci*. 2020;21(15):5276. doi:10.3390/ijms21155276

426. Lee N, Jang WJ, Seo JH, Lee S, Jeong CH. 2-Deoxy-d-Glucose-Induced Metabolic Alteration in Human Oral Squamous SCC15 Cells: Involvement of N-Glycosylation of Axl and Met. *Metabolites*. 2019;9(9):188. doi:10.3390/metabo9090188

427. Roessner U, Nahid A, Chapman B, Hunter A, Bellgard M. Metabolomics – The Combination of Analytical Biochemistry, Biology, and Informatics. In: *Comprehensive Biotechnology*. Elsevier; 2011:447-459. doi:10.1016/B978-0-08-088504-9.00052-0

428. Dodo K, Fujita K, Sodeoka M. Raman Spectroscopy for Chemical Biology Research. *J Am Chem Soc*. 2022;144(43):19651-19667. doi:10.1021/jacs.2c05359

429. Maquelin K, Kirschner C, Choo-Smith LP, et al. Identification of medically relevant microorganisms by vibrational spectroscopy. *J Microbiol Methods*. 2002;51(3):255-271. doi:10.1016/S0167-7012(02)00127-6

430. Larion M, Dowdy T, Ruiz-Rodado V, et al. Detection of Metabolic Changes Induced via Drug Treatments in Live Cancer Cells and Tissue Using Raman Imaging Microscopy. *Biosensors (Basel)*. 2018;9(1):5. doi:10.3390/bios9010005

431. Plakas K, Rosch LE, Clark MD, et al. Design and evaluation of Raman reporters for the Raman-silent region. *Nanotheranostics*. 2022;6(1):1-9. doi:10.7150/ntno.58965

432. Nunn AVW, Guy GW, Bell JD. The quantum mitochondrion and optimal health. *Biochem Soc Trans*. 2016;44(4):1101-1110. doi:10.1042/BST20160096

433. Stoker ML, Newport E, Hulit JC, West AP, Morten KJ. Impact of pharmacological agents on mitochondrial function: A growing opportunity? *Biochem Soc Trans*. 2019;47(6). doi:10.1042/BST20190280

434. Meng Z, Petrov GI, Yakovlev V V. Microscopic coherent Raman imaging using low-cost continuous wave lasers. *Laser Phys Lett*. 2013;10(6):065701. doi:10.1088/1612-2011/10/6/065701

435. Zhao M, Ma J, Li M, et al. Cytochrome P450 Enzymes and Drug Metabolism in Humans. *Int J Mol Sci*. 2021;22(23):12808. doi:10.3390/ijms222312808

436. Abramczyk H, Surmacki JM, Brozek-Pluska B. Redox state changes of mitochondrial cytochromes in brain and breast cancers by Raman spectroscopy and imaging. *J Mol Struct*. 2022;1252:132134. doi:10.1016/j.molstruc.2021.132134

437. Abramczyk H, Brozek-Pluska B, Kopeć M. Double face of cytochrome c in cancers by Raman imaging. *Sci Rep*. 2022;12(1). doi:10.1038/s41598-022-04803-0

438. Surmacki JM, Abramczyk H. Confocal Raman imaging reveals the impact of retinoids on human breast cancer via monitoring the redox status of cytochrome c. *Sci Rep*. 2023;13(1). doi:10.1038/s41598-023-42301-z

439. Kakita M, Kaliaperumal V, Hamaguchi H. Resonance Raman quantification of the redox state of cytochromes b and c in-vivo and in-vitro. *J Biophotonics*. 2012;5(1):20-24. doi:10.1002/jbio.201100087

440. Wang Y, Mohsen AW, Mihalik SJ, Goetzman ES, Vockley J. Evidence for Physical Association of Mitochondrial Fatty Acid Oxidation and Oxidative Phosphorylation Complexes. *Journal of Biological Chemistry*. 2010;285(39):29834-29841. doi:10.1074/jbc.M110.139493

441. Ripple MO, Abajian M, Springett R. Cytochrome c is rapidly reduced in the cytosol after mitochondrial outer membrane permeabilization. *Apoptosis*. 2010;15(5):563-573. doi:10.1007/s10495-010-0455-2

442. Vacca RA, Valenti D, Bobba A, Merafina RS, Passarella S, Marra E. Cytochrome c Is Released in a Reactive Oxygen Species-Dependent Manner and Is Degraded via Caspase-Like Proteases in Tobacco Bright-Yellow 2 Cells en Route to Heat Shock-Induced Cell Death. *Plant Physiol*. 2006;141(1):208-219. doi:10.1104/pp.106.078683

443. Brown GC, Borutaite V. Regulation of apoptosis by the redox state of cytochrome c. *Biochimica et Biophysica Acta (BBA) - Bioenergetics*. 2008;1777(7-8):877-881. doi:10.1016/j.bbabio.2008.03.024

444. Xu J, Lodge T, Kingdon C, et al. Developing a Blood Cell-Based Diagnostic Test for Myalgic Encephalomyelitis/Chronic Fatigue Syndrome Using Peripheral Blood Mononuclear Cells. *Advanced Science*. 2023;10(30). doi:10.1002/advs.202302146

445. Cheng X, Liang H, Li Q, et al. Raman spectroscopy differ leukemic cells from their healthy counterparts and screen biomarkers in acute leukemia. *Spectrochim Acta A Mol Biomol Spectrosc*. 2022;281:121558. doi:10.1016/j.saa.2022.121558

446. Ma B, Zhang Y, Ma J, Chen X, Sun C, Qin C. Spatially resolved visualization of reprogrammed metabolism in hepatocellular carcinoma by mass spectrometry imaging. *Cancer Cell Int*. 2023;23(1):177. doi:10.1186/s12935-023-03027-0

447. Ali A, Abouleila Y, Shimizu Y, et al. Single-Cell Screening of Tamoxifen Abundance and Effect Using Mass Spectrometry and Raman-Spectroscopy. *Anal Chem*. 2019;91(4):2710-2718. doi:10.1021/acs.analchem.8b04393

448. Corbett EC, Zichy V, Goral J, Passingham C. Fourier transform Raman studies of materials and compounds of biological importance—II. The effect of moisture on the molecular structure of the alpha and beta anomers of d-glucose. *Spectrochim Acta A*. 1991;47(9-10):1399-1411. doi:10.1016/0584-8539(91)80231-7

449. Hanna K, Krzoska E, Shaaban AM, Muirhead D, Abu-Eid R, Speirs V. Raman spectroscopy: current applications in breast cancer diagnosis, challenges and future prospects. *Br J Cancer*. 2022;126(8):1125-1139. doi:10.1038/s41416-021-01659-5

450. Wu M, Wang S, Pan S, Terentis AC, Strasswimmer J, Zhu X. Deep learning data augmentation for Raman spectroscopy cancer tissue classification. *Sci Rep*. 2021;11(1):23842. doi:10.1038/s41598-021-02687-0

451. Criscuolo D, Avolio R, Matassa DS, Esposito F. Targeting Mitochondrial Protein Expression as a Future Approach for Cancer Therapy. *Front Oncol*. 2021;11. doi:10.3389/fonc.2021.797265

452. Richter U, Lahtinen T, Marttinen P, et al. A Mitochondrial Ribosomal and RNA Decay Pathway Blocks Cell Proliferation. *Current Biology*. 2013;23(6):535-541. doi:10.1016/j.cub.2013.02.019

453. Kushnareva Y, Newmeyer DD. Bioenergetics and cell death. *Ann N Y Acad Sci*. 2010;1201(1):50-57. doi:10.1111/j.1749-6632.2010.05633.x

454. Wokoun U, Hellriegel M, Emons G, Gröndker C. Co-Treatment of breast cancer cells with pharmacologic doses of 2-deoxy-D-glucose and metformin: Starving tumors. *Oncol Rep*. 2017;37(4):2418-2424. doi:10.3892/or.2017.5491

455. Fath MA, Diers AR, Aykin-Burns N, Simons AL, Hua L, Spitz DR. Mitochondrial electron transport chain blockers enhance 2-deoxy-D-glucose induced oxidative stress and cell killing in human colon carcinoma cells. *Cancer Biol Ther*. 2009;8(13):1228-1236. doi:10.4161/cbt.8.13.8631

456. Sobhakumari A, Orcutt KP, Love-Homan L, et al. 2-deoxy-D-glucose suppresses the in vivo antitumor efficacy of erlotinib in head and neck squamous cell carcinoma cells. *Oncol Res*. 2016;24(1):55-64. doi:10.3727/096504016X14586627440192

457. Yan L, Sundaram S, Rust BM, Picklo MJ, Bukowski MR. Metabolomes of Lewis lung carcinoma metastases and normal lung tissue from mice fed different diets. *J Nutr Biochem*. 2022;107:109051. doi:10.1016/j.jnutbio.2022.109051

458. Mangalhara KC, Varanasi SK, Johnson MA, et al. Manipulating mitochondrial electron flow enhances tumor immunogenicity. *Science (1979)*. 2023;381(6664):1316-1323. doi:10.1126/science.abq1053

459. Masoud R, Reyes-Castellanos G, Lac S, et al. Targeting Mitochondrial Complex I Overcomes Chemoresistance in High OXPHOS Pancreatic Cancer. *Cell Rep Med*. 2020;1(8):100143. doi:10.1016/j.xcrm.2020.100143

460. Toubai T, Kuroda J, Suehiro Y, et al. A Phase 1 Trial of OPB-111077 in Combination with Bendamustine (B) and Rituximab (R) in Patients with Relapsed or Refractory (R/R) Diffuse

Large B-Cell Lymphoma (DLBCL): Preliminary Results of Dose-Escalation Stage. *Blood*. 2023;142(Supplement 1):4464-4464. doi:10.1182/blood-2023-179716

Appendix

Appendix A. Full complex I gene ranking of cell lines conducted by Dr Jonanthan Lees (Oxford Brookes University)

Model Name	Rank Score	Tissue	Tissue Status	Cancer Type
HGC-27	31	Stomach	Metastasis	Gastric Carcinoma
NB7	29	Peripheral Nervous System	Metastasis	Neuroblastoma
CAL-51	28	Breast	Metastasis	Breast Carcinoma
D-423MG	27	Central Nervous System	Tumour	Glioblastoma
MDA-MB-468	26	Breast	Metastasis	Breast Carcinoma
SF295	26	Central Nervous System	Unknown	Glioblastoma
OCUB-M	26	Breast	Metastasis	Breast Carcinoma
MKN28	26	Stomach	Metastasis	Gastric Carcinoma
Detroit562	26	Head and Neck	Metastasis	Head and Neck Carcinoma
RKO	26	Large Intestine	Tumour	Colorectal Carcinoma
EW-7	26	Bone	Metastasis	Ewing's Sarcoma
KON	25	Head and Neck	Tumour	Oral Cavity Carcinoma
RL95-2	25	Endometrium	Tumour	Endometrial Carcinoma
OCI-AML2	25	Haematopoietic and Lymphoid	Tumour	Acute Myeloid Leukemia
SW1088	25	Central Nervous System	Tumour	Low Grade Glioma
OCI-AML3	25	Haematopoietic and Lymphoid	Tumour	Acute Myeloid Leukemia
OVK-18	24	Ovary	Metastasis	Ovarian Carcinoma
UACC-893	24	Breast	Tumour	Breast Carcinoma
TOV-112D	23	Ovary	Tumour	Ovarian Carcinoma
GAMG	23	Central Nervous System	Tumour	Glioblastoma
SAS	22	Head and Neck	Tumour	Oral Cavity Carcinoma
Ca9-22	22	Head and Neck	Tumour	Head and Neck Carcinoma
SNG-M	21	Endometrium	Metastasis	Endometrial Carcinoma
OVCA420	21	Ovary	Tumour	Ovarian Carcinoma
FADU	21	Head and Neck	Tumour	Head and Neck Carcinoma
NCI-H1155	20	Lung	Metastasis	Non-Small Cell Lung Carcinoma
MC-IXC	20	Bone	Metastasis	Ewing's Sarcoma
ES-2	20	Ovary	Tumour	Ovarian Carcinoma
NCI-H520	20	Lung	Tumour	Squamous Cell Lung Carcinoma
U251	20	Central Nervous System	Tumour	Low Grade Glioma
UWB1.289	20	Ovary	Tumour	Ovarian Carcinoma

NCI-H23	19	Lung	Tumour	Lung Adenocarcinoma
SW1573	19	Lung	Tumour	Lung Adenocarcinoma
NB13	19	Peripheral Nervous System	Metastasis	Neuroblastoma
MFE-296	18	Endometrium	Tumour	Endometrial Carcinoma
LP-1	18	Haematopoietic and Lymphoid	Tumour	Plasma Cell Myeloma
TYK-nu	18	Ovary	Tumour	Ovarian Carcinoma
HCT-15	17	Large Intestine	Tumour	Colorectal Carcinoma
NCI-H2087	17	Lung	Metastasis	Lung Adenocarcinoma
BE2-M17	17	Peripheral Nervous System	Tumour	Neuroblastoma
KYSE-220	16	Oesophagus	Tumour	Oesophageal Squamous Cell Carcinoma
KYSE-140	16	Oesophagus	Tumour	Oesophageal Squamous Cell Carcinoma
OVISE	16	Ovary	Metastasis	Ovarian Carcinoma
8-MG-BA	15	Central Nervous System	Tumour	Glioblastoma
TGW	15	Peripheral Nervous System	Tumour	Neuroblastoma
GI-1	15	Central Nervous System	Tumour	Glioblastoma
KYSE-510	15	Oesophagus	Tumour	Oesophageal Squamous Cell Carcinoma
KP-N-YS	15	Peripheral Nervous System	Unknown	Neuroblastoma
MDA-MB-361	14	Breast	Metastasis	Breast Carcinoma
SK-MG-1	14	Central Nervous System	Unknown	Low Grade Glioma
KNS-62	14	Lung	Metastasis	Squamous Cell Lung Carcinoma
KP-4	14	Pancreas	Metastasis	Pancreatic Carcinoma
HCC2998	14	Large Intestine	Tumour	Colorectal Carcinoma
SK-N-AS	14	Peripheral Nervous System	Metastasis	Neuroblastoma
TC-71	14	Bone	Tumour	Ewing's Sarcoma
SW626	14	Large Intestine	Metastasis	Colorectal Carcinoma
LK-2	13	Lung	Tumour	Squamous Cell Lung Carcinoma
A549	13	Lung	Tumour	Lung Adenocarcinoma
Hs-683	13	Central Nervous System	Tumour	Low Grade Glioma
HCC1187	13	Breast	Tumour	Breast Carcinoma
SK-N-FI	13	Peripheral Nervous System	Metastasis	Neuroblastoma
OVMIU	13	Ovary	Tumour	Ovarian Carcinoma
LB1047-RCC	12	Kidney	Unknown	Kidney Carcinoma
JHU-022	12	Head and Neck	Unknown	Oral Cavity Carcinoma
EW-1	12	Bone	Metastasis	Ewing's Sarcoma
no-11	12	Central Nervous System	Tumour	Glioblastoma
DU-145	12	Prostate	Metastasis	Prostate Carcinoma
NB5	12	Peripheral Nervous System	Metastasis	Neuroblastoma

A2780	12	Ovary	Tumour	Ovarian Carcinoma
PL4	12	Pancreas	Unknown	Pancreatic Carcinoma
A2780ADR	12	Ovary	Tumour	Ovarian Carcinoma
C2BBe1	12	Large Intestine	Tumour	Colorectal Carcinoma
LC-1-sq	11	Lung	Tumour	Squamous Cell Lung Carcinoma
COLO-320-HSR	11	Large Intestine	Tumour	Colorectal Carcinoma
PA-TU-8988T	11	Pancreas	Metastasis	Pancreatic Carcinoma
MIA-PaCa-2	11	Pancreas	Tumour	Pancreatic Carcinoma
PCI-38	11	Head and Neck	Unknown	Head and Neck Carcinoma
MCF7	11	Breast	Metastasis	Breast Carcinoma
NCI-N87	10	Stomach	Metastasis	Gastric Carcinoma
VMRC-LCD	10	Lung	Unknown	Lung Adenocarcinoma
COLO-684	10	Endometrium	Tumour	Endometrial Carcinoma
NH-12	10	Peripheral Nervous System	Tumour	Neuroblastoma
MDA-MB-453	10	Breast	Metastasis	Breast Carcinoma
LB771-HNC	10	Head and Neck	Unknown	Head and Neck Carcinoma
AGS	10	Stomach	Tumour	Gastric Carcinoma
EC-GI-10	10	Oesophagus	Metastasis	Oesophageal Squamous Cell Carcinoma
NCI-H1975	9	Lung	Tumour	Lung Adenocarcinoma
HCC1806	9	Breast	Tumour	Breast Carcinoma
ESO26	9	Oesophagus	Tumour	Oesophageal Adenocarcinoma
GP5d	9	Large Intestine	Tumour	Colorectal Carcinoma
FLO-1	9	Oesophagus	Tumour	Oesophageal Adenocarcinoma
ES5	9	Bone	Tumour	Ewing's Sarcoma
PE-CA-PJ15	9	Head and Neck	Tumour	Oral Cavity Carcinoma
RERF-GC-1B	9	Stomach	Metastasis	Gastric Carcinoma
OVCAR-8	8	Ovary	Tumour	Ovarian Carcinoma
LN-229	8	Central Nervous System	Tumour	Glioblastoma
LoVo	8	Large Intestine	Metastasis	Colorectal Carcinoma
EVSA-T	8	Breast	Metastasis	Breast Carcinoma
DAN-G	8	Pancreas	Tumour	Pancreatic Carcinoma
CAPAN-1	8	Pancreas	Metastasis	Pancreatic Carcinoma
NCI-H1944	7	Lung	Metastasis	Lung Adenocarcinoma
SK-N-DZ	7	Peripheral Nervous System	Metastasis	Neuroblastoma
NUGC-3	7	Stomach	Metastasis	Gastric Carcinoma
NB69	7	Peripheral Nervous System	Tumour	Neuroblastoma
A2058	7	Skin	Metastasis	Melanoma

EBC-1	7	Lung	Tumour	Squamous Cell Lung Carcinoma
NCI-H1869	6	Lung	Metastasis	Non-Small Cell Lung Carcinoma
23132-87	6	Stomach	Tumour	Gastric Carcinoma
MOG-G-UVW	6	Central Nervous System	Tumour	Low Grade Glioma
A375	6	Skin	Tumour	Melanoma
HCC1143	6	Breast	Tumour	Breast Carcinoma
CAL-27	6	Head and Neck	Tumour	Oral Cavity Carcinoma
HCE-4	6	Oesophagus	Tumour	Oesophageal Squamous Cell Carcinoma
KP-1N	6	Pancreas	Unknown	Pancreatic Carcinoma
NCI-H2170	6	Lung	Tumour	Squamous Cell Lung Carcinoma
HuP-T4	6	Pancreas	Metastasis	Pancreatic Carcinoma
SNU-61	6	Large Intestine	Metastasis	Colorectal Carcinoma
HSC-4	6	Head and Neck	Tumour	Oral Cavity Carcinoma
COR-L23	6	Lung	Metastasis	Non-Small Cell Lung Carcinoma
OE33	6	Oesophagus	Tumour	Oesophageal Adenocarcinoma
SNU-1	5	Stomach	Tumour	Gastric Carcinoma
LS-1034	5	Large Intestine	Tumour	Colorectal Carcinoma
LNZTA3WT4	5	Central Nervous System	Tumour	Low Grade Glioma
LS-411N	5	Large Intestine	Tumour	Colorectal Carcinoma
BHY	5	Head and Neck	Tumour	Oral Cavity Carcinoma
EW-16	5	Bone	Unknown	Ewing's Sarcoma
NB17	5	Peripheral Nervous System	Metastasis	Neuroblastoma
ESS-1	5	Endometrium	Tumour	Other Solid Carcinomas
SJSA-1	5	Bone	Tumour	Osteosarcoma
EGI-1	5	Biliary Tract	Tumour	Biliary Tract Carcinoma
EFO-27	5	Ovary	Metastasis	Ovarian Carcinoma
CAL-33	5	Head and Neck	Tumour	Oral Cavity Carcinoma
RCM-1	5	Large Intestine	Unknown	Colorectal Carcinoma
PC-14	5	Lung	Tumour	Lung Adenocarcinoma
HARA	5	Lung	Tumour	Squamous Cell Lung Carcinoma
OVCAR-3	5	Ovary	Metastasis	Ovarian Carcinoma
IGROV-1	5	Ovary	Tumour	Ovarian Carcinoma
HT55	5	Large Intestine	Tumour	Colorectal Carcinoma
TE-10	5	Oesophagus	Tumour	Oesophageal Squamous Cell Carcinoma
HEC-1	5	Endometrium	Tumour	Endometrial Carcinoma
T47D	5	Breast	Metastasis	Breast Carcinoma

TE-9	5	Oesophagus	Metastasis	Oesophageal Squamous Cell Carcinoma
PEO1	4	Ovary	Metastasis	Ovarian Carcinoma
HCC1395	4	Breast	Tumour	Breast Carcinoma
KNS-42	4	Central Nervous System	Tumour	Glioblastoma
TOV-21G	4	Ovary	Tumour	Ovarian Carcinoma
AM-38	4	Central Nervous System	Tumour	Glioblastoma
TE-8	4	Oesophagus	Tumour	Oesophageal Squamous Cell Carcinoma
LS-513	4	Large Intestine	Tumour	Colorectal Carcinoma
A172	4	Central Nervous System	Tumour	Glioblastoma
PEO4	4	Ovary	Metastasis	Ovarian Carcinoma
T98G	4	Central Nervous System	Tumour	Glioblastoma
JHOS-2	4	Ovary	Tumour	Ovarian Carcinoma
JHOS-4	4	Ovary	Tumour	Ovarian Carcinoma
HPAF-II	4	Pancreas	Metastasis	Pancreatic Carcinoma
Hey	4	Ovary	Tumour	Ovarian Carcinoma
PCI-15A	4	Head and Neck	Unknown	Head and Neck Carcinoma
CL-11	4	Large Intestine	Tumour	Colorectal Carcinoma
SCH	4	Stomach	Tumour	Gastric Carcinoma
MFM-223	4	Breast	Metastasis	Breast Carcinoma
HSC-39	4	Stomach	Unknown	Gastric Carcinoma
MHH-ES-1	4	Bone	Metastasis	Ewing's Sarcoma
NB6	3	Peripheral Nervous System	Metastasis	Neuroblastoma
A2780cis	3	Ovary	Tumour	Ovarian Carcinoma
DiFi	3	Large Intestine	Metastasis	Colorectal Carcinoma
NCI-H1355	3	Lung	Metastasis	Lung Adenocarcinoma
SCC-9	3	Head and Neck	Tumour	Oral Cavity Carcinoma
JHU-029	3	Head and Neck	Tumour	Head and Neck Carcinoma
RKN	3	Soft Tissue	Tumour	Other Solid Carcinomas
DOV13	3	Ovary	Unknown	Ovarian Carcinoma
NCI-H1993	3	Lung	Metastasis	Lung Adenocarcinoma
KATOIII	3	Stomach	Metastasis	Gastric Carcinoma
769-P	3	Kidney	Tumour	Kidney Carcinoma
OC-314	3	Ovary	Metastasis	Ovarian Carcinoma
Caov-4	3	Ovary	Metastasis	Ovarian Carcinoma
OE21	3	Oesophagus	Tumour	Oesophageal Squamous Cell Carcinoma
no-10	3	Central Nervous System	Tumour	Glioblastoma
PA-TU-8902	3	Pancreas	Tumour	Pancreatic Carcinoma
COLO-205	3	Large Intestine	Metastasis	Colorectal Carcinoma

KYSE-410	3	Oesophagus	Tumour	Oesophageal Squamous Cell Carcinoma
22RV1	3	Prostate	Tumour	Prostate Carcinoma
NB10	3	Peripheral Nervous System	Metastasis	Neuroblastoma
SW48	3	Large Intestine	Tumour	Colorectal Carcinoma
SNU-81	3	Large Intestine	Tumour	Colorectal Carcinoma
KURAMOCHI	3	Ovary	Metastasis	Ovarian Carcinoma
KLE	3	Endometrium	Tumour	Endometrial Carcinoma
KYSE-150	3	Oesophagus	Tumour	Oesophageal Squamous Cell Carcinoma
KP-N-YN	3	Peripheral Nervous System	Metastasis	Neuroblastoma
SU-DHL-5	3	Haematopoietic and Lymphoid	Tumour	B-Cell Non-Hodgkin's Lymphoma
LU-99A	3	Lung	Tumour	Non-Small Cell Lung Carcinoma
LXF-289	3	Lung	Tumour	Lung Adenocarcinoma
TE-4	3	Oesophagus	Metastasis	Oesophageal Squamous Cell Carcinoma
HCC-78	3	Lung	Metastasis	Lung Adenocarcinoma
BICR10	3	Head and Neck	Tumour	Oral Cavity Carcinoma
SU-DHL-8	3	Haematopoietic and Lymphoid	Metastasis	B-Cell Non-Hodgkin's Lymphoma
SUIT-2	3	Pancreas	Metastasis	Pancreatic Carcinoma
AsPC-1	3	Pancreas	Metastasis	Pancreatic Carcinoma
BICR78	3	Head and Neck	Tumour	Oral Cavity Carcinoma
SF126	3	Central Nervous System	Tumour	Glioblastoma
PCI-30	2	Head and Neck	Unknown	Head and Neck Carcinoma
PANC-03-27	2	Pancreas	Tumour	Pancreatic Carcinoma
PANC-04-03	2	Pancreas	Tumour	Pancreatic Carcinoma
CHP-212	2	Peripheral Nervous System	Tumour	Neuroblastoma
PANC-10-05	2	Pancreas	Tumour	Pancreatic Carcinoma
SU-DHL-10	2	Haematopoietic and Lymphoid	Metastasis	B-Cell Non-Hodgkin's Lymphoma
SNU-C5	2	Large Intestine	Tumour	Colorectal Carcinoma
AU565	2	Breast	Metastasis	Breast Carcinoma
T-T	2	Oesophagus	Tumour	Oesophageal Squamous Cell Carcinoma
BB30-HNC	2	Head and Neck	Unknown	Head and Neck Carcinoma
hTERT-RPE-1	2	Eye	Transformed	Non-Cancerous
CAS-1	2	Central Nervous System	Tumour	Glioblastoma

SCC90	2	Head and Neck	Metastasis	Head and Neck Carcinoma
SK-GT-4	2	Oesophagus	Tumour	Oesophageal Adenocarcinoma
SCC-4	2	Head and Neck	Tumour	Oral Cavity Carcinoma
SK-MES-1	2	Lung	Metastasis	Squamous Cell Lung Carcinoma
RMG-I	2	Ovary	Tumour	Ovarian Carcinoma
BxPC-3	2	Pancreas	Tumour	Pancreatic Carcinoma
TE-5	2	Oesophagus	Tumour	Oesophageal Squamous Cell Carcinoma
COLO-680N	2	Oesophagus	Tumour	Oesophageal Squamous Cell Carcinoma
RERF-LC-Sq1	2	Lung	Tumour	Squamous Cell Lung Carcinoma
A253	2	Head and Neck	Tumour	Head and Neck Carcinoma
SK-N-SH	2	Peripheral Nervous System	Metastasis	Neuroblastoma
RCC-FG2	2	Kidney	Tumour	Kidney Carcinoma
PSN1	2	Pancreas	Tumour	Pancreatic Carcinoma
SK-PN-DW	2	Central Nervous System	Tumour	Other Solid Carcinomas
PCI-4B	2	Head and Neck	Unknown	Head and Neck Carcinoma
SW1990	2	Pancreas	Metastasis	Pancreatic Carcinoma
HOP-62	2	Lung	Tumour	Lung Adenocarcinoma
OVCAR-5	2	Ovary	Unknown	Ovarian Carcinoma
DBTRG-05MG	2	Central Nervous System	Tumour	Glioblastoma
NCI-H1568	2	Lung	Metastasis	Lung Adenocarcinoma
NCI-H1650	2	Lung	Metastasis	Lung Adenocarcinoma
GB-1	2	Central Nervous System	Tumour	Glioblastoma
NCI-H2023	2	Lung	Metastasis	Non-Small Cell Lung Carcinoma
DOK	2	Head and Neck	Tumour	Oral Cavity Carcinoma
MFE-280	2	Endometrium	Tumour	Endometrial Carcinoma
MDA-MB-231	2	Breast	Metastasis	Breast Carcinoma
NCI-H3118	2	Head and Neck	Unknown	Head and Neck Carcinoma
MDST8	2	Large Intestine	Tumour	Colorectal Carcinoma
LOU-NH91	2	Lung	Tumour	Squamous Cell Lung Carcinoma
ES8	2	Bone	Tumour	Ewing's Sarcoma
HCT-116	2	Large Intestine	Tumour	Colorectal Carcinoma
KMS-11	2	Haematopoietic and Lymphoid	Metastasis	Plasma Cell Myeloma

HO-1-u-1	2	Head and Neck	Tumour	Oral Cavity Carcinoma
HSC-3	2	Head and Neck	Tumour	Oral Cavity Carcinoma
D-542MG	2	Central Nervous System	Tumour	Glioblastoma
JIMT-1	2	Breast	Metastasis	Breast Carcinoma
JHU-011	2	Head and Neck	Unknown	Head and Neck Carcinoma
IST-MEL1	2	Skin	Tumour	Melanoma
HuP-T3	2	Pancreas	Tumour	Pancreatic Carcinoma
COLO-824	2	Breast	Metastasis	Breast Carcinoma
MDA-MB-436	2	Breast	Metastasis	Breast Carcinoma
Hs-578-T	2	Breast	Tumour	Breast Carcinoma
OV-90	2	Ovary	Metastasis	Ovarian Carcinoma
L-363	1	Haematopoietic and Lymphoid	Tumour	Plasma Cell Myeloma
EW-22	1	Bone	Unknown	Ewing's Sarcoma
SNU-C1	1	Large Intestine	Metastasis	Colorectal Carcinoma
KYSE-270	1	Oesophagus	Tumour	Oesophageal Squamous Cell Carcinoma
LS-180	1	Large Intestine	Tumour	Colorectal Carcinoma
KYSE-450	1	Oesophagus	Tumour	Oesophageal Squamous Cell Carcinoma
KYAE-1	1	Oesophagus	Tumour	Oesophageal Adenocarcinoma
HCC1937	1	Breast	Tumour	Breast Carcinoma
SW620	1	Large Intestine	Metastasis	Colorectal Carcinoma
ARH-77	1	Haematopoietic and Lymphoid	Transformed	Non-Cancerous
SW837	1	Large Intestine	Tumour	Colorectal Carcinoma
HCC1954	1	Breast	Tumour	Breast Carcinoma
T84	1	Large Intestine	Metastasis	Colorectal Carcinoma
HCC38	1	Breast	Tumour	Breast Carcinoma
KP-3	1	Pancreas	Metastasis	Pancreatic Carcinoma
KINGS-1	1	Central Nervous System	Tumour	Low Grade Glioma
IM-95	1	Stomach	Tumour	Gastric Carcinoma
42-MG-BA	1	Central Nervous System	Tumour	Glioblastoma
LU-65	1	Lung	Tumour	Non-Small Cell Lung Carcinoma
MCAS	1	Ovary	Unknown	Ovarian Carcinoma
MDA-MB-415	1	Breast	Metastasis	Breast Carcinoma
EFO-21	1	Ovary	Metastasis	Ovarian Carcinoma
OSC-20	1	Head and Neck	Metastasis	Oral Cavity Carcinoma
OSC-19	1	Head and Neck	Metastasis	Oral Cavity Carcinoma

OPM-2	1	Haematopoietic and Lymphoid	Tumour	Plasma Cell Myeloma
PANC-08-13	1	Pancreas	Tumour	Pancreatic Carcinoma
OACM5-1	1	Oesophagus	Metastasis	Oesophageal Adenocarcinoma
NCI-H650	1	Lung	Tumour	Lung Adenocarcinoma
NCI-H322M	1	Lung	Tumour	Lung Adenocarcinoma
NCI-H226	1	Lung	Metastasis	Mesothelioma
ROS-50	1	Haematopoietic and Lymphoid	Tumour	B-Cell Non-Hodgkin's Lymphoma
Becker	1	Central Nervous System	Tumour	Low Grade Glioma
NCI-H1299	1	Lung	Metastasis	Non-Small Cell Lung Carcinoma
NCI-H1915	1	Lung	Metastasis	Non-Small Cell Lung Carcinoma
BICR22	1	Head and Neck	Metastasis	Oral Cavity Carcinoma
EPLC-272H	1	Lung	Tumour	Other Solid Carcinomas
SF539	1	Central Nervous System	Tumour	Glioblastoma
HCC-15	0	Lung	Tumour	Squamous Cell Lung Carcinoma
U-87-MG	0	Central Nervous System	Tumour	Glioblastoma
LS-123	0	Large Intestine	Tumour	Colorectal Carcinoma
TMK-1	0	Stomach	Unknown	Gastric Carcinoma
OAW-42	0	Ovary	Metastasis	Ovarian Carcinoma
D-502MG	0	Central Nervous System	Tumour	Glioblastoma
SNB75	0	Central Nervous System	Tumour	Glioblastoma
IM-9	0	Haematopoietic and Lymphoid	Transformed	Non-Cancerous
KM12	0	Large Intestine	Tumour	Colorectal Carcinoma
OCI-LY-19	0	Haematopoietic and Lymphoid	Tumour	B-Cell Non-Hodgkin's Lymphoma
SKN-3	0	Head and Neck	Unknown	Head and Neck Carcinoma
PANC-02-03	0	Pancreas	Tumour	Pancreatic Carcinoma
YH-13	0	Central Nervous System	Tumour	Glioblastoma
SK-MEL-2	0	Skin	Metastasis	Melanoma
ESO51	0	Oesophagus	Tumour	Oesophageal Adenocarcinoma
NCI-H358	0	Lung	Tumour	Lung Adenocarcinoma
PCI-6A	0	Head and Neck	Unknown	Head and Neck Carcinoma
LCLC-97TM1	0	Lung	Tumour	Non-Small Cell Lung Carcinoma
SNU-16	0	Stomach	Metastasis	Gastric Carcinoma
HCC70	0	Breast	Tumour	Breast Carcinoma
NCI-H3122	0	Lung	Tumour	Lung Adenocarcinoma
CAL-72	0	Bone	Tumour	Osteosarcoma

DK-MG	0	Central Nervous System	Tumour	Glioblastoma
COLO-678	0	Large Intestine	Metastasis	Colorectal Carcinoma
NCI-H1755	0	Lung	Metastasis	Lung Adenocarcinoma
LNCaP-Clone-FGC	0	Prostate	Metastasis	Prostate Carcinoma
RPMI-8226	0	Haematopoietic and Lymphoid	Tumour	Plasma Cell Myeloma
ES4	0	Bone	Tumour	Ewing's Sarcoma
KYSE-520	0	Oesophagus	Tumour	Oesophageal Squamous Cell Carcinoma
KYSE-70	0	Oesophagus	Tumour	Oesophageal Squamous Cell Carcinoma
SU8686	0	Pancreas	Metastasis	Pancreatic Carcinoma
NMC-G1	0	Central Nervous System	Tumour	Low Grade Glioma

Appendix B. Top contributing wavelengths separating treatment groups by LDA, comparing A549 and H460 NSCLC cells under different glucose concentrations

Band Peak	Molecule	Contribution	Mean Peak Area			
			A549 11 mM	A549 1 mM	H460 11 mM	H460 1 mM
407	Glucose	Energy metabolism	0.391	0.362	0.370	0.122
445	N-C-S bend	LD1	0.455	0.409	0.384	0.215
481	Glycogen	LD1	0.696	0.642	0.609	0.356
525	Phosphatidylserine	LD1, LD2	0.831	0.810	0.812	0.386
573	Tryptophan/ cytosine/ guanine	LD2	0.605	0.598	0.596	0.199
608	Cholesterol	LD2	0.135	0.128	0.128	0.048
621	Phenylalanine	LD1	0.393	0.388	0.385	0.153
720	Adenine	LD2	0.811	0.748	0.814	0.321
750	Cytochrome *c*	Mitochondrial metabolism	0.758	0.739	0.802	0.408
781	Cytosine	LD1	0.946	0.886	1.063	0.720
810	Nucleic acids	LD2	0.391	0.398	0.463	0.304
815	Proline/ hydroxyproline/tyrosine	LD2	0.424	0.449	0.494	0.344
855	Proline/ tyrosine	LD2	0.644	0.701	0.777	0.619
876	Hydroxyproline	LD1	0.644	0.701	0.777	0.619
913	Glucose	Energy metabolism	0.146	0.149	0.165	0.236
933	Proline	LD1, LD2	0.983	1.008	1.112	0.986
1082	Carbohydrates	LD2	0.316	0.315	0.350	0.206
1094	DNA	LD2	0.793	0.794	0.897	0.448
1125	Glucose	Energy metabolism	0.817	0.812	0.814	0.376
1150	Glycogen	LD2	0.238	0.246	0.242	0.131
1168	Lipids	Lipid metabolism	0.300	0.293	0.297	0.155
1208	Hydroxyproline/ tyrosine/ tryptophan/ phenylalanine	LD2	0.887	0.910	1.001	0.475
1255	Lipids	Lipid metabolism	3.431	3.550	3.755	2.830
1311	Cytochrome *c*	Mitochondrial metabolism	4.710	4.842	5.082	4.164
1465	Lipids	Lipid metabolism	5.496	5.536	5.573	4.891
1583	Cytochrome *c*	Mitochondrial metabolism	2.052	2.044	2.018	0.979
1618	Tryptophan	LD1, LD2	1.328	1.376	1.351	1.089
1656	Amide I / lipid stretching	LD1, LD2	4.272	4.362	4.499	4.709
1738	Lipids	LD2	0.600	0.560	0.571	0.181
2700	Stretching of -CH, -NH, and -OH	LD1, LD2	1.944	1.903	1.925	2.149
3059	Aromatic stretching	LD1, LD2	2.682	2.814	2.734	3.648
3240	Water	LD1, LD2	0.517	0.504	0.496	0.760
3300	-OH stretching	LD1, LD2	1.099	1.154	1.089	1.838

Appendix C. Top contributing wavelengths separating treatment groups by LDA, comparing A549 cells with NBS037 and AA treatment

Band Peak	Molecule	Contribution	Mean Peak Area			
			A549 Untreated	A549 NBS0.5 μM	A549 NBS1 μM	A549 AA
337	NBS037	LD1, LD2	0.357	0.463	0.357	0.242
357	Polyhydroxybutyrate	LD2	0.209	0.146	0.209	0.196
395	NBS037	LD1, LD2	0.328	0.493	0.328	0.208
407	Glucose	Energy metabolism	0.190	0.295	0.067	0.130
481	Glycogen	LD2	0.576	0.496	0.576	0.439
490	Cholesterol	LD2	0.263	0.234	0.263	0.163
573	Tryptophan/ cytosine/ guanine	LD1	0.337	0.506	0.337	0.265
576	Phosphatidylinositol	LD1	0.130	0.157	0.130	0.099
610	NBS037	NBS037	0.335	0.378	0.335	0.233
642	Tyrosine	LD1, LD2	0.175	0.264	0.175	0.132
667	Cysteine	LD1, LD2	0.336	0.475	0.336	0.247
673	NBS037	NBS037	0.365	0.505	0.365	0.260
702	Cholesterol	LD1, LD2	0.150	0.210	0.222	0.097
720	Adenine	LD2	0.455	0.660	0.455	0.355
750	Cytochrome *c*	Mitochondrial Metabolism	0.587	0.755	0.587	0.485
913	Glucose	Energy metabolism	0.256	0.177	0.256	0.261
968	Lipids	LD1	0.182	0.353	0.182	0.194
993	NBS037	NBS037	0.843	1.314	0.843	0.900
1022	NBS037	LD2	0.929	1.164	0.929	0.938
1100	NBS037	NBS037	0.864	1.345	0.864	0.878
1125	Glucose	LD2	0.541	0.768	0.541	0.475
1168	Lipids	Lipid metabolism	0.246	0.289	0.246	0.240
1255	Lipids	Lipid metabolism	3.059	3.636	3.059	3.383
1290	Cytosine	LD1	0.956	1.113	0.956	1.069
1299	NBS037	NBS037	0.785	0.888	0.785	0.867
1311	Cytochrome *c*	Mitochondrial metabolism	4.488	5.071	4.488	4.933
1377	NBS037	NBS037	0.483	0.553	0.483	0.509
1404	CH deformation	LD2	0.362	0.421	0.362	0.382
1444	NBS037	NBS037	0.964	1.039	0.964	1.099
1465	Lipids	LD1	4.994	5.515	4.994	5.446
1513	Cytosine	LD2	0.213	0.222	0.213	0.201
1558	Tyrosine	LD1	0.354	0.492	0.354	0.364
1575	Guanine/ adenine	LD1	0.980	1.342	0.980	1.065
1583	Cytochrome *c*	Mitochondrial metabolism	1.456	1.984	1.456	1.545
1584	NBS037	NBS037	1.071	1.458	1.071	1.167

1618	Tryptophan	LD1	1.380	1.613	1.380	1.580
1716	C-C of phosphatidylserine	LD1	0.094	0.172	0.094	0.088
1738	Lipids	LD1	0.280	0.489	0.280	0.207
2700	Stretching of -CH, NH, and -OH	LD1, LD2	1.962	1.877	1.962	1.674
3057	NBS037	NBS037	2.614	2.272	2.614	2.723
3059	Aromatic stretching	LD1, LD2	3.349	2.852	3.349	3.413
3240	Water	LD1, LD2	0.679	0.493	0.679	0.518
3300	-OH stretching	LD1, LD2	1.752	1.250	1.752	1.654

Appendix D. Top contributing wavelengths separating treatment groups by LDA, comparing H460 and A549 cells with NBS037 and AA treatment

Band Peak	Molecule	Contribution	Mean Peak Area				
			H460 11mM	H460 NBS0.5μM	H460 NBS1μM	H460 AA	A549 11mM
337	NBS037	NBS037	0.547	0.298	0.276	0.242	0.603
395	NBS037	NBS037	0.678	0.266	0.225	0.212	0.712
407	Glucose	Energy metabolism	0.370	0.159	0.138	0.136	0.391
481	Glycogen	LD1, LD2	0.609	0.512	0.484	0.459	0.696
573	Tryptophan/ cytosine/ guanine	LD2	0.596	0.293	0.235	0.218	0.605
589	Glycerol	LD1	0.231	0.160	0.139	0.130	0.240
610	NBS037	NBS037	0.453	0.286	0.240	0.243	0.463
621	Phenylalanine	LD1	0.385	0.227	0.183	0.186	0.393
673	NBS037	NBS037	0.829	0.322	0.251	0.224	1.042
750	Cytochrome *c*	Mitochondrial metabolism	0.802	0.530	0.382	0.360	0.758
810	Nucleic acids	LD2	0.463	0.394	0.338	0.274	0.391
815	Proline/ hydroxyproline/ tyrosine	LD2	0.494	0.423	0.373	0.324	0.424
828	Tyrosine	LD1, LD2	0.383	0.545	0.475	0.442	0.539
855	Proline/ tyrosine	LD2	0.777	0.729	0.644	0.596	0.644
876	Hydroxyproline	LD1, LD2	0.377	0.364	0.331	0.310	0.321
898	Adenine	LD1	0.350	0.361	0.320	0.295	0.307
913	Glucose	LD1	0.165	0.181	0.154	0.143	0.146
933	Proline	LD1, LD2	1.112	1.051	0.869	0.813	0.983
993	NBS037	NBS037	1.271	0.873	0.774	0.718	1.129
1022	NBS037	NBS037	1.252	0.975	0.967	0.909	1.168
1054	Nucleic acids/ PHB	LD1	0.353	0.296	0.302	0.282	0.356
1100	NBS037	NBS037	1.442	0.910	0.864	0.786	1.289
1125	Glucose	Energy metabolism	1.157	0.681	0.426	0.563	1.122
1150	Glycogen	LD1, LD2	0.242	0.176	0.172	0.148	0.238
1168	Lipids	Lipid metabolism	0.297	0.211	0.194	0.178	0.300
1255	Lipids	Lipid metabolism	3.755	3.095	3.246	3.200	3.431
1299	NBS037	NBS037	0.884	0.811	0.825	0.828	0.812
1311	Cytochrome *c*	Mitochondrial metabolism	5.082	4.501	4.489	4.537	4.710
1377	NBS037	NBS037	0.583	0.480	0.968	0.439	0.545
1444	NBS037	NBS037	0.997	1.065	1.118	1.175	0.952
1465	Lipids	Lipid metabolism	5.573	5.162	5.310	5.417	5.496

1583	Cytochrome *c*	Mitochondrial metabolism	2.018	1.247	1.188	1.201	2.052
1584	NBS037	NBS037	1.462	0.938	0.939	0.966	1.481
1618	Tryptophan	LD1	1.579	1.328	1.452	1.503	1.563
1637	Amide I/ Lipid stretching	LD1	4.231	4.644	4.927	5.082	4.012
2700	Stretching of -CH, NH and -OH	LD1, LD2	1.925	1.841	1.772	1.787	1.944
3057	NBS037	NBS037	2.139	2.684	2.675	2.725	2.108
3059	Aromatic stretching	LD1, LD2	2.734	3.405	3.374	3.427	2.682
3240	Water	LD1, LD2	0.496	0.629	0.665	0.625	0.517
3300	-OH stretching	LD1, LD2	1.089	1.679	1.759	1.715	1.099

Appendix E. Achievements throughout the duration of my DPhil

Conferences attended

2020 International Society for Cancer Metabolism 7th Annual Meeting, online.

2021 International Society for Cancer Metabolism 8th Annual Meeting, online.

MitOX, Oxford.

Oxford Immunology Symposium 2021, online.

Oxford Metabolic Health Symposium, online.

Drug Tolerant Persister Cells, online.

2022 MitOX, Oxford.

Mitochondrial Medicine - Therapeutic Development 2022, online.

2023 OXCODE Symposium, Oxford.

CRUK Annual Symposium, Oxford.

MitOX, Oxford.

2024 MitOx, Oxford.

Presentations

2023 **Abstract and poster at OXCODE Symposium, Oxford.**

Stoker, M., Hulit, J., and Morten, K. Targeting mitochondrial metabolism as a promising therapeutic strategy in cancer upon early detection of OXPHOS dependence in tumour and metastatic cells.

Abstract and poster at CRUK Annual Symposium, Oxford.

Stoker, M., Hulit, J., Higgins, G., and Morten, K. Targeting mitochondrial metabolism as a promising therapeutic strategy in cancer.

Abstract, poster, and short talk at MitOX.

Stoker M., Hulit, J., Higgins, G., and Morten, K. Targeting mitochondrial metabolism as a promising therapeutic strategy in cancer.

2024 **Abstract and poster at MitOx, Oxford.**

Stoker M., Hutchinson S., Morten, K., and Huang, W. Developing Raman microspectroscopy to determine the OXPHOS /glycolysis status of cells.

Short talk at Nuffield Department of Women's and Reproductive Health Science Day

Targeting mitochondrial metabolism as a promising therapeutic strategy in cancer.

Awards

2022 **CRUK Development Fund**

Stoker, M. and Morten, K. Developing Raman microspectroscopy to determine the OXPHOS /glycolysis status of patient tumours. Collaborators: Huang, W., Harris, A., Higgins, G., and Lord, S.

Other achievements

2021 Blue Boat selection for the Oxford v Cambridge Boat Race.

Blades in Summer Torpids (W1).

Gold in annual international Sveti Duje regatta, Croatia.

2022 Osiris selection for the Oxford v Cambridge Reserve Race.

Blades in Summer Eights (M1).

2024 World Record for Longest Continual Row (10 days) with St. Peter's College Boat Club.